UC-94c
LBL-20503 c.1

Lawrence Berkeley Laboratory
UNIVERSITY OF CALIFORNIA

RECEIVED
LAWRENCE
BERKELEY LABORATORY
6 1986
LIBRARY AND
DOCUMENTS SECTION

Materials & Molecular Research Division

AN ELLIPSOMETRIC SPECTROSCOPY STUDY OF ANODICALLY FORMED SILVER (I) OXIDE FILMS ON SILVER

S.T. Mayer* and R.H. Muller
(*M.S. Thesis)

December 1985

For Reference
Not to be taken from this room

Prepared for the U.S. Department of Energy under Contract DE-AC03-76SF00098

LBL-20503 c.1

DISCLAIMER

This document was prepared as an account of work sponsored by the United States Government. While this document is believed to contain correct information, neither the United States Government nor any agency thereof, nor the Regents of the University of California, nor any of their employees, makes any warranty, express or implied, or assumes any legal responsibility for the accuracy, completeness, or usefulness of any information, apparatus, product, or process disclosed, or represents that its use would not infringe privately owned rights. Reference herein to any specific commercial product, process, or service by its trade name, trademark, manufacturer, or otherwise, does not necessarily constitute or imply its endorsement, recommendation, or favoring by the United States Government or any agency thereof, or the Regents of the University of California. The views and opinions of authors expressed herein do not necessarily state or reflect those of the United States Government or any agency thereof or the Regents of the University of California.

LBL-20503

An Ellipsometric Spectroscopy Study of Anodically Formed Silver (I) Oxide Films on Silver

Steven Thomas Mayer* and R.H. Muller

*M.S. Thesis

Lawrence Berkeley Laboratory
University of California
Berkeley, California 94720

December 1985

AN ELLIPSOMETRIC SPECTROSCOPY STUDY OF ANODICALLY FORMED SILVER (I) OXIDE FILMS ON SILVER

Steven T. Mayer

Materials and Molecular Research Division
Lawrence Berkeley Laboratory
and
Department of Chemical Engineering
University of California
Berkeley, California 94720

ABSTRACT

Spectroscopic ellipsometry has been used in combination with electrochemical measurements to determine details of the nucleation process of silver oxide anodically formed on silver in 1M KOH solutions. Spectroscopic ellipsometry is shown to be sufficiently sensitive to determine parameters pertaining to the growth rate and morphology of crystalline oxide films.

The anodic film starts as a submonolayer and then grows into a uniform multilayer. At potentials below a nucleation potential (approximately 200 mV versus Ag/AgCl 4M KCl), current efficiencies for film growth are small, because most of the oxidized material dissolves. When a certain degree of supersaturation is reached (23X saturation), a crystalline oxide is nucleated. The crystals grow, in part, by the transfer of oxide from the uniform multilayer with the rate of oxide growth controlled by the rate of incorporation of dissolved material at the crystal/solution interface. Due to the high solubility of small nuclei, a transfer of material from smaller to larger crystals occurs in the early stages of crystal growth. A theoretical model of a dissolution/precipitation process is presented for the current response to an applied potential step.

TABLE OF CONTENTS

CHAPTER 1 -- LITERATURE REVIEW 1

Formation of Surface Layers on Silver 1

Kinetics and Morphology 1

Mechanisms of Film Growth 9

Heterogeneous Electrocrystallization 11

Objective of the Present Study 22

References 23

Figure Captions 28

Figures 29

CHAPTER 2 -- EXPERIMENTAL TECHNIQUES AND PROCEDURES 30

Ellipsometric Principles 30

Optical Measurement Systems 32

Data Acquisition Routines 34

Instrument Calibrations 36

A) Wavelength Calibration of the Digital Encoder 36

B) Calibration of the Faraday Cells 37

Data-Reduction Routines 38

Electrochemical Measurements 40

Errors Due to Ellipsometer Components 40

Experimental Procedures 43

A) Surface Preparation 43

B) Electrolyte Preparation 44

C) Cell Preparation 45

D) Experimental Execution 46

Post-Experiment Electrode Treatment 47

Conclusions 47

References 49

Tables 51

Figure Captions 54

Figures 56

CHAPTER 3 -- MEASUREMENTS 71

Optical Properties of Silver and Silver Oxide 71

Galvanostatic Experiments 72

Cyclic-Voltammetry and Potential-Ramping Experiments 76

Potentiostatic Experiments 81

Potential Pulse and Corrosion Measurements 84

Scanning Electron Micrographs 85

Conclusions 88

References 90

Tables 91

Figure Captions 92

Figures 96

CHAPTER 4 -- CALCULATIONS AND RESULTS 135

Calculations of the Primary Current Distribution 135

Ellipsometric Principles for Modeling 136

Optical Models 141

Data-Fitting Routines 146

Modeling Potentiostatic Current Transients 148

Interpretations of Potential Sweep Measurements 154

Interpretations of Galvanostatic Optical Measurements 157

Interpretations of Potentiostatic Optical Measurements 161

Conclusions 166

References 168

Tables 170

Figure Captions 172

Figures 178

ACKNOWLEDGEMENTS 218

CHAPTER 1

LITERATURE REVIEW

FORMATION OF SURFACE LAYERS ON SILVER

There has been an ongoing interest in the anodic silver/silver oxide electrochemical couple for at least 40 years. This system is of both academic and practical interest. The major application of this couple is in the Ag/AgO electrode in batteries that have a large energy-to-mass ratio. The system is highly reversible and has an anodic-to-cathodic charge ratio approaching unity under certain conditions. Silver, being a relatively noble metal, has a standard redox potential of +0.7996 V for the formation of silver ion versus the normal hydrogen electrode (NHE) [1]. The solubility product of silver(I) oxide has been quoted as 2.0×10^{-8} M/l, and the standard potential for the formation of silver(I) oxide is +334 mV versus NHE (+112 mV versus Ag/AgCl 4M KCl reference electrode) [1]. Because of this high redox potential, the power output of any cell that uses this reaction can be great. Also, the formation of the different valence-state oxides occurs in clearly separate stages. The system is academically interesting in that voltammetric and optical studies show a variety of intriguing results and both the physical and chemical method of film formation is still unclear, despite all the work done on the system.

KINETICS AND MORPHOLOGY

Zimmerman [3] showed that Ag is first oxidized to Ag_2O and then to AgO. The initial reaction rate increases with applied potential, but

some form of activation and then passivation of the surface was evident in the transient current responses. Early studies showed that silver oxide batteries had a two-step reduction only at low current drains [2]. At higher drains, only a one-step reduction was found, with the potential corresponding to that of Ag_2O reduction. This one step reduction indicates that the higher-valence oxide (AgO), with its higher redox potential, was reduced to Ag_2O prior to reduction to silver.

The surface-layer reaction products were identified by Wales and Burbank [4], who used x-ray diffraction and showed that Ag_2O preceded the formation of AgO. Their measurements, as well as those made later by Briggs et al. [5], indicated a crystalline oxide product, and these crystals formed as distinct centers rather than as expansions of the silver lattice [4]. The orientation of these products seems to be primarily of the (111) faces, but some (110) faces were seen at glancing angles of incidence [5]. Based on x-ray diffraction, scanning electron micrographs (SEM), and electron-diffraction measurements, the morphology of the films formed on silver were described as multilayered [5]. SEM photographs were made at various stages of the galvanostatic and potentiostatic charging processes. An underlayer of crystals with maximum diameters of 200 Å (called the "primary layer") forms first. Later larger oxide crystals of smaller number density form on top of the primary layer (secondary crystals). Crystals with different crystallographic orientations are reported to show variation in crystal size distributions, with the Ag_2O (111) orientations showing the smallest standard deviation in size. Also, potentiostatic secondary-crystal size distributions were reported to be narrower than those of crystals formed

by galvanostatic charging, and the total number density of crystals has been found to increase with potential and current density. Because of the lack of difference in shape or size of the crystallites with applied potential, it was concluded that the overall kinetics was not controlled by the kinetics at the metal-oxide interface. Finally, a tertiary layer of small (50-200 Å) crystals was found to form on top of the secondary crystals. This general description of a multilayer structure is compatible with more recent ellipsometric studies [6-10]. However, other authors have described the surface layers as being porous [12,13], continuous [8,13,14], and hydrated [6-8].

From the linear dependence of the solubility of Ag_2O with OH^- at moderate hydroxide concentration, Johnston et al. [15,16] proposed that the major soluble species is AgO^- ion. The existence of a silver oxide ion has been supported by chemical-stability studies [17]. While a hydrated form of this ion has been mentioned as the soluble species in the literature as $Ag(OH)_2^-$ [11,12,17], calculations by Pound et al. [18] of electrochemical thermodynamic data for the system show that AgO^- is the most soluble ion at high pH, with silver ion the most soluble species at lower pH. The solubility of Ag_2O is reported to pass through a minimum at a pH of around 12, where its solubility is 1.9×10^{-6} M/l. The stability of AgO^- increases with temperature in aqueous solutions. Pound reported that AgO is thermodynamically unstable in aqueous solutions [18].

One of the most widely used techniques in electrochemistry today is repetitive triangular potential-sweep voltammetry (RTPS), also known as cyclic voltammetry. Responses for these types of experiments generally

show four characteristic anodic peaks for the Ag/Ag_2O system, and they are referred to as the A1 to A4 peaks (see Figure A1). The first peak, "A1," was originally identified by Dirske and DeVries [19], who reported a potential of formation of +52 mV versus saturated calomel electrode (SCE) (+105 mV vs. Ag/AgCl 4M KCl) on polycrystalline electrodes. They assigned this peak to AgOH formation, accompanied by a slight dissolution of the electrode. Our results led us to a similar conclusion, and a number of other authors are in agreement with this general conclusion as well [9,11,22,27,28,30]. For instance, thermodynamic calculations by Pound et al. [18] show that AgO^- should form before bulk silver oxide. Others have interpreted the A1 peak as due to carbonate impurities [12,20], since it is possible to form Ag_2CO_3 in alkaline solution [21]. Stonehart believed that the A1 peak arose due to the manner of the production of silver, since the peak was not observed upon oxidation of silver eletrodeposited from plating paths. The effect of carbonate levels on the voltammograms has since been studied [9], and there was no effect on the A1 peak. The size and appearance of this peak also appears to depend on the crystal face, with the Ag(110) face being more reactive than the Ag(111) face [10]. Also, the open-circuit solution contact time and the time of cycling affects whether the A1 peak is observed [22]. This peak has also been referred to as the A1' peak by Perkins et al.[35]. Earlier authors who don't report the existence of peak A1 [100 mV < E_p < 190 mV] refer to the sequence of peaks as A1, A2, and A3, which we here refer to as A2, A3, and A4. It is important that the reader of the literature understand this discrepancy.

The A2 and A3 peaks (around +200 and +400 mV vs. Ag/AgCl 4M KCl, respectively) have generally been associated with the formation of bulk oxides. Hampel and Tomkiewicz [13] stated that the A2 peak is still the "initial stages of oxidation." Hampson [23] explained the A2 peak as the preferential oxidation of surface atoms of low coordination numbers. Teijelo et al. [8] said that the A2 and A3 peaks are different hydrates of silver oxide. The A4 peak (formation potential of around +550 – 600 mV vs. Ag/AgCl 4M KCl) is the formation of AgO, and this peak will not be discussed in this dissertation. All ellipsometric measurements made in this dissertation were of films formed at potentials below +250 mV versus Ag/AgCl, 4M KCL.

Galvanostatic experiments were one of the earliest types of electrochemical experiments performed, due mainly to the fact that galvanostatic current sources were commercially available before "potentiostats." In a galvanostatic experiment the flux of the electroactive species is kept constant. The typical polarization curve [5,24–28] for a galvanostatic charging of silver/silver oxide shows a rising potential that peaks early but later has a shallow dip. These features are most prevalent at lower current densities and higher temperatures [24]. This first region is usually considered the formation of Ag_2O, as x-ray and electron-diffraction studies have shown [5], but the reason for the apparent autocatalytic potential dip has not been given an adequate explanation. Later, there is a steep rise to a potential that Cahan [25] says coincides with complete coverage of the surface with Ag_2O. A discontinuity is usually present following this steep rise, and the potential falls to the AgO formation-potential range. After the AgO

formation plateau is reached, the potential rises again, and oxygen is seen to evolve from the electrode. The use of the galvanostatic technique is complicated by a changing double-layer charging current with time.

Potentiostatic experiments are generally easier to interpret since, to a first-order approximation, the concentration of electroactive species at the interface is kept constant. Potential-step measurements have been reported before [9,12,13,28–30]. Generally, these responses show falling current transients with time. Current versus inverse square-root time curves are linear at low overpotentials [12,30]. At higher potentials (greater than 200 mV vs. Ag/AgCl 4M KCl) a transient minimum and maximum occur and the potential necessary to observe of this peak is temperature dependent [30]. Talik et al. associated the current maximum with the "commencement of significant formation of Ag_2O at the surface by the dissolution-precipitation process." Pound has also said that this maximum infers nucleation of a surface phase. However, no theoretical reasoning for these conclusions has been given. An attempt to reproduce the current response by the 2-dimensional nucleation-and-growth model given by Armstrong, Pearce and Thirsk [31] has been unsuccessful [12]. Therefore, while a number of authors have attributed the current transient peak to the formation of a surface phase, the role of several simultaneous processes such as dissolution, crystal incorporation of material, changing surface coverage and crystal overlap on the current response has not been adequately discussed in the literature.

There are a number of possible chemical reactions that may be taking place in this system. The dissolution of silver as an oxygenated

ion,

$$Ag + 2OH^- \longrightarrow AgO^- + H_2O + e^- \quad , \tag{1A}$$

is more likely than the dissolution of silver ion,

$$Ag \longrightarrow Ag^+ + e^- \quad , \tag{2A}$$

as shown by a stability study [18]. A calculation of the equilibrium potential for reactions 1 and 2 give 6 mV and 240 mV vs Ag/AgCl 4M KCl respectively. This calculation assumes a pH of 14 and an activity of silver ion (AgO^- or Ag^+) of 10^{-5} M/l (approximately silver oxides reported solubility at pH 14) [18]. Droog et al. [9] do not feel that equation 1A describes the reaction of the A1 peak because their results exhibited a different pH dependence than that predicted by equation 1A. Further, an adsorbed form of the oxygenated species can be proposed as

$$Ag^* + OH^- \longrightarrow (AgOH) + e^- \quad , \tag{3A}$$

where "*" symbolizes an adsorption site and "( )" symbolizes an adsorbed species.

The reaction products from equations 1A–3A could undergo further reactions. For instance, the adsorbed species in equation 3A could undergo a second-order surface reaction given by

$$2(AgOH) \longrightarrow (Ag_2O) + H_2O \quad . \tag{4A}$$

Surface diffusion of the adsorbed species might play an important role in this reaction mechanism. Also, direct oxidation of the surface could proceed by

$$2Ag^{*} + 2OH^{-} \longrightarrow Ag_2O + H_2O + 2e^{-} \quad . \tag{5A}$$

Both of these two interfacial reactions are questionable, due to the physical limitation of the mobility of chemically adsorbed species and the necessity of two surface sites being in close proximity.

A possible consecutive reaction for the formation of solid oxide from solution is

$$2AgO^{-} + 2H_2O \longrightarrow 2AgOH + 2OH^{-} \longrightarrow Ag_2O + H_2O + 2OH^{-} \quad . \tag{6A}$$

In this reaction it is proposes that the dehydrated hydroxy argentate(I) or a hydrated form of the ion will precipitate as a solid. Another homogeneous reaction possibility is the reaction of silver ion with a dehydrated hydroxy argentate(I) ion:

$$Ag^{+} + AgO^{-} \longrightarrow Ag_2O \quad . \tag{7A}$$

However, as pointed out before, the solubility of silver ion is very low in alkaline solutions. Both reactions 6A and 7A may be thermodynamically possible on a bulk scale, but the necessary energy barriers associated with a nucleation process must be overcome prior to the formation of the solid oxide. This is one reason why the oxide may not appear even at large values of supersaturation.

Solid-state diffusion of oxygen into the lattice is another possibility. Oxygen transport into the crystal via lattice-defect sites or some other transport mechanism would be inherently orders of magnitude slower than transport in a liquid medium. Such a reaction might proceed as indicated in equation 8A:

$$(OH^-) + e^- \longrightarrow O^{-2} + H \quad . \tag{8A}$$

This reaction is then followed by diffusion of the oxygen ion followed by reaction of the oxygen with neutral silver in the metal crystal.

Dissolution of solid silver oxide can occur by the reverse of any of the above reactions. For instance,

$$Ag_2O + 2OH^- \longrightarrow 2AgO^- + H_2O \tag{9A}$$

may show the process of dissolution of silver in alkaline solution.

MECHANISMS OF FILM GROWTH

A solid-state model of film growth of an oxide layer generally requires that the film formation take place somewhere between the solid/film and film/electrolyte boundary. For the simple case, where the reaction occurs at the film/electrolyte boundary and the process is diffusion controlled, a parabolic law of film growth should be followed [32,33]. When the electronic conductivity of a nonstoichiometric n-type semiconductive oxide is the limiting factor in the kinetics of growth, a logarithmic oxidation law should prevail [34]. For the silver/silver oxide system, this mechanism would suggest that hydroxyl groups react at the film/electrolyte interface. The film would thicken as O^{-2} diffuses to the metal surface and reacts at the metal/film surface. This process would be controlled by the formation of a semiconductive oxide. A modification of this mechanism would be to have the reaction occurring throughout the film as a concentration profile of reacting species is set up in the film.

A porous-film model allows diffusion to proceed in the oxide layer within electrolyte-filled pores. An increase in the film resistance is due to filling of the pores with oxide. When a nonprotective porous oxide layer is formed, the oxidation rate is controlled by the rate of transport of material to the oxide interface. To a first approximation, the transport rate is independent of oxide thickness and depends on temperature only. That is, transport to the oxide is uniform inside the pore with respect to time, for which a linear growth rate with time is obtained [32].

One of the most frequently referred-to mechanisms for the silver/silver oxide system is the dissolution/precipitation mechanism. In this mechanism dissolution of silver is the first step. The dissolved silver then reacts with water. The formation of an oxide film occurs by the precipitation of the dissolved material from a supersaturated solution. This would follow from equation 6A. However, the overall reaction could be controlled by various steps in the kinetics or transport of materials. There are two possible controlling processes at the metal/solution interface. If the charge-transfer process of the formation of the ionic silver species is rate-determining, then a Butler-Volmer equation should predict the current-potential characteristics of the system. If diffusion from the interface to the bulk solution is the major controlling factor, a standard diffusion equation for a planar interface may be used to reproduce the current responses. On the other hand, if the rate is limited at the solution/crystal boundary, the process may be controlled by either the diffusion to the crystal or incorporation into the crystal lattice.

HETEROGENEOUS ELECTROCRYSTALLIZATION

There are some special features of electrocrystallization that make its analysis different from that of crystalization by vapor-deposited crystallization and crystalization from solutions. Part of this difference is due to the number of possible ways that crystal growth can occur on an electrode. These ways have been enumerated by Fleischmann and Thirsk [36]. The most notable ways for crystal growth to occur are: (a) the new phase may be formed on an inert substrate by electrodeposition of ions in solution, or on a substrate of the same material; (b) the new phase may be formed from the parent substrate by electrodissolution followed by precipitation from solution, or the ion may pass from the substrate through the new phase to the solution interface, with a portion of the ions reacting there to form an advancing surface layer; or (c) the new phase may be a transformation of a previous surface phase such as the one formed in (b). The most notable distinction between process (a) versus process (b) or (c) is that the nucleating species in (a) is found only on the electrode surface, while in (b) or (c) the ionic species formed are generally in the solution, possibly undergoing further reactions with the solvent. We can see that (b) and (c) generally will include three-dimensional nucleation, and growth will start at these nucleation centers. The electrode will become covered by the new phase as growth continues and crystal overlap. Only process (a) can establish a steady state, since multilayer metal structures will offer little electrical resistance to further deposition. It is quite different for case (b) or (c), where the growing surface layers (a salt or oxide) may offer a finite electrical and diffusion resistance.

It has been noted [37] that if all processes taking place before ion deposition and growth are fast (e.g., fast charge transfer and diffusion through the solution) and surface layers electrical resistances are small (as in the early stages of growth), then the problem will again reduce to one of electrocrystallization, with the rate-determining step being the growth of the nuclei.

Most current mathematical theories of crystal growth do not consider any distinction between the various types of crystals morphologies, and therefore there is not a good a theoretical bridge between the initiation of nucleation and the type of nucleus formed. Also, it is not always clear whether crystal growth via direct deposition or surface diffusion to a lattice site in a growing crystal would be the favored path of lattice building. Bockeris and Conway have noted that there may be many favored sites where particular portions of the overall charge transfer can take place [37].

The growth of a new phase on a substrate should result in a lattice structure similar to that of the underlying lattice, particularly if the deposition rate is slow. The structure of the first monolayers is energetically favored to be of the same orientation as the substrate. The study of nucleation from an epitaxial view ignores the kinetic aspects of the problem (which are discussed later), and so is of limited use for any quantitative analysis. However, epitaxial considerations in the embryonic stage of nucleation may be related directly to the site density and energy distribution of nucleation sites. As early as 1930, Volmer [51] said that the work needed to form a nucleus in a supersaturated-solution phase is lowered by boundary faces. Stranski

[39] discussed the nature of a forming crystal and talked of the stability of small nuclei in equilibrium with the supersaturated solution. He proposed that formation embryonic nuclei form in an adsorption layer, driven by surface diffusion, and that there are distinct diffusion paths that may play a role in crystallographic growth.

The theories of Stranski, and later of Pangroff [40] are useful because of the insight they give to the relation between the role of crystal-plane surface energy and equilibrium formation. Their calculations involve the relationships between the various energies of formation of different crystal planes ([111],[110],[100]) for formation on a face-centered and body-centered crystal. Only forces of the first, second, and third nearest neighbors were considered. The results of these calculations showed that, at low supersaturation, the [111] plane will form preferentially on an fcc face, with the order of the work of formation of the different planes given by

$$W_{111} < W_{100} < W_{110} \quad . \tag{10A}$$

However, at high supersaturations,

$$W_{110} < W_{100} < W_{111} \quad . \tag{11A}$$

Further, at intermediate supersaturations the work of formation of the various planes is the same. Finally, at very high supersaturations, where the chemical potential is high and the value of W_{ijk} is insignificant, random distributions are again expected. This may explain why one plane is preferred to another, but it gives no information as to the rate of formation of nuclei. Indeed, as mentioned by Fleischmann and

Thirsk [36], epitaxial studies of thin surface layers and the ideas of small-misfit-value probably have dominated the subject of nucleation more than is warranted by experimental facts. Attention should more appropriately be centered on models of nucleus growth, which is inherently a dynamic problem, influenced by diffusion, concentration, temperature, time, surface forces, and growth inhibition.

Geometric models for the nucleation process generally neglect the effects of ion transport to the growth centers from the solution and consider only the process of the growth due to area and charge-transfer-rate constraints. The growth rate is governed by potential dependent rate constants. One of these is the nucleation rate constant "A" (nuclei/cm^2/sec), which tells us how the number of sites for growth changes with time. According to Fleischmann and Thirsk [41,42], if the nucleation takes place at a number of preferred sites (N_0) on the substrate, and the probability of forming a nucleus is "uniform" in time, the number of growing sites is given by

$$N(t) = N_o(1-e^{-At}) \tag{12A}$$

This equation implies a progressive nucleation whose rate of formation is proportional to the fraction of sites remaining unnucleated (first-order process). In general, "A" is a function of potential, which is related to the surface concentration of the dissolved species of the nucleating material. Limiting forms of equation 12A are given by

$$N(t) = N_o \tag{13A}$$

when At >> 1.0 (instantaneous nucleation) and

$$N(t) = AN_o t = A_1 t \tag{14A}$$

for At<<1.0 (linear growth).

For a constant potential condition, it is assumed that the growth-rate constant is time-independent, and the current into a single crystallite is given by

$$I_c = nFkS \quad . \tag{15A}$$

Here, S is the surface area of the growing center and k is the growth constant. It is therefore assumed that the growth rate is controlled by the rate of incorporation of material into the growing center, given by the rate constant k. By using material conservation for a growing hemispherical particle, the relation between the particle's mass and radius can be found, and the current into a growing crystal can be determined as a function of time. We should note that in the later stages of crystal growth the centers will overlap and the area available for electrodeposition becomes restricted. If the surface layer offers an infinite electrical or diffusion resistance, then the reaction would have to stop when the electrode surface is completely covered by the crystals. More recent work on geometrical modeling of crystal growth has concentrated on the effects of geometrical overlap (overlapping diffusion fields).

Fletcher and Smith [38] have used the basic ideas of Fleischmann et al. to develop a theoretical response of a galvanostatic experiment by finding the functional form of E(t) that would allow i(t)=constant. The basic assumption in their work was the validity of Fleischmann's work, as well as instantaneous changes in surface coverage with small changes

in potential. The calculations showed that: (1) as time progresses from zero, the potential decreases from infinity to E(min) at a time t(min); (2) after t(min), the potential rises again to infinity; (3) at a later time the potential goes to infinity, and (4) the minimum occurs at 50% coverage. Fletcher's model contains no "leakage" of current to the charging of a double layer or dissolution of ions into solution. At later stages in the charging process, the local current density between the growing crystals must increase (due to the loss of total surface area). This in turn will increase the surface potential. Homogeneous nucleation may occur later.

H. Angerstien-Kozlowska et al.[43] proposed a two-dimensional film-nucleation model for the formation of monolayers governed by random (Langmuir) adsorption. They calculated current responses for a variety of different instantaneous and potential-dependent forms of the nucleus formation rate. They gave the rate of formation of nuclei as

$$j = \frac{dN}{dt} = \beta(1-\Omega)\exp(E/b) \quad . \tag{16A}$$

Here, β is the normalized nucleation rate, Ω is the surface coverage of nuclei, E is the overpotential, and b is a constant. No explanation is given for the exponential form of the potential dependence, but it may imply that the nucleation process is directly related to the charge transfer process, and that this is the same for all nucleation sites. The dependence of the nucleation rate on uncovered area is usually referred to as an "ingestion" model. The general result of these calculations show that the pseudocapacitance (current/sweep rate), coverage at peak current, and the half-peak width were independent of sweep rate

only for a totally irreversible process. With reversibility, the pseudocapacitance will increase toward infinity, and the coverage at peak current and the half-peak widths decrease. Therefore, the current-response wave for potential sweeping experiments will become higher and narrower with increasing reversibility. The calculations of Angerstein-Kozlowska et al. seem to be of limited use because of the complexity of the calculations, and their dimensionality. Their ideas were expanded on by Bosco and Rangarajan [46]. They tried to distinguish between an "ordered" and a "gaseous" electrochemically formed monolayer. They pointed out that the primary difficulty in answering this question arises from the kinetic nature of the phenomenon, since it is not straightforward to relate the well-established notions of phase transition to nonequilibrium measurements as in a potential sweep. The general features that show up in a phase formation are given by them as:

(1) sharp RTPS peaks,

(2) discontinuity in the adsorption isotherm,

(3) non monotonic potentiostatic transients,

(4) the appearance of spikes in galvanostatic transients, and

(5) large changes in the slope of reflectivity vs. charge.

Since none of the above features point to phase transition unambiguously (these features can arise for other reasons as well), models for the response of a linear potential sweep in the presence of nucleus formation were proposed. Butler-Volmer kinetic expressions were invoked, with both Langmuir and Frumkin adsorption isotherms considered. Plots are given [46] of the characteristic parameters observed in the form of

peak potential, peak current, and half-peak width. Diagnostic criteria are given for the determination of the various rate processes in the form of analytic limits and computed curves of the above variables versus sweep rate. A model for the formation of a condensed adsorption film presupposing a two-dimensional one-step nucleation according to an exponential law has been proposed by Retter recently [47].

In a later article by Angerstein-Kozlowska et al. [44], and later expanded on by Bosco and Rangarajan [45], the kinetic behavior of a nucleation and growth-controlled surface process under potentiostatic and linear sweep conditions was investigated with a 3-D growth model. They [44,45] treat nucleation as a random process proceeding at a rate determined by the free-surface fraction $(1-\Omega)$. They schematically show that the nucleation process can proceed either by formation of new growth centers or through addition to existing centers. In these calculations, the $(1-\Omega)$ factor enters into the kinetic equations not only because of the growth-overlap effect but also because of the decrease in the total number of unnucleated sites covered by growing nuclei. These effects are incorporated into the calculation of the so-called "expectation number." However, in this paper, as in the earlier paper on 2-D adsorption and growth [43], numerical results are dimensional and are therefore of limited use. Solutions of a generalized arbitrary time dependence of nucleation are given by Bosco and Rangarajan [45], with specific calculations for a 3-D growth model with a linear potential sweep. Subcases are given as instantaneous and progressive nucleation with ohmic-drop corrections applied.

Fletcher and Lwin have recently proposed a geometrical model with a twist [48]. They point out that the major problem with existing models is that probabilistic effects in space and time are ignored (specific reference is given to the work of Fleischmann and Thirsk [41], Bosco and Rangarajan [45,46], and earlier work of Fletcher [38]). It is implicitly assumed that heterogeneous nucleation occurs at active sites on the electrode surface, and that each of these sites has precisely the same activation energy for nucleation. Probabilistic effects in space are usually ignored by assuming a large electrode and long time scales, so nucleation is considered a smooth process in space. However, the assumption that there is a unique activation energy for nucleation is weak. This becomes very clear when we remember that nucleation rates have a nonlinear dependence on activation energies, so that small spreads in activation energies would lead to a rather large distribution of nucleation rates. Fletcher says that simultaneous calculations of both probabilistic space and time effects are immense, and he therefore reverts to considering time and space effects independently and multiplying their effects. The probabilistic effects in space have generally been considered to be given by the calculation of the expectation number. Fletcher assumes that the interaction of particles (as in the effects of overlap) are separate from the probabilistic effects in time of the nucleation phenomenon, as would be reasonable early in the nucleation growth process. The effects of the change in this function from a Gaussian to a Dirac delta function are impressive.

Very little work has been done on diffusion-controlled crystal growth. Only the work of Kappus[49] will be discussed here. In the

early stages of discharge the supersaturation of ions in the vicinity of the electrode will increase until nucleated crystallites form. These crystallites can act as sinks for the anodic products that are formed and will reduce the supersaturation. Small crystals will disappear if the now-increasing critical radius exceeds their radius. Kappus has used the classical ideas of homogeneous nucleation, but, as shown by Vermilyea [50], the normal interfacial tension can be replaced by a simple combination of the solid-solid and two liquid-solid interfacial tensions. We start with the free energy, F, of a spherical subcritical cluster with radius r in a supersaturated solution given by

$$F = 4\pi\sigma r - 4\pi r^3 RT\ln(C/C_{sat})/3v_m \quad . \tag{17A}$$

In equation 17, v_m is the molar volume, C the concentration, and C_{sat} the saturation concentration of infinitely large crystals. There is a maximum free energy, and the radius of this maximum (the so-called critical radius) is given by

$$r = 2\sigma v_m/RT\ln(C/C_{sat}) \quad , \tag{18A}$$

and the critical free-energy barrier is given by

$$F^* = F(r^*) = 16\pi\sigma v_m/3[RT\ln(C/C_{sat})] \quad . \tag{19A}$$

As long as the of subcritical clusters change size slower than the whole system does, an equilibrium size distribution of subcritical clusters will exist. Next, the equilibrium population of subcritical clusters with radius r is given by a Boltzmann distribution:

$$f(r) = f_o e^{-F(r)/kT} \quad . \tag{20A}$$

where f_o is the total number of nucleation sites. Kappus writes the following equation as the equation for the growth of the spherical crystallite under diffusion control:

$$\frac{dr}{dt} = v_m D \frac{C-\bar{C}(r)}{r} \quad . \tag{21A}$$

Here D is the diffusion constant and $\bar{C}(r)$ is the saturation concentration of a crystal with radius r. Hence, equation 21 implies that the diffusion is a one-dimensional problem with the characteristic boundary layer thickness of the radius of the particle. The relationship for the saturation concentration as a function of particle radius is given by a Gibbs-Thompson relation

$$\bar{C}(r) = C_{sat} e^{2v_m \sigma / RTr} \tag{22A}$$

An exact solution for equation 21 can be given for the case of constant concentration:

$$r(t) = r_o^2 + 2v_m D(C-C_{sat})t \tag{23A}$$

where r_o denotes the starting radius of the crystal. The radial distribution function of supercritical nuclei is given by :

$$f(r,t) = r[r^2-2v_m D(C-C_{sat})t] \times f[(r^2-2v_m D(C-C_{sat})t),0] \quad . \tag{24A}$$

This result shows that the distribution of crystallites shifts to larger radii and becomes less broad with time under the constant concentration case. More complex cases are considered with the inclusion of recrystallization and constant current.

OBJECTIVES OF THE PRESENT STUDY

Silver has been chosen as a model system for the investigation of the nucleation and growth behavior of anodic films. Despite the numerous studies done on the Ag/Ag_2O system, a number of questions remain about the chemistry and controlling processes for this electrochemical reaction. One of the objectives of this study is to look at the Ag/Ag_2O reaction on a submicroscopic scale, and to investigate the surface chemistry and physical processes involved by using the direct in-situ optical technique of ellipsometry. This study was undertaken to further our understanding of the relation between the charging processes and the microstructure of the surface films. Questions remain as to the reason for the A1 and A2 cyclic-voltammetry charging peaks. By using spectroscopic ellipsometry, the micromorphology of the film formation at various potentials was derived. Scanning electron micrographs have been used to complement this study, both as an aid in developing optical modeling and for support for optical-model interpretations. Various standard voltammetric techniques were used as well. Silver single crystals were used to assure a more uniform surface and allow interpretations at the submonolayer level.

REFERENCES FOR CHAPTER 1

1. Standard Potentials in Aqueous Solutions. Allen J. Bard, Robert Parsons and Joseph Jordan, ed. Marcel Dekker, Inc., 1985. p. 294-312.

2. Glicksman, R. and C. K. Morehouse, J. Electrochem. Soc. 104 (1957) 589.

3. Zimmerman, J. G., Trans. Elec. Soc. 68 (1935) 231.

4. Wales, Charles P., and J. Burbank, J. Electrochem. Soc. 112 (1965) 13.

5. Briggs, G. W. D., M. Fleischmann, D. J. Lax, and H. R. Thirsk, Trans. Faraday Soc. 64 (1968) 3120.

6. Smith, Craig G., Ph.D. Thesis, Dept. of Chemical Engineering, University of California, Berkeley. August, 1978.

7. Muller, Rolf H. and Craig G. Smith, Surf. Sci. 96 (1980) 375.

8. Teijelo, M. Lopez, J. R. Vilche, and A. J. Arvia, J. Electroanal. Chem. 162 (1984) 207.

9. Droog, John M. M., Peter T. Alderliesten, and Gosse A. Bootsma, J. Electroanal. Chem. 99 (1979) 173.

10. Droog, John M. M., J. Electroanal. Chem. 115 (1980) 225.

11. Giles, R. D., J. A. Harrison, and H. R. Thirsk, J. Electroanal. Chem. 22 (1969) 375.

12. Tilak, B. V., R. S. Perkins, H. A. Kozlowska, and B. E. Conway, Electrochim. Acta. 17 (1972) 1447.

13. Hepel, Maria, and Micha Tomkiewicz, J. Electrochem. Soc. 131 (1984) 1288.

14. Hepel, Maria, and Micha Tomkiewicz, J. Electrochem. Soc. 132 (1985) 32.

15. Johnston, H. L., F. Cuta, and A. B. Garrett, J. Am. Chem. Soc. 55 (1933) 2311.

16. Johnston, H. L., F. Cuta, and A. B. Garrett, J. Am. Chem. Soc. 56 (1934) 1250.

17. Antikainen, P. J., Sirkka Hietanen, and Lars Gunnar Sillen, Acta Chem. Scand. 14 (1960) 95.

18. Pound, Bruce G., Digby D. MacDonald, and John W. Tomlinson, Electrochim. Acta. 24 (1979), 929.

19. Dirkse, Thedford P., and Dale B. De Vries, J. Electroanal. Chem. 63 (1959) 107.

20. Stonehart, P., and F. P. Portante, Electrochim Acta. 13 (1968) 1805.

21. Cotton, F. A., and Geoffrey Wilkinson, Advanced Inorganic Chemistry, A Comprehensive Text. John Wiley and Sons Inc. 1980. 4th Ed. p. 969.

22. Giles, R. D., and J. A. Harrison, J. Electroanal. Chem. 27 (1970) 161.

23. Hampson, MacDonald Lee, J. Electroanal. Chem. 45 (1973) 149.

24. Dignam, M. J., H. M. Barrett, and G. D. Nagy, Can. J. Chem. 47 (1969) 4253.

25. Cahan, B. D., J. B. Ockerman, R. F. Amlie, and P. Ruetschi, J. Electochem. Soc. 107 (1960) 725.

26. Gibbs, D. B., B. Roa, R. A. Griffin, and M. J. Dignam, J. Electrochem. Soc. 122 (1975) 1167.

27. Droog, John M. M., and F. Huisman, J. Electroanal. Chem. 115 (1980) 211.

28. Pound, Bruce G., Digby D. MacDonald, and John W. Tomlinson, Electrochim. Acta. 25 (1980), 563.

29. Fleischmann, M., D. J. Lax, and H. R. Thirsk, Trans. Far. Soc. 64 (1968) 3128.

30. Pound, Bruce G., Digby D. MacDonald, and John W. Tomlinson, Electrochim. Acta. 25 (1980), 1293.

31. Armstrong, R. D., L. Pearce, and H. R. Thirsk, Electrochim. Acta. 14 (1969) 949.

32. DiBenedetto, A. T. The Structure and Properties of Materials. McGraw-Hill Book Co. 1967. p. 462–465.

33. K. Hauffe, Oxidation of Metals, Plenum Press. New York. 1965.

34. Good, Robert J., "Passivity of Metals and Semiconductors." Michel Froment, ed., Elsevier, 1983. p. 43.

35. Perkins, R. S., B. V. Tilak, B. E. Conway, and H. A. Kozlowska, Electrochim. Acta, 17 (1972) 1471.

36. Fleishmann, M., and H.R. Thirsk, "Metals Deposition and Electrocrystalization," in Advances in Electrochemisty and Electrochemical Engineering. Vol. 3. P. Delahay and C.W. Tobias editors, John

Wiley and Sons, New York. 1963.

37. Bockeris, J., and B.E. Conway, Electrochemical Acta, 3 (1961) 340.

38. Fletcher, S., and A. Smith, Can. J. Chem., 56 (1978) 908.

39. Stranski, I. N., Naturwissenschaften, 23 (1943) 144.

40. Pangaroff, N. A., Electrochim. Acta, 7 (1962) 139.

41. Fleischmann, M., and H.R. Thirsk, J. Electochem. Soc., 110 (1963) 688.

42. Armstrong, R.D., M. Fleischmann, and H.R. Thirsk, J. Electroanal. Chem. 11 (1966) 208.

43. Angerstien-Kozlowska, H., B.E. Conway, and J. Klinger, J. Electroanal. Chem. 87 (1978) 301.

44. Angerstien-Kozlowska, H., B.E. Conway and J. Klinger., J. Electroanal. Chem. 87 (1978) 321.

45. Bosco, E., and S. Rangarajan, J. Chem. Soc. Faraday Trans. 77 (1981) 483.

46. Bosco, E., and S. Rangarajan, J. Electroanal. Chem. 129 (1981) 25.

47. Retter, U., J. Electroanal. Chem. 179 (1984) 25.

48. Fletcher, S., and T. Lwin, Electrochim. Acta. 28 (1983) 237.

49. Kappus, W., Electrochim. Acta. 28 (1983) 1529.

50. Vermilyea, D. A., "Anodic Films," in Advances in Electrochemisty and Electrochemical Engineering. Vol. 3. P. Delahay and C.W. Tobias, ed., John Wiley and Sons, New York. 1963.

51. Volmer, M., Die Kinetik der Phasenbildung, Steinkopff, Dresden und Leipzig, 1939.

FIGURE CAPTION FOR CHAPTER 1

1A. Cyclic voltammogram of Ag(111) in 1M KOH. Only the first sweep is shown. Potentials are made with reference to Ag/AgCl 4M KCl/M KCl.

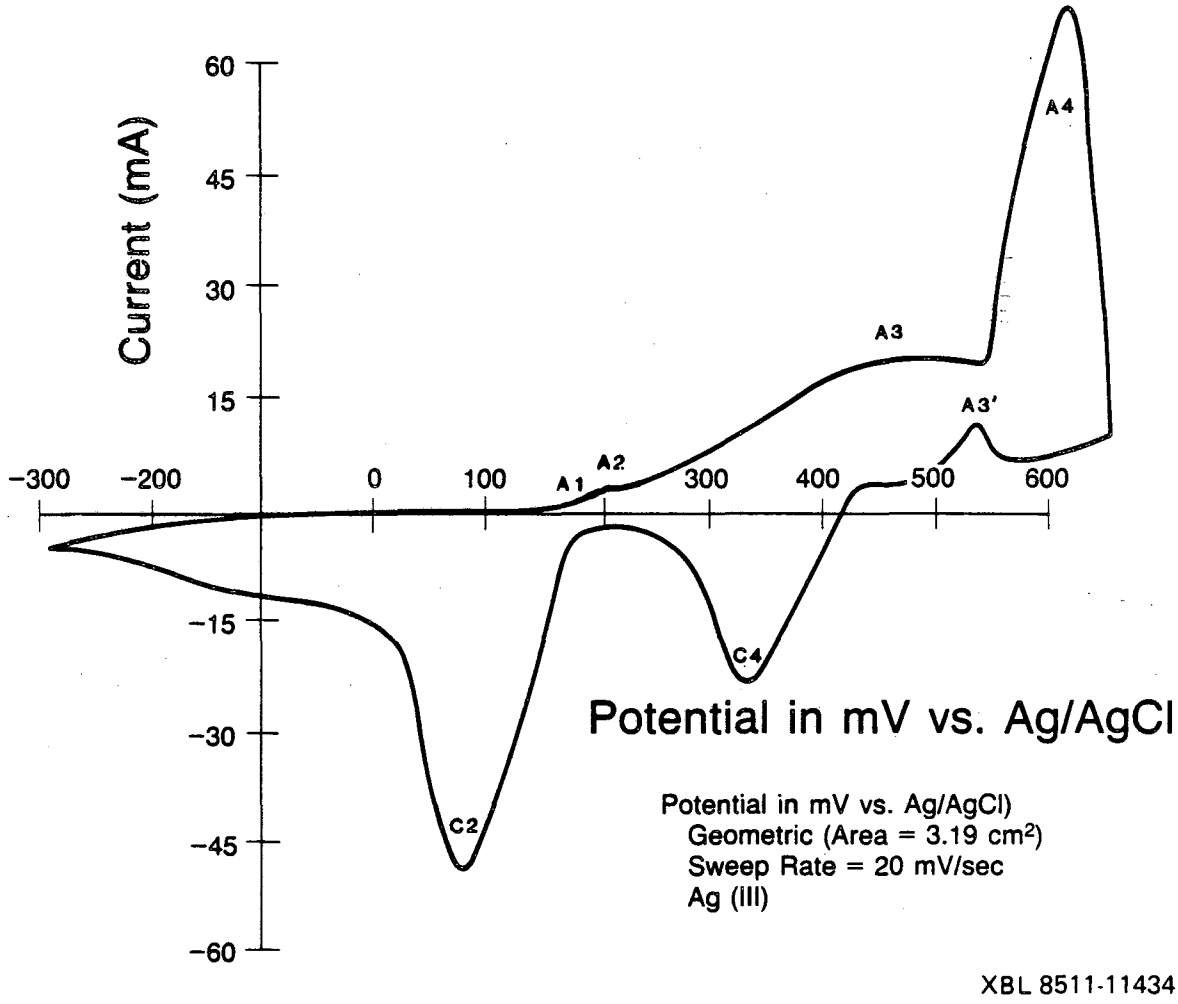

XBL 8511-11434

FIGURE A1

CHAPTER 2

EXPERIMENTAL TECHNIQUES AND PROCEDURES

ELLIPSOMETRIC PRINCIPLES

While the theoretical aspects of ellipsometry are covered in detail by many authors [1-4], only a brief treatment of the application of ellipsometry to this study is given here. Detailed derivations of electromagnetic theory on which the classical theory of ellipsometry is based are not given here; these derivations can be found in standard references on the subject [14,15]. Optical modeling will be discussed in the section on data interpretation.

Ellipsometry is an optical technique used for the characterization of interfaces and films by observing the transformation of the polarization of light. The light beam is classically thought of as an electromagnetic transverse wave. To completely describe the state of a monochromatic light wave, one needs to specify the wavelength, phase, propagation direction, amplitude, and orientation of the electric-field vector in space. For description of reflection of light the electric-field vector is divided into two components, known as the "s" and "p" components. The s-component is oriented normal to the plane of incidence, while the p-component lies in the plane of incidence. The plane of incidence is defined as the plane containing the incident and reflected beams (Figure B1). When the s- and p-components are in phase, the light is said to be linearly polarized, because the electric-field vector forms a line in a plane perpendicular to the direction of propagation. When the two components are not in phase, the tip of the

resultant electric-field vector traces a helix in space, and the light is said to be elliptically polarized (Figure B2). This is the most general form of polarization of light.

The phase difference (delta) and relative amplitude [tan(psi)] of the s- and p-components are used to characterize the state of polarization of light, and the ellipsometer measures the change in phase and relative amplitude of the light reflected from an interface. Additional information about the interface can be obtained by changing either the wavelength or the angle of incidence of light. A spectroscopic ellipsometer has the advantage over a monochromatic ellipsometer in that spectral features such as absorption peaks and troughs can be detected. Also, a single scan ideally represents one surface morphology whose physical characteristics are independent of the light probe's wavelength. Since the dimensionless optical-path length is inversely proportional to wavelength, dimensions of the surface layers relative to the incident wavelength are made. One scan of a surface is therefore equivalent to several simultaneous independent measurements. These spectral measurements allow one greater certainty in interpreting the data. These interpretations can be (1) the refractive indices of the substrate and film, (2) the film thicknesses, (3) the morphological makeup of the film, and (4) the anisotropies existing in the film. Multiple films (layers) have been used before for the interpretation of ellipsometric data [5,6,9,11] and were employed in this study as well.

Ellipsometry is one of the few techniques that allows the direct in-situ measurement of the formation of a surface layer at a metal/solution interface. Even at the fastest scan rate used in this

investigation the ellipsometer resolution (0.025 degree) is sufficient to detect the formation of a submonolayer. By making a suitable choice of the conditions of an electrochemical experiment, one can determine the effect of changing either the electrolyte composition or the charging method on the growth of solid films in-situ. The changing optical characteristics of a growing film with time allow the interpretation of the changes in micromorphology and its effect on the charging process. It is for these reasons that ellipsometry is a very powerful tool for the better understand the silver/silver oxide system.

OPTICAL MEASUREMENT SYSTEMS

The instrument used in this study has been described previously [7,8]. Compensation is automatic (self-nulling), and the instrument can follows spectral changes in the surface optical properties with time. One scan requires about 3.5 seconds to complete. In a typical experiment data on wavelength, delta, psi, time, current, and potential are all collected and optical data is stored by an LSI 11/73 computer for later interpretation. The ellipsometer has a nulling time of about 1 ms accomplished by use of magneto-optical Faraday cores. The working resolution is approximately 0.025 degrees, depending on the scan rate and wavelength. Its slew rate is about 1600 deg/sec, which can be compared to about 0.35 μm/sec of film growth. Analog and digital signal averaging are employed when possible to improve the resolution.

The polarizer-compensator-analyzer (PCA) ellipsometer configuration of optical components was used (Figure B3). White light from the 75-watt xenon lamp is passed through a continuously variable interference

filter (CVF) positioned between the light source and the first Glan-Thompson prism telescope. Monochromatic light is thus obtained with a bandwidth of about 10 nm from a wavelength of 370 to 750 nm.

The light beam enters a Glan-Thompson prism and is linearly polarized. The transmission axes of the Glan-Thompson prism is set by computer-controlled digital-encoder positioners, with a resolution of 0.01 degree. The monochromatic linearly polarized light subsequently passed through a Faraday cell, which allows rapid rotation of the polarization plane while maintaining a linear polarization state. The Faraday cells are solenoid coils with a magneto-optical glass core. Calibration of the rotation with applied current as a function of wavelength allows one to operate this instrument in a very fast self-nulling spectral-scanning mode.

From the Faraday cell, the light beam enters an achromatic Fresnel rhomb quarter-wave compensator. The design of this compensator is based on the relative phase changes of light on internal reflection from three glass-air interfaces. After the light has passed through the compensator it passes through an iris diaphragm. The iris is set to a diameter of approximately 1 mm. The transverse coherence length of the incident light can be calculated by [3]

$$\sigma = 0.16 \frac{\lambda r}{s} \tag{1B}$$

where s is the pinhole diameter, r is the distance from the pinhole, and λ is the wavelength of the incident light. For the experimental apparatus used, r is 15 cm, and s is 1 mm. Using equation 1B, we find that the transverse coherence length is 10–17 μm in the spectral ranges

used. This is much greater than the separation of the surface features observed in this work. After passing through the Fresnel rhomb compensator, the light beam is elliptically polarized. With the correct state of elliptical polarization incident on the specimen, linear polarization is restored on reflection. After reflection, the now restored linearly polarized light passes through another Faraday cell and Glan-Thompson prism whose combined rotation and fixed azimuths are perpendicular to the azimuth of the reflected beam.

Error signals for the polarizer and analyzer are determined by two phase sensitive detectors. These error signals are used in a feedback circuit to minimize (null) the photomultiplier response. The Faraday cell rotations (at the null setting) are used to determine the change in the state of polarization due to reflection. A description of the electronics of the apparatus has been presented before [7-9].

DATA ACQUISITION ROUTINES

Computer software for the spectroscopic ellipsometer has been presented before [10]. A number of these programs were adapted for use with the motor-driven digital encoders to provide computer-controlled azimuths of the Glan-Thompson polarizers when the dynamic range of the Faraday cells is approached. Thus, the ellipsometer can now follow spectral changes with high speed resolution and unlimited range. The program "DYNSPE" is an adaptation of the program "SEV002," written by Farmer [10]. DYNSPE allows multifile time-resolved spectra to be stored, as well as allowing computer feedback control of the azimuths of the Glan-Thompson polarizers. By sensing the current levels in the

Faraday cells of the previous scan, DYNSPE determines whether a change in the position of the polarizing prism is necessary, and what direction the prism should be rotated in order to keep the amount of Faraday-cell rotation within the dynamic range of the instrument. In this manner the problem of signal loss due to changes in the optical properties of the surface during an experiment has been eliminated.

A listing of DYNSPE, as well as other programs used in this thesis, is given in a separate report [17]. DYNSPE stores the digitalized current levels, which are supplied via the analog-to-digital converter, in an unformatted data file. Also stored in this file is information pertaining to the present settings of the ellipsometer, the experimental identification, and the time at which the data scan was started and finished. A series of files is then stored on a floppy disk, ready for data conversion. These files are recognized as unconverted data by the first symbol in their file name, starting with the number 0. This prefix identifies the type of data that the file contains. Following this prefix is the four-letter file-class name, which is then followed by the data-file number. File number one refers to the first scan in time, number two to the second scan, and so forth. An example is

0GOOD0.026 ⟶ 0 GOOD 0.026 ,

which is then the twenty-sixth unconverted data file for experiment "GOOD." A data-file class hence contains all the optical experimental information. In order to convert the data to delta and psi values, which are independent of the instrument used to perform the measurements, the instrument must be calibrated.

INSTRUMENT CALIBRATIONS

The proper calibration of any instrument is imperative for the accurate quantitative interpretation of data. Therefore, painstaking efforts were undertaken to assure that the spectroscopic ellipsometer was properly calibrated with respect to wavelength and Faraday-cell rotation.

A) WAVELENGTH CALIBRATION OF THE DIGITAL ENCODER

The first calibrations performed was the correlation of the continuously variable interference filters' digital-encoder position with the transmitted wavelength. This was done by use of a set of narrow-band interference filters.

The procedure for calibrating the digital encoder is as follows. First, a specimen is aligned in the ellipsometer. Any reflecting surface can be used. Next, a monochromatic filter of known transmitted wavelength is placed in the path of the beam. Either the program SEV002 or DYNSPE can be used to collect data on channels 7 or 8. These channels display the photomultiplier current. After data are collected with a number of different monochromatic plates, the data should be plotted as current versus ADCUs (analog-to-digital conversion units). The current peaks indicate that the transmitted wavelength is that of the monochromatic plate. An example is shown in Figure B4. Two peaks are seen because the filter passes through the visible spectrum twice per revolution. A linear regression is used to determine the relation between the encoder count and the transmitted wavelength, and these results are placed in a data file named "WLCALC.DAT." This data file is

required in most spectral-ellipsometry programs. Figure B5 shows that, after we have correctly correlated the CVF encoder position with transmitted wavelength, the two transmission peaks are seen to coincide at a single wavelength.

The encoder calibration should be checked regularly. Also, if any adjustments are made to the encoder-CVF connections or if the CVF is replaced, recalibration will be necessary.

B) CALIBRATION OF THE FARADAY CELLS

Previous work with the present instrument has shown that the Faraday rotation of a polarized beam of light by magneto-optical glass rods subjected to strong magnetic fields shows large spectral dependence. In the linear response region the rotation is proportional to the magnetic-field strength at a fixed wavelength. Calibration is necessary to determine the proportionality constant of polarization rotation as a function of wavelength. The procedure has been described previously [8–10] and will not be repeated here. Data for calibration of the Faraday cells are stored in the file named "FARADY.DAT."

After some initial measurements, it became apparent that the proper selection of Faraday-cell glasses had to be made to achieve the best performance of the instrument. Figure B6 shows a scan of an anodized silver surface using an SF6 glass as the Faraday cores in both the analyzer and polarized solenoids. The scan-noise level is large (approximately ±3 degrees) when the reflectivity of the surface has been reduced by the formation of a surface layer. Occasionally an artificial increase in delta at lower wavelengths was observed. Experiments with other Faraday cores have shown that these poor results have at least two

causes. The intensity of the light entering the photomultiplier is reduced by the absorption of light in the Faraday cores. Light losses caused by the absorption and scattering of light at the electrode surface have a similar effect. These signal losses cause the instrument to search for a null with an insufficient light signal by increasing the current in the solenoids. Eventually the instrument "peaks out," with the currents achieving their maximum limits. In order to circumvent this problem, we investigated using other glass cores. Cores of very high transmittance have very small Verdet coefficients (e.g. BK7 glass), whereas SF6 glass has large Verdet coefficients and low transmittances (Table B1). For the silver-electrode system, delta varies from approximately 30 degrees at 400 nm to 90 degrees at 700 nm. It was necessary, therefore, to use a core with the ability to rotate the light about 60 degrees. Only the SF6 core can do this. On the other hand, our early experiments showed that psi would vary only 5–10 degrees over the visible spectrum, so that a core with high light transmission could be used. The final choice was to use an SF6 core in the polarizer solenoid and an SF2 core in the analyzer solenoid. The results of an experiment similar to that in Figure B6 is shown in Figure B7. Very low noise is achieved here because of the greater transmitted optical signal. High scan rates with low noise were made possible by this choice of components.

DATA-REDUCTION ROUTINES

Once the instrument calibrations are known and stored in a data file, the data can be converted. The program "CONVER" is a multifile-conversion routine of a file class. The converted data are stored with the same file name as the unconverted experimental file except that the

file prefix for the data output of this program is the letter "C." Both the calibration data files "WLCALC.DAT" and "FARADY.DAT" are required for these calculations. The program is written to search device "DY1" for the data, so it is necessary to assign the device where the data are stored with the logical name "DY1" in order to run this program. Once this is done, the program can be run and will convert up to 50 data files of a file class to wavelength dependent values of delta and psi.

Signal averaging can be performed both digitally and with an analog circuit. The program "SMTH" performs digital signal averaging. A file-class name and the number of converted data files to be averaged are the required input data. The signal-averaged spectra are put into a new data file, whose name can be up to nine characters in length. An example of a signal-averaged spectrum with respect to the nonsignal-averaged data files is shown in Figure B8.

Digital signal averaging was done to collect high-accuracy values of the dielectric constants of the clean silver substrate. The scan rate was kept the same for both the pre-experiment surface optical properties and the experiment itself. The clean-surface signal-averaged values of delta and psi can then be fed to the program "RISURF" [12] for conversion to refractive index and extinction coefficient versus wavelength. These files are used as input data in the optical modeling routines.

A number of smaller programs have been written for the general conversion and output of pertinent data. Only a few will be mentioned here. A complete listing is given in a separate report [18]. The program "TIMER" was written to generate the average relative time of each

data file with respect to the start of the experiment. The program "RECALL", written by Farmer [9,10], can recall any unformatted data file and display data either digitally of graphically. The program "MINUS" [10] takes the difference between two spectra and stores this difference in a new data file. The program "DATFIL" [17] takes unformatted data and transfers the data into a formatted data file for data transfer to the LBL 8600 computers. This allows the data to be processed and plotted by either the LSI 11/73 or the LBL mainframe computers. Figure B9 show the result of a galvanostatic experiment at a current density of 200 $\mu A/cm^2$ on a 3-D plot.

ELECTROCHEMICAL MEASUREMENTS

Electrochemical measurements were made on an EG&G Princeton Applied Research model 273 potentiostat/galvanostat. This instrument allows one to generate a large variety of waveforms for electrochemical experiments. Data are then sent to an X-Y recorder. A digital coulometer and an ohmic drop (IR) compensation feature make interpretation of experimental results easier. A range setter allows increased accuracy results recorded on the in X-Y charts.

ERRORS DUE TO ELLIPSOMETER COMPONENTS

Errors due to various components in the ellipsometer can be eliminated to different degrees [4,16]. Errors due to deviations in polarizer and analyzer alignment can be virtually eliminated by four-zone averaging. Errors due to deviation of the compensator's retardation from quarter-wave character can be only partially eliminated. Finally, errors due to deviations in compensator azimuth cannot be reduced.

Since the measurements done for this thesis required fast scanning, on the order of 3 sec/scan, and four-zone measurements require about 2 minutes to complete, four-zone measurements were not possible. The major cause of the increased time for a four-zone measurement is the time required for mechanical manipulation of the three component azimuths.

A four-zone program presented previously [12] was used to gather data at various azimuth positions of the polarizer, analyzer, and compensator. Figures B10 and B11 compare four-zone measurements made with the compensator at different positions. These scans were run on an internal-reflection prism whose back face was coated with vapor-deposited aluminum. It is evident from the graph that errors in delta are greatly reduced as the azimuth of the compensator is changed. However, errors in psi are not effected by changes in the compensators position. Indeed, most of the errors remain. Program "OPTCOM" [17] was written to calculate the standard deviation of the one zone spectra (which comprise the four zone measurement) with respect to a four-zone averaged spectrum. Table B2 shows the effect of changing the azimuth position of the analyzer and compensator on the calculated standard deviation. We reduced the errors due to azimuth position as much as possible by minimizing the calculated standard deviation. As expected, changing the polarizer azimuth changed the calculated standard deviation in delta, and changes in analyzer azimuth showed up as changes in the calculated standard deviation of psi. Similar results were observed with four-zone measurements of silver surfaces in 1M KOH. We decided to make our measurements in the zone which was closest to the four-zone

averaged.

Some measurement errors were reduced in this manner. However, the question of the relative magnitude of various errors sources remains. The errors due to incorrect azimuth position of the analyzer and polarizer appear to have been corrected by the procedure discussed above. It is believed that only a small portion of the remaining error is due to the polarizer and analyzer azimuths because these errors were easily distinguishable. Therefore, we believe that the compensator is the major error source remaining.

Deviations of compensator retardation (birefringence and uncertainties in reflection angles inside the compensator), parasitic-beam errors, and axial-alignment errors can all contribute to a compensator operating in a non-ideal manner. Axial alignment was not adjusted, and no analysis for this error source has been performed. However, it is reasonable to assume that the error due to errors in incidence angle are small, since our alignment procedures are accurate to within 0.1 degree. Parasitic beams arise from reflections from various optical elements and cell windows. Parasitic beams are reduced by using a pinhole in the focal plane of the analyzer, since parasitic beams are not focused on the optical axis. The pinhole effectively prevents parasitic beams from reaching the photodetector. This topic is presented in more detail elsewhere [4,16]. Errors are also associated with the manufacture of the Frenel rhomb compensator. The basic design equation of these compensators has been given by Azzam and Bashara [3]. As shown in Figure B12, the phase change of a three-reflection Frenel rhomb depends strongly on both the refractive index and the shaping of the element.

Table B3 shows the error in compensation due to a mechanical construction (i.e. angle of glass/air interface) limitations. Table B3 also shows the changes in quarter wave compensation that might arise due to changes in the refractive index of the glass over the visible spectrum. (Optical glass can be obtained whose refractive index varies by ±0.015 in the spectral range [13]). The result in Table B3 yields the conclusion that even with this small variance in refractive index, differences in quarter-wave character can still be as large as 0.5 degree. Also, while two possible angles can achieve a quarter-wave compensation, the smaller angle allows a better design. In order to achieve an accurate quarter-wave Frenel rhomb, one has two possible options: (1) the device can be made of a glass with a nearly constant refractive index, or (2) the glass can have its surface coated with a dielectric whose properties are such that the ratio of the refractive index of the glass and optical coating are constant.

EXPERIMENTAL PROCEDURES

A) SURFACE PREPARATION

Silver single crystals of [111] orientation were cut from a single crystal manufactured by Orion Chemical Company (99.999% purity). The orientation was determined by x-ray diffraction to be within less than 1 degree of the desired surface plane (see Figure B13). A surface-preparation procedure similar to that used before [5,6,12] was used here. Mechanical polishing was done first with a series of silicon carbide papers to the 0000 grit. Water rinsing during the sanding as well as ultrasonic shaking in water between changes in grit size minimized

scratching due to particle transfer from one grit size to the next. The electrode was then polished with 6-, 1-, and 1/4-micron diamond paste on a microfelt-backed mechanical polishing wheel. Between each change in diamond-paste size, the electrode was rinsed and was placed in the ultrasonic shaker. After the electrode was polished with the 1/4- micron paste, the electrode was washed in a series of organic solvents (methyl ethyl ketone, acetone, and ethyl alcohol) and then in distilled water. Following this treatment, the electrode was chemically polished with a solution of 100 cm^3 0.2M KCN and 2 cm^3 30% H_2O_2. This procedure involved dipping the electrode in the solution for 5 seconds. Finally, the electrode was rinsed again with distilled water and placed in a fresh 1M KOH solution until it was used in an experiment. Prior to all experiments, the electrode was placed at a potential of -800 mV vs. Ag/AgCl for 15 seconds to reduce any remaining surface oxides.

B) ELECTROLYTE PREPARATION

Solutions of 1M KOH were prepared using ultrapure water (Harleco Co., resistance greater than 10^7 ohm/cm), which is essentially free from particulates and all soluble contaminants. Two type of potassium hydroxide were used. The first was an ultrapure grade produced by Alfa Products. The second was an analytical reagent grade manufactured by Mallinckrodt, Inc. No difference in results could be attributed to the type of potassium hydroxide used. Therefore, most experiments used only the analytical-grade KOH. All solutions were prepared and stored in tetrafluoroethylene (Teflon) containers, a substance known to be highly inert to alkaline environments. Titrations were performed so that the molarity was known to ±1%. The solution was then placed in a pre-

electrolysis, degassing chamber. The chamber consists of a Teflon separatory funnel with a Teflon sparger for degassing and two Pt screens for pre-electrolysis. First a potential difference of 1.0 volt was applied between the two electrode screens for 4 hours. This procedure ensured that any residual electrochemically active species were removed. Then the solution was degassed by passing 99.9999% pure argon saturated with water from a 1M KOH solution through the electrolyte. The electrolyte was then passed into the cell through Teflon tubing for an experiment. A picture of all of the apparatus is shown in Figure B14.

C) CELL PREPARATION

The electrochemical cell used in these experiments was made of Teflon (Figure B15). The volume containing the electrolyte was approximately 244 cm^3 (5 cm × 6.5 cm × 7.5 cm). Light passed through two BK7 glass windows (Esco Products, Oakridge, N.J., birefringence < 9 nm/m) at normal incidence and hit the silver surface at an incident angle of 75 from normal. The cell was cleaned with nitric acid to remove any organic contaminants and was stored in distilled water for one day. Prior to the injection of the electrolyte into the cell for an experiment, the cell was purged of oxygen by passing water-saturated argon into the cell compartment. This procedure was done to minimize any oxygen diffusion into the electrolyte from any residual air left in the upper portion of the cell. The counter-electrode (90% Pt/Rh screen, 6.5 × 7.5 cm) was periodically removed and anodized to remove any deposited species.

D) EXPERIMENTAL EXECUTION

Once the cell, electrode, and electrolyte had been prepared, the silver electrode was put in place, the system purged, and the electrolyte was then introduced. The reference electrode was placed in a separate compartment approximately 80 cm from the working electrode. Ohmic compensation corrections calculated and experimentally determined were found to be small for the currents used in this study. Once the electrical connections were made, the ellipsometer was aligned. Motor-driven actuators allowed very quick alignment due to immediate feedback between the experimenter and movement in the position-controlling joystick. Once angular alignment was made in the plane if incidence, the beam was centered on the electrode. Spectral scans of the silver surface were taken after 5–10 minutes in the electrolyte. Next, the potential of the working electrode was brought to −800 mV for 15 seconds, and then the circuit was opened. After approximately 5 minutes the surface potential of the clean electrode was established at −75 to −45 mV (vs. Ag/AgCl 4M KCl), and a scan of the surface was made. This is believed to be characteristic of a clean silver surface. Comparisons of the two spectra were made. If a large change was found (greater than 0.1 degree), the procedure was repeated. Also, the optical properties of the surface were compared with results found in previous experiments. Only after a clean surface had been obtained did we proceed with the anodization process.

In a typical experiment, five parameters were recorded as a function of time: wavelength, delta, psi, either potential or current (depending on the type of experiment), and charge. The ellipsometric

measurements were stored in the computer, whereas the electrochemical measurements were recorded on an X-Y recorder. At the start of an experiment, two start buttons were pressed simultaneously, the computer-acquisition and the potentiostat start buttons.

POST-EXPERIMENT ELECTRODE TREATMENT

Once a given experiment was finished, the electrode was removed from the electrochemical cell for further ex-situ study. The procedure for removing the electrode is as follows. The solution is drained from the cell, after which the cell top is opened. Distilled water is added to the cell slowly to avoid disturbing any loose surface layers. The distilled water is left in the cell for 5 minutes, and then the cell is drained. This procedure is then conducted repeatedly. The electrode is then removed from the cell and is placed in a dessicator containing anhydrous $CaSO_4$ under vacuum for at least 24 hours prior to SEM analysis. The time delay between the removal of the electrode from the cell and the SEM analysis was found to be necessary in order to achieve high-resolution SEM photographs. Charging at the surface was evident when the specimen was not place in the dessicator, and so it is believed that either the removal of water from the Ag_2O crystals or the decomposition of the oxide significantly increased the conductivity of the surface layers.

CONCLUSIONS

Some sources of instrumental errors have been discussed, as well as software used for data acquisition and the necessary calibration of the instruments. The procedure and experimental technique described above

allowed us to take spectroscopic-ellipsometry data as well as electrochemical data of the silver/silver oxide system during the anodic charging process both quickly and accurately.

REFERENCES FOR CHAPTER 2

1. Passaglia, E., R. R. Stromber, and J. Kruger, ed. "Ellipsometry in the Measurements of Surfaces and Thin Films: Symposium Proceedings, Washington 1963." National Bureau of Standards Miscellaneous Publication 256.

2. Bashara, N. M., and R. M. A. Azzam, ed. "Ellipsometry: Proceedings of the Third International Conference Ellipsometry." North-Holland Publishing Co. 1976.

3. Azzam, R. M. A., and N. M. Bashara. Ellipsometry and Polarized Light. North-Holland Publishing Company, 1977.

4. Muller, Rolf H. "Principles of Ellipsometry." in Advances in Electrochemistry and Electrochemical Engineering. Vol. 9. P. Delahay and C. W. Tobias, ed. John Wiley & Sons, New York, 1973.

5. Smith, Craig Gordon. Ph. D. Thesis, Dept. of Chemical Engineering, University of California, Berkeley, August 1978. LBL-8082.

6. Muller, Rolf H., and Craig G. Smith. Surf. Sci. 96 (1980) 375.

7. Mathieu, H. J., D.E. McClure, and R. H. Muller. Rev. Sci. Instrum. 45 (1974) 798.

8. Muller, R. H., and Joseph C. Farmer. Rev. Sci. Instrum. 55 (1984) 371.

9. Farmer, Joseph C. Ph. D. Thesis, Dept. of Chemical Engineering, University of California, Berkeley, March 1983. LBL-15607.

10. Farmer, Joseph C. Ph. D. Thesis, Dept. of Chemical Engineering, University of California, Berkeley, March 1983. Appendix. LBL-15525.

11. Armstrong, M. J., and Rolf H. Muller. Dept. of Chemical Engineering, University of California, Berkeley, December, 1984. LBL-18599.

12. Steiger, R. F., J. M. Morabito, Jr., G. A. Somorjai, and R. H. Muller. Surf. Sci. 14 (1969) 279.

13. Malitson, I. H., J. Opt. Soc. 55 (1965) 252.

14. Stone, J., Radiation and Optics. McGraw-Hill Co., New York, 1963.

15. Born, M., and E. Wolf, Principles of Optics. Pergamon Press, New York, 1964.

16. Smith, Craig G., Janet S. Remer, and Rolf H. Muller, "Corrections for Component Imperfections and Azimuth Errors in an Automatic SELF-Compensating Ellipsometer." LBL-7303.

17. Mayer, Steven T., M.S. Thesis, Departent of Chemical Engineering, University of California, Berkeley. Appendix. To be published. LBL-20677.

Table B1 [11]

Verdat Coefficients And Transmittance For Various Glasses Used In The Ellipsometer Faraday Cells

Glass	Verdet Coefficient (min/OE cm) at Wavelength, nm			Internal Transmittance (%) for 2.5-cm Thickness at Wavelength, nm		
	450	500	600	370	400	440
BK7	0.031	0.024	0.016	96.	98.4	98.9
F2	0.076	0.058	0.038	91.	97.	98.3
SF2	0.085	0.065	0.043	85.	97.	99.
SF6	0.142	0.108	0.070	4.	56.	93.

Table B2

Changes In 4-Zone Standard Deviations
With Various Components Azymuths

Relative Polarizer Position (Deg)	Relative Analyzer Position (Deg)	Relative Compensator Position (Deg)	Delta Standard Deviation (Deg)	Psi Standard Deviation (Deg)
0.50	0.50	0.00	2.35	1.36
0.50	0.50	0.50	0.58	1.19
0.50	0.50	1.00	1.02	1.42
0.50	0.50	2.00	2.33	1.20
0.50	0.50	3.00	6.41	1.24
0.50	0.50	4.00	8.83	1.24
0.50	0.00	1.25	1.29	0.85
0.50	1.00	1.25	1.16	1.41
0.50	-1.00	1.25	1.14	1.36
0.50	2.00	1.25	1.25	2.30
0.50	-2.00	1.25	1.18	2.33

Table B3

Design Calculations for An Achromatic Frenel Rhomb Compensator

Refractive Index	Angle 1	Error due to Refractive Index Changes*	Error due to Angular Uncertainty†	Angle 2	Error due to Refractive Index Changes	Error due to Angular Uncertainty
1.400	-	-	-	-	-	-
1.425	18.35	0.63	0.22	20.95	1.15	0.40
1.450	17.33	0.50	0.31	22.25	2.65	0.76

*Assumed error in refractive index in operating spectral range is 0.01.

†Assumed error in internal angle of reflection is 0.1 degrees.

FIGURE CAPTIONS FOR CHAPTER 2

B1. Definition of s- and p-components of elliptically polarized light. Definition of the plane of incidence.

B2. Elliptically polarized light has the s- and p-components out of phase. The resulting electric-field vecotr traces a helix in space.

B3. Spectral scanning, self nulling ellipsometer optics.

B4. Transmission versus encoder count for a narrow-band filter (wavelength = 680.0 nm).

B5. Transmission versus wavelength of a narrow-band filter (wavelength = 435.8 nm).

B6. Spectra of silver anodized in 1M KOH for 65 seconds at 0.200 mA/cm^2. SF6 glass used in both the analyzer and polarizer Faraday cells.

B7. Spectra of silver anodized in 1M KOH for 52 Seconds at 0.200 mA/cm^2. SF6 glass used in polarizer Faraday cell. SF2 glass used in analyzer Faraday cell.

B8. An example of digital signal averaging for the substrate optical property.

B9. 3-D plot of the result for a galvanostatic experiment, current density 200 $\mu A/cm^2$.

B10. Four-zone measurements of an internal reflection prism whose back face is coated with vapor deposited aluminum. The optical properties of internal reflection prisms made in this manner are highly

reproducable (stable) because the glass/metal interface is not exposed to the enviroment. This measurement was made with the compensator azimuth 1.5 degrees from its optimum setting, and the polarizer and analyzer at their optimum setting.

B11. Similar four-zone measurement as shown in Figure B9, but in this figure the compensator is at an azimuth setting which has minimized the four-zone standard deviation.

B12. Relative phase change of the s- and p- components of light on passing through a three-reflection Frenel rhomb compensator. Phi is the angle between a line parellel to the incident beam and the glass/air interface where the first reflection occurs.

B13. X-ray diffraction pattern of a Ag(111) single crystal.

B14. Photograph of experimental apparatus.

B15. Photograph of electrochemical cell.

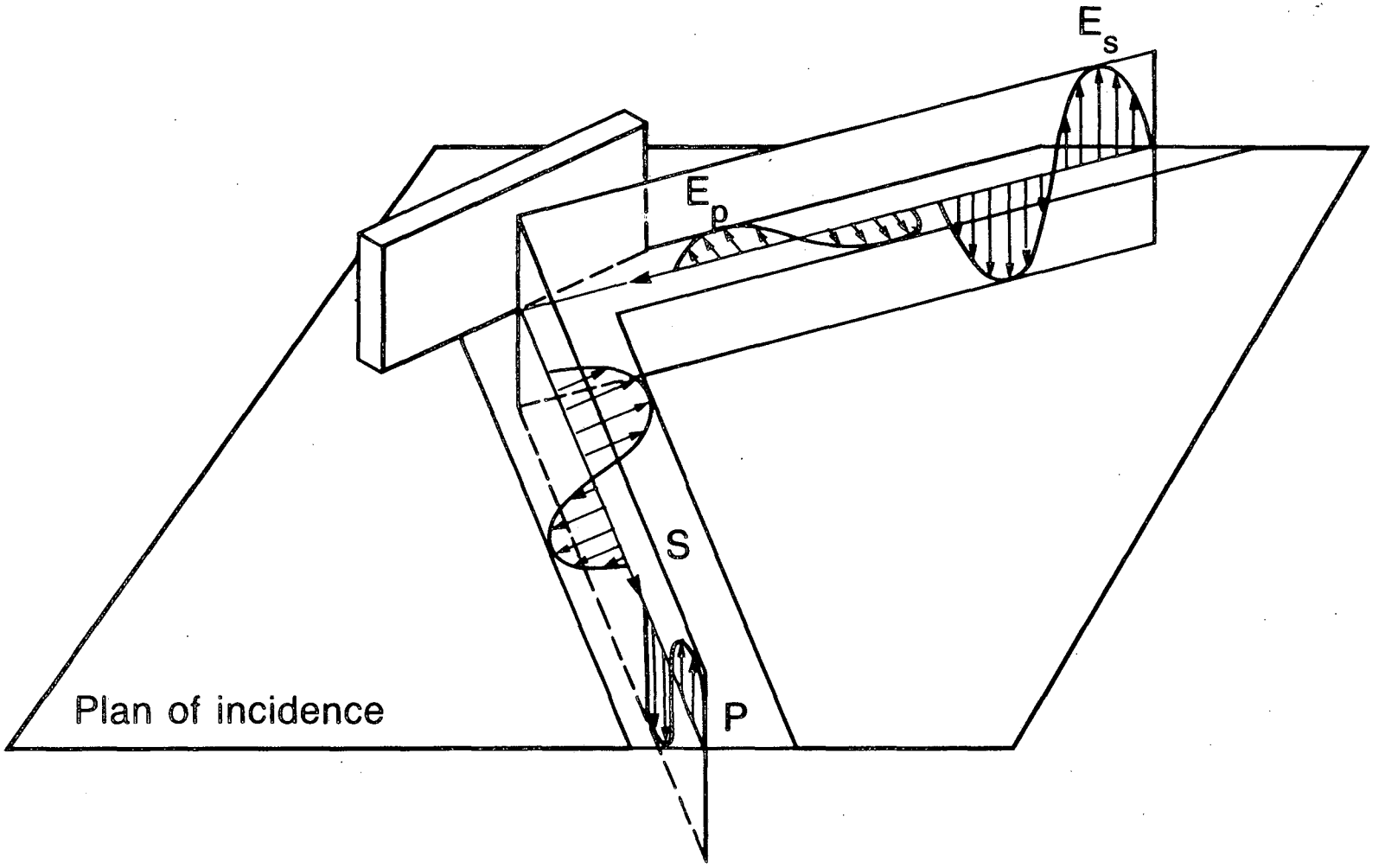

XBL 8511-11465

FIGURE B1

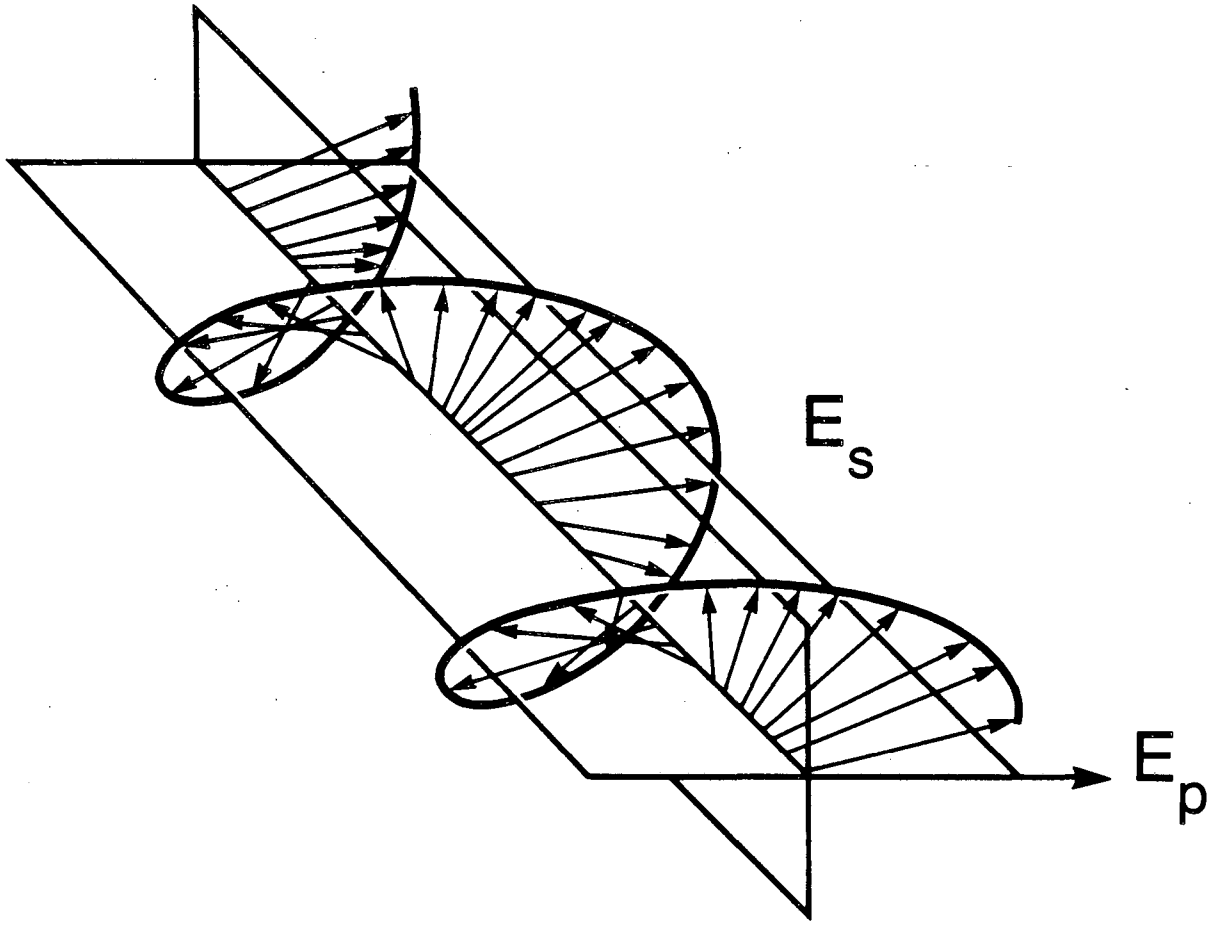

XBL 8511-11459

FIGURE B2

SPECTRAL SCANNING, SELF-NULLING ELLIPSOMETER OPTICS

1. high pressure Xe lamp
2. rotating interference filter
3. collimator
4. Glan-Thompson polarizer
5. Faraday cell polarizer
6. Fresnel rhomb achromatic retarder
7. electrochemical cell (or Auger)
8. analyzer Faraday cell
9. analyzer Glan-Thompson prism
10. collimator
11. spectrally "flat" detector
12. rotary incremental digital encoder
13. spectral scanner drive motor

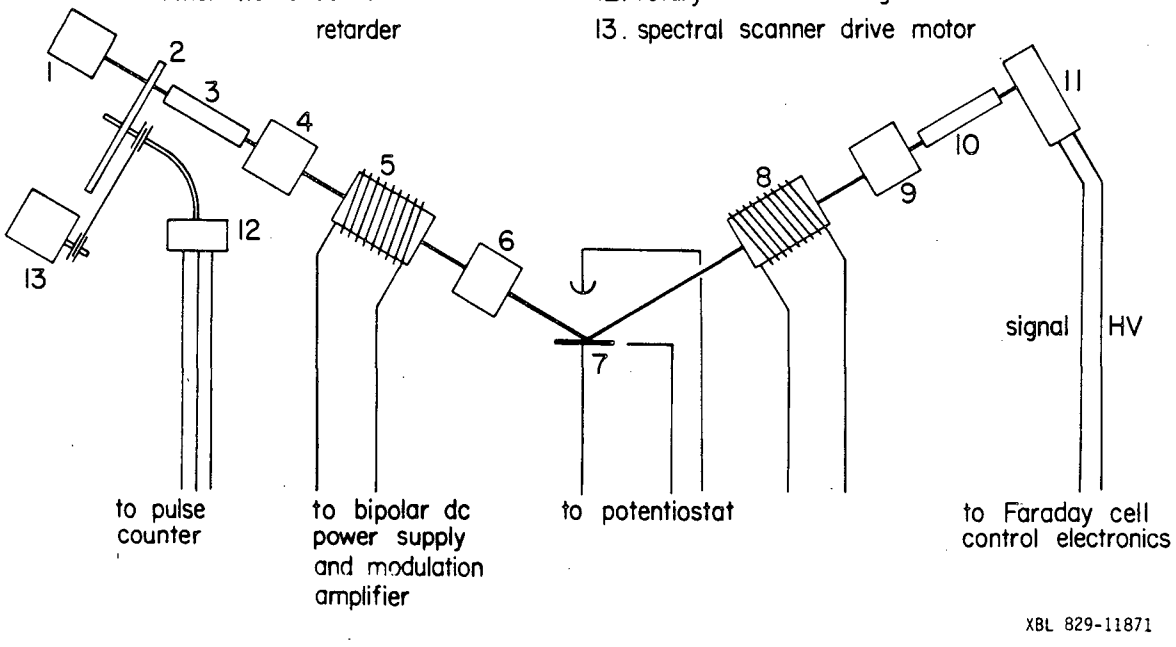

FIGURE B3

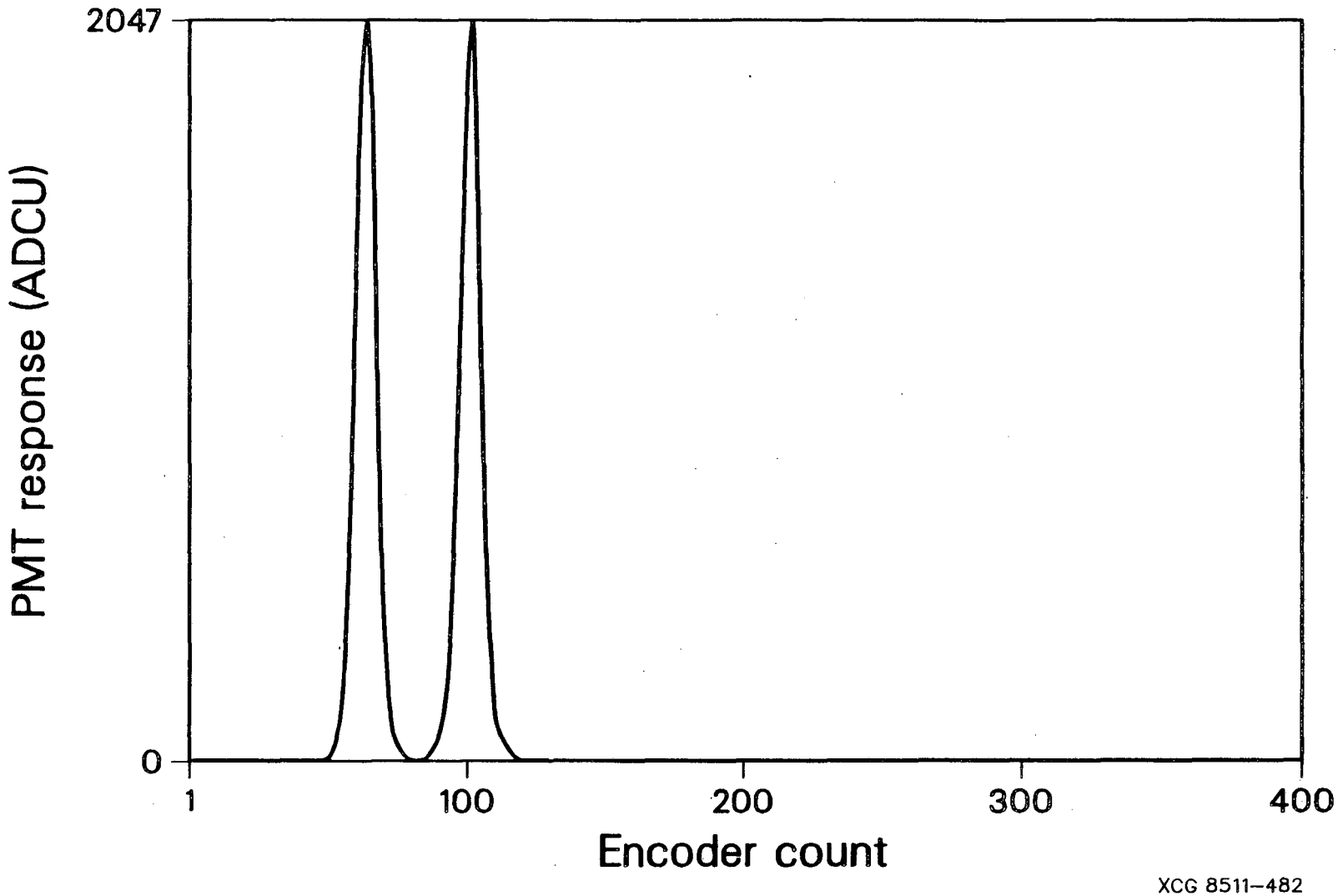
2047
0
PMT response (ADCU)
1
100
200
300
400
Encoder count
XCG 8511-482

FIGURE B4

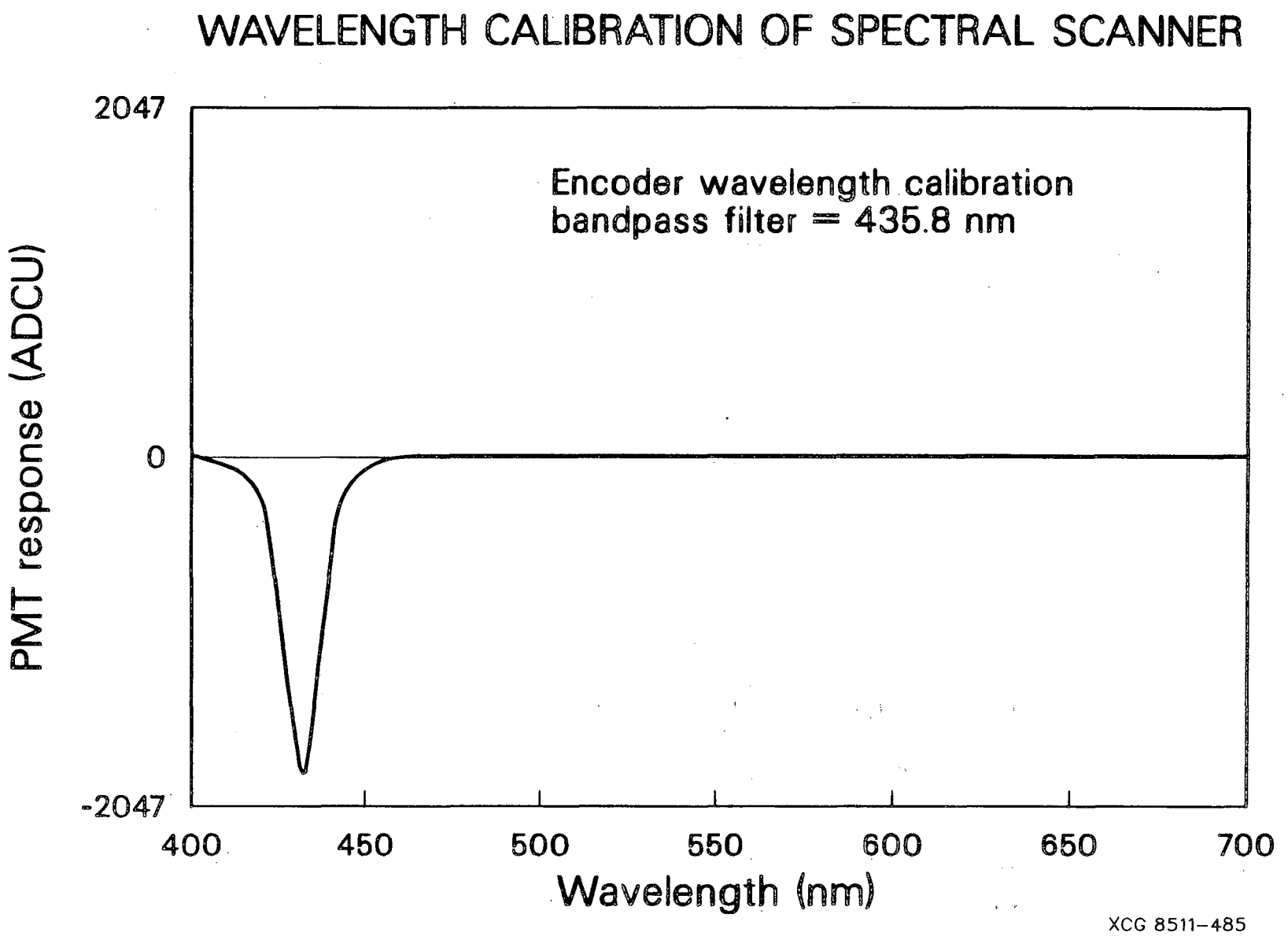
WAVELENGTH CALIBRATION OF SPECTRAL SCANNER
Encoder wavelength calibration
bandpass filter = 435.8 nm
2047
0
-2047
PMT response (ADCU)
400
450
500
550
600
650
700
Wavelength (nm)
XCG 8511-485

FIGURE B5

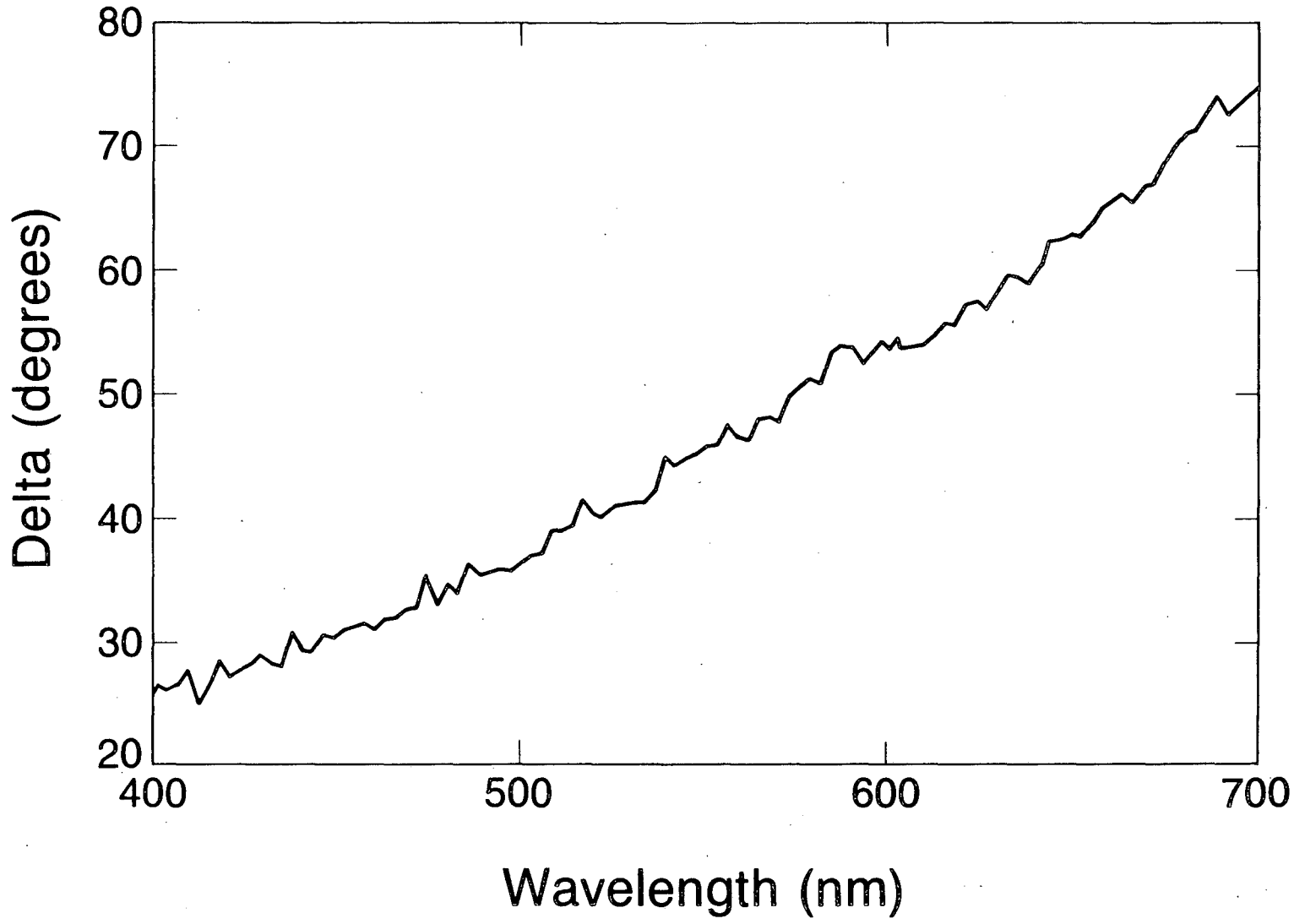

XBL 8511-11429

FIGURE B6

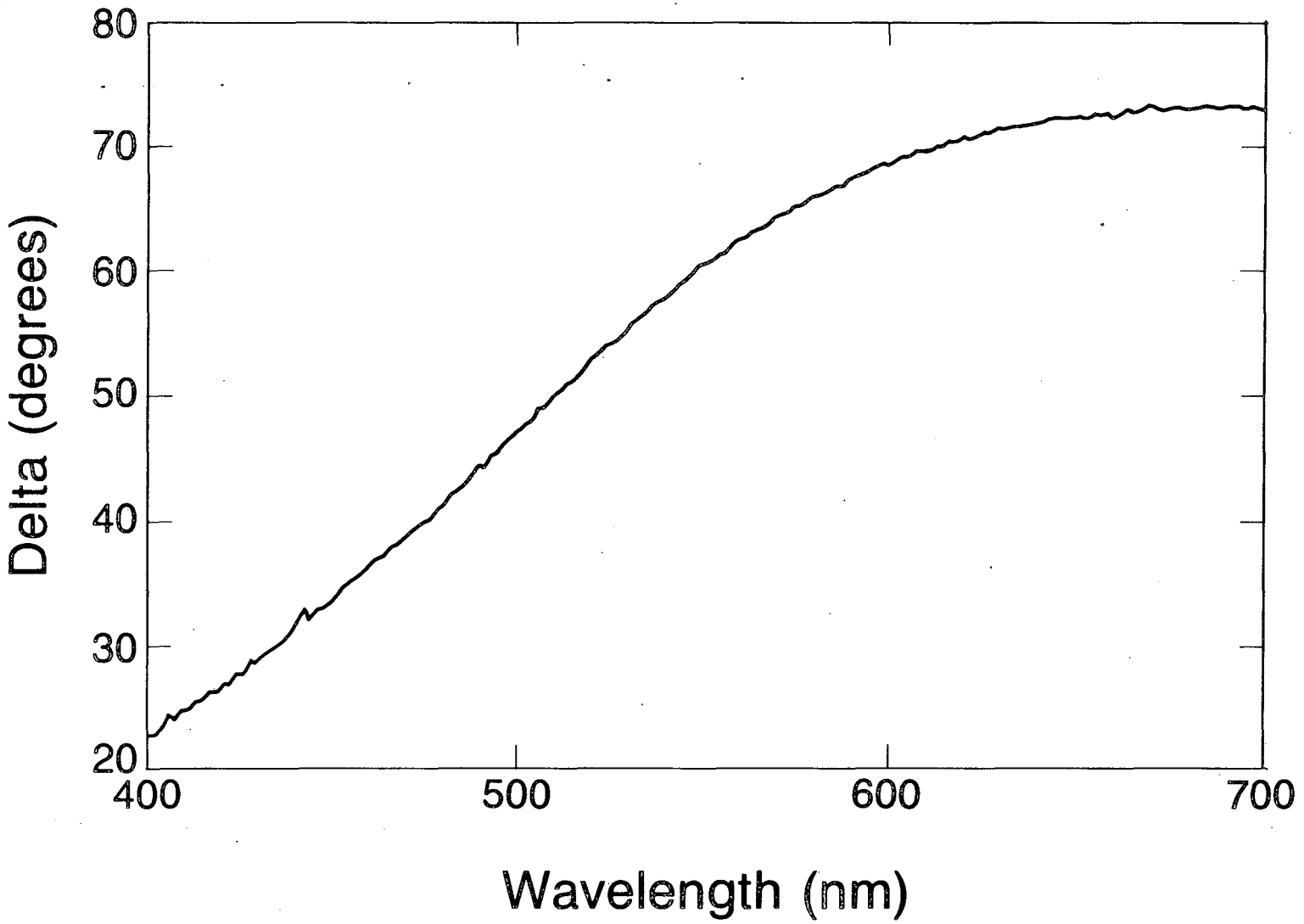

XBL 8511-11430

FIGURE B7

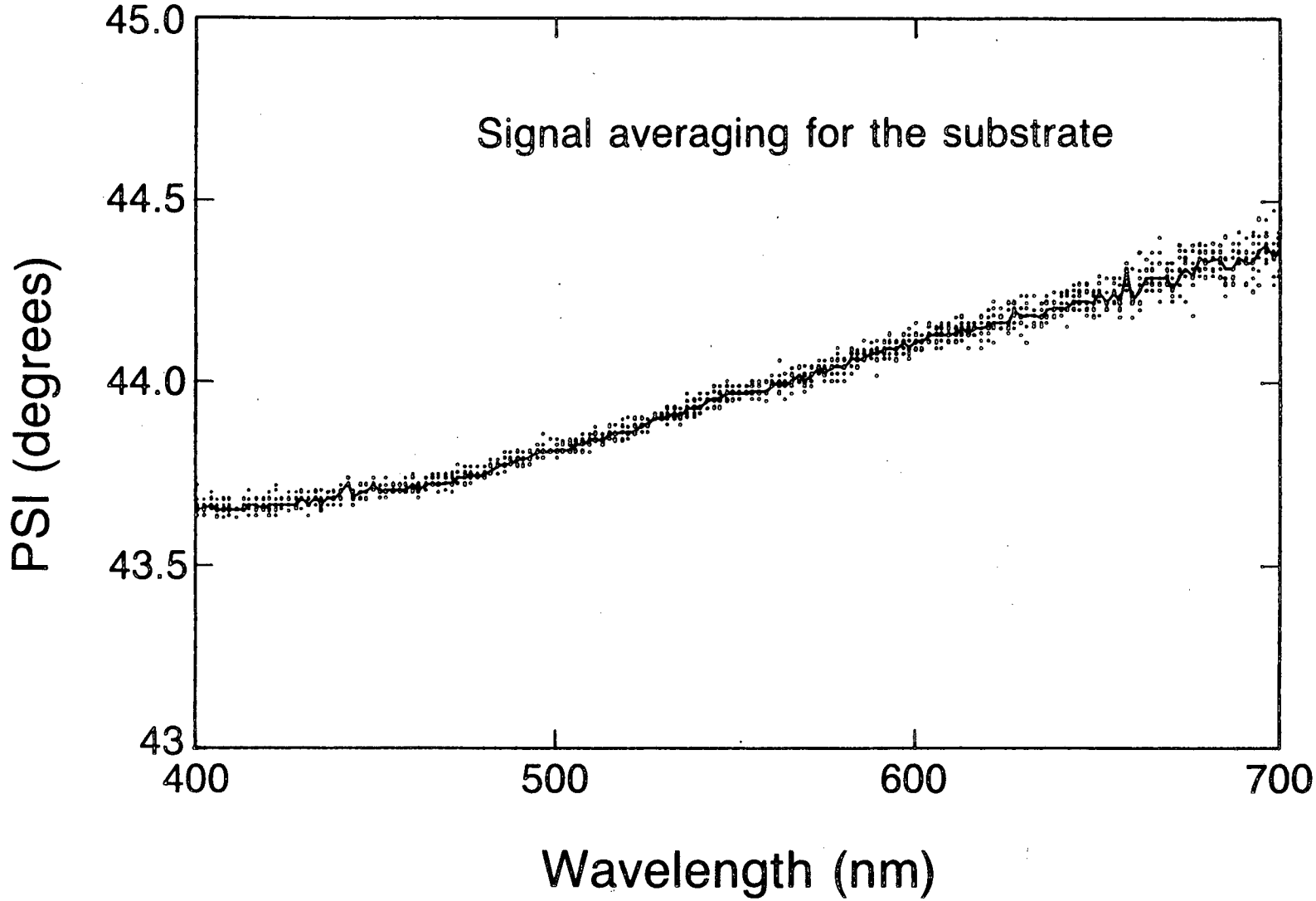

XBL 8511-11443

FIGURE B8

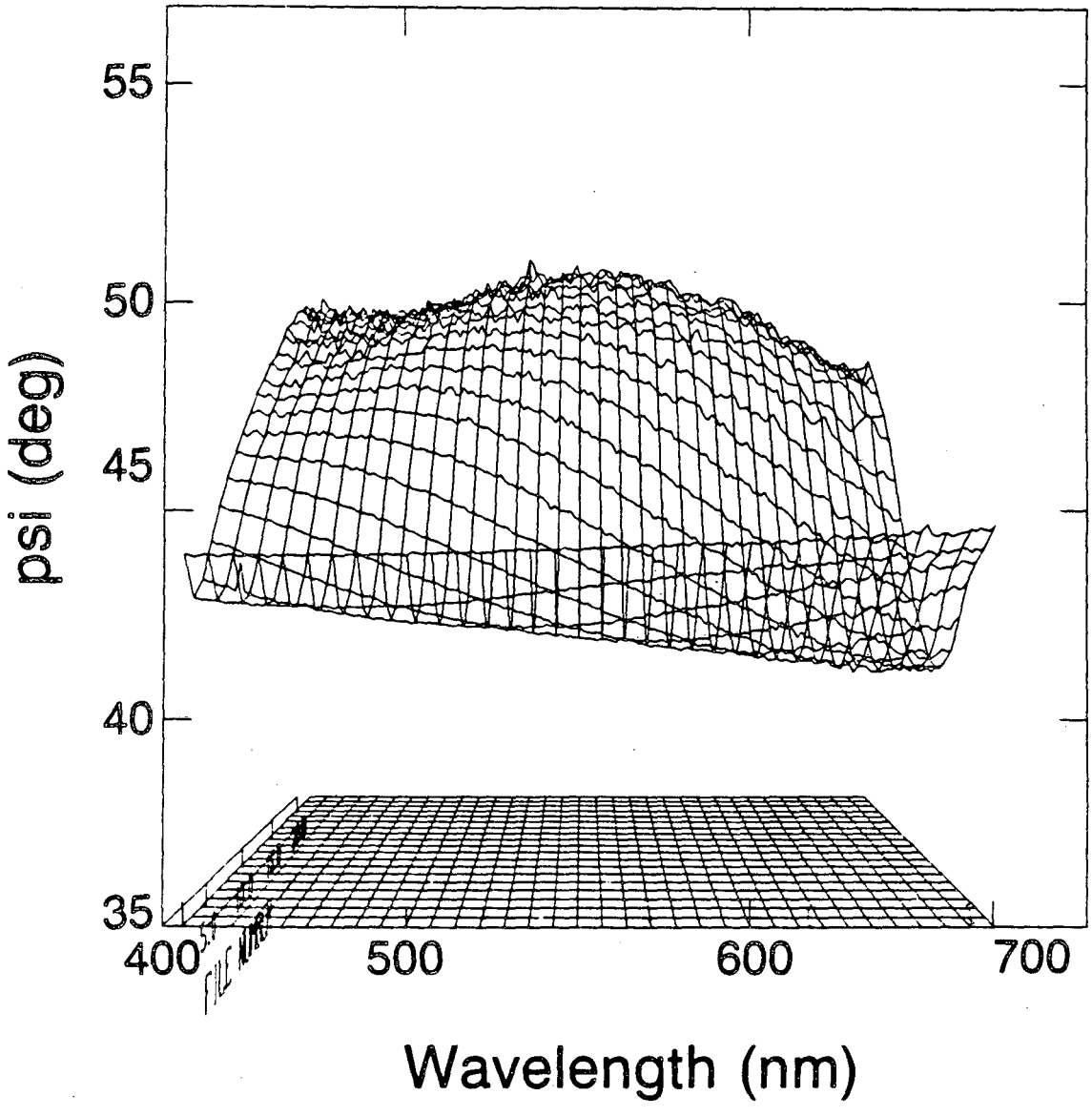

XBL 8511-12737

FIGURE B9

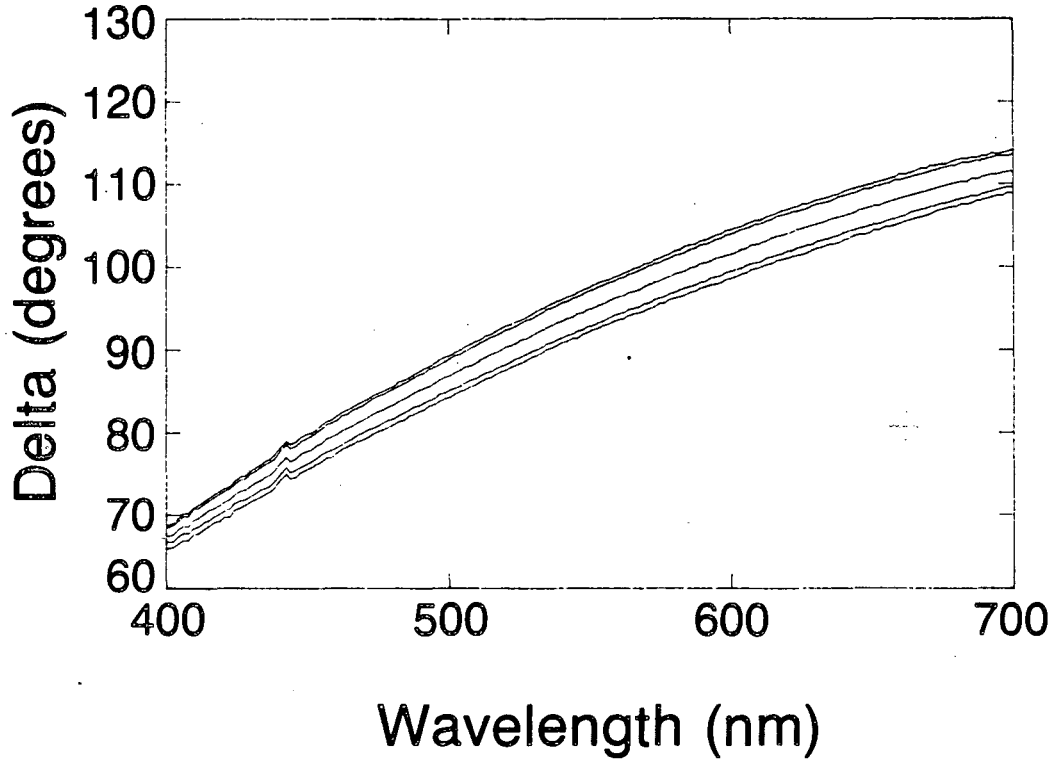

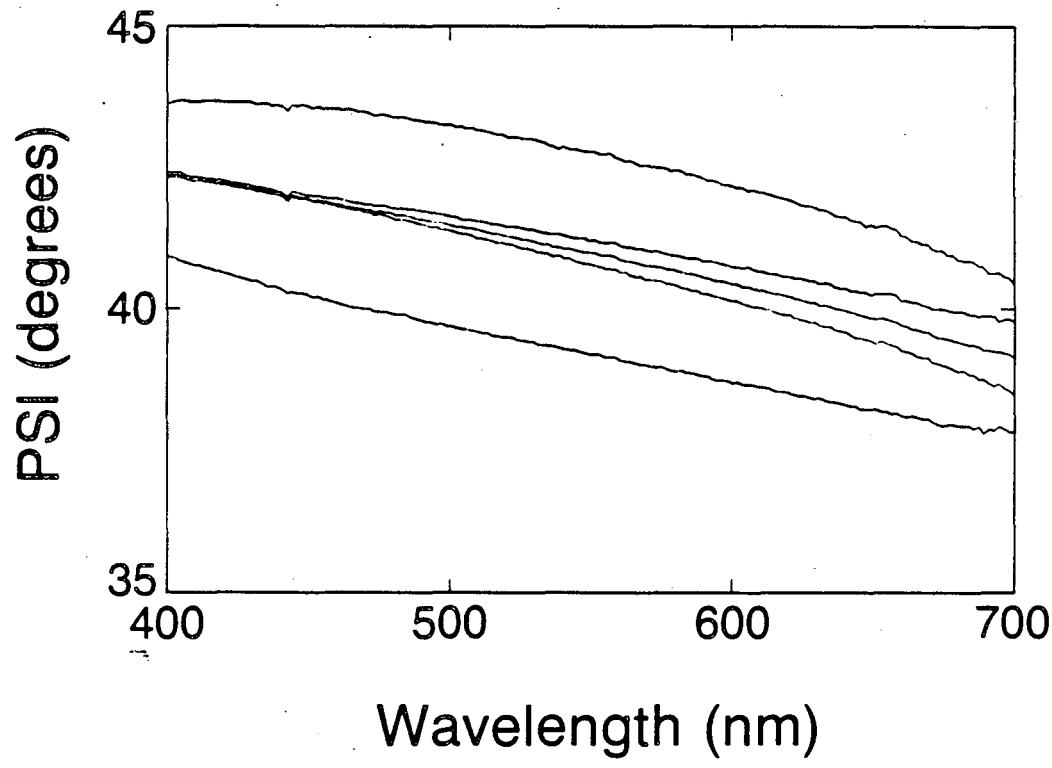

XBL 8511-11444

FIGURE B10

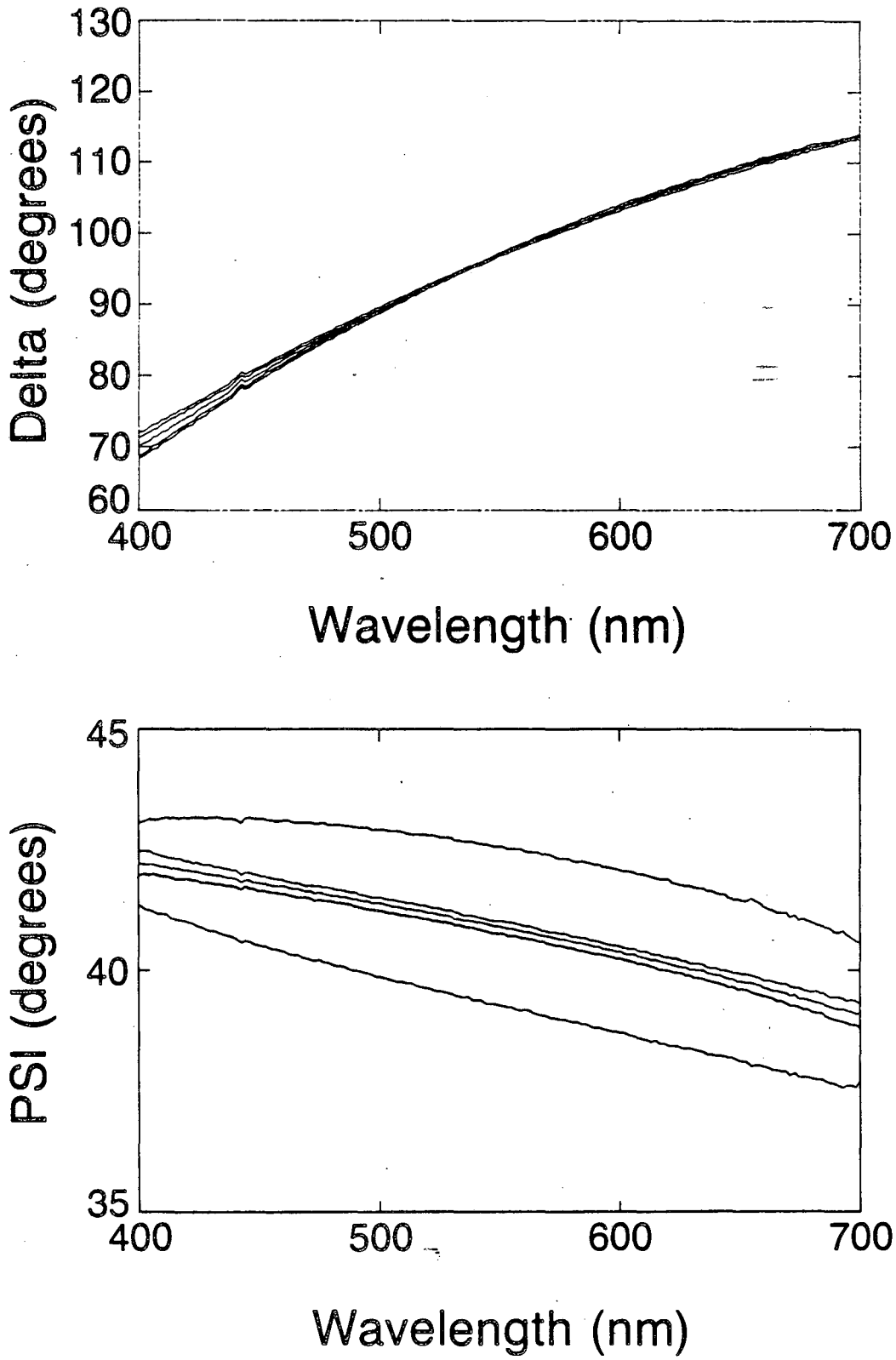

XBL 8511-11445

FIGURE B11

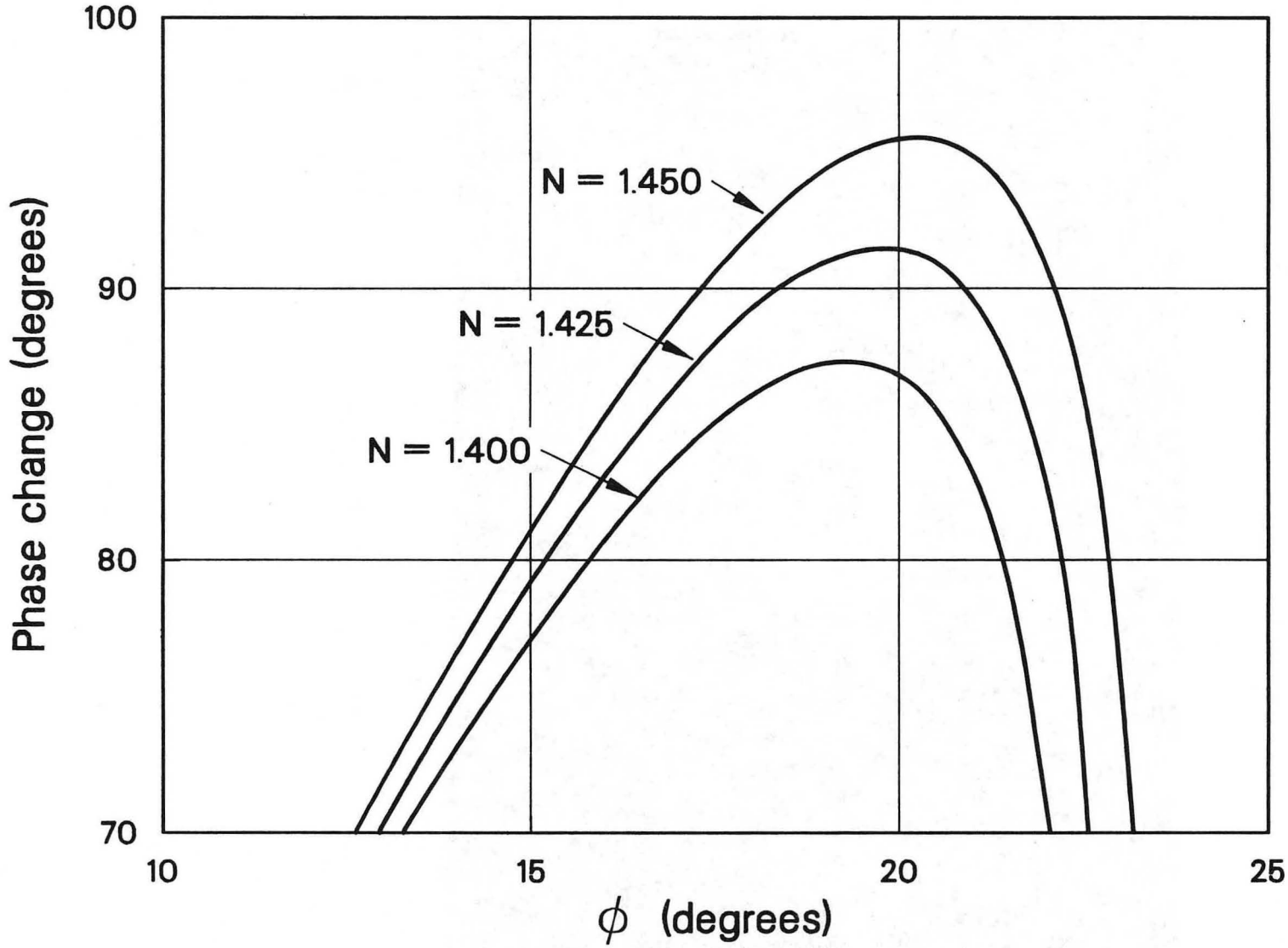

XCG 8511–484

FIGURE B12

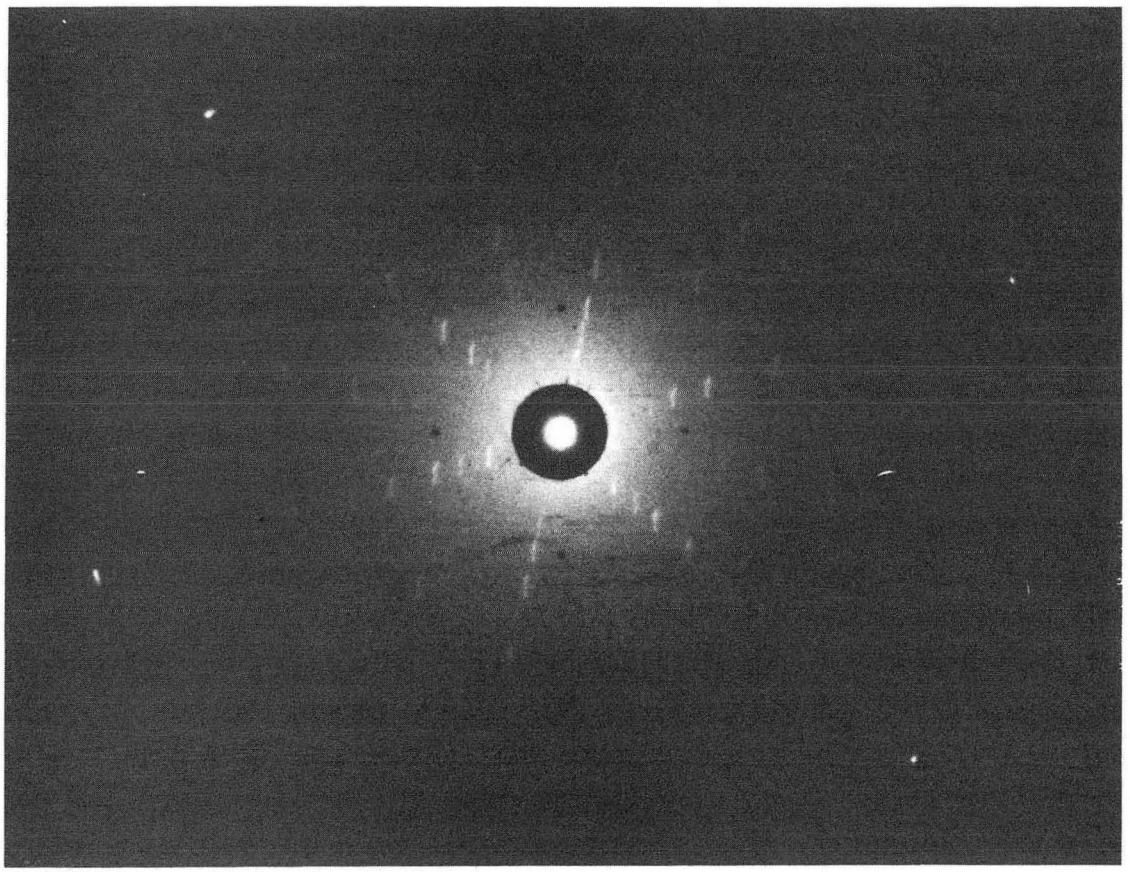

XBB 850-9042

FIGURE B13

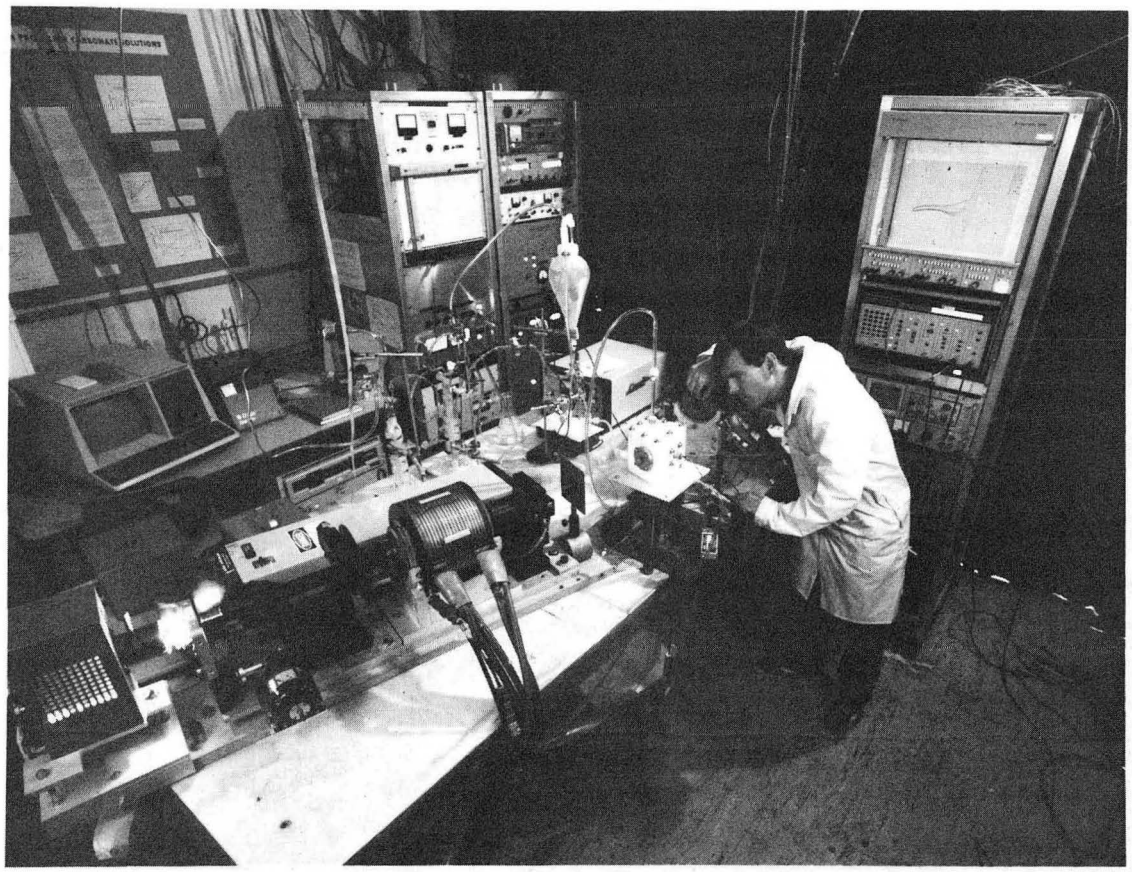

CBB 858-7021

FIGURE B14

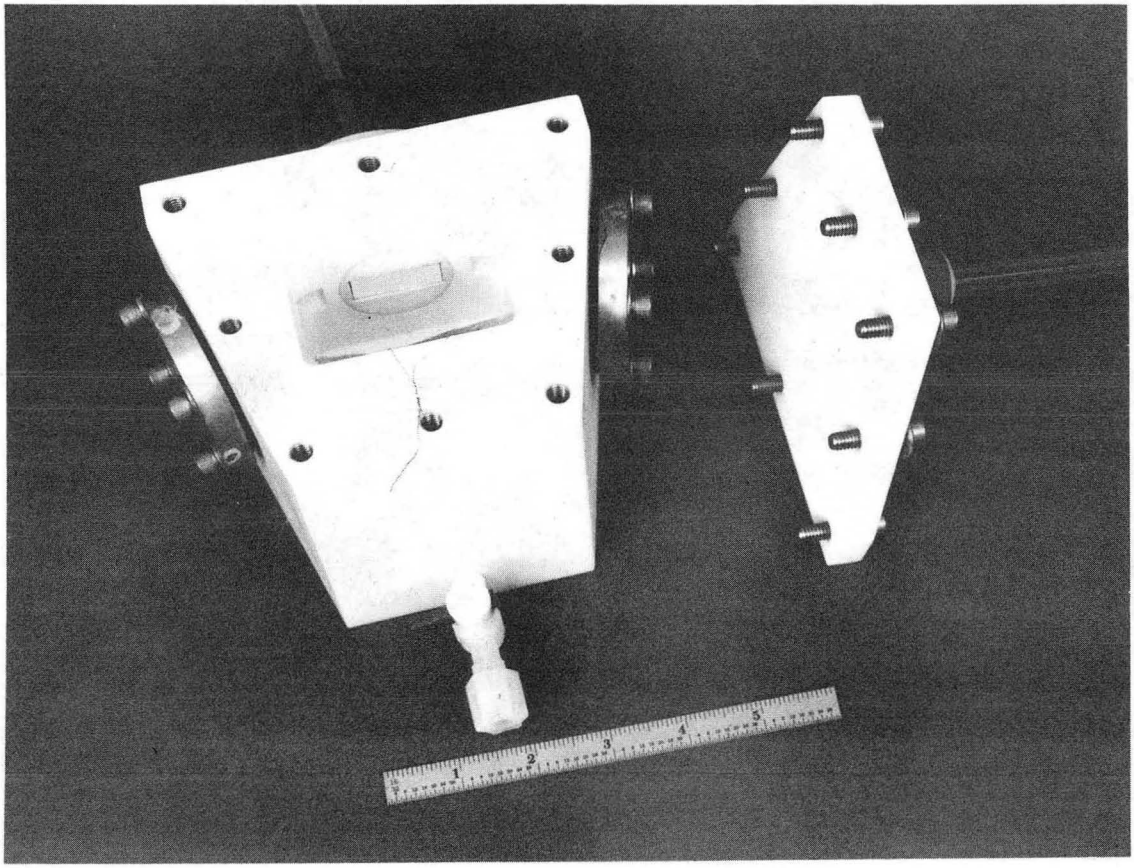

CBB 858-7019

FIGURE B15

CHAPTER 3

MEASUREMENTS

OPTICAL PROPERTIES OF SILVER AND SILVER OXIDE

The optical properties of the polished silver substrate were determined in contact with 1M KOH using a spectroscopic ellipsometer. For every experimental run a clean surface spectral scan was made and the complex refractive index of the substrate was determined. The refractive index determined for each clean surface was later used in the data-reduction routines. Figure C1 shows the average refractive index of silver as determined from 32 separate experiments on Ag(111). The value of the refractive index ranges from 0.15 to C.08 in the spectral range studied. Figure C2 shows the extinction coefficient of silver. The extinction coefficient is almost a linearly increasing function of wavelength. Table C1 compares the data obtained here with some values from the literature at various wavelengths. Our values are reasonably consistent with the refractive-index values reported earlier. The values obtained for the extinction coefficient tend to be slightly lower than those observed by others. Figure C3 and C4 show the standard deviation of the refractive index determined from 32 separate experiments. These results indicate that the optical properties of the surface were largely reproducible.

The refractive index of silver(I) oxide was determined in two ways for this thesis. First, silver oxide powders were compressed isostatically to 110 KPSI in a die. The resulting solid was then embedded in an epoxy resin and polished. The surface examined was brownish-black and

optically smooth. The results of the ellipsometer measurements are shown in Figures C5 and C6. The tailings at the UV and IR spectral ends are believed to be artificially produced by the absorption of light in the Faraday cores. This would cause an insufficient signal to reach the photomultiplier, giving erroneous results. If the two ends of the spectra are neglected the refractive index of Ag_2O oxide is not a strong function of wavelength. The values obtained here are close to those obtained earlier by Smith [1,2]. Values used for the refractive index of silver(I) oxide surface films were considered to be constant with wavelength for this study. The optical properties of the silver anodic layers which form early during galvanostatic experiments and form in the A1 region for potentiostatic experiments were determined by optimization of the refractive index and extinction coefficient (see chapter 4). Both of these method used to determine the refractive index of silver oxide indicate that the refractive index of silver oxide is approximately 1.81-0.28i. This value was used as the refractive index of silver oxide when the refractive index was not treated as a parameter.

GALVANOSTATIC EXPERIMENTS

Ellipsometric/Galvanostatic experiments for this system have been done before [1,2]. In the present study we wanted to look closely at the role of the forming surface layer on the potential response. Spectral data were found to be important if one wants to determine the relationship between the formation of the surface layers and galvanostatic potential response.

Current densities in the range of 50 to 200 $\mu A/cm^2$ were studied here. At these small current densities the changes in optical properties of the surface due to the growing film are sufficiently slow so that one can use an ellipsometer. Also, films that form at lower current densities are more easily modeled, mainly due to their relatively simple morphology. At higher current densities, where the number density of secondary crystals is large, optical changes are very rapid. Interpretation of the data is therefore extremely difficult.

Figure C7 shows psi for a series of scans made for charging at a current density of 75 $\mu A/cm^2$. From this figure we can see that the relative amplitude is virtually unchanged for the first 55 seconds of the experiment (compact layer thickness = 14.2 Å), but it then changes rapidly with strong spectral dependence. This induction time appears to be a general phenomenon. During the induction period the relative phase parameter (delta) changes more rapidly than psi (a ratio of about 10 to 1). After the induction period psi changes rapidly, and the ratio of relative changes of delta to psi reaches a 2 to 1 ratio. Therefore, the surface is appears to be virtually unchanged until a time when there is a rapid change in psi. The time for this change decreases with increasing current density up too about 175 $\mu A/cm^2$, where the change is to rapid to be measured by our spectral ellipsometer.

Figure C8 shows the changes in delta for the anodization of Ag(111) at 150 $\mu A/cm^2$. For the first few seconds the change in delta are approximately proportional to wavelength. After about 30 seconds, the change in delta is larger (10 degrees) at higher wavelengths than at lower ones. For the next 30 seconds, the reverse is true: a change in

delta of about 10 degrees occurs in the high-frequency ranges with small changes (<5 degrees) at low frequencies. This sequence of events occurs in all of the galvanostatic experiments. Finally, Figure C9 shows the changes in psi for this experiment. For the first few seconds psi decreases at all wavelengths. Next, psi starts to increase at low wavelengths, while psi continues to decrease at higher wavelengths. Eventually, psi starts to increase at high wavelengths. Figures C10 and C11 shows the derivates of delta and psi with time (numerically approximated).

Larger optical changes were generally observed at higher current densities for the same total charge passed. As shown in Figure C12, psi shows larger optical changes at a higher current density than at lower densities for the same total charge. In fact, these changes are similar to those seen for a time "evolution" at any given current density. This would be expected if a larger fraction of the total current is attributed to a dissolution process at lower current densities.

Potential measurements were made in addition to the optical measurements for galvanostatic experiments. Figure C13 show the potential response to a galvanostatic current step of 75 $\mu A/cm^2$. The shape of this curve is typical for the galvanostatic experiments done here. These results show a sharp initial increase in potential from the open-circuit rest potential. Next, the rate of change of potential decreases, reaching a plateau at around 200 mV. The duration of this plateau increases with decreasing current density. After some time the potential starts to increase again and reaches another plateau at 210-225 mV. The second plateau potential increases with current

density. The result we obtained did not generally show any strong dip in potential, as reported by Dignam et al. [3], though some decrease was seen for some experimental runs. Dignam's solutions were saturated with Ag_2O. On switching to open circuit after the anodization, the potential initially drops swiftly and then decreases linearly. The potential drops well below the first anodization plateau. Figure C14 shows the potential versus time for a similar experiment, except that the switch to open circuit was made prior to reaching the second plateau. The potential drop that occurs on switching to open circuit is larger if one does not allow the anodization to proceed to the second plateau region. Dignam et al. [3] said that the overpotential decreases with current density in this current range. If the overpotential were largely caused by surface charge transfer processes, the overpotential should be constant for any given current density. If the overpotential were predominantly cause by an increasing compact film resistance, we would expect a larger potential drop with a greater total charge passed. The experimental results do not support these hypotheses. If massive surface-crystal growth is associated with the second peak and surface crystals are only beginning to form in the first potential plateau region, the potential during the first plateau is a measure of a pseudosteady state between the formation of silver electroactive species and the uptake of the these reaction product into surface crystals. When the current is shut off, diffusion from the surface will decrease the surface concentration of electroactive silver species. When there are many relatively large crystals on the surface, the concentration of silver ions can be maintained by dissolution of the surface crystals. It follows then, that the potential will drop less for the electrode that has more

surface oxide than for one that does not, provided the crystal layer covers only a small fraction of the total surface. If we refer back to Figure C7, relatively large changes in psi occur after approximately 50 seconds into the experiment. This corresponds to the a point at the beginning of the first plateau in the potential response shown in Figure 13C. This correspondence between the rapid change in the optical properties of the surface and the stabilization of the potential has been seen at all current densities studied here.

CYCLIC-VOLTAMMETRY AND POTENTIAL-RAMPING EXPERIMENTS

Cyclic-Voltammetry (repetitive triangular potential sweeping, RTPS) and potential-ramping experiments were performed to obtain an overview of the specific processes that occur during the charging and discharging process and to try to associate various anodic peaks found in cyclic voltammograms with physical or chemical processes of the Ag_2O system. The general phenomenological results obtained here agree with those reported by other authors (see the literature review chapter of this report). It has been reported that cyclic-voltammetric results are specific to crystal orientation [4]. Results here pertain to the Ag(111) face only. Spectroscopic-ellipsometry measurements were made only for slow potential-ramping experiments. Fixed-wavelength measurements during cyclic voltammetry were done when higher sweep rate were involved.

Figure A1 shows a first-cycle RTPS voltammogram obtained for the Ag(111) face at a sweep rate of 20 mV/sec. While the general characteristics of this figure are similar to those reported in the litera-

ture, differences include a merging of the A1 and A2 peaks and smaller current densities. Hepel and Tomkiewicz noted that the surface should be roughened in order to see the A1 peak [5]. The A3 and A4 peaks are of similar size and occur at the same potentials as those reported in the literature (400 and 600 mV, respectively). The A3 peak that we observed here is broad, similar to that shown by Hepel and Tomkiewicz [5], Pound et al. [6], and Droog et al. [7]. Note that Pound labels the peak that occurs at 400 mV the A2 peak. It is important that the reader of the literature understands which voltammetric peak is being discussed, since many others use the same name for different peaks. The anodic A4 peak is larger than the A3 peak, but it is not as sharp as that seen by others [4,5]. A minor anodic peak is observed after sweep reversal at 525 mV, which may represent a continued formation of Ag_2O by a mechanism similar to that associated with the A3 peak. This peak has been seen before [5]. The cathodic C4 (325 mV) peak is smaller than the cathodic C3 peak (75 mV).

A "window opening" voltammogram was performed to search for anodic and cathodic peaks associated with the A1 process. Figure C15 shows the results up to a peak potential of 170 mV. These results show no clear anodic or cathodic peaks. Droog [4] also found no distinct anodic peak in this potential range for Ag(111). The waves in the Cyclic-voltammogram are similar in form to those generated by Casadio for reversible anodic dissolution of electrode material inhibited by a redox adsorption process [8]. When one continues to sweep out to higher reversal potentials (Figure C16), a truly uncommon waveform develops. The cathodic wave develops a very broad peak whose location moves to

lower potentials with increasing reversal potential. This appears to be to the formation of the C2 process. The anodic current wave increases (the current is greater at the same potential) as we continue to increase the reversal potential. In this particular experiment, a complete cyclic-voltammogram is developed up to 500 mV (Figure C17), where we now observe the three peaks associated with the Ag-to-Ag_2O transformation. The A1 and A2 peaks are much clearer here than those seen in Figure A1. When we cycle in the A1 region after going to the reversal potential of 500 mV, we obtain the results shown in shown in Figure C18. Anodic and cathodic peaks are now observed. The voltammogram shown in Figure C18 is similar to those reported by Droog et al. [7] for polycrystalline silver. The surface appears to have reformed itself to a more surface-active arrangement, with a change in the associated potential characteristics.

Simultaneous cyclic-voltammetry/fixed-wavelength ellipsometry measurements were made at sweep rates ranging from 5 to 20 mV/second. Various reversal potentials were used. Figures C19 and C20 show the changes in delta and psi for an experiment with a sweep rate of 10 mV/second and a reversal potential of 175 mV. Very little change is seen in the surface optical properties up to a potential of 75–100 mV. Above 160 mV, a more rapid change in optical properties starts to occur. Figure C21 shows the current versus potential for a sweep rate of 5 mV/second and a reversal potential of 180 mV. Figure C22 shows the charge passed versus potential for a sweep rate of 20 mV/second and a reversal potential of 175 mV. Looking at these figures, we make the following observations:

1. The total optical changes are smaller than those associated with a surface monolayer.

2. Total charge passed is much larger than that necessary for the formation of a monolayer.

3. There is an immediate reversal of the optical properties of the surface after a change in sweep direction (Figures C19 and C20).

4. The rate of change of delta and psi is much slower after sweep reversal than it is with the positive sweep direction (Figures C19 and C20).

5. There is a continuing anodic current even after the sweep direction has been reversed (Figure C21).

6. The anodic to cathodic charge ratio (Q_a/Q_c) over a cycle is greater than one, indicating an irreversible process (Figure C22).

7. Very small permanent changes in the optical properties of the substrate (delta <0.05 degree, psi <0.01 degree) are observed for peak potentials below about 180 mV. Above this reversal potential, the original surface optical properties can not be obtained and the surface is reformed and microroughened.

We can infer from these results that these initial optical changes are probably associated with a surface-absorbed species, possibly a reaction intermediate (e.g., a surface absorbed hydroxide ion). The surface coverage of this species appears to depend on both surface potential and the concentration of the electroactive species in solution. Finally, we

believe that the observed surface species is most likely a reaction product. These conclusions are based on the following arguments, related to the list above. Observation 1 allows us to say that some submonolayer adsorption process is occurring. Observation 2 allows us to conclude that this submonolayer species does not account for the total charge passed. Some cocurrent dissolution process is occurring. Observations 3, 4, and 5 must be looked at together. While the surface potential appears to be the major contributing factor to the surface coverage, observation 4 and 5 indicate that the surface concentration of optically observed species also depends on the electro-active species concentration in the diffusion boundary layer. Since the anodic current continues upon sweep reversal, the diffusion process must be fast with respect to changes in surface concentration of the soluble species. Intuitively we can see this because, if the diffusion process were slow compared to the rate of change in the surface concentration, the current would immediately change sign upon a reversal of sweep direction. Any differential change in surface concentration would change the sign of the concentration gradient at the surface, yielding a sign change in the observed current. When the concentration profile is "stiff" (i.e., slow) with respect to the governing time constant of the surface reaction rate, the current will change sign immediately with a change in sweep direction. If the reverse is true, we expect to see an anodic current that continues after sweep-direction reversal. We therefore believe that the surface species that the ellipsometer detects is an adsorbed product whose desorption is slow.

Potential-ramping experiments were performed at a slow sweep rate (0.5 to 0.2 mV/sec). The spectral-ellipsometry parameter changes are shown in Figure C23, and the voltammetric results are shown in Figure C24. The sweep began at an open-circuit potential of the clean silver surface (about −50 mV) and was stopped at 200 mV. Optically, there are three notable regimes. The first regime is for potentials lower about 100 mV. Very small changes (delta <0.2 degree) occur. This regime of small changes has been seen by Droog [4], but his experiments were performed at larger sweep rates (20 mV/sec) and with an off-null technique. For potentials between about 100 mV to 190 mV, significantly larger changes occur, but these optical changes still correspond to only a few monolayers. The third regime occurs for a potential above 190 mV, where large spectral changes in both delta and psi are observed. If we turn to the current response for this sweep, we can also identify three distinct regimes. The first has very low currents that increase linearly with potential (0.09 $\mu A/cm^2/mV$). A discontinuity in the slope of the current curve is seen at around 100 mV, where the slope increases fourfold (0.35 $\mu A/cm^2/mV$). At a potential of 185 mV, another discontinuity is seen in the slope of the current response, and the current increases dramatically at first but later decreases toward what may have been a peak had we allowed the sweep to progress further in potential. It is intriguing that the optically observed changes coincide with changes in the current response.

POTENTIOSTATIC EXPERIMENTS

Potential-step experiments were performed using the ellipsometer in both the spectral and fixed-wavelength mode. Spectral scanning was

effective for determining optical changes for processes occurring after the first second. Figure C25 shows the changes in delta for some potential-step experiments done at a fixed-wavelength. The same electrode was used for all of these potential step measurements. After one potential step run was made, the potential was set to −300 mV for 20 minutes (reducing any silver in solution or oxide on the surface). Then another potential step (to a higher potential than the previous potential step) was made. There is an initial, very rapid relative phase change, which is followed by a second region of much slower changes in delta. Examination of the data shows that the initial changes in delta occur within the first 1/2 second after the step change in potential. The magnitude of the change is approximately that which would be associated with the formation of a monolayer. For potential steps to potentials greater than 160 mV and less than 200 mV there is no apparent different in the rate of change of delta with time (at this wavelength), but at 200 mV, the rate of change in delta with time increases dramatically. Further, when the potential is reversed after a potential-step anodization, the optical properties of the reformed surface are permanently changed when the anodization is done at potentials greater than 170 mV. However, the permanent changes are much larger (5 degrees in delta) for reformed surface after anodization at potentials greater than 200 mV than for potentials less than 200 mV (less than 0.5 degrees in delta).

The result obtain at a fixed wavelength are not in total agreement with our spectral measurement (see Chapter IV, and figure D30). The spectral measurements done with potential steps showed a significant

increase in the rate of change in optical parameters (growth rate of the film) in the potential range of 160-190 mV. However, spectral measurements were not made on reformed surfaces. These reformed surfaces may not consist of only Ag(111) planes, and this may help explain the discrepancy.

Spectral-ellipsometry results for potential-step experiments show very slow changes in both delta and psi for potentials below 190 mV. For potential steps below 160 mV, no changes are found in delta or psi after the initial rapid change. The measurements were made for 10 minutes after the original potential step was made. Again, the initial change occurs well before the first scan is completed. Large spectral changes are seen for potential steps greater than 200 mV. Unlike the galvanostatic experiments, ellipsometric parameters undergo relatively large changes after the potential step is applied. Indeed, in a potential-step experiment, the surface concentration is kept constant with time. Therefore, when the surface potential is high enough to support nucleation of oxide crystals, we would expect to see those changes occur for all potential above some minimum potential (see Chapter IV, on interpretation of nucleation experiments). Some experimental uncertainty will arise due to the problems associated with reproducing a surface with nucleating centers of the same energy distribution. Despite this inherent problem, it appears that there is a well defined potential region where the number of nucleation site increase dramatically on the silver surface that we prepared.

The current responses for a variety of potential-step experiments are shown in Figures C26–C28. For potentials below 200 mV, the current

decreases monotonically for any given potential and increases with increasing potential. No steady-state current is observed. For potentials slightly above 200 mV, the initial decreasing current passes through a minimum and then starts to increase again. Later, a maximum in current is observed. This general behavior has been seen before [9,10]. For potentials above about 215 mV, the minimum becomes shallow, and a current that is nearly constant with time is observed for long periods of times. Finally (not shown in these figures) the currents tend toward zero at a later time.

POTENTIAL-PULSE AND CORROSION MEASUREMENTS

This last class of optical measurements was performed to investigate the stability of the surface films that form very early on the silver electrode. Various pulse lengths were applied (10 to 520 seconds) at a fixed potential of 200 mV. This potential value was chosen since it was felt that good control over the extent of crystal growth could be obtained at the potential where the surface crystals are first observed to form. Figure C29 shows the changes in psi for a 280-second pulse. We note that psi is virtually unchanged for long periods when we go to the open circuit. The surface layer does not appreciably corrode or restructure itself. This latter statement is true, since even if the surface material is redistributed without dissolution, we would still expect to see changes in the optical properties of the surface. The fact that the optical properties of the surface are constant for long periods in an unsaturated solution shows that dissolution into the bulk is small when there is a relatively large amount of charge (>5 mC/cm^2) stored on the surface in the form of crystals. Figure C30

shows results of the change in psi for a 50-second potential pulse at 200 mV. Optical changes occur after we switch to open circuit. As seen in Figure C30, psi continues to change in a direction that corresponds to larger amounts of surface material even after an open-circuit potential is established. This growth later stops, and then corrosion/dissolution of the surface film is apparent as the delta and psi values approach those of the substrate. Finally, Figure C31 shows the results of the changes in psi for a 30-second pulse. Here, no continued growth is seen after open circuit, but the corrosion/dissolution of the surface layer is again apparent. The fact that the optical properties of the substrate surface are regained after open-circuit corrosion/dissolution strongly indicates that neither surface roughening nor surface smoothing occurs during the anodization of the silver electrode at low overpotentials.

SCANNING ELECTRON MICROGRAPHS

An electron microscope (ISI-DS-130) has been used in this study to (1) observe the micromorphological structure of the thin films (and therefore aid in the choice of an optical model) and (2) to compare ellipsometric results with electron-microscope results.

The anodization process was interrupted at various times during potential-step experiments to deduce changes in the surface-film properties with time. Three points in the potentiostatic-current response were chosen for terminating the anodization. The first end point corresponds to the local minimum in the current. SEM photographs of surfaces whose anodizations were terminated at this point show what

appears to be very small crystal forming, but they are difficult to observe. Figure C32 and C33 are pictures of silver oxide crystals formed by a potential step to 200 mV for 285 seconds (21.8 mC/cm^2). This anodization was stopped after the current minimum and before the current maximum (see Figure C27). Crystals of various sizes, distributed unevenly over the surface, can be seen. The surface coverage is moderate (<20%), and the average crystals diameter is about 1500–2500 Å. Crystals as small as 300 Å can also be observed. No crystalline underlayer appears in these photographs, though a porous "Swiss cheese" substrate is seen. Figures C34 and C35 are photographs of an anodization carried out under the same conditions as those in figures C32 and C33, but the experiment was allowed to continue until a peak in the current was observed (375 seconds, 37.5 mC/cm^2). The first observation is that the surface coverage of the crystals is greater with the larger total charge. Also, the size of the average crystals is larger with increasing total charge passed (6000 Å). Finally, the 60-degree angle between different Ag_2O surfaces indicates a preferential formation of (111) planes.

Earlier workers have stated that an underlayer ("primary layer") forms prior to the nucleation of large Ag_2O crystals ("secondary layer") (see literature review). As indicated earlier, our potential-step measurements indicated the growth of a layer that was very thin and whose growth rate decreased with time. It was felt that a series of small potential steps might allow one to grow a reasonably thick primary layer. The thickness of the growing oxide was monitored with the ellipsometer, and the current passed was monitored with the potentiostat.

Potential-step measurements were made in a sequence from −50 mV (open circuit) to 190 mV, then to 210 and finally 230 mV. Large changes in psi indicated that nucleation had started after the potential step to 230 mV was made. Figure C36 show that this anodized surface (total charge 41.7 mC/cm^2) has a lower number density of secondary crystals than those formed with a single potential step. But this is not the only difference. These crystals have smaller crystals on top of them that were not evident in Figures C32–C35. This tertiary layer has been reported before (see literature review section). Also, in Figures C32–C35, the silver substrate appears to have a "Swiss-cheese" pitting, which is not evident in Figure C36. One explanation of this pitted structure might be that dissolution occurs at various parts along the electrode surface at different rates. Local variations in the surface activities of the silver atoms that arise from local defects and changes in exposed surface planes could cause such a phenomenon. Figure 35C shows an alignment of the pits with the direction of polishing. While single-crystal surfaces are inherently more uniform than polycrystalline surfaces, exclusive exposure of one surface plane over large distances is not guaranteed by the procedure used for surface preparation in this work. However, we would expect some uniform orientation at the dissolved locations if this dissolution process was the cause of the pitting. This is not observed. It is possible that the underlayer is a porous oxide underlayer. However, we would expect a porous oxide to be filled as charge is passed. If we compare figures C32 and C34, the pores of the "Swiss cheese" are larger with measured total charge passed. Therefore, we can not exclude either possible explanation for surface pitting. Higher-magnification pictures of the surfaces in

figures C32-C35 would have been helpful, but they were not possible due to instrumental malfunctions at that time.

Figures C37 to C39 are higher magnification pictures of the same surface shown in Figure C36. We can conclude from Figures C37 and C39 that the tertiary-layer crystals are approximately 150 Å in diameter. It is impossible to determine any crystallographic orientation of the tertiary crystals from these pictures. Finally, Figure C39 is a high-magnification picture of the underlayer seen between the secondary crystals. These primary-layer crystals are about the same size as the tertiary-layer crystals. The surface coverage of these crystals is large (75%), but at most these crystals could account for only about 10% of the total charge passed. The secondary crystals form with a lower surface coverage (15%) but account for as much as 80% of the total charge passed. The conclusion that a majority of the charge is stored in the secondary layer has been stated before [1,2].

CONCLUSIONS

The results discussed in this section have enabled us to draw qualitative conclusions about the method in which Ag_2O surface layers form on a silver substrate in 1M KOH. By making a variety of electrochemical experiments and using ellipsometry and scanning electron microscopy for optical studies of the surface layers formed, we have been able to show that the manner of anodization plays an important role in the morphology and appearance of the various surface structures.

Optical result of galvanostatic experiments initially show small changes in delta and psi which later increase dramatically.

Potentiostatic experiments below 160 mV show little changes in delta and psi with time. Between 160 mV and 190 mV, small time dependent optical changes are observed. Above 190 mV, large changes in delta and psi are observed. Slow potential sweeping experiments done with simultaneous spectroscopic ellipsometry also show three distinct regimes of oxide products formed. Fixed wavelength potential sweeping experiments show that an absorbed surface layer (perhaps the reaction product itself) account for only a small portion of the total charge passed in the Al potential region. Ellipsometric results indicate that the surface desorption of the reaction products is slow compared to the rate of diffusion of reaction products.

Scanning electron micrographs show three distinct silver oxide crystal structures. Small (<300 Å in diameter), high number-density crystals exists below a layer of larger, lower number density crystals. The larger crystals (Secondary crystals) also have a layer of smaller crystals (tertiary layer) on top of them. Secondary crystals of silver oxide show preferential formation of (111) planes on silver (111) surfaces.

The nucleation of secondary crystals is suppressed by forming the oxide with a number of small (20 mV) potential step. The number density of secondary crystals is smaller when the they are formed in this manner. The secondary crystals account for a majority of the surface material.

REFERENCES FOR CHAPTER 3

1. Smith, Craig G., Ph.D. thesis, Dept. of Chemical Engineering, University of California, Berkeley, August 1978.

2. Muller, Rolf H., and Craig G. Smith, Surf. Sci. 96 (1980) 375.

3. Digham, M. J., H. M. Barrett, and G. D. Nagy, Can. J. Chem. 47 (1969) 4253.

4. Droog, John M. M., J. Electroanal. Chem. 115 (1980) 225.

5. Hepel, Maria, and Micha Tomkiewicz, J. Electrochem. Soc. 131 (1984) 1288.

6. Pound, Bruce G., Digby D. MacDonald, and John W. Tomlinson, Electrochim. Acta. 25 (1980), 563.

7. Droog, John M. M., Peter T.. Alderliesten, and Gosse A. Bootsma, J. Electroanal. Chem. 99 (1979) 173.

8. Casadio, Sergio., J. Electroanal. Chem. 67 (1976) 123-128.

9. Tilak, B.V., R. S. Perkins, H.A. Kozlowska, and B. E. Conway, Electrochim. Acta. 17 (1972) 1447.

10. Pound, Bruce G., Digby D. MacDonald, and John W. Tomlinson, Electrochim. Acta. 25 (1980), 1293.

TABLE C1

Comparison Of The Optical Properties
Of Silver Found In This Study With The Literature

Wavelength (NM)	Refractive Index	Reference
400.8	0.14-1.30i	*
400.0	0.06-2.03i	4
397.5	0.05-2.07i	5
450.2	0.12-2.03i	*
451.0	0.04-2.49i	4
450.1	0.04-2.67i	5
500.5	0.12-2.56i	*
496.0	0.03-2.89i	4
496.0	0.05-3.09i	5
549.4	0.11-3.08i	*
546.1	0.18-3.61i	1
551.1	0.04-3.36i	4
548.8	0.06-3.57i	5
600.2	0.10-3.57i	*
605.0	0.05-3.78i	4
633.1	0.10-3.87i	*
632.8	0.38-3.71i	2
632.8	0.05-4.54i	3
635.9	0.05-4.04i	4
700	0.08-4.49i	*
708.6	0.06-4.61i	4
704.6	0.04-4.84i	5

* This study

1. Muller, Rolf H., and Craig G. Smith, Surf. Sci. 96 (1980) 375.

2. Droog, J. M. M., P. T. Alderliesten and G. A. Bootsma, J. Electroanal. Chem. 99 (1979) 173.

3. Albers, H., J. M. M. Droog, and G. A. Bootsma, Surf. Sci. 64 (1977) 1.

4. Flaten, C. J. and E. J. Stern, Phy. Rev. B 11 (1975) 638.

5. Johnson, P.B. and R. W. Christy, Phy. Rev. B, 12 (1972) 4370.

FIGURE CAPTIONS FOR CHAPTER 3

C1. Average refractive index of silver, based on 32 different polished silver surfaces.

C2. Extinction coefficient of silver, based on 32 different polished silver surfaces.

C3. Standard deviation of calculated refractive index based on measurement of 32 different polished silver surfaces.

C4. Standard deviation of calculated extinction coefficient based on measurement of 32 different polished silver surfaces.

C5. Refractive index of an isostatically compressed (110 Kpsi) powder of silver (I) oxide which was polished.

C6. Extinction coefficient of an isostatically compressed (110 Kpsi) powder of silver (I) oxide which was polished.

C7. Changes in Psi for various charging times at a current density of 75 $\mu A/cm^2$. 1) 55 seconds. 2) 84 seconds. 3) 120 seconds.

C8. Delta spectra for a charge density of 150 $\mu A/cm^2$. 1) Substrate. 2) 2.3 seconds. 3) 35 seconds. 4) 78 seconds.

C9. Psi spectra for a charge density of 150 $\mu A/cm^2$. 1) Substrate. 2) 2.3 seconds. 3) 35 seconds. 4) 78 seconds.

C10. Derivate of delta spectra for a charge density of 150 $\mu A/cm^2$. 1) 2.3 seconds. 2) 35 seconds. 3) 78 seconds.

C11. Derivate of psi spectra for a charge density of 150 $\mu A/cm^2$. 1) 2.3 seconds. 2) 35 seconds. 3) 78 seconds.

C12. Change in psi for a fixed total charge passed (11.9 mC/cm^2) at various current densities. 1) 75 $\mu A/cm^2$. 2) 100 $\mu A/cm^2$. 3) 200 $\mu A/cm^2$.

C13. Potential for a galvanostatic experiment (75 $\mu A/cm^2$). Experiment was allowed to progress to the second plateau.

C14. Potential for a galvanostatic experiment (75 $\mu A/cm^2$). Experiment was not allowed to progress to the second plateau.

C15. A "window opening" cyclic voltammogram of Ag(111) performed at 20 mV/sec up to 170 mV vs. Ag/AgCl 4M KCl. The "window opening" preceded in the direction of increasing anodic potential, and occurred in steps of 10 mV after the completion of each cycle. Total electrode area is 3.19 cm^2.

C16. A "window opening" cyclic voltammogram of Ag(111) performed at 20 mV/sec from 150 to 300 mV vs. Ag/AgCl 4M KCl. This is a continuation of the experiment shown in Figure C15.

C17. A cyclic voltammogram of silver up to the A3 peak (500 mV) established after many cycles. This is a continuation of the experiment shown in Figures C15 and C16.

C18. Cyclic voltammogram in the same potential region as in Figure C15 after the potential has been cycled to a peak potential of 500 mV.

C19. Delta for a cyclic voltammetry experiment with peak potentials of -250 and 175 mV vs. Ag/AgCl 4M KCl. Wavelength 514.5 nm.

C20. Psi for a cyclic voltammetry experiment with peak potentials of -250 and 175 mV vs. Ag/AgCl 4M KCl. Wavelength 514.5 nm.

C21. Cyclic voltammogram of Ag(111). Sweep rate 5 mV/sec. Reversal potentials −240 and 180 mV vs. Ag/AgCl 4M KCl.

C22. Charge versus potential for the first cycle of a cyclic voltammogram (20 mV/sec). Lower curve is the anodic sweep and the upper curve is the cathodic sweep direction. Sweep reversals were made at −200 and 175 mV vs. Ag/AgCl 4M KCl.

C23. Observed and modeled changes in delta and psi for a potential ramp experiment. Sweep rate 0.5 mV/sec.

C24. Current response to a potential sweep at 0.5 mV/sec.

C25. Ellipsometric results for various potential step experiments. The same silver surface was used for a series of potential steps experiments. Dissolved silver and oxide formed were reduced between potential steps.

C26. Current transient of Ag(111) for a potential step to 190 mV vs. Ag/AgCl 4M KCl. Geometric area=3.19 cm^2.

C27. Current transient of Ag(111) for a potential step to 200 mV vs. Ag/AgCl 4M KCl. Geometric area=3.19 cm^2.

C28. Current transient of Ag(111) for a potential step to 250 mV vs. Ag/AgCl 4M KCl. Geometric area=3.19 cm^2.

C29. 1) Psi after anodization at 200 mV for 285 seconds. The anodization is terminated at this point. 2) Psi spectra 5 minutes later.

C30. Silver anodized for 50 seconds at 200 mV. 1) Substrate spectra. 2) Spectra after 50 seconds of anodization. Open circuit follows. 3) Corrosion (open circuit) for 18 seconds. 4) Corrosion for 4

minutes. 5) Corrosion for 8 minutes.

C31. Silver anodized for 30 seconds at 200 mV. 1) Substrate spectra. 2) Spectra after 30 seconds of anodization. Open circuit follows. 3) Corrosion (open circuit) for 4 minutes, 45 seconds. 4) Corrosion for 9 minutes, 45 seconds.

C32. Scanning electron micrograph of a Ag (111) surface anodized at 200 mV for 285 seconds. Charge passed 21.8 mC/cm^2.

C33. Same surface as in Figure C31. Higher magnification.

C34. Scanning electron micrograph of a Ag (111) surface anodized at 200 mV for 375 seconds. Charge passed 37.5 mC/cm^2.

C35. Same surface as in Figure C33. Higher magnification.

C36. Scanning electron micrograph of a Ag(111) surface anodized by a series of three potential pulses. The first two potential pulses were for 10 minutes (-50 to 190 and 190 to 210 mV). A third potential pulse from 210 to 230 mV was applied for approximately 3 minutes. Total charge passed was 41.7 mC/cm^2.

C37. Scanning electron micrograph of and individual secondary crystal from the same surface shown in Figure C35.

C38. Scanning electron micrograph of the same crystal as shown in Figure C36. Higher magnification.

C39. Scanning electron micrograph of the same surface shown in Figure C35-C37. Photograph was taken of a region between secondary crystals.

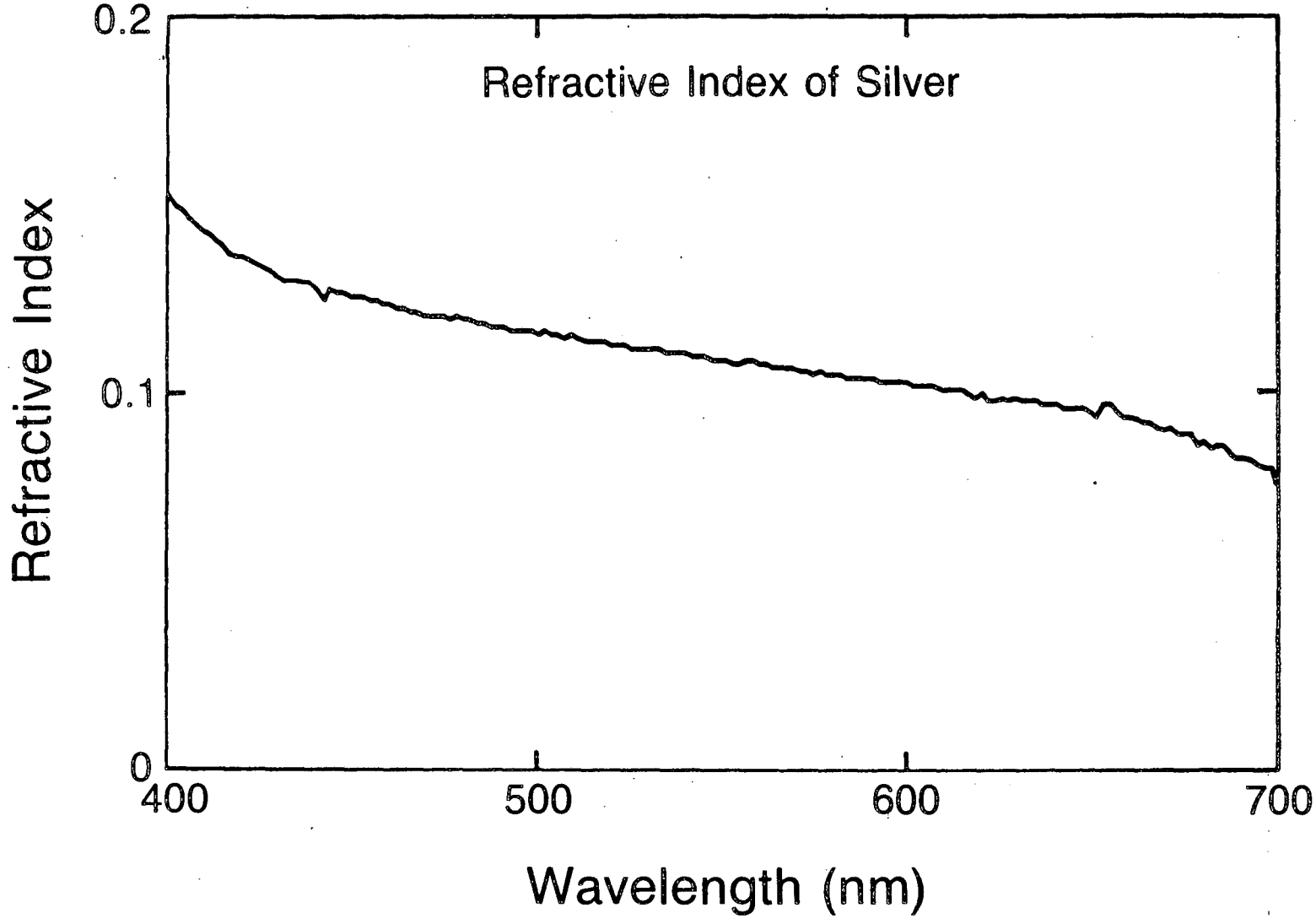

XBL 8511-12723

FIGURE C1

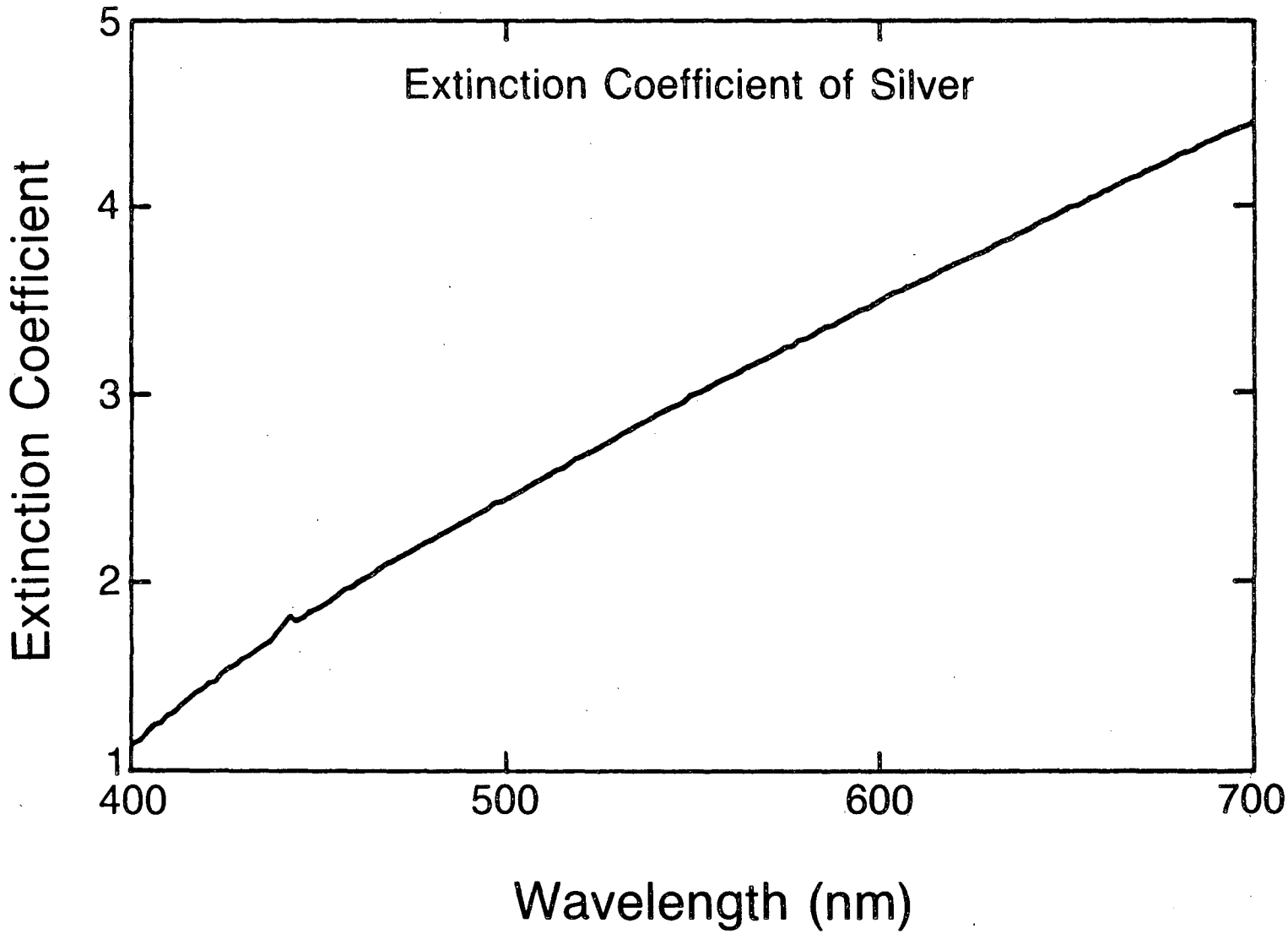

XBL 8511-12721

FIGURE C2

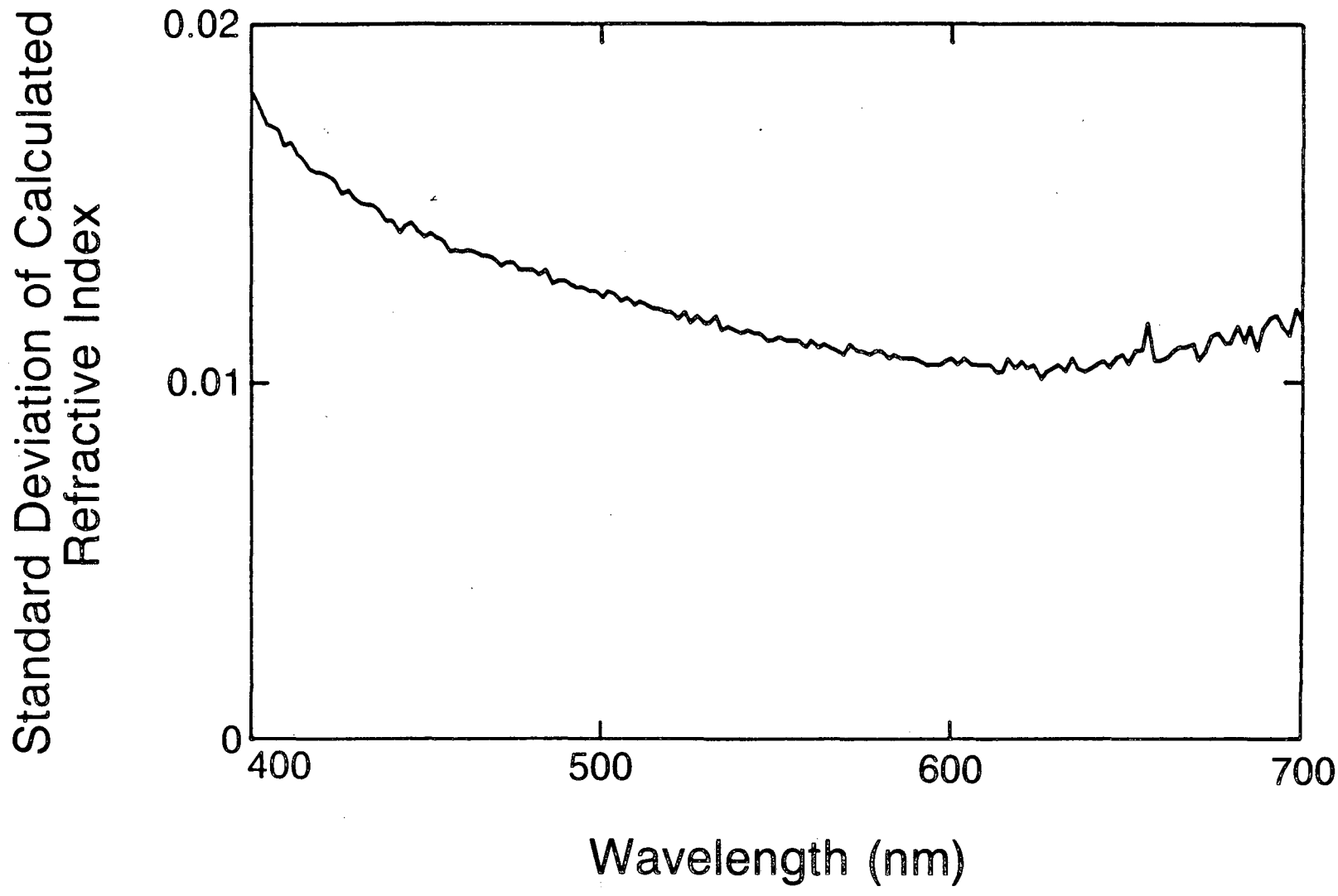

XBL 8511-12724

FIGURE C3

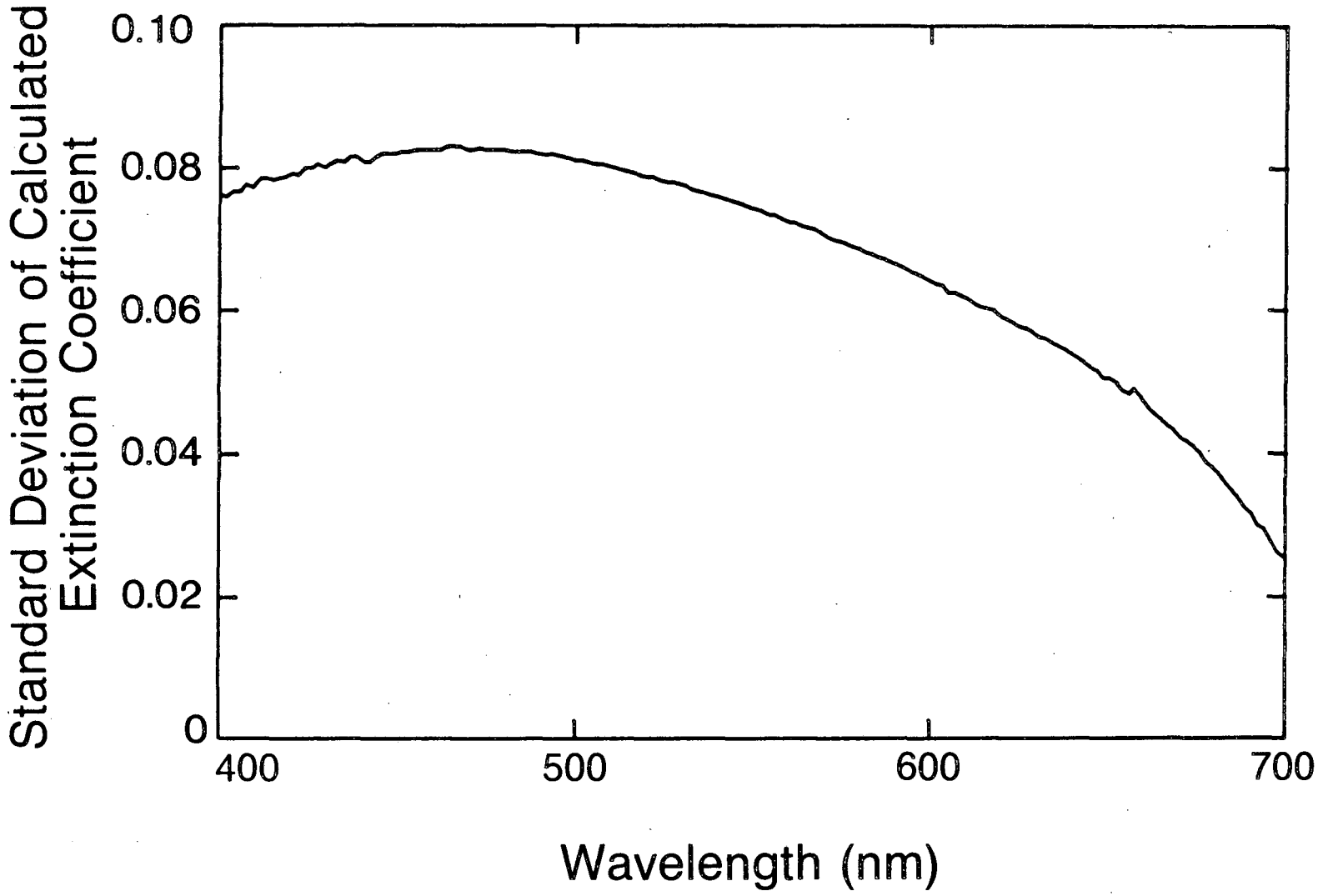

XBL 8511-12720

FIGURE C4

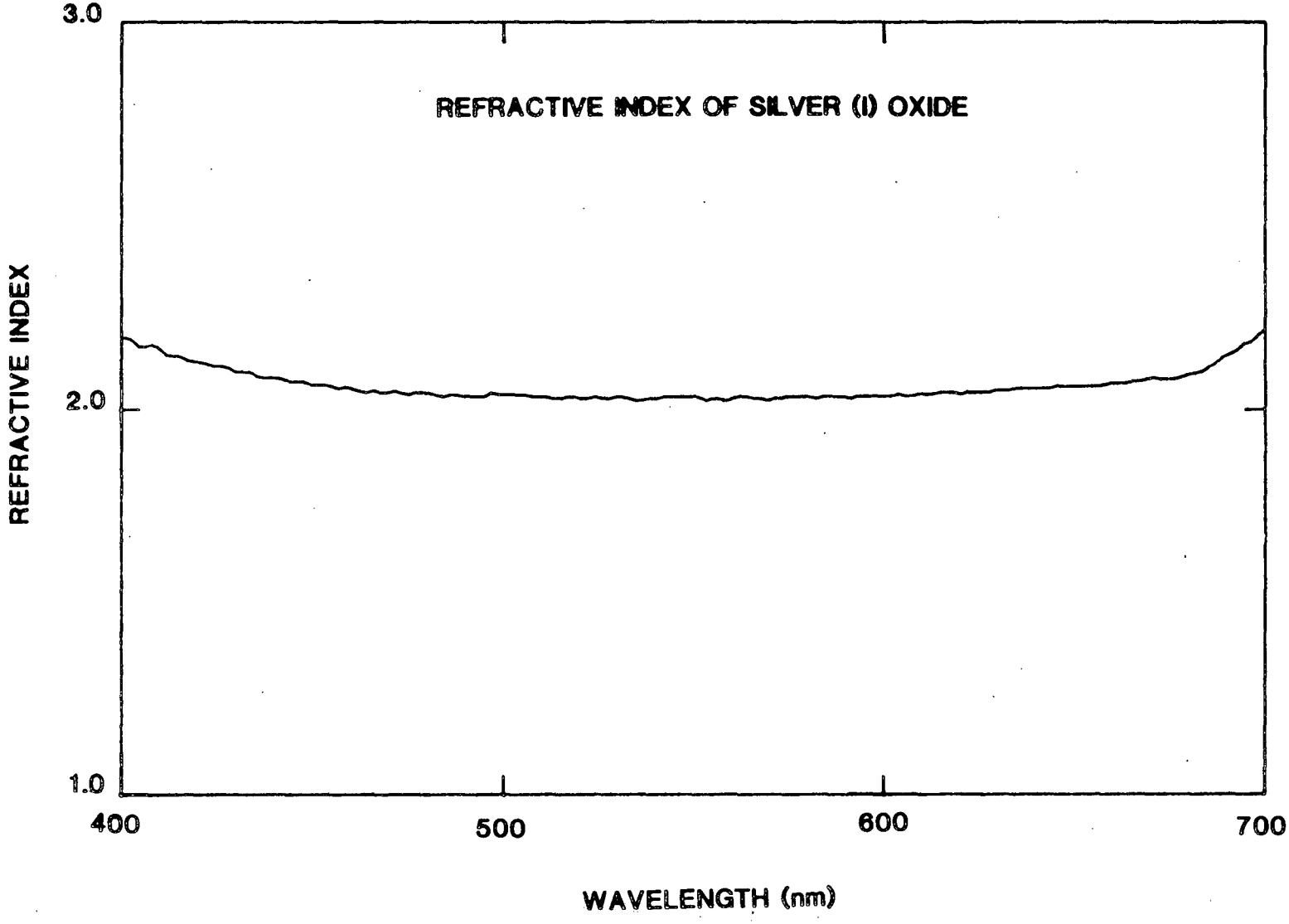

XBL 8512-5007

FIGURE C5

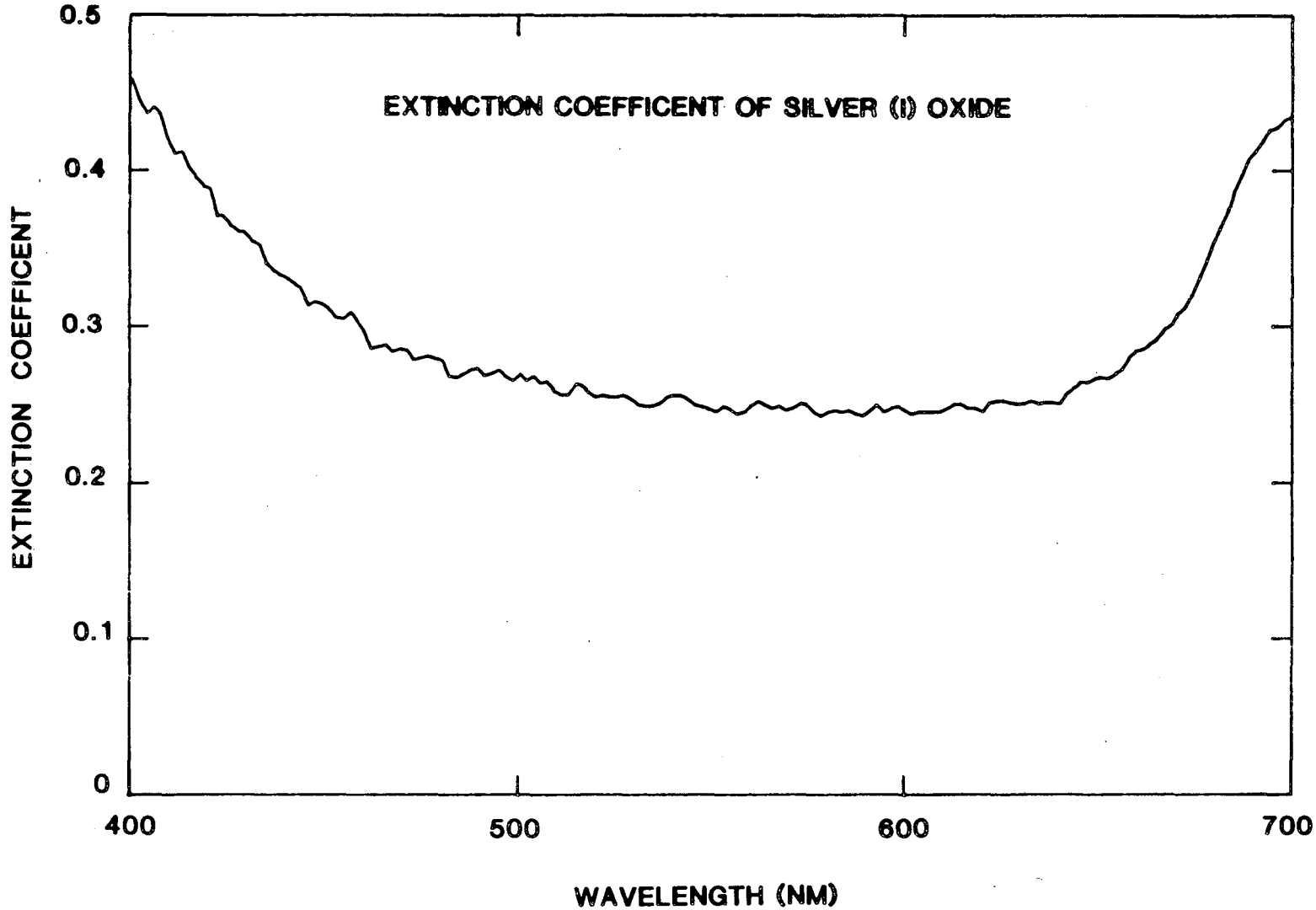

XBL 8512-5009

FIGURE C6

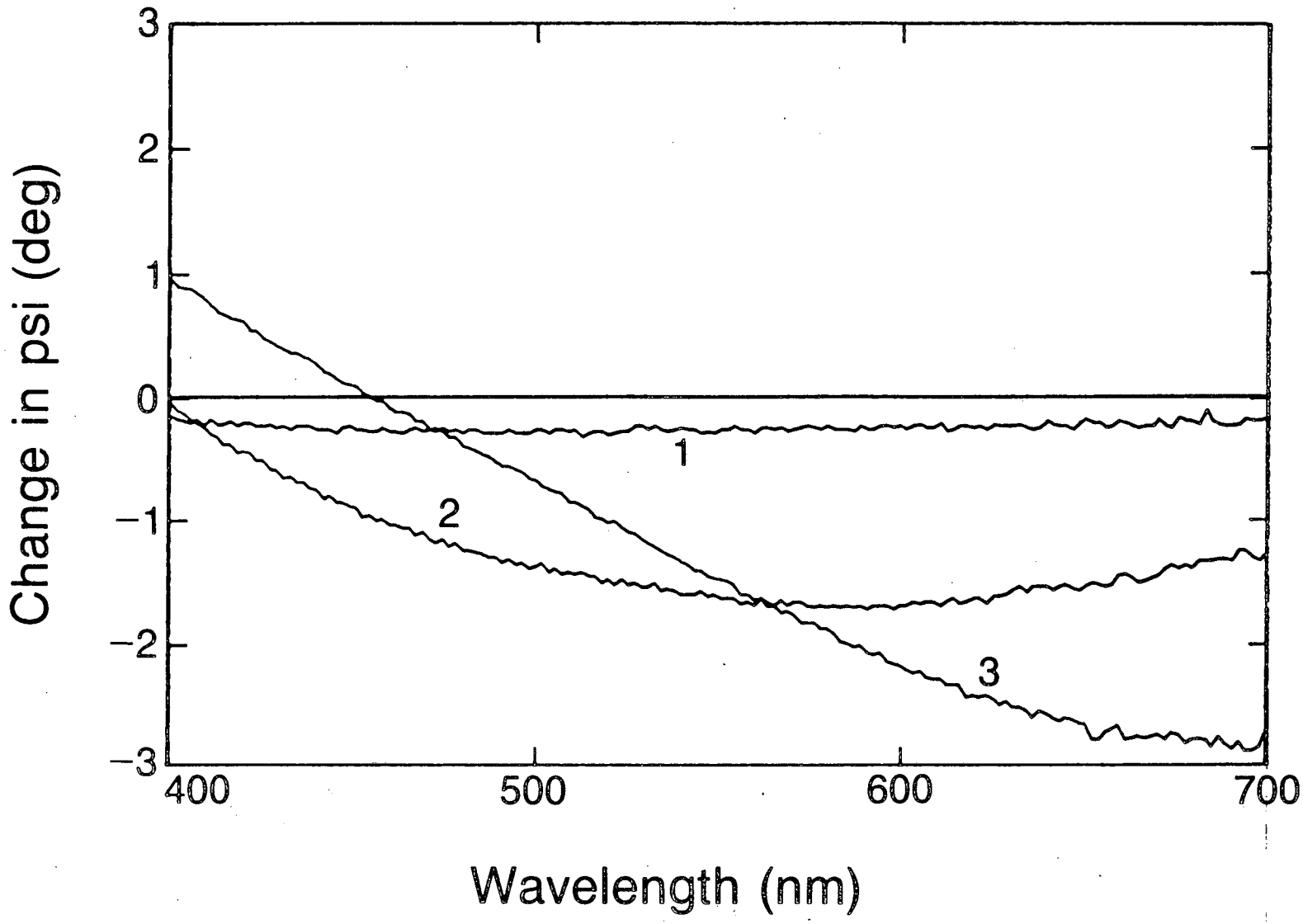

XBL 8511-12719

FIGURE C7

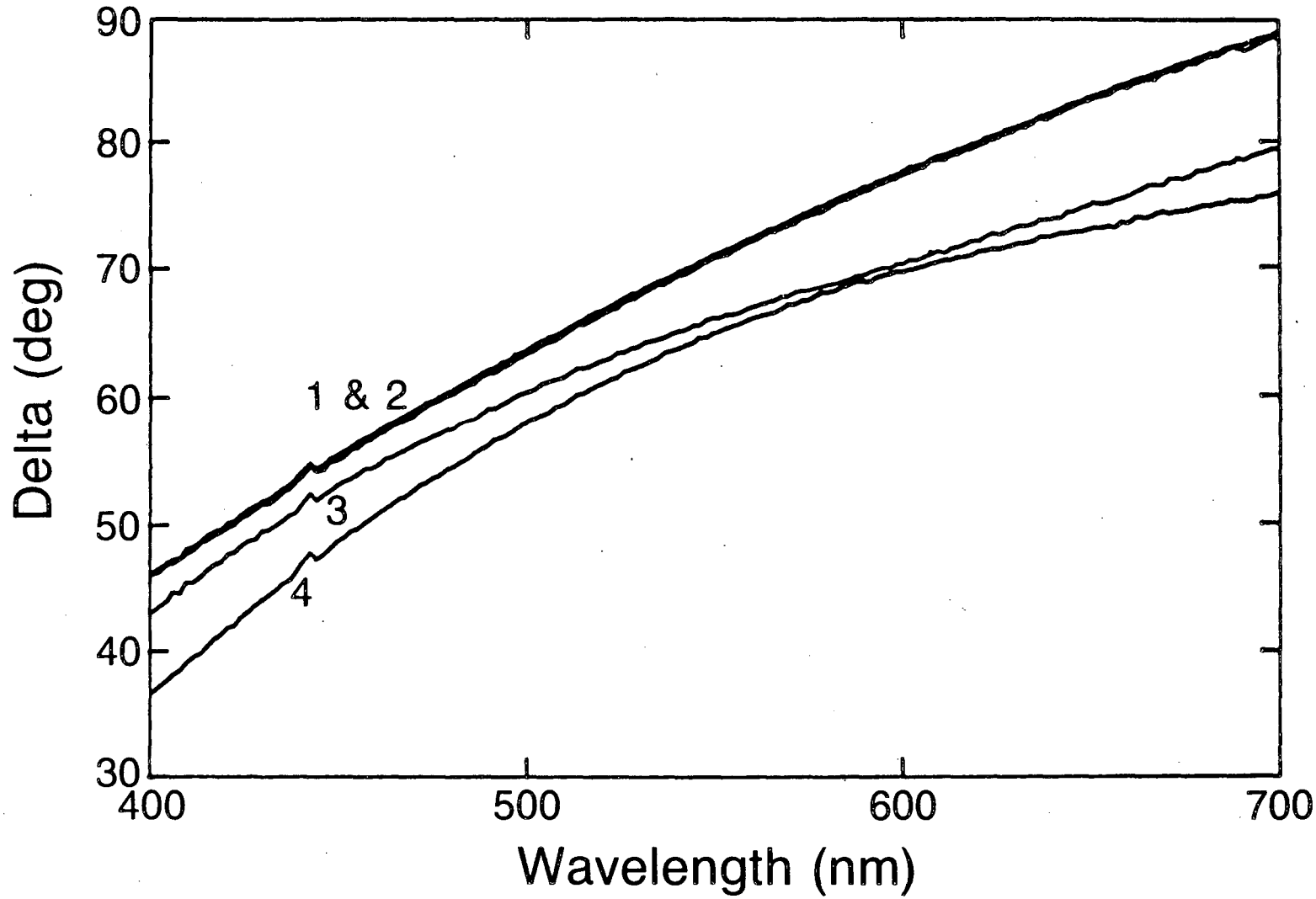

XBL 8511-12748

FIGURE C8

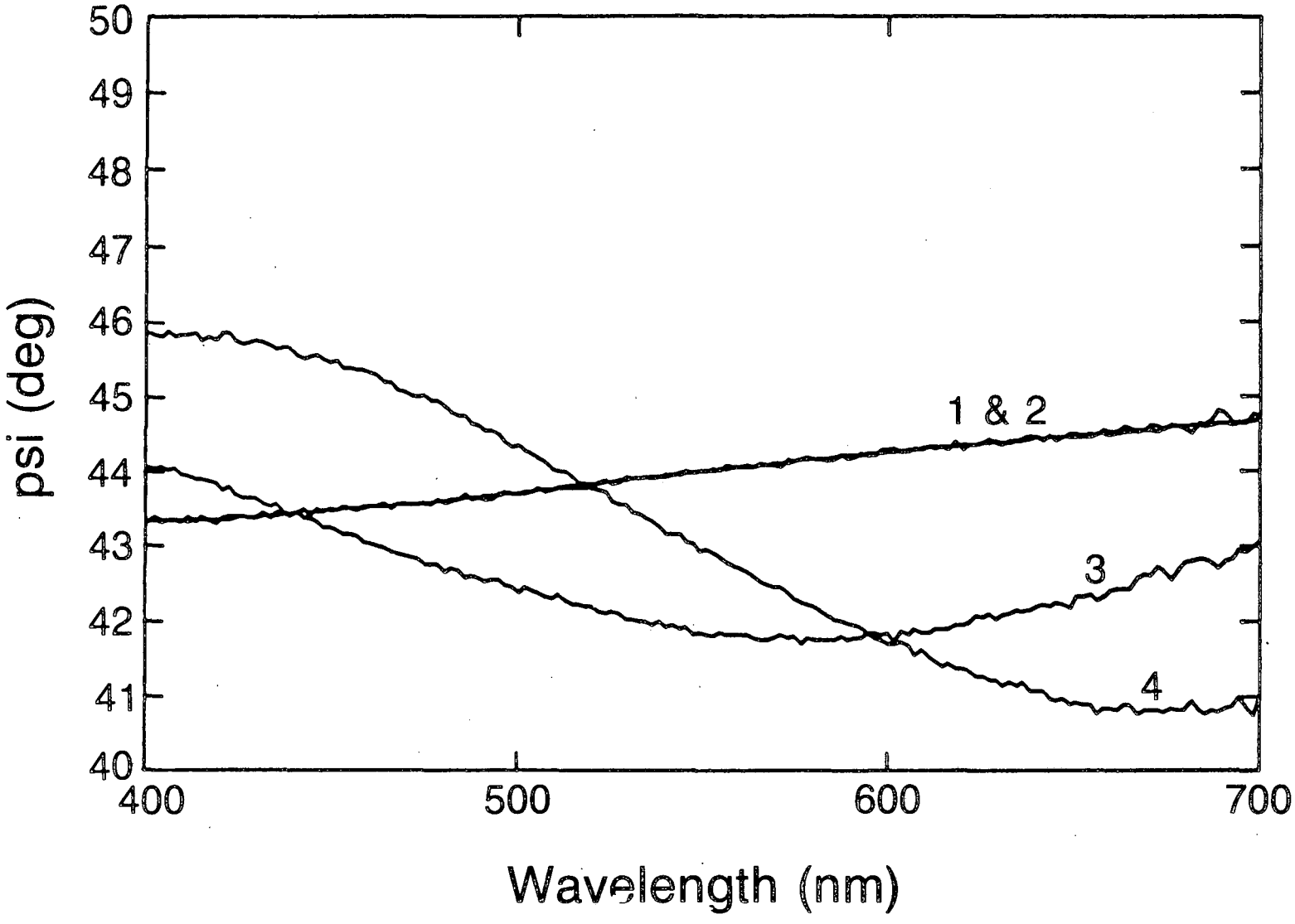

XBL 8511-12750

FIGURE C9

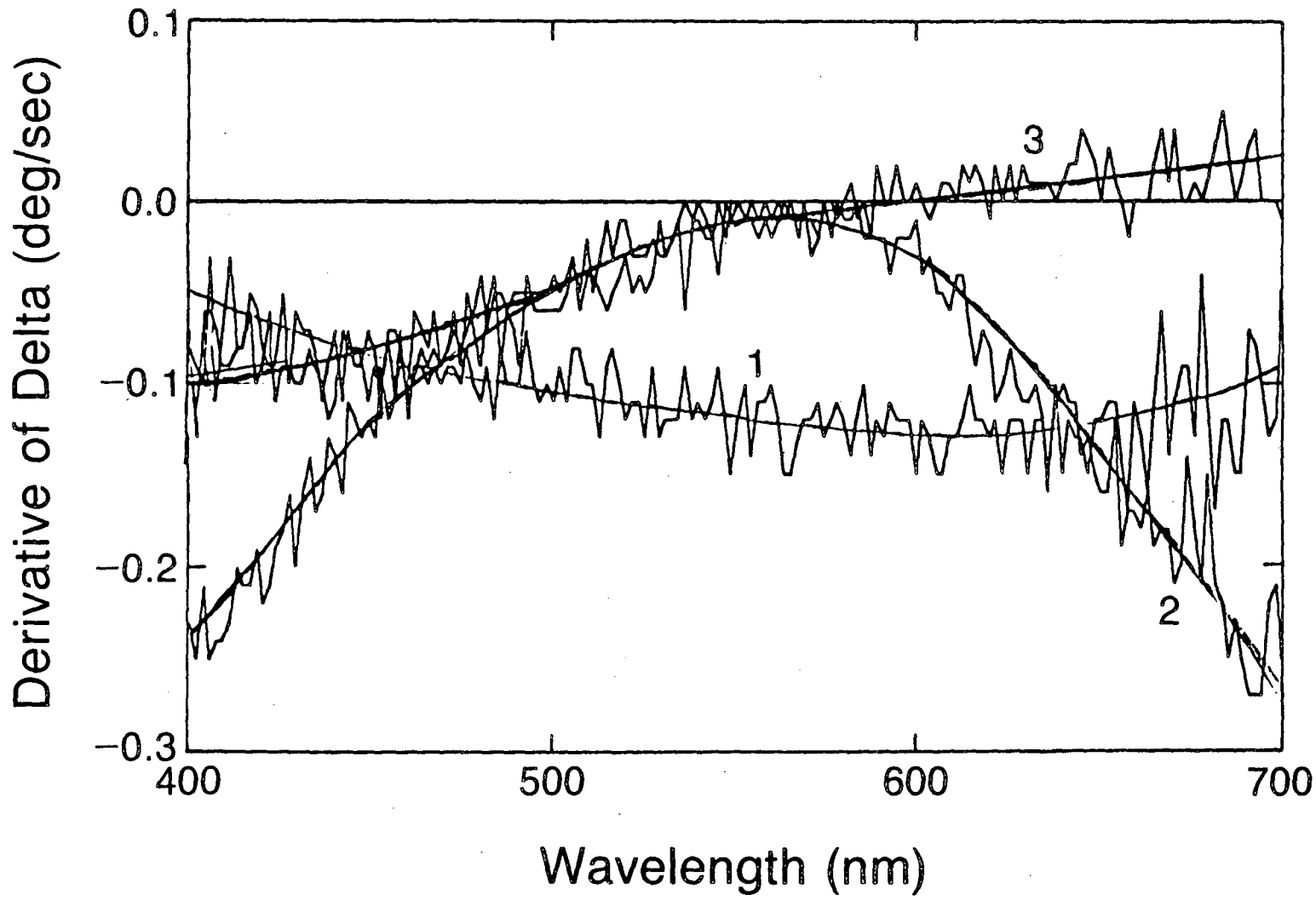

XBL 8511-12746

FIGURE C10

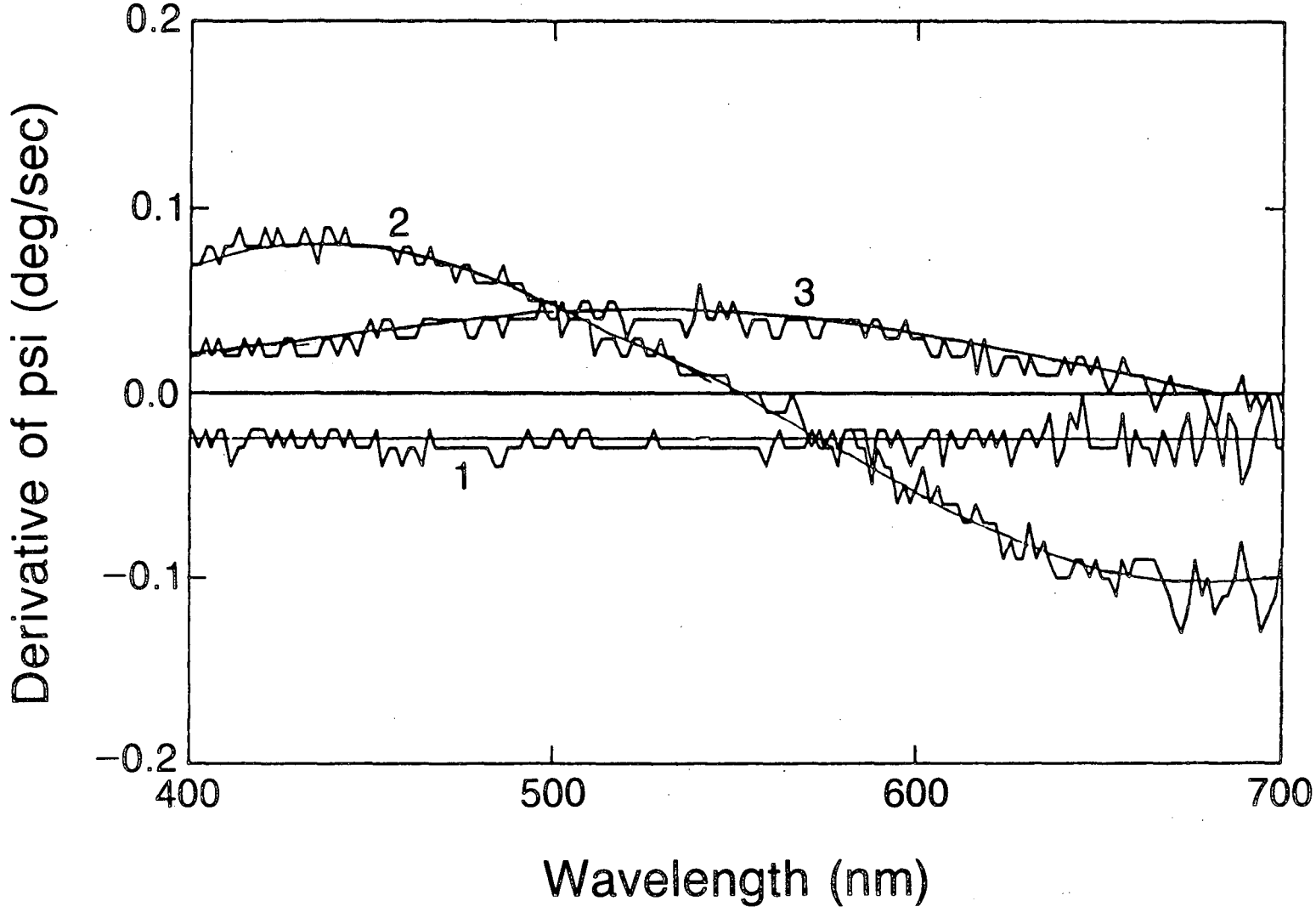

XBL 8511-12745

FIGURE C11

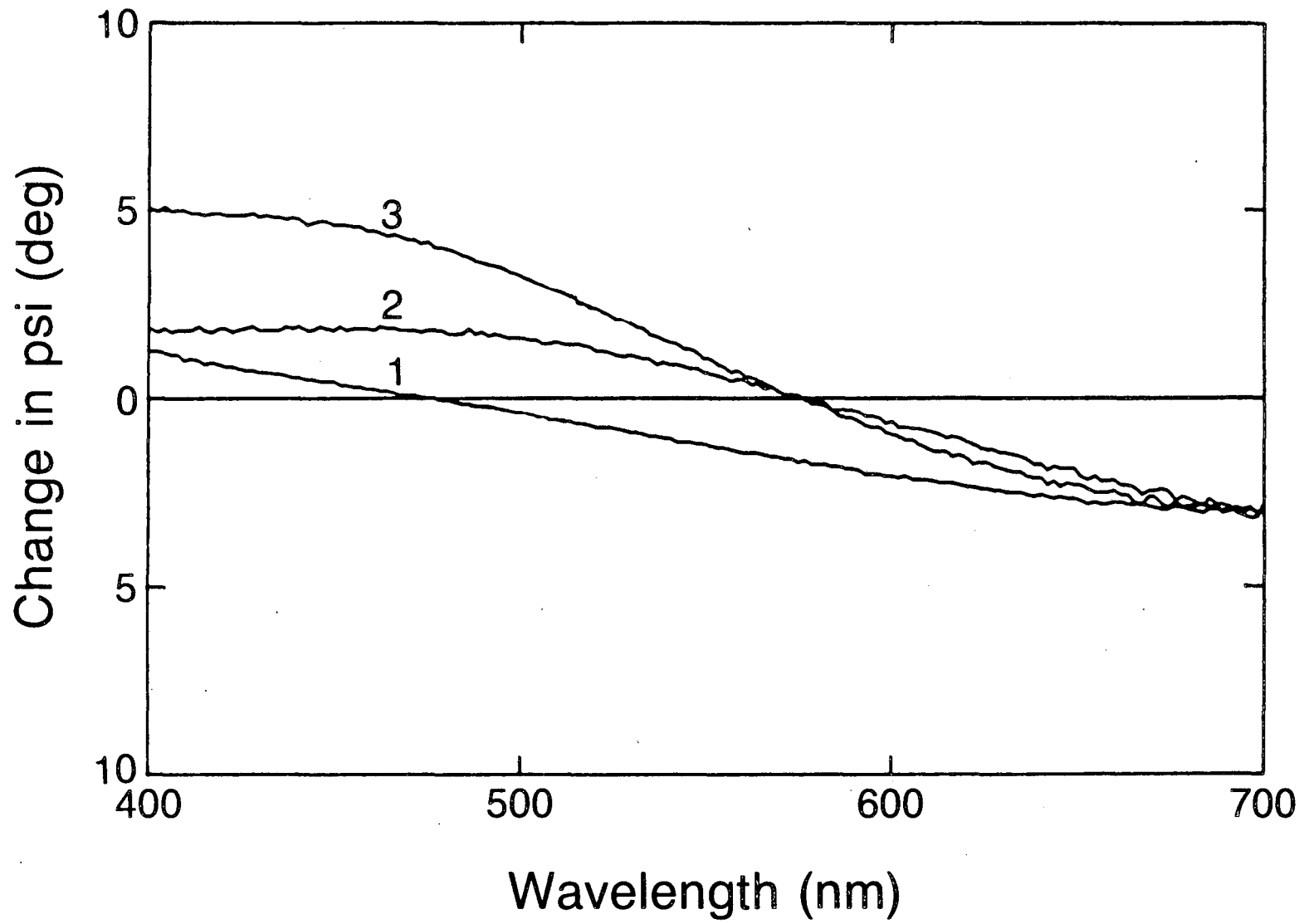

XBL 8511-12749

FIGURE C12

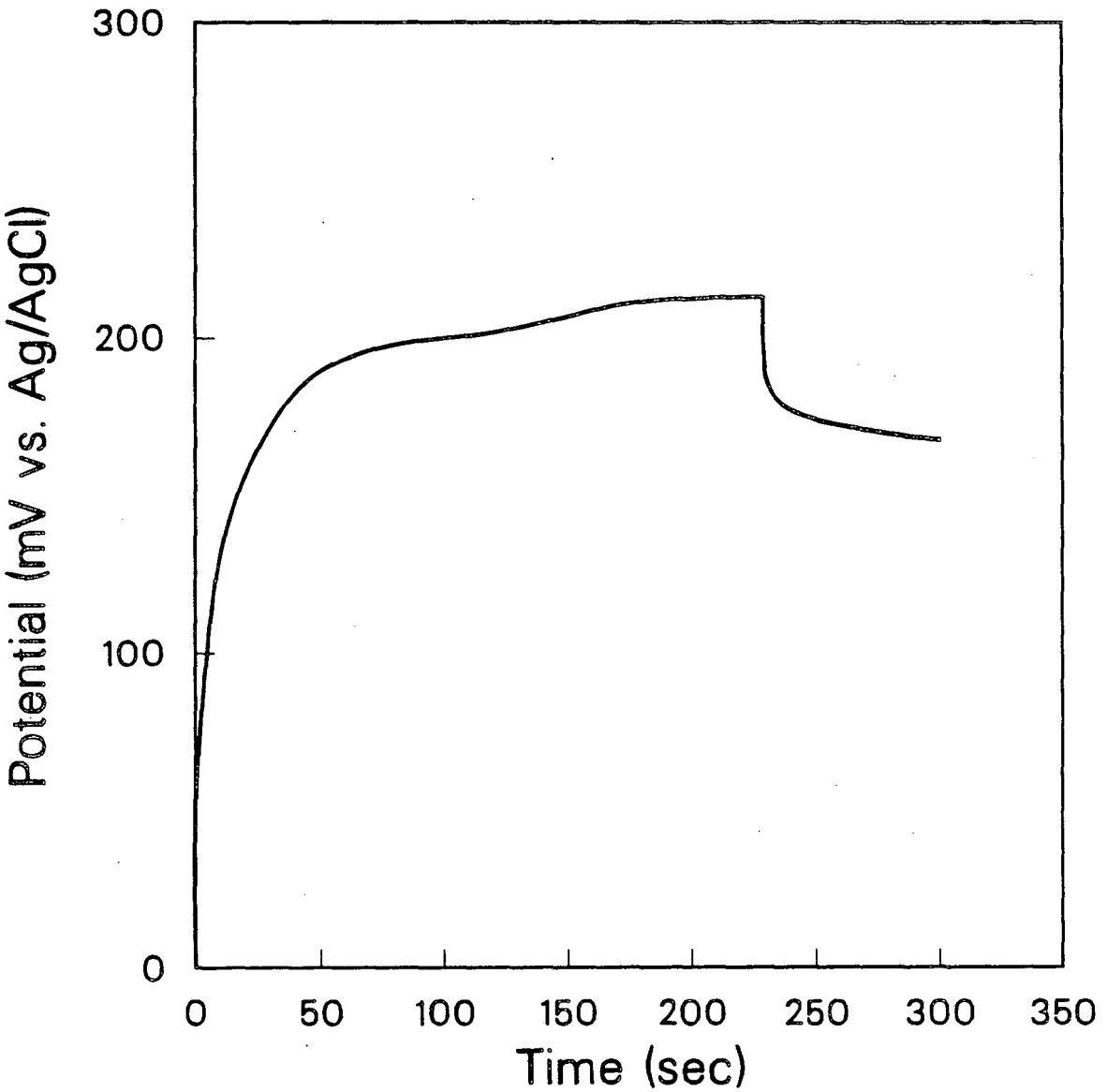

FIGURE C13

XCG 8511-478

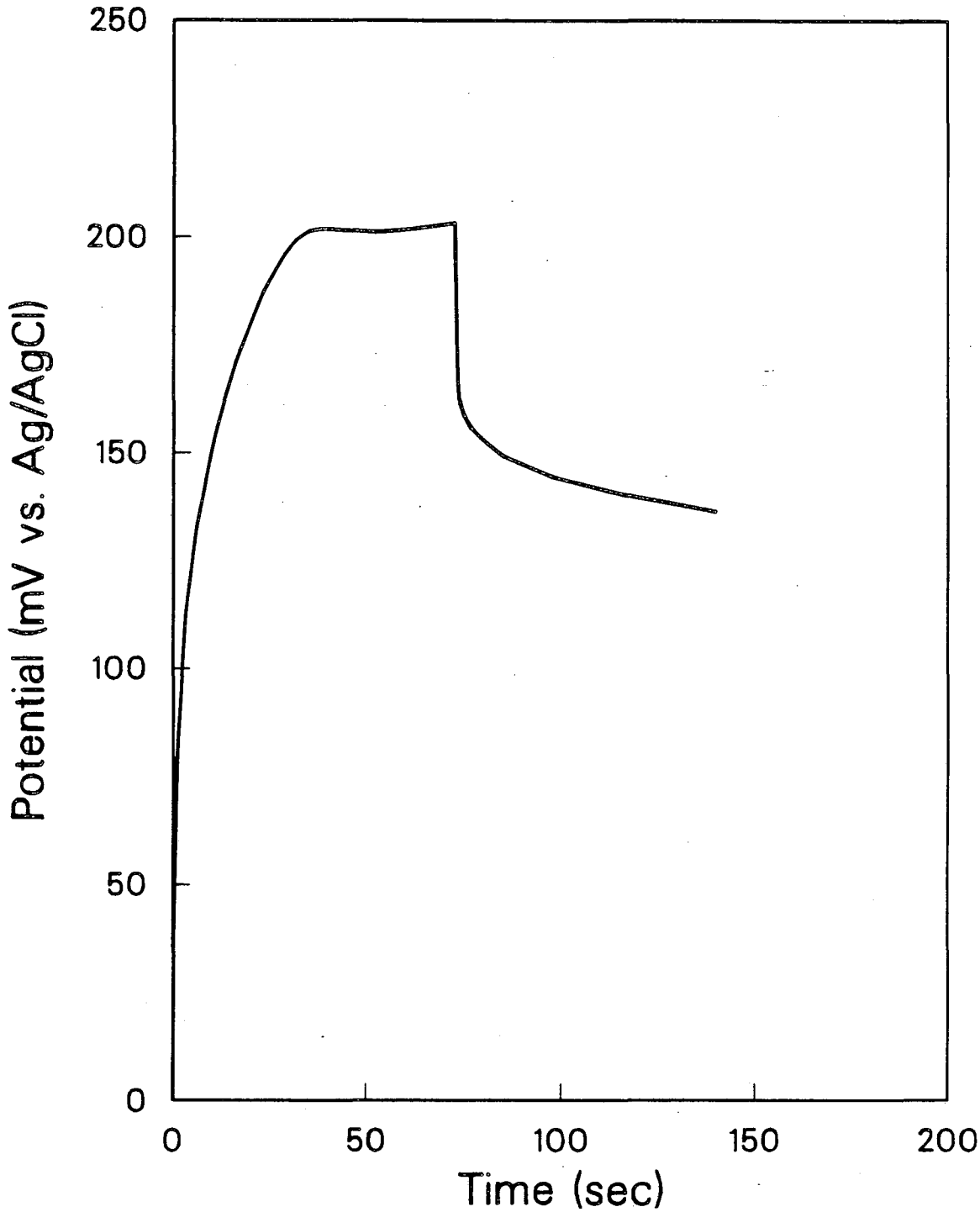

FIGURE C14

XCG 8511-477

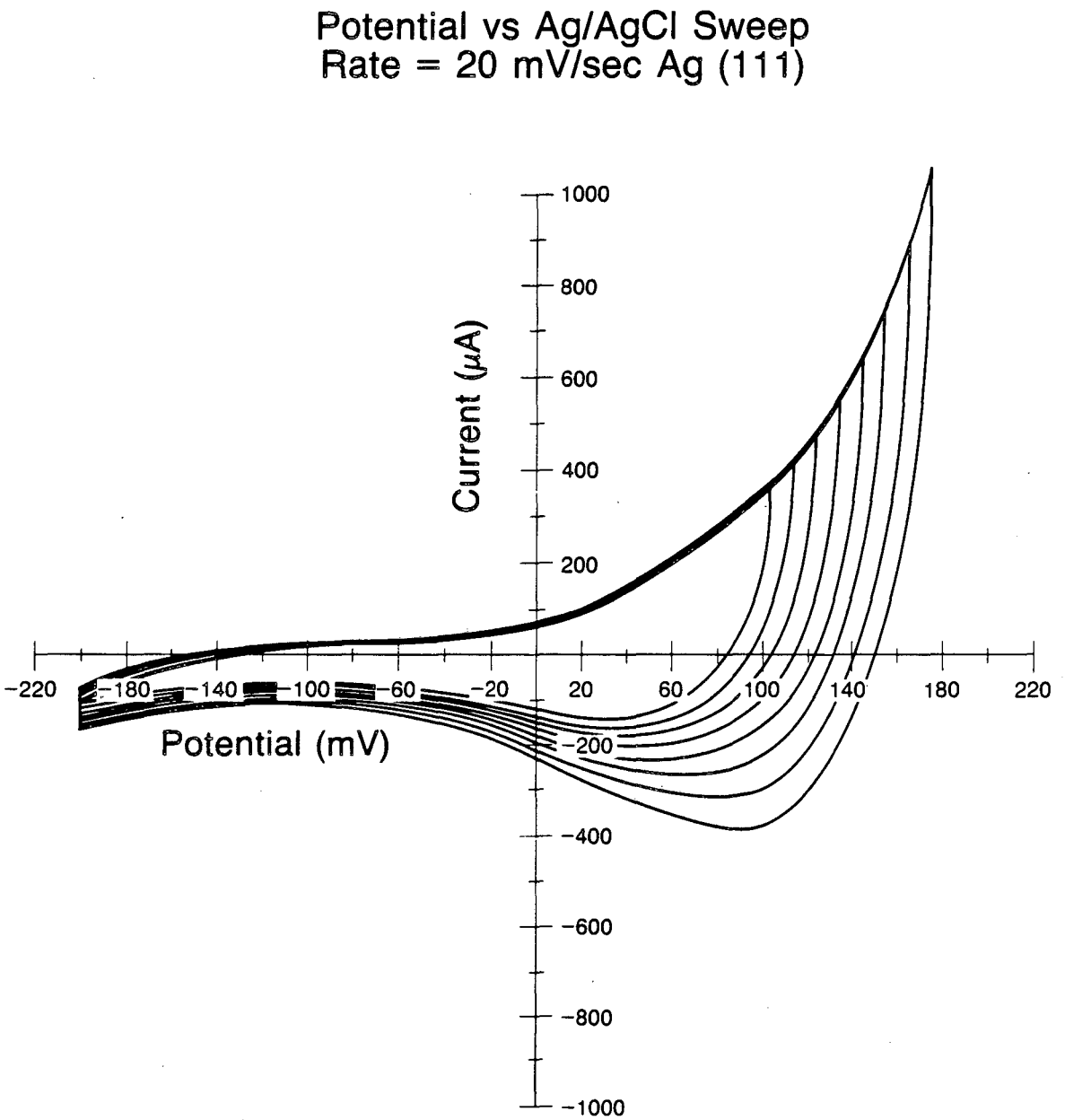

XBL 8511-11468

FIGURE C15

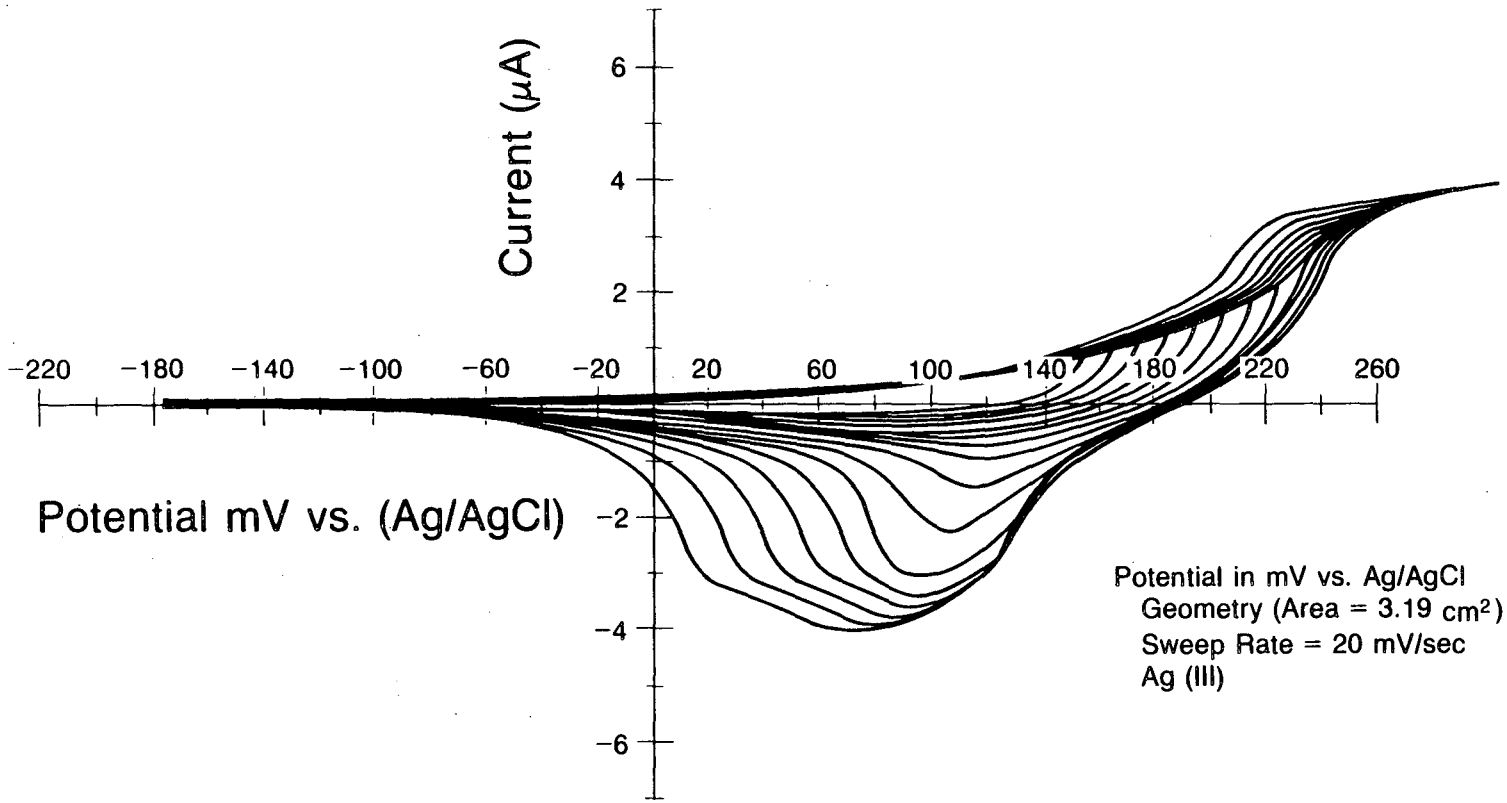

XBL 8511-11447

FIGURE C16

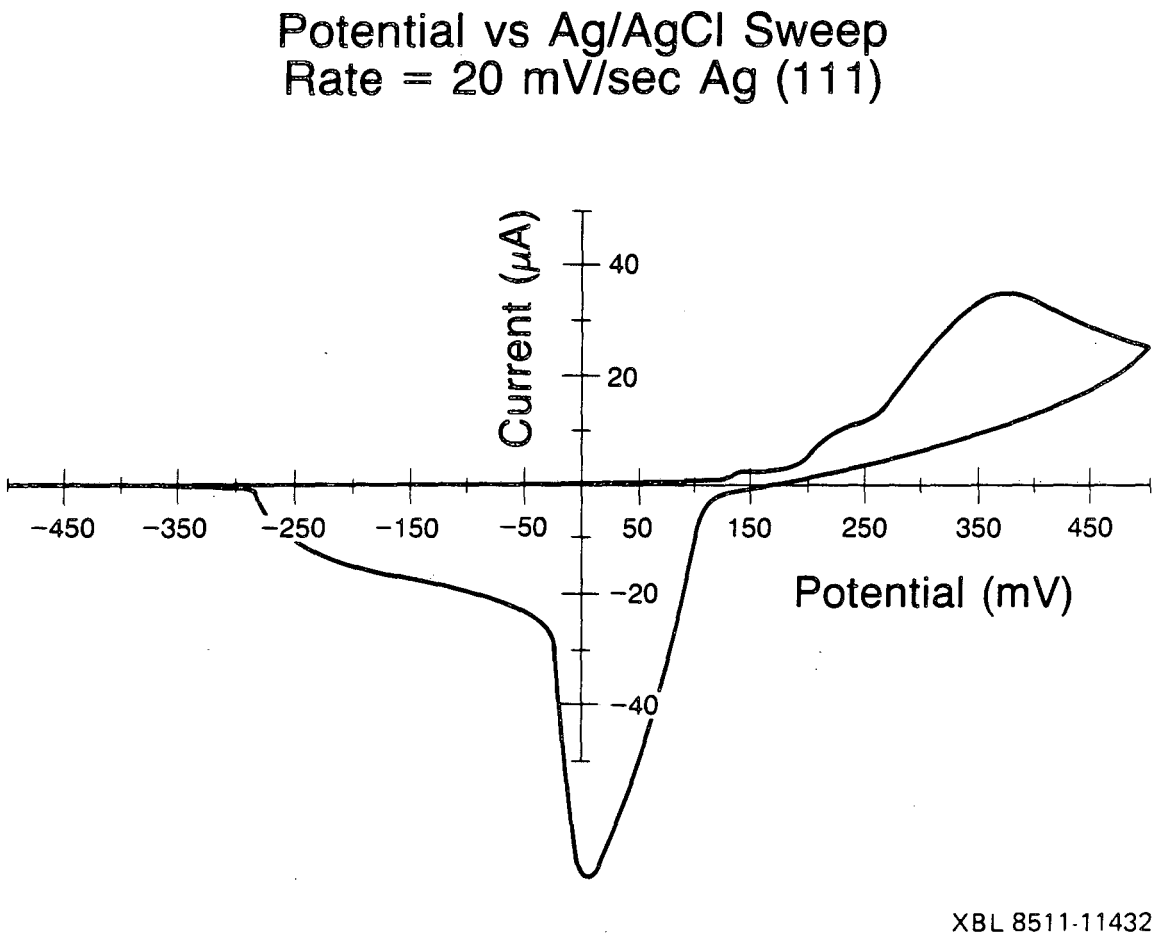
Potential vs Ag/AgCl Sweep
Rate = 20 mV/sec Ag (111)
Current (μA)
40
20
-20
-40
-450
-350
-250
-150
-50
50
150
250
350
450
Potential (mV)
XBL 8511-11432

FIGURE C17

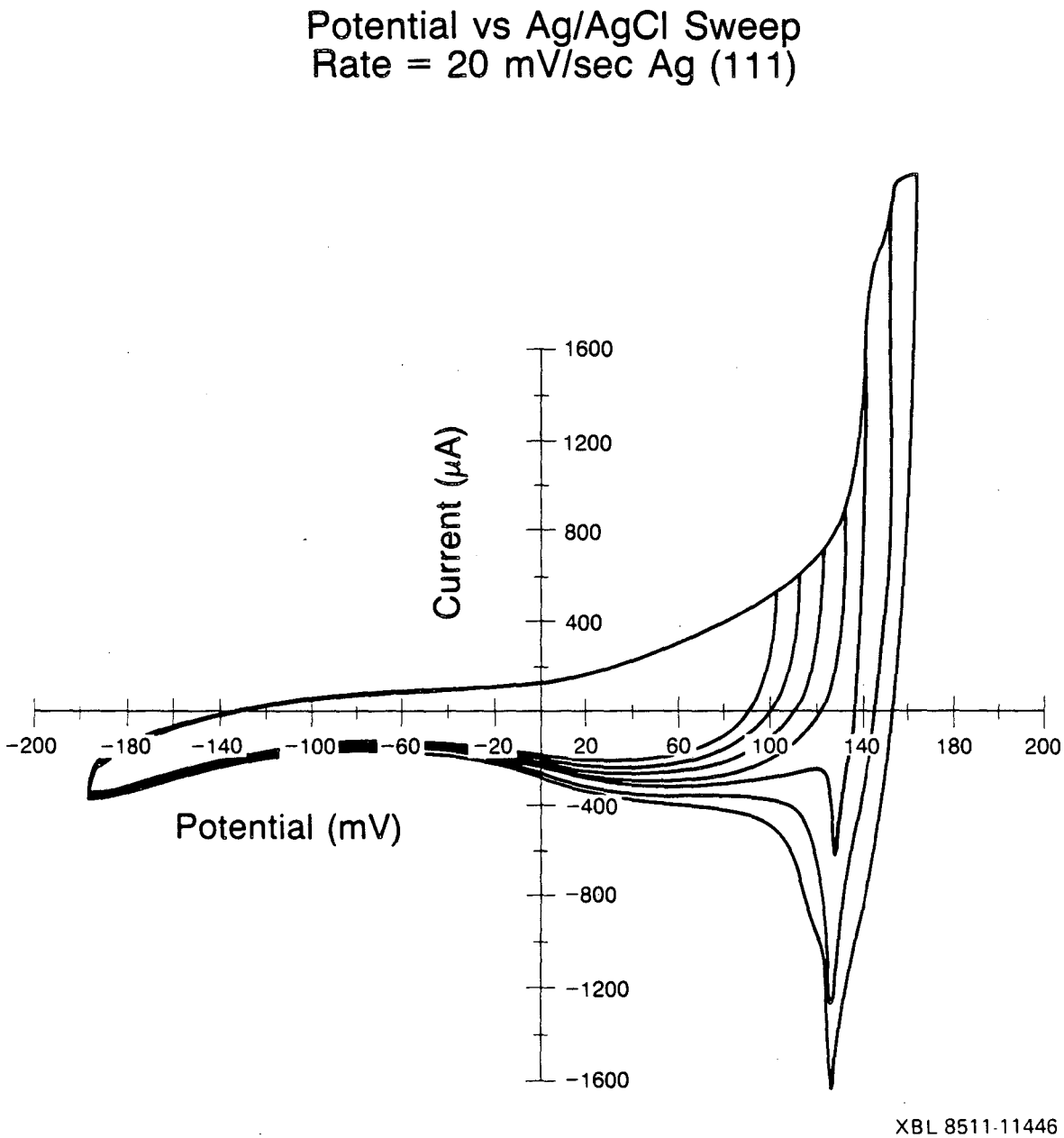
Potential vs Ag/AgCl Sweep
Rate = 20 mV/sec Ag (111)
Current (μA)
1600
1200
800
400
-400
-800
-1200
-1600
-200
-180
-140
-100
-60
-20
20
60
100
140
180
200
Potential (mV)
XBL 8511-11446

FIGURE C18

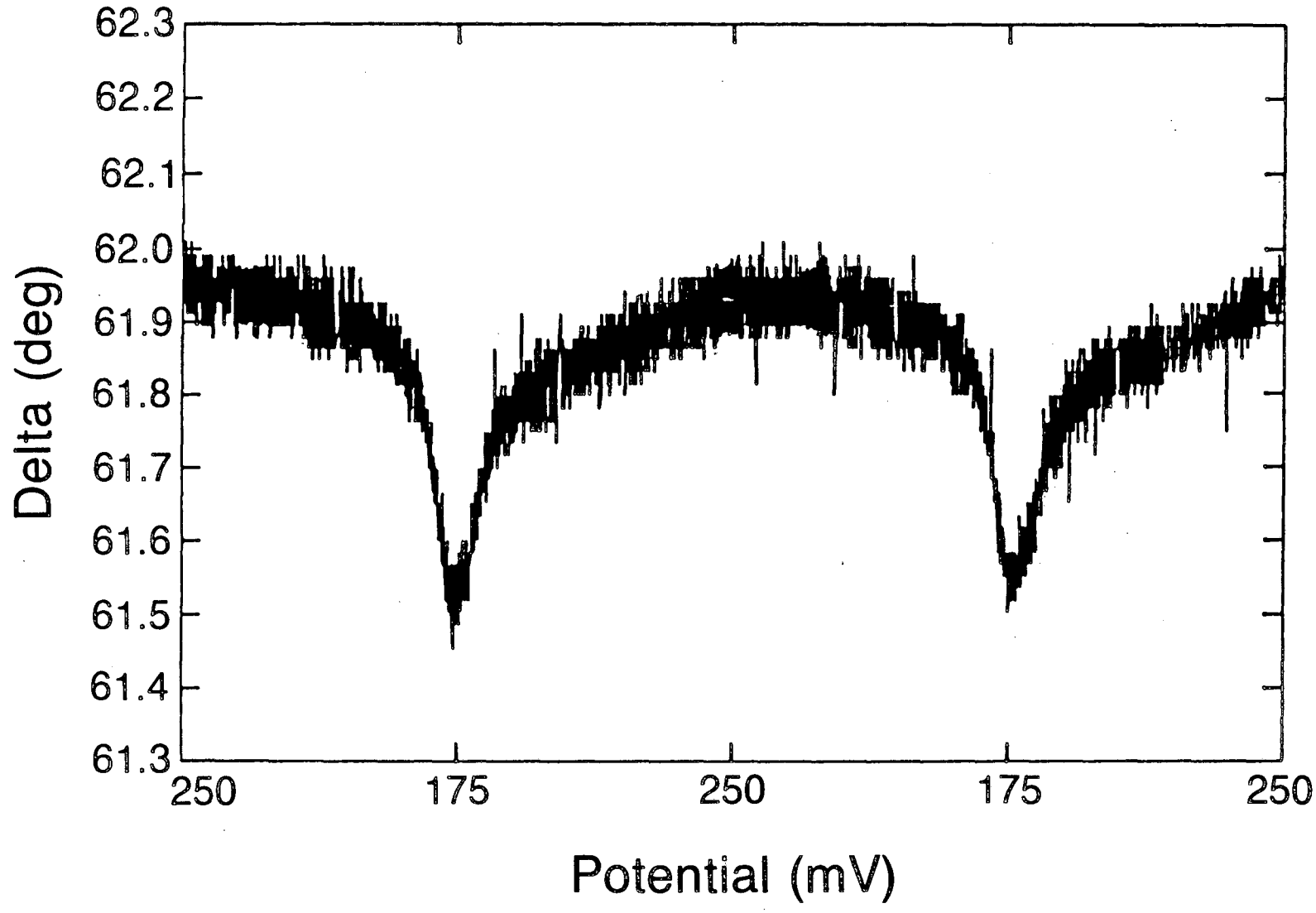

XBL 8511-12726

FIGURE C19

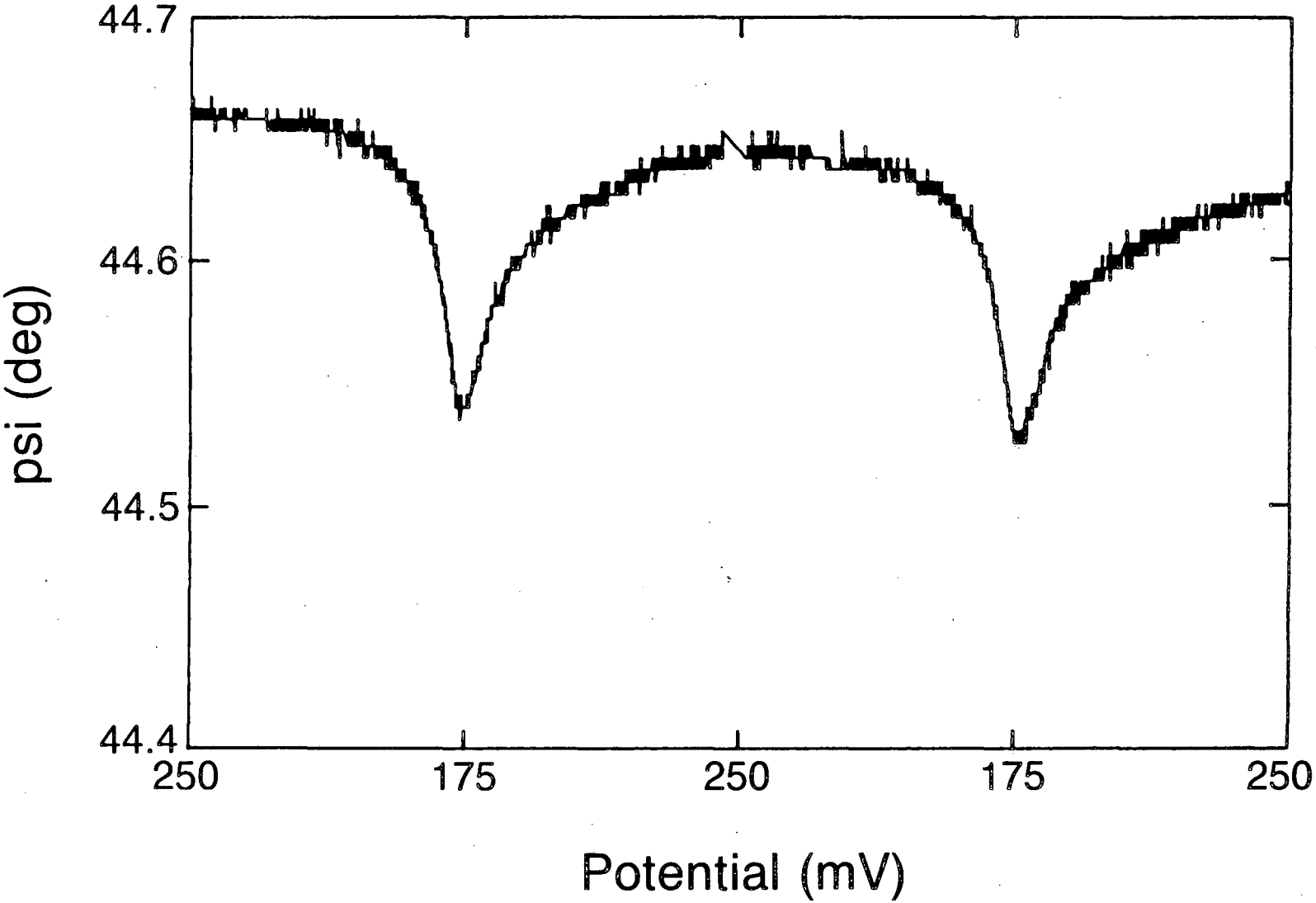

XBL 8511-12725

FIGURE C20

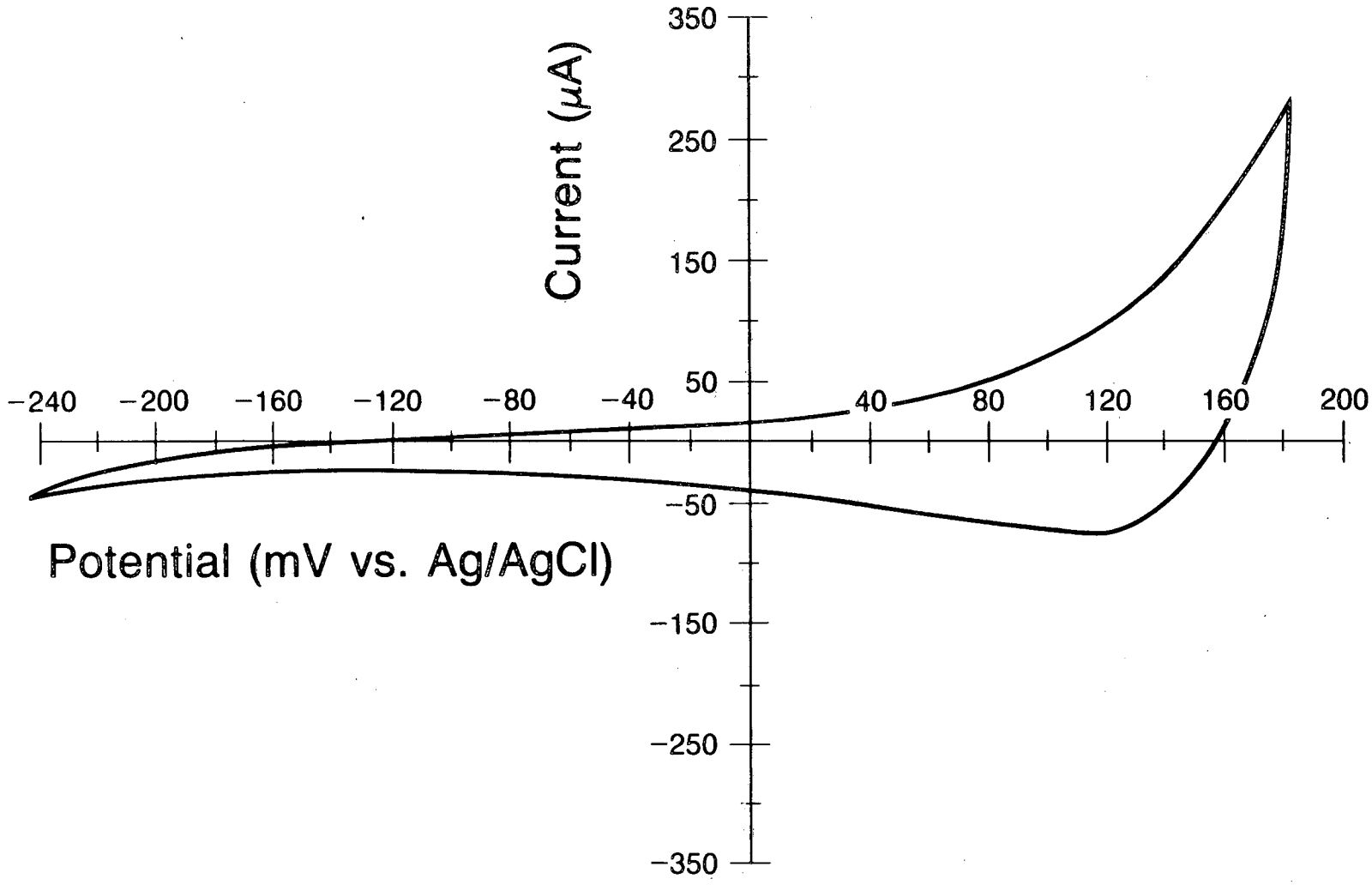

XBL 8511-11461

FIGURE C21

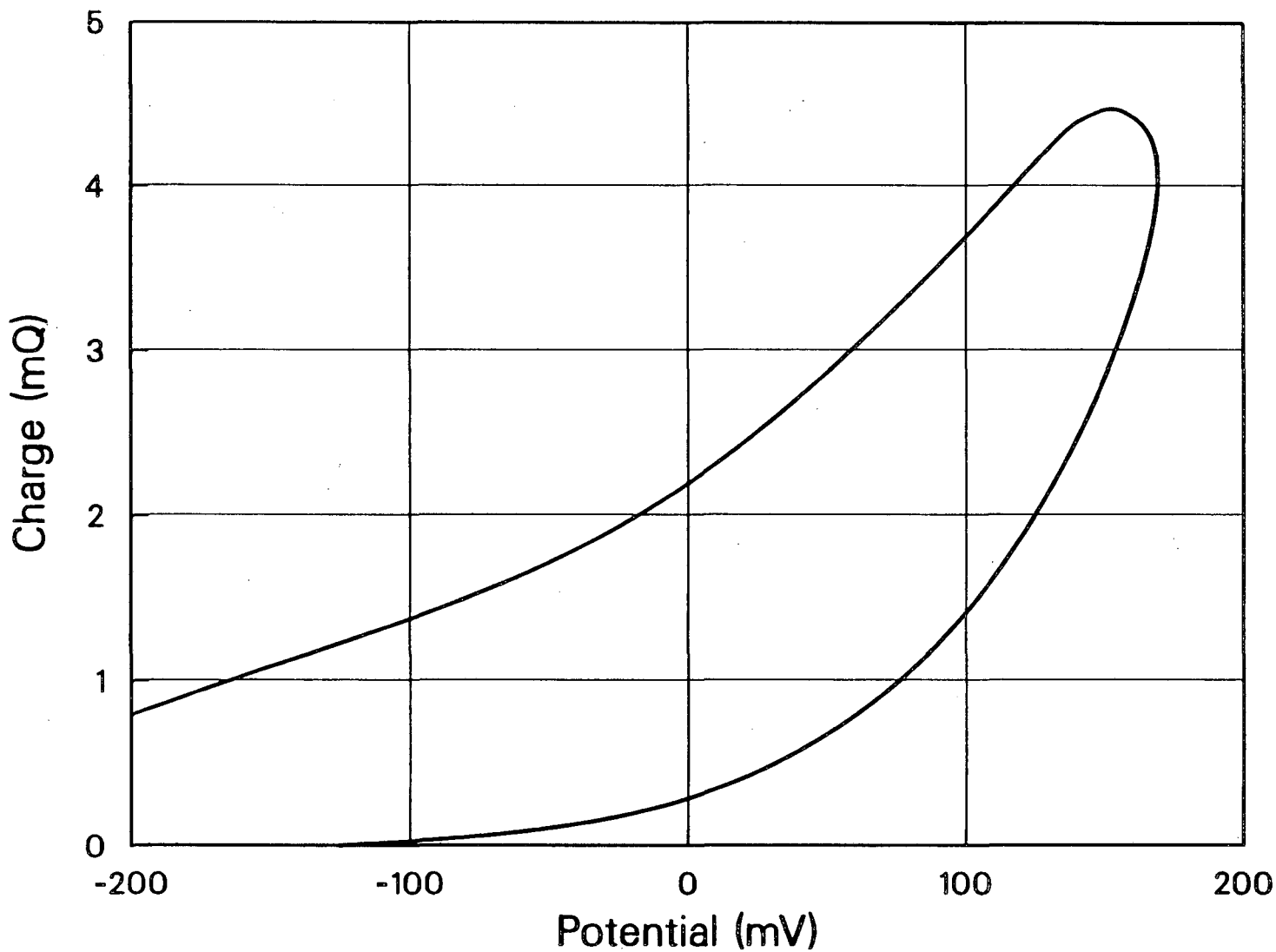

FIGURE C22

XCG 8511-483

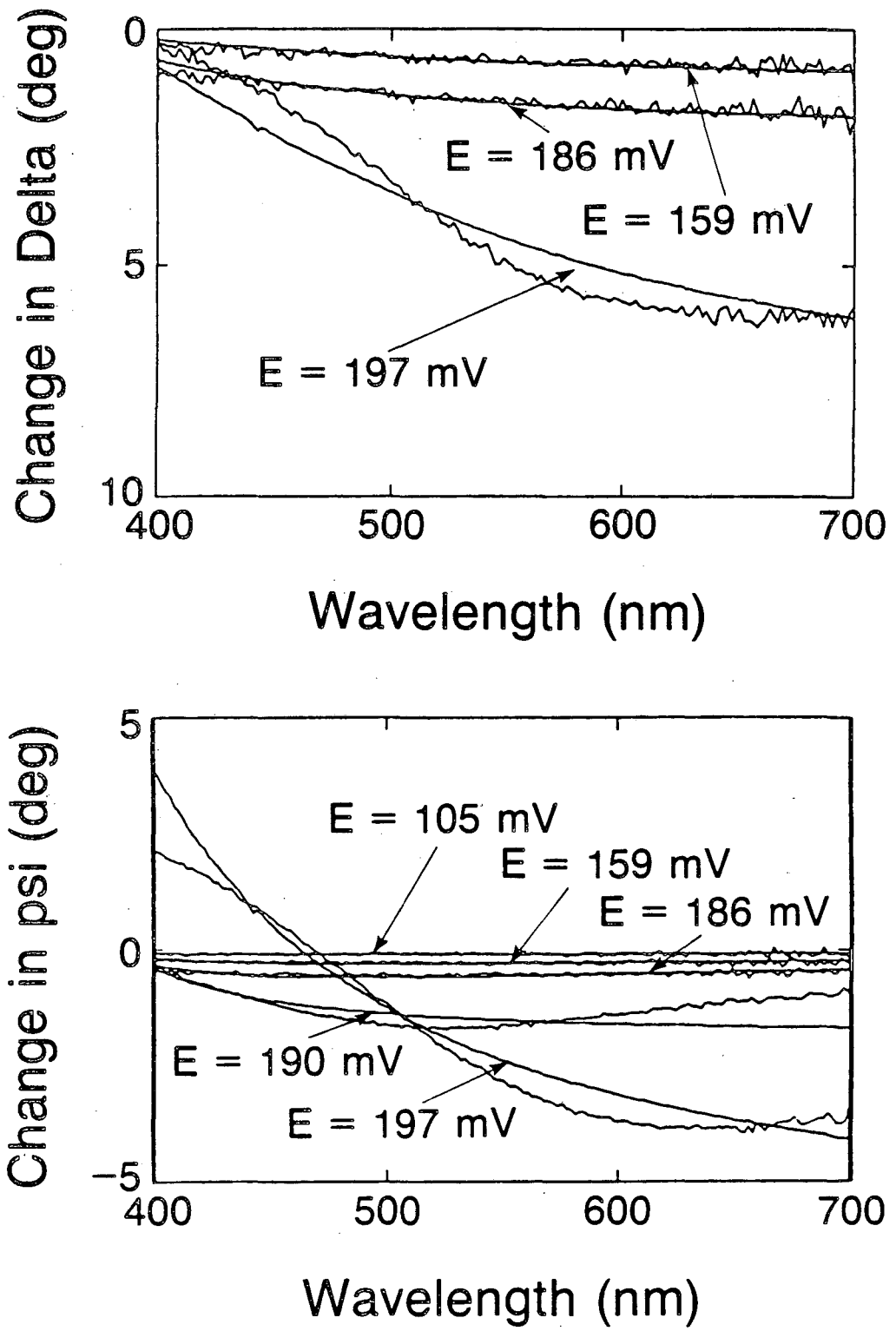

XBL 8511-12751

FIGURE C23

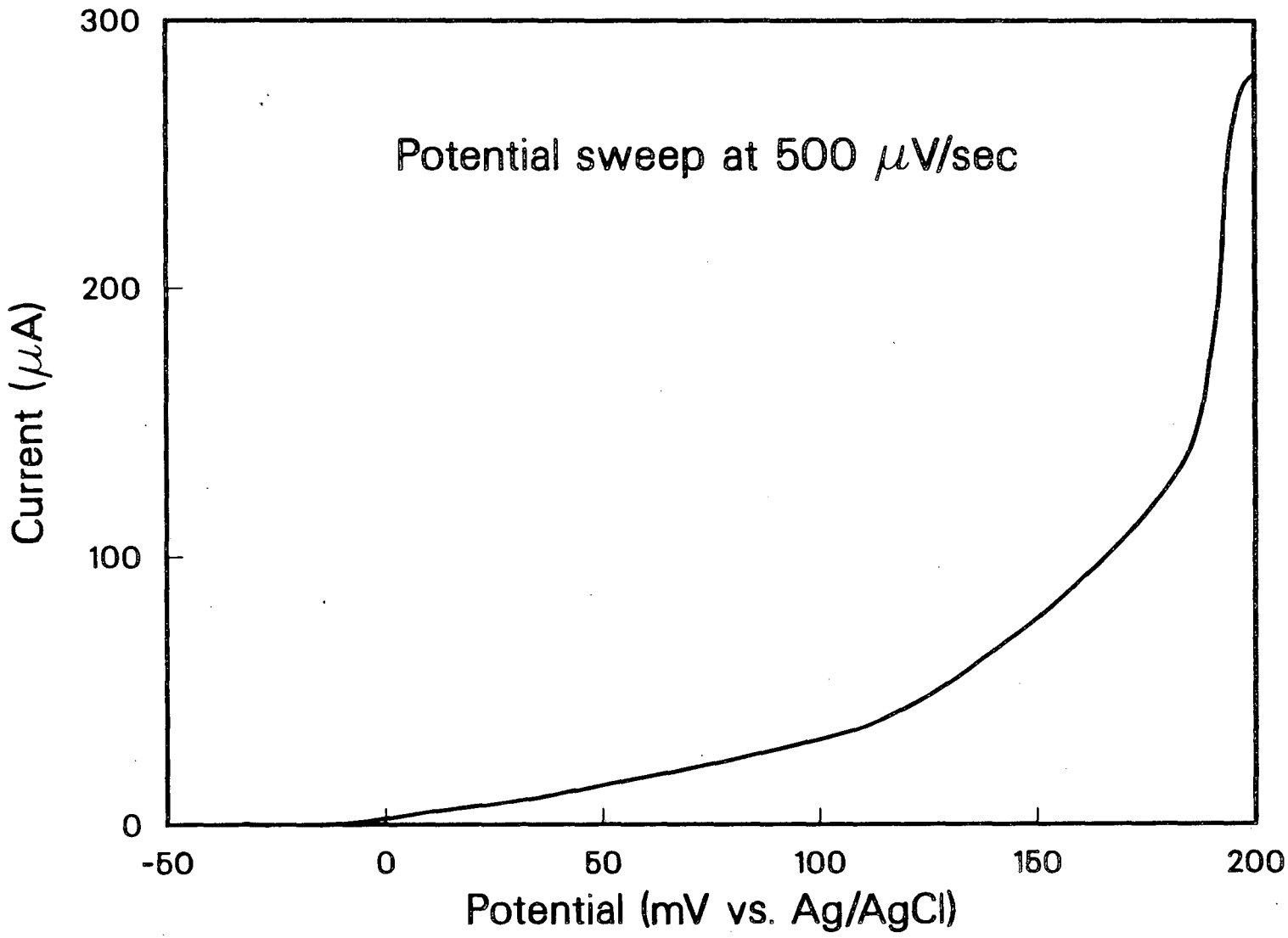

FIGURE C24

XCG 8511-479

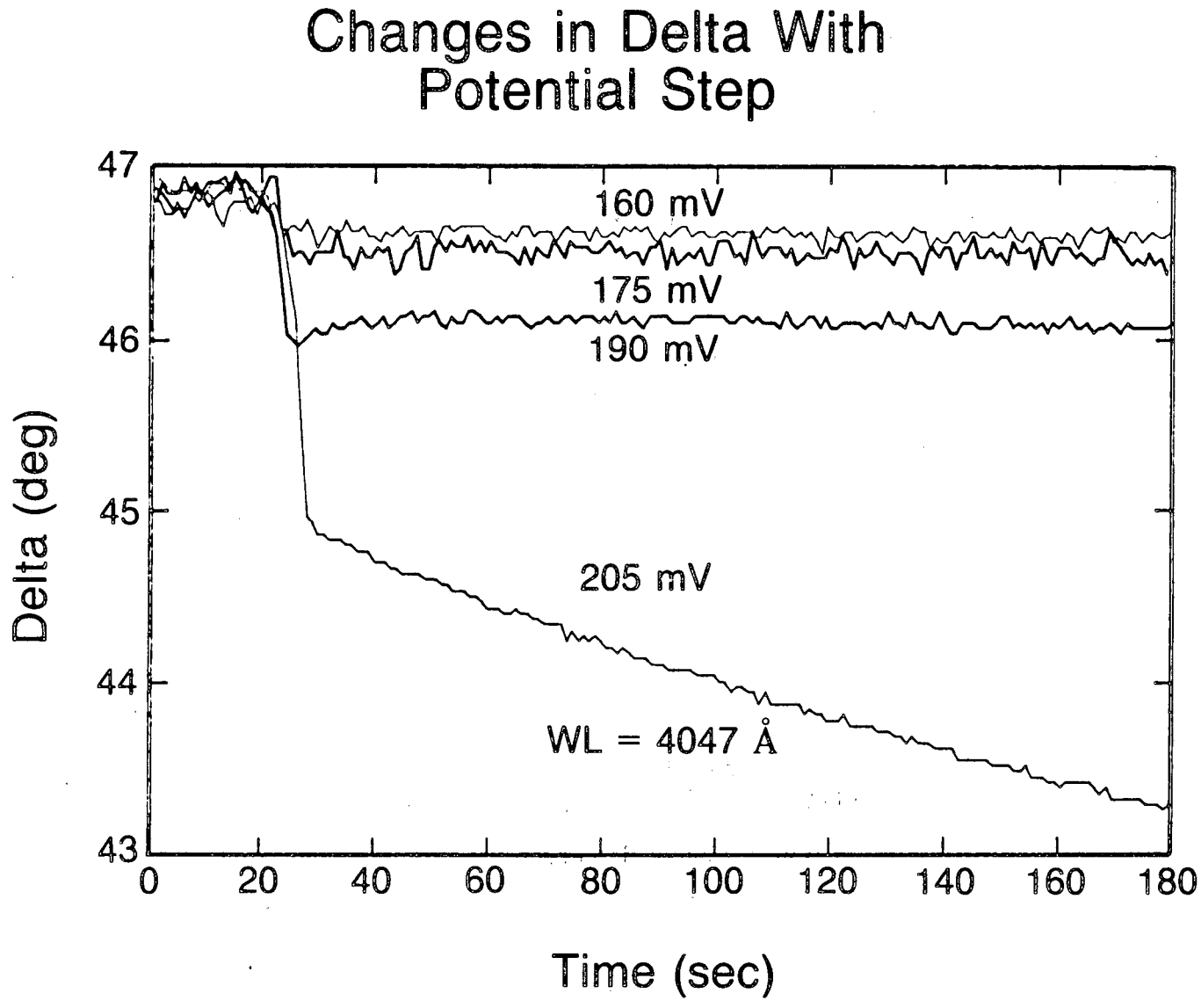

FIGURE C25

XBL 8511-12722

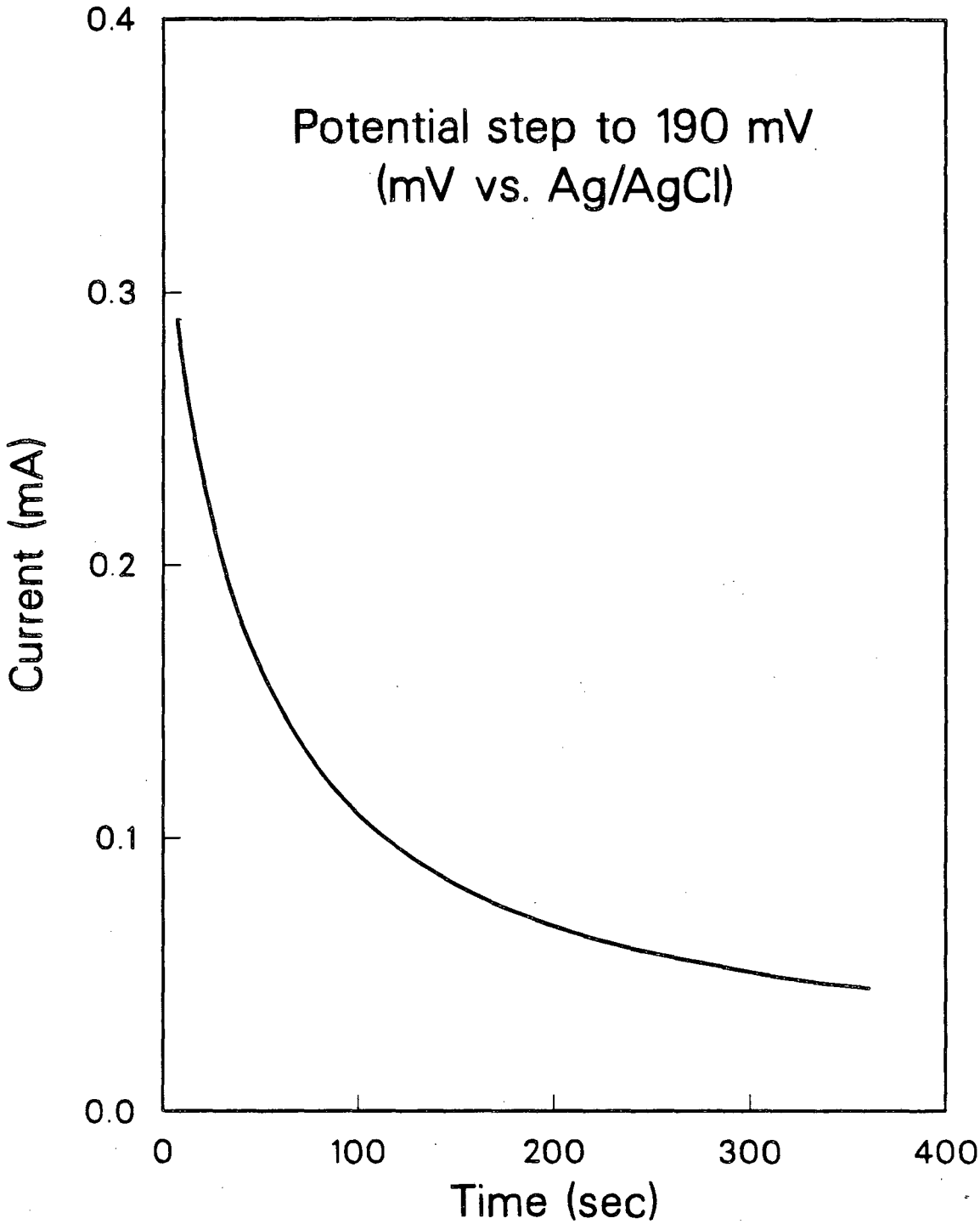

FIGURE C26

XCG 8511-481

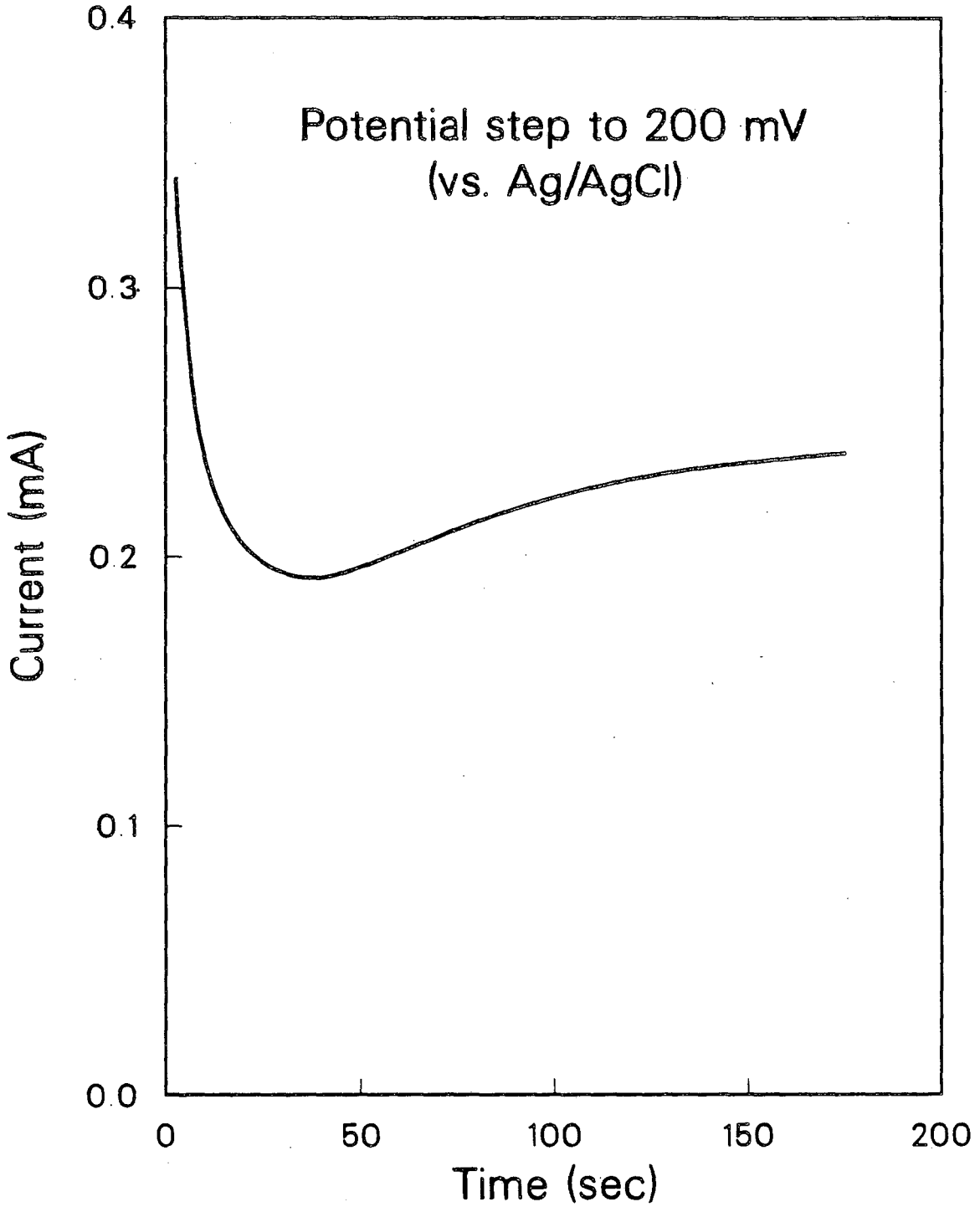

FIGURE C27

XCG 8511-480

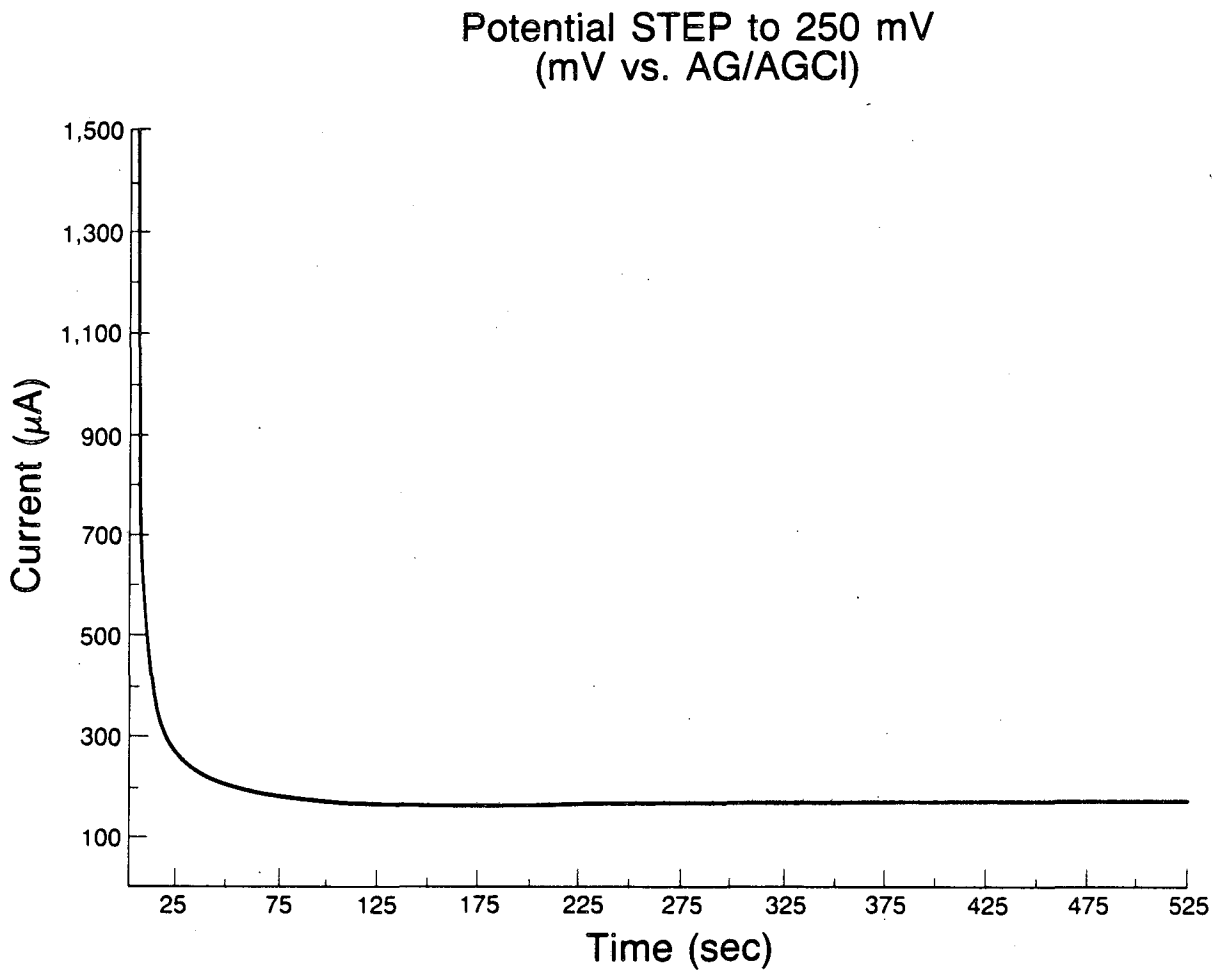

XBL 8511-11460

FIGURE C28

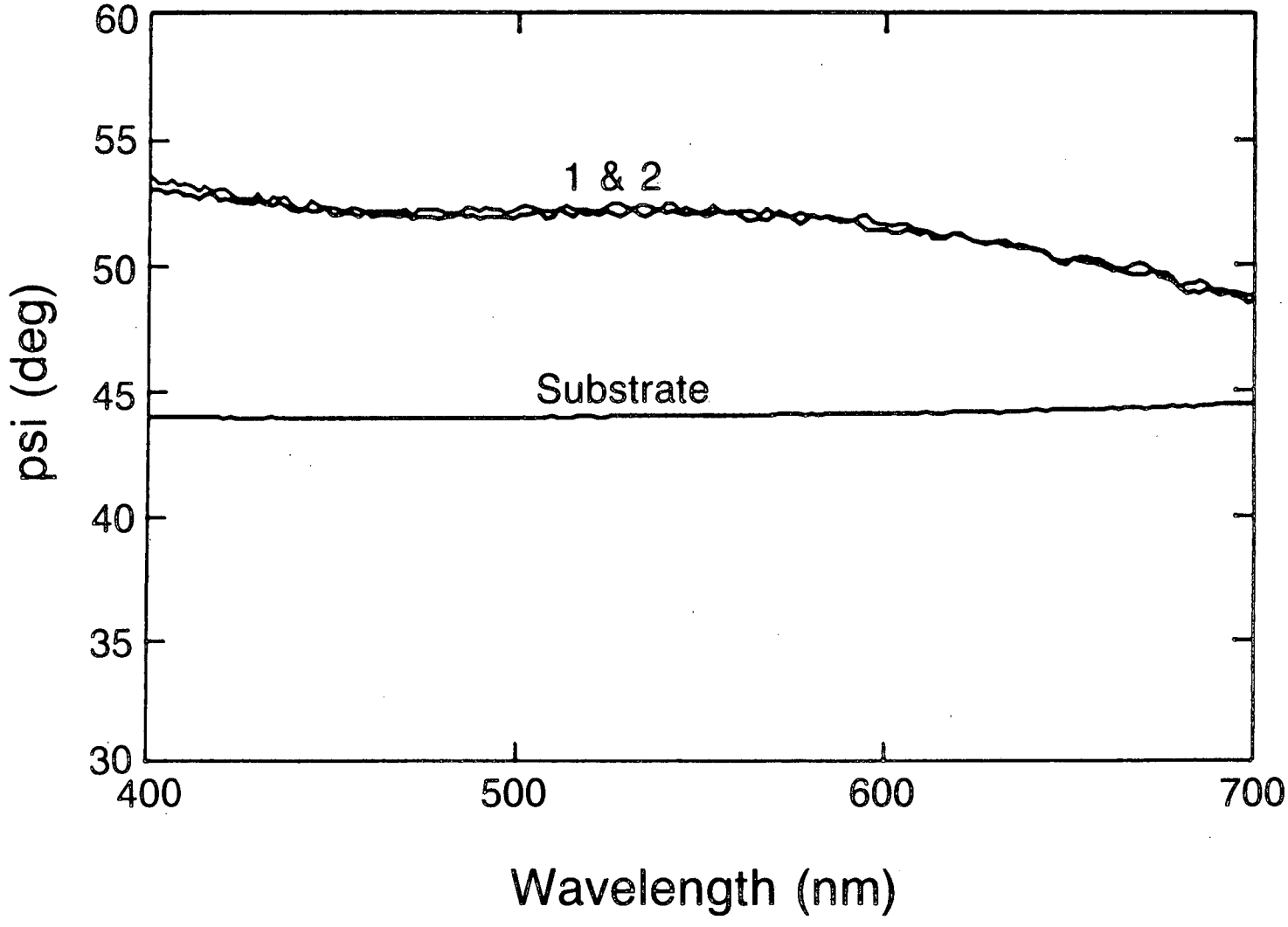

FIGURE C29

XBL 8512-4949

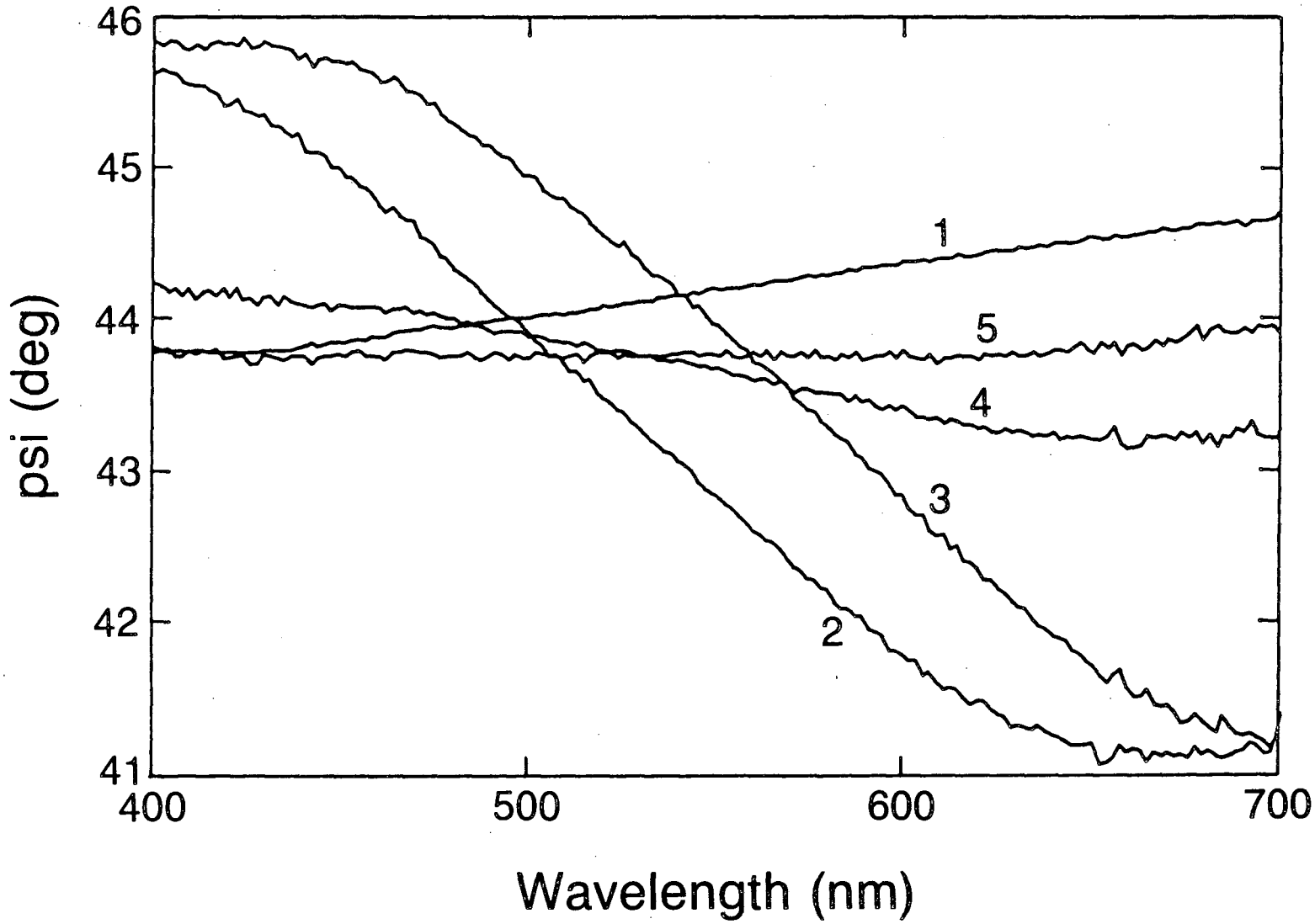

XBL 8511-12747

FIGURE C30

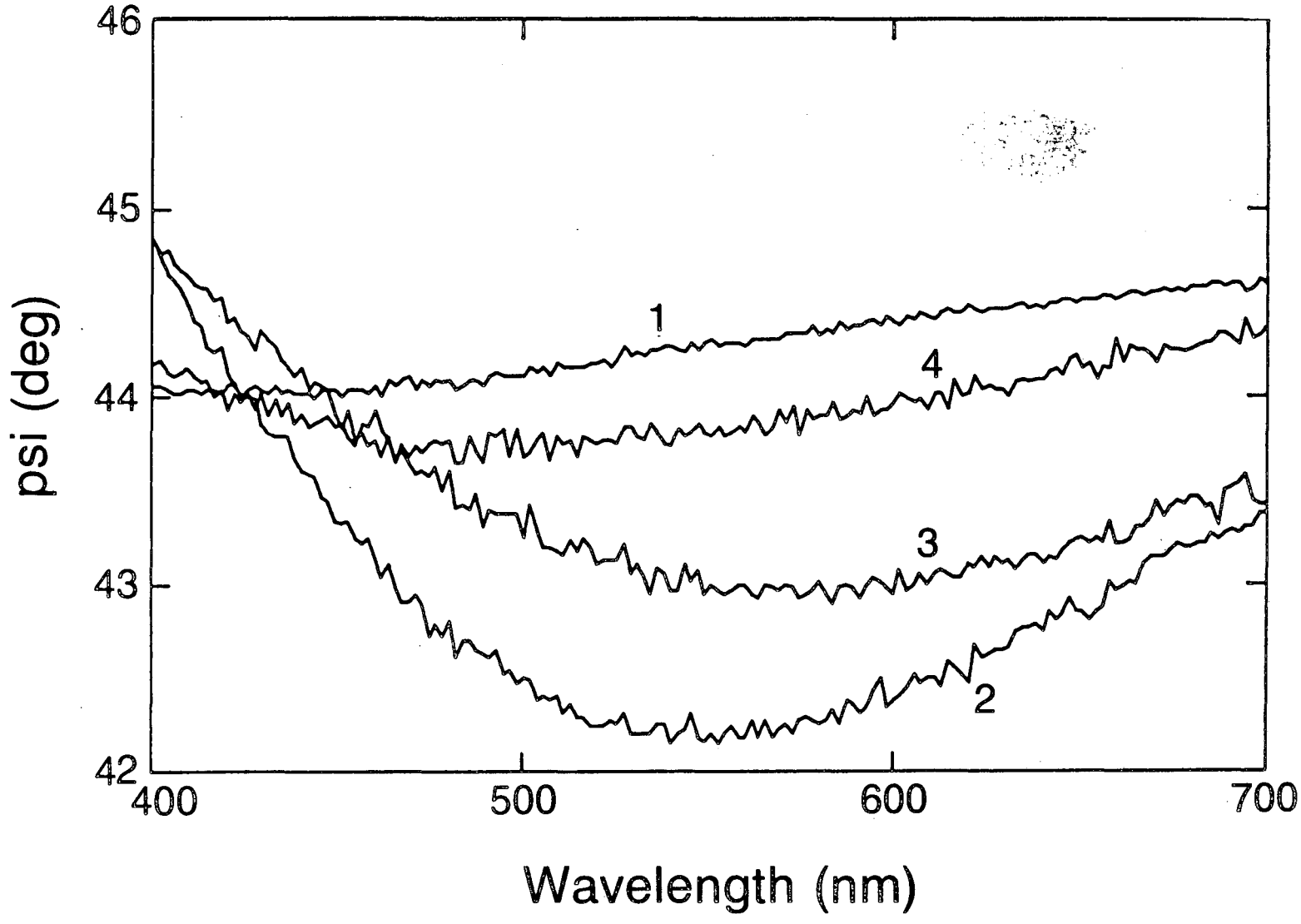

XBL 8511-12727

FIGURE C31

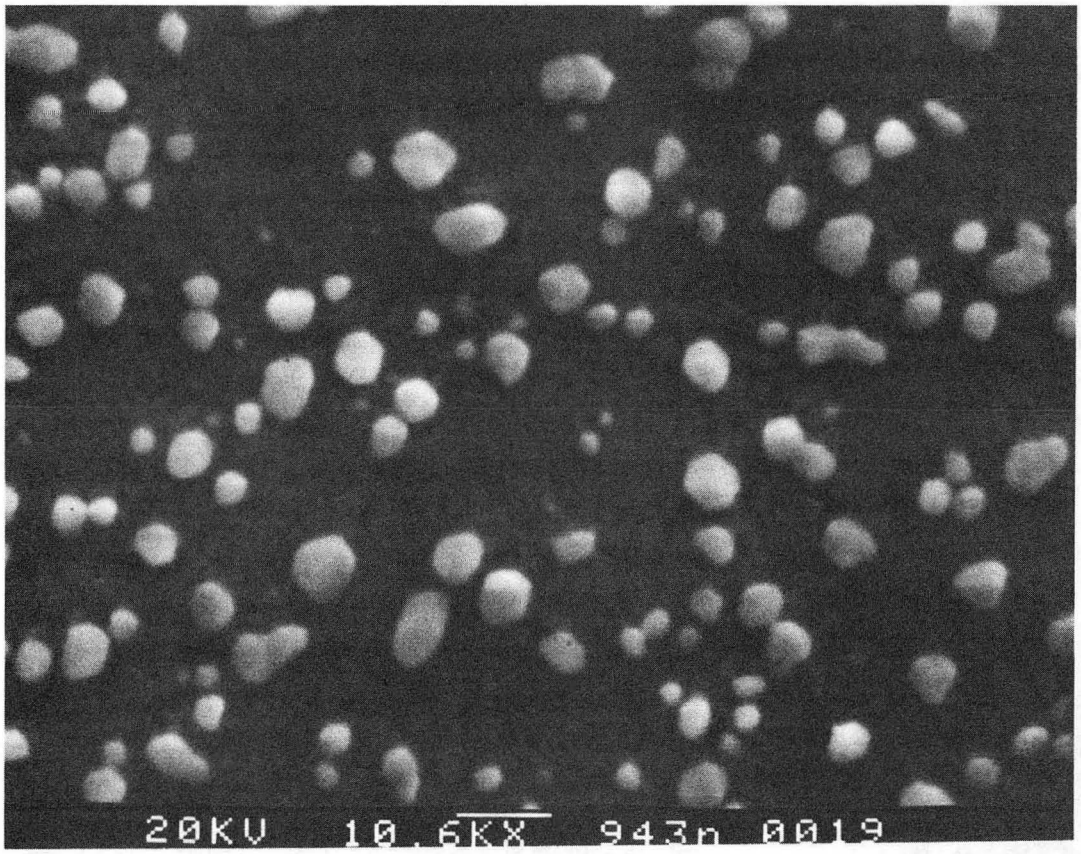

XBB 859-7232

FIGURE C32

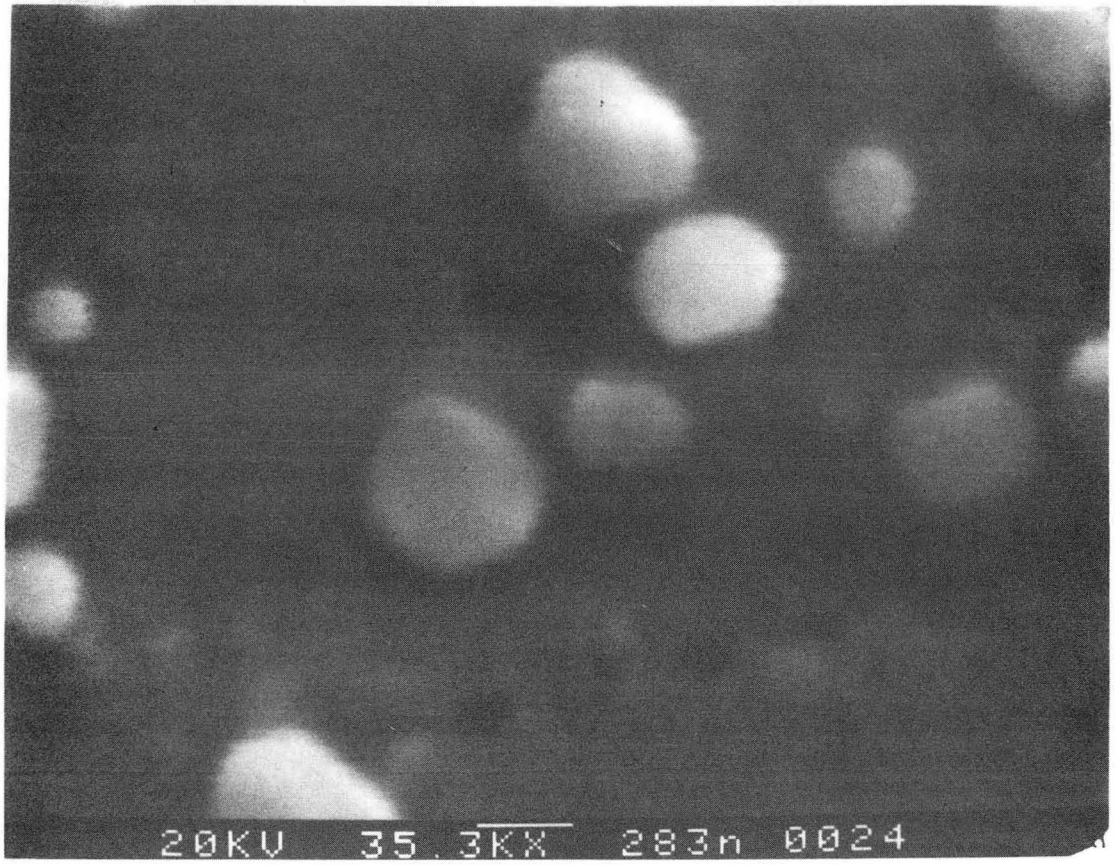

XBB 859-7131

FIGURE C33

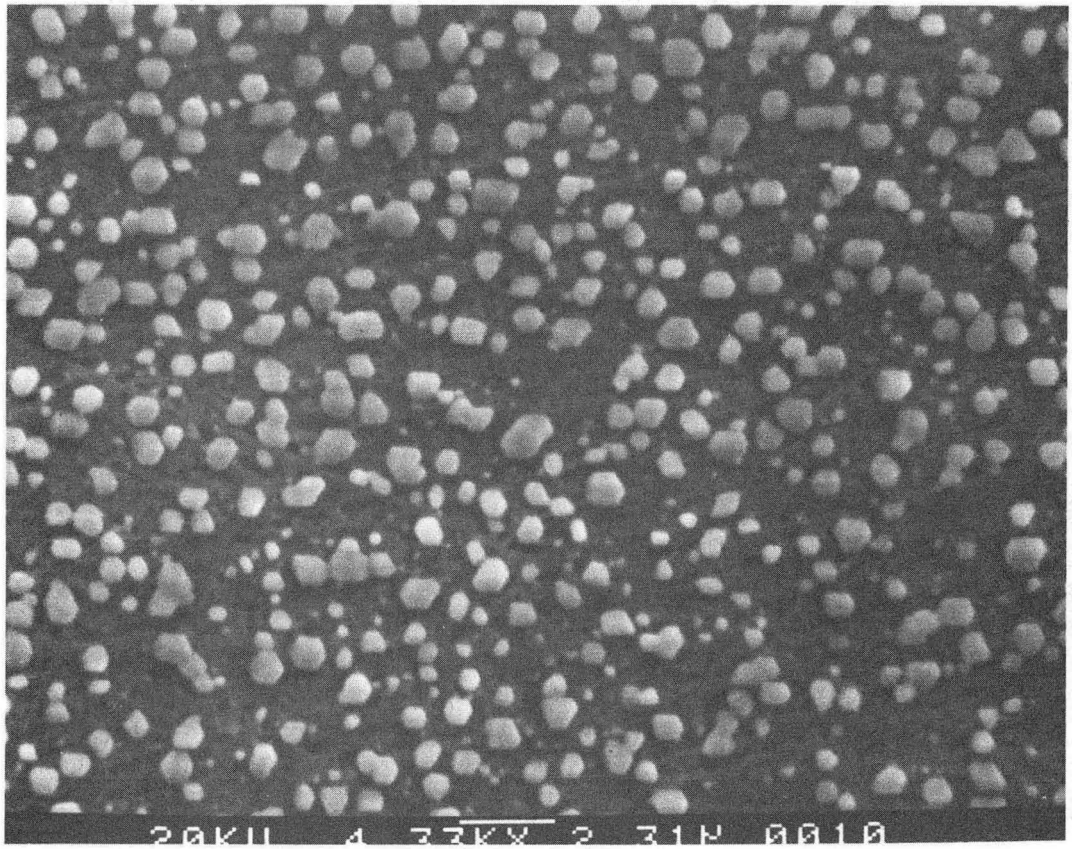

XBB 859-7234

FIGURE C34

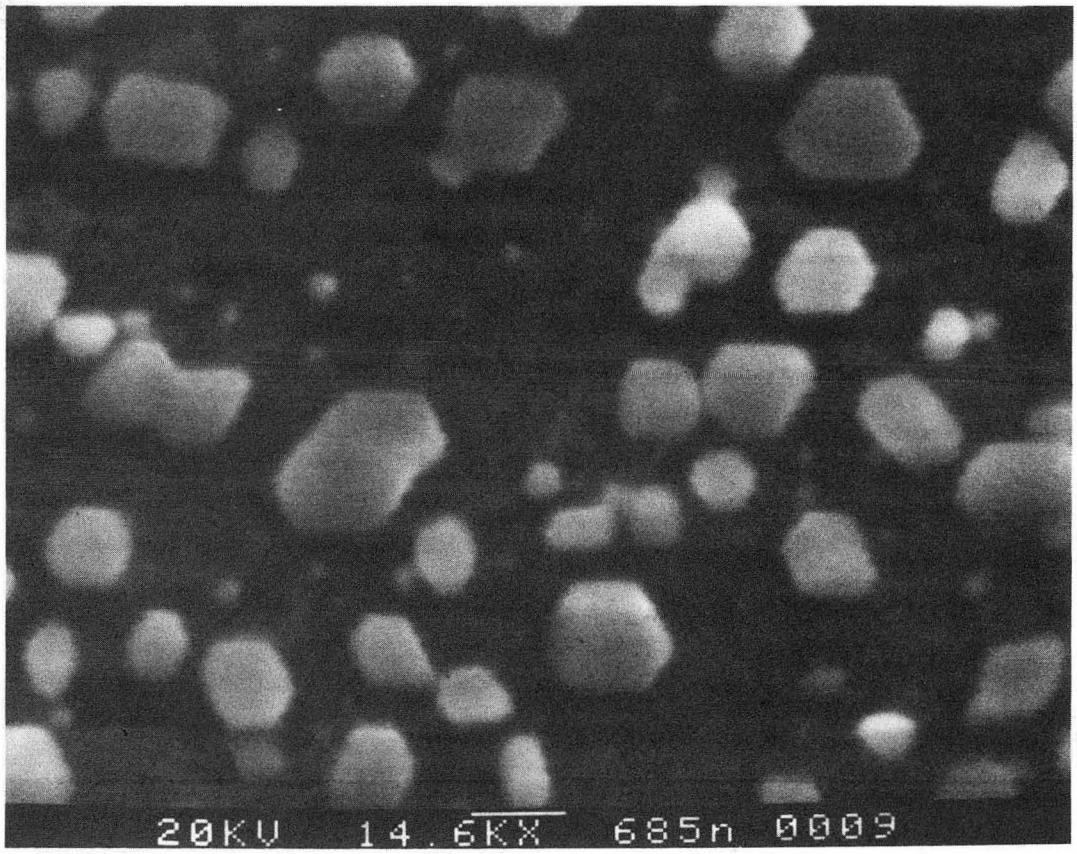

XBB 859-7235

FIGURE C35

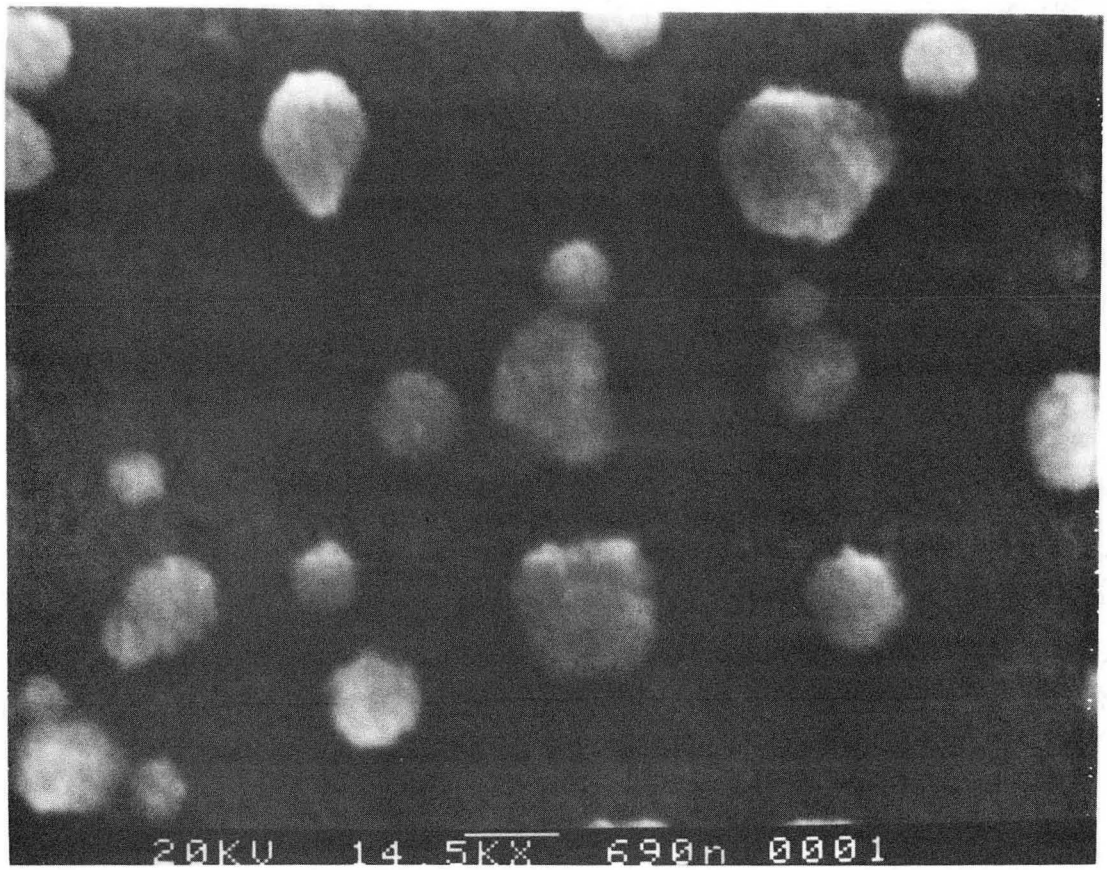

XBB 859-7129

FIGURE C36

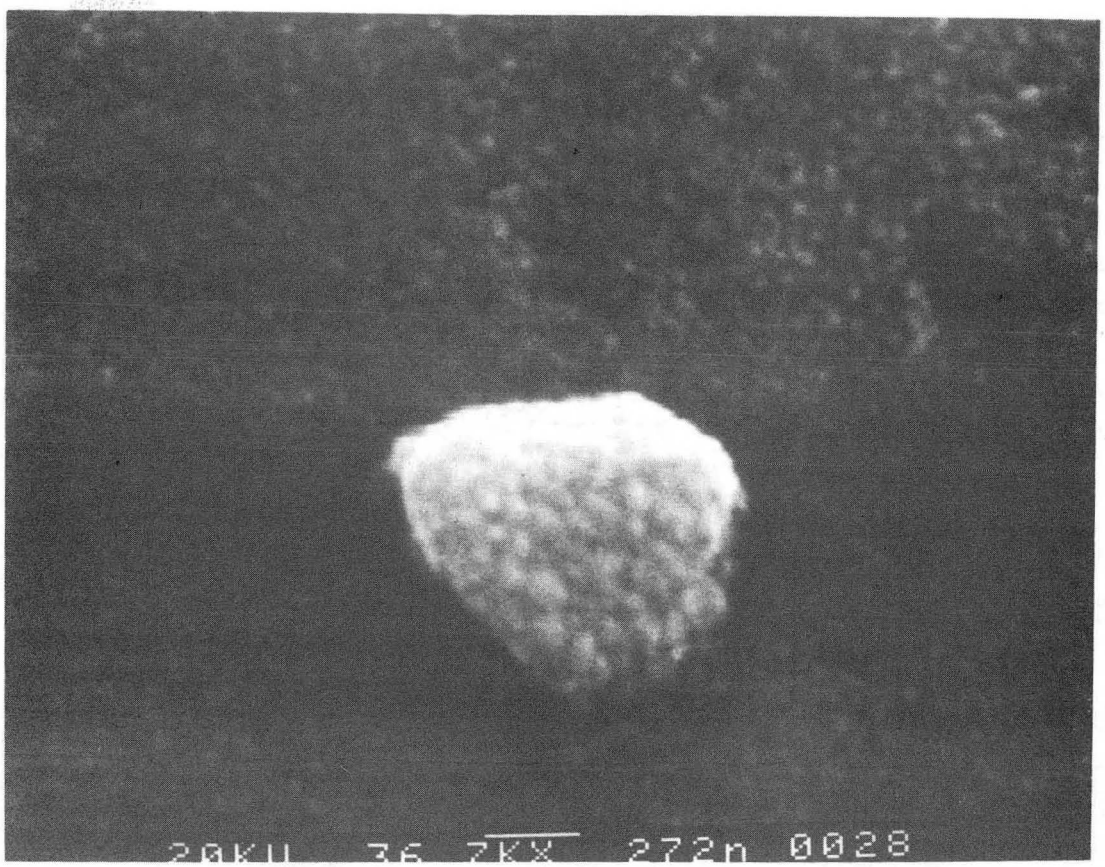

XBB 859-7130

FIGURE C37

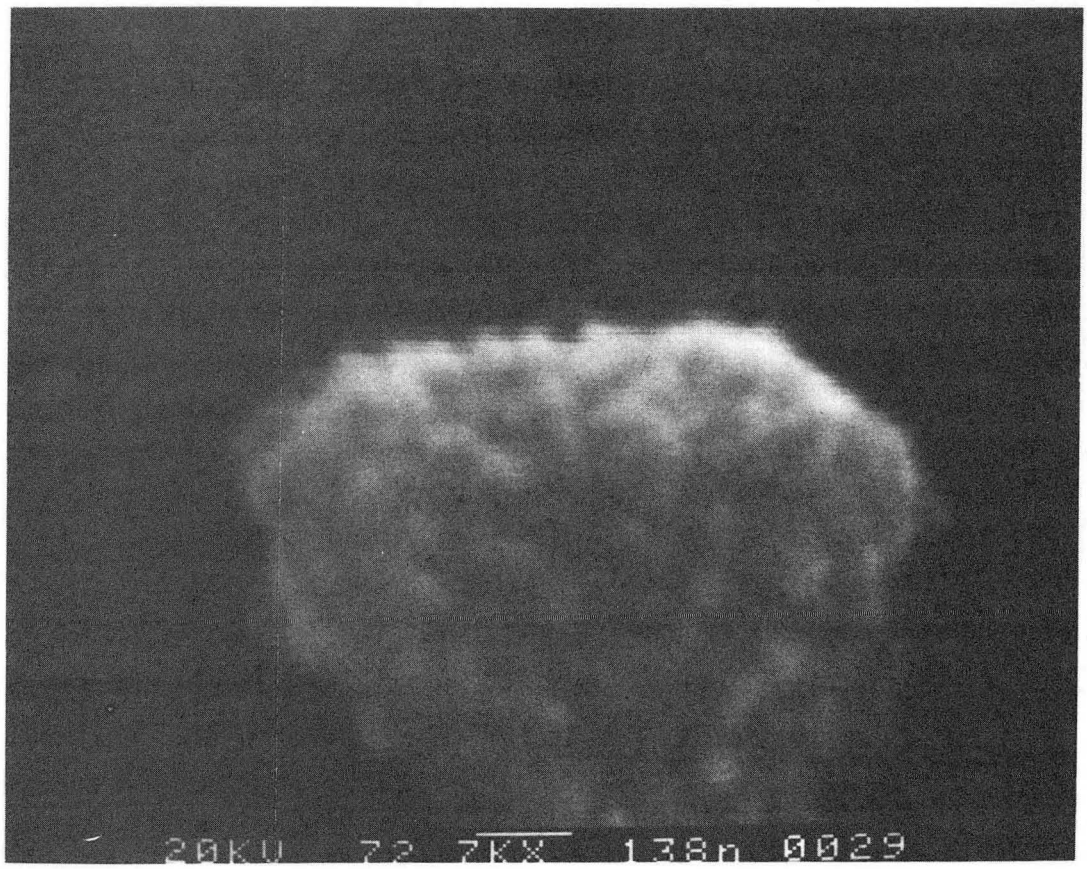

XBB 859-7128

FIGURE C38

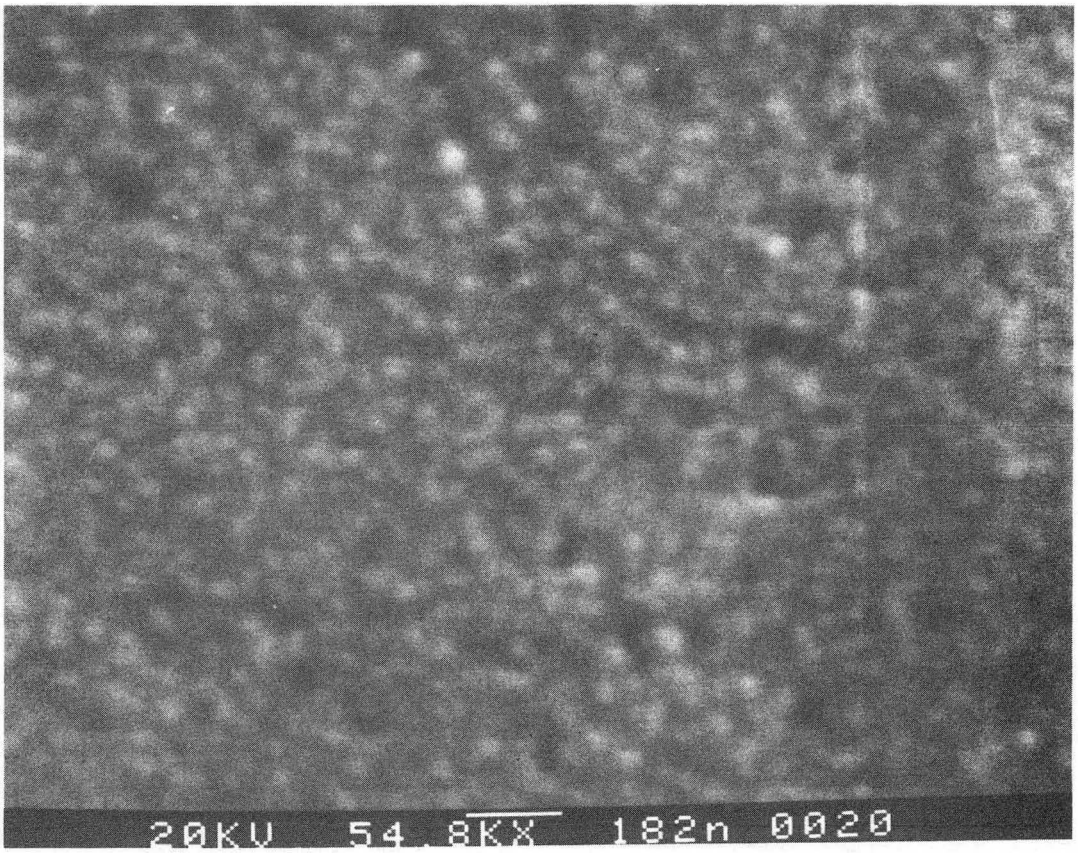

XBB 859-7236

FIGURE C39

CHAPTER 4

CALCULATIONS AND RESULTS

CALCULATION OF THE PRIMARY CURRENT-DISTRIBUTION

The primary-current distribution was calculated to indicate the uniformity of the current over the region probed by the ellipsometer. For a typical incident beam of 3 mm in diameter one can calculate that the beam strikes the surface forming an ellipse with a major axis of 11.6 mm and minor axis of 3 mm. This size compares with the dimension of the crystal of 30 mm long by 12 mm high. The current at the outer edge of the beam on the surface should be approximately equal to the current at the center of the electrode for the optical model to be valid.

The primary current-distribution was calculated by forming a finite-difference form of the Laplace equation in the three-dimensional space similar to that of the cell used. The boundary conditions were,

1. Constant potential at the working-electrode surface.
2. Constant potential at the counter-electrode surface.
3. No flux at the insulating boundaries (image points were used).

In addition, center-line symmetry (i.e., no flux across points of symmetry) was used to reduce the memory necessary for the calculation. The FORTRAN program "CURDIS" was written to find the solution to the three-dimensional potential profile and to take the normal derivative at the surface to give the local current density. This calculation uses a simple relaxation technique to find the solution. The results of the

finite-difference calculation are shown in Figure D1. Note that the current is uniform up to about 75% of the distance from the center to the edge in the vertical direction and 90% of the distance from the center to the edge in the horizontal direction. This can be compared to the beam size of 25% of the vertical distance and about 40% horizontal distance. It is therefore reasonable to say that the current density is uniform over the section of the surface studied.

ELLIPSOMETRIC PRINCIPLES FOR MODELING

Quantitative analysis of ellipsometric data is possible when one uses a suitable model to interpret the ellipsometric results. Spectroscopic ellipsometry has been used to determine compositions and structures of thin films on various surfaces. Sensitivity to submonolayer coverages and microstructure have made ellipsometry a powerful technique for addressing problems in film formation. In situ characterization of submonolayer underpotential film of Pb on Cu has been investigated previously using classical models [1,2]. Ellipsometric results from multilayer film structures can be interpreted using classical principles.

All optical models that we used to interpret the ellipsometric results are classical. That is, matter is treated as a continuum. The optical model generally used first in trying to reproduce experimental data is the homogeneous-film model. This model considers the surface layer to be a simple, planar, homogeneous, isotropic film. The model uses the results obtained by Drude [3] (equation 1D) for the reflection of a slab of material placed between two other semi-infinite media:

$$R_j = \frac{r_{01,j} + r_{12,j}\, e^{-iD}}{1 + r_{01,j}\, r_{12,j}\, e^{-iD}} . \tag{1D}$$

In equation 1D, $r_{01,j}$ is the reflection coefficient of the s- or p-component at the solution/film interface, and $r_{12,j}$ is the reflection coefficient of the s- or p-component at the film/metal interface. The Fresnel reflection coefficients are calculated by

$$r_{01,p} = \frac{\tan(\phi_o - \phi_f)}{\tan(\phi_o + \phi_f)} \tag{2D}$$

$$r_{01,s} = -\frac{\sin(\phi_o - \phi_f)}{\sin(\phi_o + \phi_f)} \tag{3D}$$

$$r_{12,p} = \frac{\tan(\phi_f - \phi_s)}{\tan(\phi_f + \phi_s)} \tag{4D}$$

$$r_{12,s} = -\frac{\sin(\phi_f - \phi_s)}{\sin(\phi_f + \phi_s)} \tag{5D}$$

and the phase delay is given by

$$D = 4\pi(T/\lambda) n_f \cos(\phi_f) . \tag{6D}$$

T is the oxide thickness and λ is the wavelength of light (in vacuum). The propagation direction, ϕ_i, used in the Drude equation are calculated by a complex form of Snell's law:

$$n_o \sin(\phi_o) = n_f \sin(\phi_f) = n_s \sin(\phi_s) \tag{7D}$$

where n_o, n_f, and n_s are the (complex) refractive indices of the solution, film, and substrate, respectively. The substrate and ambient

refractive indexes can be found experimentally. Therefore the ellipsometric parameters delta and psi contain information about the refractive index and thickness of the surface layer. When one uses the homogeneous-film model it is assumed that the optical properties of the surface film are uniform. Despite this limitation the homogeneous-film model has been used for adsorption studies where submonolayer films are treated as films with a fraction-of-monolayer thickness [4,5] or as films of monolayer thickness whose refractive index changes with coverage (see discussion below on effective-medium-approximations). More complex forms of the Drude equation can be used to represent films whose optical constants change with the distance normal to the surface [6-8]. This is generally accomplished by dividing the film into many smaller layers oriented parallel to the surface. The procedure for this type of calculation is as follows.

1. Calculate delta and psi for a substrate covered by a film of thickness equal to the thickness increment and optical properties determined by an assumed functional relationship with depth.

2. Calculate new apparent optical constants for this film/substrate combination.

3. Add the next film increment, and repeat steps 1 and 2 until the final thickness is reached.

This procedure can enable one to use the Drude equation to determine both the thickness and composition profile of a thin film.

When a region of space contains more than one chemical constituent, the optical properties of the material in that space are a mixture of the optical properties of the pure constituents. Effective-medium-theories (EMTs) are used as "mixing rules" to derive optical properties of the composite media. Three EMTs most commonly used are the Lorentz-Lorentz (LL) EMT, the Maxwell-Garnett (MG) EMT [10], and the Bruggeman effective medium approximation (EMA)[11]. These models represent a heterogeneous dielectric mixture by a single parameter, the volume fraction. The dielectric mixing-function equation for all of these models can be written as [12,13]:

$$\frac{\epsilon-\epsilon_k}{\epsilon+2\epsilon_k} = \sum_{i=1}^{n} \theta_i \frac{\epsilon_i-\epsilon_k}{\epsilon_i+2\epsilon_k}, \tag{8D}$$

where ϵ_i, ϵ_k and ϵ_i are the dielectric functions of the effective medium, host medium, and inclusions media, respectively. The volume fractions of the various inclusion materials are represented by θ_i. The underlying assumptions are that 1) only dipole interactions occur and 2) the inclusions are spherical [14]. Therefore, the EMTs models discussed here differ only in what is considered the "host" media.

The LL EMT was developed to approximate the dielectric function of a point dipole of polarizability (α) in a vacuum [13]. By use of the Clausius-Mosotti relation,

$$\frac{4}{3}\pi n_i \alpha_i = \frac{\epsilon_i-1}{\epsilon_i+2}, \tag{9D}$$

the dielectric function of the composite material can be determined using equation 8D. The MG approximation assumes that the background

host is one of the inclusion materials. Therefore, a composite material of two substances will have one of the substances acting as the host. As pointed out by Aspens[13], MG-calculated effective-medium dielectric functions will differ based on the inclusion material chosen as the "host." A choice has to be made, and this choice is particularly difficult when the volume fractions of the inclusion materials are near 50%. To avoid the ambiguity in choosing a host medium, Bruggeman [10] replaced the host medium with the effective medium in equation 8D. All of the EMTs approach the same result in the limit of pure substances.

Figures D2 and Figure D3 show different calculated effective medium refractive indices for a porous silver oxide/water composite based on the three EMTs. The real part of the refractive index of the composite is almost identical for the EMA and the two MG models. The calculated refractive index varies nearly linearly as a function of void fraction. The LL model predicts a slightly lower refractive index of the effective medium. The calculated extinction coefficients are more sensitive to the model chosen and are slightly nonlinear in volume fraction. However, for any given extinction coefficient the difference in the calculated oxide volume fraction given by the different models would not exceed 7%. The Bruggeman EMA has been used in this study largely because 1) the Bruggeman model reduces to the Lorentz-Lorentz or Maxwell-Garnet models in the limit of the volume fraction and 2) the Bruggeman model provides intermediate results for the calculation of the refractive index. While the choice of the correct effective-medium model can be important, the results of this work were not sensitive enough to make a quantitative assessment as to which model best fits the

data. This lack of sensitivity is largely due to the fact that the effective-medium model was used to represent the hydration of the "secondary" silver oxide crystals, and the model of the optical response of the crystal layer is an approximation in itself.

The principle of coherent superposition of light (also referred to as the "island-film model") has generally been used when a film is discontinuous in the plane parallel to the surface (extensions of its use are discussed in the section on optical models specifically developed for this thesis). The general equation used for the coherent superposition of light in ellipsometry is

$$R_j = \Omega r_{fj} + (1-\Omega) r_{sj} , \qquad (10D)$$

where Ω is the fractional area of the surface covered by the film and r_{sj} and r_{fj} are the s- or p-components of the light reflected from the bare and film-covered surfaces, respectively. These reflection coefficients are calculated in the same manner discussed above. The coherent-superposition principle is extremely useful because it allows one to make a two-dimensional interpretation of a film's morphology (thickness and coverage). The coherent-superposition principle can be used when the surface structures are small with respect to the transverse coherence length of the incident light, which is 10–17 μm for the present arrangement of our apparatus.

OPTICAL MODELS

All of our optical models employ various combinations of the principles indicated above. Figure D4 is an artist representation of the

various optical models used to try to reproduce the experimentally observed ellipsometric data. Table D1 describes the various models. Figures D6 and D7 show the calculated changes in delta and psi for a homogeneous nonporous film (model 0, $n_f = 1.81-0.28i$) for different thicknesses. Strong spectral dependence is seen. The calculated psi spectra show a peak in the visible spectral range for thicknesses greater than about 500 Å. Changes in delta are approximately linear for smaller film thicknesses, but for thicknesses greater than 300 Å changes in delta are highly nonlinear. Figures D8 and D9 show the calculated delta and psi spectra for a homogeneous film 600 Å thick of varying porosity (model 2). The spectra calculated for these films are significantly different from those of model 0. Finally, Figures D10 and D11 show calculated delta and psi spectra as a function of varying surface coverage for an island film, 600 Å thick (model 5). The spectra calculated for the non-porous island film show a peak in psi for all coverages, indicating that the spectral changes in psi for a 600 Å homogeneous island film only decrease the magnitude of the peak with reduced surface coverage.

A clear comparison of the spectra shown in Figures D6-D13 can be made when we compare the calculated spectra for the different models with films containing the same amount of material. Figures D12 and D13 compare the results for a film containing the equivalent of 150 Å of a nonporous homogeneous film. Despite the fact that all of the computed spectra would predict the same amount of surface material, the differences in morphology change the calculated spectra dramatically. The introduction of the spectroscopic ellipsometer makes it possible to

determine not only the amount of material present at a surface, but also its microstructure.

General characteristic changes associated with changing thickness, porosity, and coverage can be seen from Figures D6–D13. As shown in Table D1 and Figure D4 and D5, more complicated duplex film models were also developed to reproduce the experimental data. It is difficult to graphically show the effects of various parameters on the predicted responses for more complex duplex-film models due to the large number of parameters involved. Model 0 (homogeneous film with variable n and k) was very successful in modeling the results of the initial films formed in galvanostatic experiments, as well as in predicting the films formed in potentiostatic experiments for potentials below 190 mV. (These are generally simple films that form prior to the nucleation of secondary crystals.) Models 9 and Q were successful in simulating the results of the more complicated crystal-covered surfaces.

Model 9 fits the data well for a majority of the surface films formed. This model contains only 4 parameters (primary- and secondary-layer thicknesses, surface coverage, and porosity of secondary crystal layer). It allows us to determine such physical parameters as changes in the number density of secondary crystals, and growth characteristics of the underlayer. The model calculations involve using equation 1D to determine the change in polarization due to the reflection of the underlayer. Next, a new effective substrate refractive index is calculated, which incorporates the optical properties of the underlayer. The optical properties of the porous crystals are determined using the Bruggemans effective medium approximation. A calculation is performed to

determine the reflection coefficients of the porous oxide crystals of a given thickness. The surface coverage of the oxide crystals is used with the coherent superposition principle (equation 10D) to determine the final optical response of this type of film.

Model Q differs from model 9 by allowing for a statistical variation of the thickness of the island film. Equation 11D allows the calculation of a normalized Gaussian surface-coverage function from a given average thickness and standard deviation of thickness:

$$\zeta(T_2, T_{AVG}) = \frac{\exp\left[\frac{1}{2}\left(\frac{T_{AVG}-T_2}{\sigma}\right)^2\right]}{\int_0^\infty \exp\left[\frac{1}{2}\left(\frac{T_{AVG}-T_2}{\sigma}\right)^2\right] dT_2} \tag{11D}$$

In equation 11D, ζ is the normalized surface coverage of crystals with a a function of thickness T_2, T_{AVG} is the average thickness of the layer, and σ is the standard deviation of layer thickness. Using the coherent-superposition principle, we can sum the effects of the bare surface (covered only with the underlayer) and the secondary crystal-covered layer, as expressed in equations 12D-16D.

$$R_j = r_{aj}(1-\Omega) + \Omega \int_0^\infty \zeta(T_2, T_{AVG})\, r_{b,j}\, dT_2 \tag{12D}$$

$$r_{a,j} = \frac{r_{02,j} + r_{23,j}\, e^{-iD_1}}{1 + r_{02,j}\, r_{23,j}\, e^{-iD_1}} \tag{13D}$$

$$r_{b,j} = \frac{(r_{01,j}+r_{12,j}e^{-iD_1})+(r_{01}r_{12}+e^{-iD_1})r_{23}e^{-iD_2}}{(1+r_{01,j}r_{12,j}e^{-iD_2})+(r_{12,j}+r_{01,j}e^{-iD_1})r_{23}e^{-iD_2}} \tag{14D}$$

with

$$D_1 = 4\pi\left(\frac{\pi}{\lambda}\right)n_1\cos(\phi_{23}) \tag{15D}$$

$$D_2 = 4\pi\left(\frac{T_2}{\lambda}\right)n_2\cos(\phi_{01}) \tag{16D}$$

Equation 14D is the equation given by Azzam [23] for reflection from a duplex (stratified) plane structure. T_1 is the (uniform) primary-layer thickness, n_1 is the primary-layer (complex) refractive index. Ω is the total fraction of the surface covered with crystals. T_2 is the thickness of the crystal with fractional surface coverage $\Omega\zeta$, T(avg) is the average thickness of the secondary crystal layer, and n_2 is the (complex) refractive index of the secondary crystals. The optical constants of the porous secondary crystals are determined by using the Bruggeman effective media approximation, as in model 9. The reflection coefficients are determined by the Fresnel equations (equations 2D-5D). Model Q reduces to model 9 in the limit as the standard deviation of secondary-crystal size approaches zero. Figure D14 shows the effect of changes in the standard deviation of the crystal sizes on a predicted psi spectra.

Figure D15 compares the error (averaged over the spectrum) in delta of the optimized results of various models for a galvanostatic experiment (current density=0.20 mA/cm^2). Errors for all model are not shown for simplicity. Models 9 and Q are found to be superior over the other models. At early formation times, an effective-film model is adequate.

Model 9 was chosen over Model Q for interpretation of the optical data of all crystal-covered surfaces. This choice was made primarily because model Q requires that the projected area distribution of the crystals be known apriori. SEM pictures generally showed a Gaussian size distribution. However, the fitting of experimental data by use of model Q was only slightly better than that using model 9. Increased uncertainties in derived quantities occurred when the statistical parameter was added, and the statistical deviation parameter had large uncertainties associated with it. Therefore, the simplier duplex film model (model 9) was chosen.

DATA-FITTING ROUTINES

A curve-fitting routine has been used to derive model parameters from the measurements. A simple stepping procedure for optimization of data was used previously in this laboratory but was found too be extremely slow for reduction of the large quantity of data gathered in spectral kinetic studies. In addition to being fast, a new process for data reduction had to be suitable to the highly nonlinear equations used in ellipsometry. A Newton-Ralphson algorithm was found to require more memory than was generally available on the PDP 11/73 (64 Kb when not using large numbers of overlays or storing intermediate results onto hard disk) and was not sufficiently stable for the required computations. A Simplex algorithm [15] was found to be stable, efficient, and suitable for the memory available. The general principle on which the Simplex algorithm is based is to sample points on a multidimensional response surface that measures the difference between the calculated and experimental data. Different error functions could be used as Simplex

response surfaces. The error function we chose has similar characteristics to a standard deviation function of the calculated and observed spectra of delta and psi.

$$E.F. = \sum_{\lambda=400}^{700} 2\,|\psi_m(\lambda) - \psi_c(\lambda)| + |\Delta_m(\lambda) - \Delta_c(\lambda)| \qquad (17D)$$

In Equation 17D, ψ_m and Δ_m are the measured values of psi and delta at wavelength λ, and ψ and Δ_c are the calculated values of psi and delta at wavelength λ. We require twice as much accuracy in psi as in delta because changes in delta are related to twice the changes in polarizer azimuth, whereas psi is related only to the change in the analyzer azimuth.

The FORTRAN source codes of the programs and subroutines used in this thesis can be found in a separate report [15]. The Simplex routine requires some standard input data prior to optimization of the spectral data. These data include refractive-index data on the substrate, assumed optical properties of the film(s), and initial guesses of the various parameter values. The optimization routine allows one to optimize around every data point in the spectrum, or to use a smaller number of evenly spaced points to increase the speed of the calculations. The routine asks for the data-class name of the experiment whose results are to be optimized and a file number with which to start and stop the calculations. The computer calls up the first data file, optimizes the results of the spectral file to the given model, stores the optimized results, and calls up the next data file. Estimates of the new data-file parameters are made based on the optimized parameters of the previous data file. When the final spectral data-file results have been

optimized, the model parameter obtained from the optimization of each spectral scan are put in a new data file whose name is chosen by the operator.

MODELING POTENTIOSTATIC CURRENT TRANSIENTS

As indicated in the measurement section of this thesis, there are two distinct current-response classes evident in the potential range studied. At low overpotentials (E < 190 mV), the current decreases monotonically with time. For higher overpotentials, the current passes first through a minimum and later through a maximum.

A theoretical treatment of the current response to a potential step under diffusion control was originally given by Cottrell [16,17]. The resulting equation is the solution to the one-dimensional unsteady-state diffusion of material into a semi-infinite medium. The boundary conditions applied require a constant surface concentration after the potential step has occurred, and a uniform initial concentration in the electrolyte phase. Cottrell's equation is

$$i(t) = nFC_s\sqrt{\frac{D}{\pi t}}, \tag{18D}$$

when the transference number and the bulk concentration of the diffusing species is zero. The integrated form of the Cottrell equation,

$$q(t) = 2nFC_s\sqrt{\frac{Dt}{\pi}}, \tag{19D}$$

gives the charge passed in a potentiostatic experiment. The Cottrell equation predicts that a plot of charge versus the square root of the time should be linear. Double-layer capacitance increases the intercept

of a charge-versus-root time plot from zero to some positive value. Figure D16 shows a plot of our data for a potential-step experiment from open circuit to 135 mV. The plot is linear and has a positive intercept. The slope of the line is related to two experimentally unknown quantities, the surface concentration and the diffusion coefficient. Literature values for the diffusion coefficient of the dissolved silver species in 1M KOH and 1M NaOH are given as approximately 1×10^{-5} cm^2/sec [7,18,23], and this value was used in this study. Using this value for the diffusion coefficient, the surface concentration was calculated for a series of potential-step measurements. The results of these calculations are shown in Figure D17, which is a plot of the logarithm of the surface concentration versus potential. This plot should be linear and have a slope of RT/nF (0.0256 V for n=1) if Nernstian behavior is obeyed. The resulting plot is found to fit the following equation:

$$E = 0.100 + 0.0419 \ln \frac{C}{5.9\times10^{-4}} , \qquad (20D)$$

The plot is linear, but the slope is found to be 0.0419 V. Therefore, while it appears that diffusion is the controlling process for the anodic currents at low overpotentials, the potential is not related to the surface concentration as would be predicted for a simple concentration overpotential. Finally, based on our results, we estimate a double-layer capacitance of 123 $\mu F/cm^2$ (based on the apparent surface area of these surfaces covered by a very thin film).

For potentials above 190 mV, the current-versus-time measurements do not fit a simple Cottrell diffusion model. As indicated before, the

current response decreases initially but increases later. Optical measurements showed the formation of surface crystals at the point where the current starts to increase again. A model that incorporates both diffusion and crystal-growth contributions to the total current is proposed (dissolution/precipitation model). We represent the total current as the sum of two parallel currents,

$$I_t = I_d + I_c \tag{21D}$$

where I_t is the total external current density , I_d is the current density due to diffusion of material into the bulk electrolyte, and I_c is the current density due to the incorporation of reaction products into the growing surface crystals. Next we assume that the diffusion current I_d can be expressed as a modified Cottrell equation

$$I_d = (1-\Omega)nFC_s\sqrt{\frac{D}{\pi t}} \tag{22D}$$

where Ω is the fractional surface coverage of crystals, C_s is the surface concentration and D is the diffusion coefficient. Next, we use the conservation of material to relate the size of the growing crystal with time:

$$\frac{dr}{dt} = \frac{J_{mass}}{\rho} = \frac{Mi_i(t)}{nF\rho} \tag{23D}$$

$$i_c(t) = \bar{i}_c\,(1-\Omega) \tag{24D}$$

In Eq. 23D, J_{mass} is the mass flux into the crystal. ρ and M are the molar density and molecular weight of the oxide, respectively. $i_c(t)$ is the current density into a crystal at time t. We assume in equation 24D

that the current-density at the crystal surface is linear with respect to crystal surface coverage. This approximation of the effect of overlapping diffusion fields on the current density at the crystal surface should be valid for small coverages (small overlapping crystal diffusion-fields). Equation 23D therefore tells us that initially the current into a crystal will be given by an incorporation current density, $\tilde{i}_c$. The total crystal current is given by the product of the number density of crystals, the incorporation rate, and the surface area of the crystals. We assume that all crystals form instantaneously after the potential step is applied, that no new crystals form later, and that all crystals grow at the same rate. A Geometric approximation of hemispherical particles is also made. Hence, we have

$$I_c(t) = N_c \tilde{i}_c \, (1-\Omega) \, 2\pi \left[r(t)^2\right] \tag{26D}$$

where N_c is the number density of surface crystals and r(t) is the radius of the hemispherical crystal at time t. For hemispherical particles, the surface coverage is related to the number density and radius of the crystals as expressed in equation 25D.

$$\Omega(t) = N_c \, \pi \left[r(t)^2\right] . \tag{26D}$$

Combining equations 23D, 24D, and 26D we obtain a differential equation given in equation 27D.

$$\frac{\rho n F}{m i_c} \, dr = \left[1 - N_c \, \pi \, (r(t)^2)\right] dt \tag{27D}$$

The solution to this equation gives

$$r = \frac{C(e^{Kt} - 1)}{1+e^{kt}} \tag{28D}$$

where

$$K = \frac{2N_c \pi CM\bar{i}_c}{nFp} \tag{29D}$$

and

$$C = \frac{1}{\sqrt{N_c \pi}} \tag{30D}$$

fi Combined use of equations 21D, 22D, 25D, and 28D gives the total external current density. The three adjustable parameters in this model are the number density of surface crystals, the crystal-incorporation current density, and the surface concentration of the diffusing species. Figure D18 shows the effects of varying the incorporation rate parameter on the current response. High-incorporation-rate current densities $\bar{i}$ give rise to larger, earlier peaks, and earlier current minima. With a larger crystal-incorporation

rate the higher current per crystal and higher rate of surface-area growth account for both the larger current peak and the decrease in time to the peak current. Figure D19 shows that larger crystal-number densities decrease the time for the current maximum and minimum and sharpen the current-response peak. However, the peak current is uneffected. Figure D20 shows that changes in surface concentration increase the initial transient current, with a decreasing relative effect at later times. The Cottrell component of the equation increases the diffusion current with increased surface concentration but has no effect on the crystal-growth process.

Some of the simplifications made above are not completely valid based on our SEM and ellipsometric results. However, we are only using this model for qualitative assessment at this time. Figure C27 show the current response for a potential step to 200 mV. While no model curve would fit exactly, the general shape and magnitude of the current response predicted by the model is correct. The parameter values used to estimate the current response are similar to those predicted by other experimental techniques. The surface concentration used to reproduce a current response observed is in general agreement with that found from an extrapolation of the results of Figure D17. The number densities of surface crystals used to reproduce the current response is close to those calculated from ellipsometric results and from SEM photographs (Table D2). No estimates of the crystal incorporation rate was made based on either SEM or ellipsometric results, though the value found by curve fitting the electrochemical measurements [0.2-0.5 mA/cm^2] appears reasonable. Finally, if we are willing to accept this model to derive parameters from the measurement, then these results indicate that the number density of surface crystals decreases with time. Results that also supports this conclusion will be presented later.

This dissolution/precipitation model makes a number of simplifying assumptions that may not be correct (e.g., instantaneous nucleation). The effects of the relaxation of these assumptions should be adequately addressed to determine how these assumptions effect the calculated current response. As mentioned above, SEM photographs have indicated that a distribution of crystal sizes is found on the surface. Whether this is due to noninstantaneous nucleation, mass transfer between grow-

ing crystal centers, or the effects of overlapping diffusion field of neighboring crystals is unclear. Some mechanism does give rise to the finite size distribution phenomenon. Also, our mathematical form for the effect of diffusion-field overlap is probably inadequate for a quantitative interpretation. However, a solution to the governing differential equations of this moving-boundary problem would not be trivial, and so a more exact solution to the expected current response for a dissolution/precipitation mechanism has not been been attempted here.

INTERPRETATIONS OF POTENTIAL-SWEEP EXPERIMENTS

Figures C23 and C24 show the optical and electrochemical measurements for a potential sweep of 500 μA/sec on a Ag(111) surface. Ellipsometric optical model predictions are superimposed on the measurement spectra in Figure C23. As indicated before, the changes in delta and psi are very small below 100 mV. Relatively larger changes occur between 100 and 180 mV. Finally, nucleation occurs at a potentials of about 190 mV for this experiment.

We modeled the films that formed before nucleation of secondary crystals as homogeneous isotropic films with an unknown refractive index and thickness. While treatment of a submonolayer as a homogeneous film is not rigorously correct, it does gives an indication of the amount of material present (the layer thickness) and changes in its morphology (changes in optical properties). The validity of ellipsometry for determining the average thickness of thin, discontinuous films has been discussed by Bennett et al. [19], and ellipsometry has been used in adsorption studies [4,5]. Figure D21 shows the equivalent-film thick-

ness of the surface layer as a function of potential. The curve has a slight inflection at 170 mV above which equivalent-film thicknesses of greater than a monolayer are observed. The change in equivalent-film thickness starts to increase above 140 mV. Nucleation occurs at a potential of around 190 mV. Figure D22 shows the optimized refractive index of the surface layer as a function of potential. A step change in the apparent refractive index of this submonolayer film is seen between 100 and 140 mV. Above 140 mV the optical properties do not change. Attempts to model the film formed at potentials below 140 mV with the optical properties of the homogeneous surface layer for films formed above 140 mV resulted in significant errors in optimized values of delta and psi. Therefore we believe that the rapid increase in effective film thickness is not due to the decrease in the calculated optical constants of the surface layer. A two dimensional phase transformation may occur at a potential around 140–150 mV. This interpretation would be consistent with the cyclic voltammetric data presented earlier for this potential region (see discussion of Figure C15). No clearly defined redox adsorption sites are indicated from our voltammetric or optical data. If the adsorbed species follows Langmuir isotherm thermodynamics, we would expect a two-dimensional phase transformation to show up as a large change in apparent film thickness and optical properties.

Figure D23 shows optimized results of the same film using a coherent-superposition model. The film thickness and optical properties of the submonolayer film were based on the values found for the equivalent-film model at a potential of 170 mV. There is no significant difference between the errors of this model and those of the

equivalent-film model. In figures D24 and D26 the thickness or coverage does not go to zero rapidly for potentials below 100 mV. This may be due to the optical effects of the double-layer; these effects have not been considered here.

Use of an effective-medium approximation to model the submonolayer film results in errors significantly larger than those predicted by the effective-film model or the coherent-superposition principle. This indicates that the change in optical response is linear in coverage and wavelength.

At potentials above 160–170 mV, a film with a multilayer thickness is formed (thickness=15.3 Å at -190 mV). Above this potential we have used optical model 9 to interpret the data as a film of crystals on top of an underlayer. For this experiment, the calculated film thicknesses of the underlayer first decreases and later increases after nucleation has occurred. Figure D24 shows the calculated thickness of the secondary crystals versus potential. These reduced results indicate a linear increase in thickness with potential. The growth rate appears to be independent of potential which we believe implies that the rate of incorporation of material into the growing centers is the rate determining step.

The number density of crystals (#/cm^2) can be found from the surface coverage (Ω) and the crystal thickness (r, Å)

$$N_c = \frac{\Omega \times 10^{16}}{\pi r^2} \tag{31D}$$

assuming that the radius (r) of hemispherical particles is equal to the

crystal thickness found by ellipsometry. The reduced data show a decreasing surface coverage as the crystals grow. Using equation 31D with our results gives a number density of growing nuclei that decreases with increasing potential. This decrease in number density was found to occur just after nucleation for all electrochemical experiments that were performed. The calculated porosity of the oxide crystals is approximately 85%. It is not altogether clear whether this value is reliable, since we may be determining an apparent porosity based on the material in the general vicinity of the crystal. Since the crystals do not form in long, planar geometries, the calculated porosity may arise due to an optical averaging of the material. Therefore, we do not wish to assert that our data indicate that the secondary crystals are extremely porous. Other experiments will have to be performed before this conclusion can be made with certainty.

INTERPRETATIONS OF GALVANOSTATIC OPTICAL MEASUREMENTS

As pointed out earlier, the optical changes in galvanostatic experiments occur in two stages representing early thin-film growth (primary layer), and nucleation of surface crystals (secondary crystals). Figure D25 shows the primary-layer initial growth for various current densities. Optical model-fit deviations for the primary layer are approximately equivalent to the random noise in the measurements. The growth of the primary layer is linear with time and increases with current density. This linear dependence may indicate that the growth rate depends only on the total charge passed. The charge corresponding to the amount of material observed at the surface is smaller (10–25%) than the total integrated charge. If the surface film is formed by a side reaction of

constant yield, a linear growth of a surface film would occur under galvanostatic conditions. Potentiostatic results also show growth of the primary layer related to a fraction of the total charge passed.

The relation between the surface concentration and current density for a one-dimensional, constant-flux diffusion from a surface was originally found by Sand [17,20]:

$$C_s = \frac{1.129}{nF} i \sqrt{\frac{t}{D}} . \qquad (32D)$$

Again, in Equation 32D, the transference number and bulk concentration of the diffusing species are assumed to be zero. The surface concentration increases with the square root of time. Initially, the concentration at the surface (and in the electrolyte) is zero. The surface concentration of silver eventually exceeds the saturation value. Nucleation will occur only after the surface concentration is sufficiently supersaturated so that the energy barriers associated with forming an oxide nucleus can be overcome. Figure D26 shows the optical interpretation of the secondary-crystal thickness as a function of time. We note that the induction time for nucleation decreases with increasing current density. This result appears reasonable, since a given degree of supersaturation can be achieved faster with a higher current density. By extrapolating the thickness curves in Figure D26 to zero thickness, we can estimate the time at which nucleation occurs. By use of equation 33D and the nucleation time, we can estimate the degree of supersaturation necessary for nucleation. A calculated value of 23 ± 5 times the saturation value of silver at this pH and temperature ($C(sat)=9.4\times10^{-5}$) [21] has been determined. Literature values for the required degree of

supersaturation have been much lower, namely 2 to 3 times the saturation value [7,22]. This discrepancy is most likely due to the manner of preparation of the electrodes and the sensitivity of the measurement technique.

Figure D26 shows that initially the secondary crystals grow at a constant rate. Later, when the crystals approach a thickness of 1500 to 2000 Å, the growth rate slows considerably. When the surface becomes highly covered with crystals, the optical model predictions start to deviate from the observed spectrum. If a model's errors were to exceed five degrees (averaged over the observed spectrum), the interpretations would be considered invalid. However, most model-fit errors were below 1.5 degrees. Figure D27 shows model 9 predictions of delta and psi together with the measured spectra for a galvanostatic experiment with a current density of 75 $\mu A/cm^2$. Comparison with the substrate spectra shows that the optical properties of the surface have changed significantly, but the model still fits the data well.

During the period just prior to crystallization, the errors of the homogeneous-film model are similar in magnitude to those of the crystal-duplex film model (model 9). The homogeneous-film model interpretation shows large increases in film thickness accompanied by changes in optical constants of the film during the early stages of nucleation. The model 9 interpretation indicates that the surface coverage of the crystals decreases initially, and only later increases after the crystals reach a thickness of around 800 Å. The model 9 interpretations also show a decrease in primary-layer thickness during the onset of nucleation (Figure D28). It may be that the secondary cry-

stal layer grows out of perturbations in the primary layer as the primary layer thickens. This would agree with the ideas put forth by Stranski (see literature review section). Model 9 interpretations also indicate that the secondary crystals that form are hydrated and that the hydration increases during crystal growth. Eventually the calculated hydration reaches 80-90%. However, as pointed out earlier, this result is questionable, since the crystal faces are not always parallel to the substrate. Finally, Figure D26 shows that the initial growth rate of secondary crystals is nearly independent of current density. This again indicates that initially the crystal growth rate is controlled at the interface of the growing center.

Figure D29 shows the ratio of the optically observed surface charge to the total charge passed for an experiment whose current density was 50 $\mu A/cm^2$. Note the increase in the charge observed at the surface at the time of nucleation (refer to Figure D26, curve A). At higher current densities, the charge ratio approaches unity after the onset of nucleation. It appears that a large portion of the dissolved material is returned to the surface as an oxide on nucleation. As mentioned above, the electrolyte near the surface is supersaturated with silver. The surface nuclei, once formed, cannot support the concentration of silver to remain significantly above the supersaturated valve. Therefore, the nuclei act as a sink for products that were previously dissolved into the solution. The apparent porosity has been used in the calculation of the amount of optically observe surface oxide. An error in this quantity could help to also account for the charge ratio being significantly less than one.

Finally, Figure D30 shows the calculated number density of crystals as a function of time for an experiment with a current density of 100 $\mu A/cm^2$. The number density decreases with time. Later, a stable number density is achieved. This phenomenon is believed to be a result of the instability of small oxide clusters. The work of Kappus (see literature review section) supports the idea that small subcritical clusters can redistribute material between themselves. The pulse experiments discussed earlier support the hypothesis that small oxide crystals have a higher activity than larger ones. Therefore, the decrease in number density of growing centers is believed to result from the preferential dissolution of small centers and the incorporation of their oxide material into neighboring larger crystals.

INTERPRETATIONS OF POTENTIOSTATIC OPTICAL MEASUREMENTS

The ellipsometric responses to potential steps for this system fall into two classes; (1) Films containing only a primary layer and (2) Complex films with nucleated secondary crystals. The current transients for these experiments have been discussed above in Chapter 3, and in the section on modeling of current responses in Chapter 4. Primary film growth can be subdivided into submonolayer and multilayer films. Figure D31 shows the thickness of the primary layer (homogeneous film model) versus the square root of time for a number of different potential step experiments. A linear relation is observed between the film thickness and the square root of time. The growth rate constant (Å $sec^{-1/2}$) increases from approximately zero to 1.25 in the potential range between 160 to 190 mV. For multilayer films, an extrapolated 4-5 Å film is found at zero time. This may be due to a very rapid increase in

coverage by the reaction intermediates and products until the surface is completely covered with a monolayer. After this initial period a slow growth of the primary layer is observed. For potential steps below 160 mV, submonolayer film thickness are observed that do not change significantly after the initial potential change. Spectroscopic ellipsometry data were collected for 10 minutes after the initial potential step.

Current transients for potential step experiments give linear plots of charge versus square root of time. Since the growth of the oxide is also linear versus square root of time, the primary films growth may be due to a parallel side reaction. Two adsorbed oxygenated silver atoms could combine to form silver oxide at the surface. These adsorbed species may also be the precurser species to the dissolution product. At potential where multilayer films form, the initial coverage of oxygenated silver may be large enough to allow such a cocurrent surface reaction. Only a small fraction of the total charge passed appears in the form of a surface oxide. These interpretations are in agreement with the interpretations of the other experiments preformed for this thesis.

In one experiment, as described in Chapter 3, a series of potential steps from −50 mV to 190, 190 to 210, and 210 and 230 mV was applied to a clean electrode so as to determine the effect of subsequent growth of the primary layer to a step change in potential. Figure D32 show the calculated film thickness (homogeneous film model) for two subsequent potential steps (−50 mV to 190 mV and 190 mV to 210 mV). Nucleation of secondary crystals has not occurred after the second potential pulse. When this potential is applied in one potential step, nucleation is

observed. Clearly, the primary layer grown in this way has suppressed nucleation. This may be due to a finite diffusion/electrical resistance across the primary layer. Figure D33 shows the thickness of the primary layer versus square root time. The second pulse time is taken as the time after the second pulse is applied. Empirically, these results can be expressed as

$$T = T_1 + k_1\sqrt{t} \qquad t < t_1 \tag{33D}$$

$$T = T_1 + k_1\sqrt{t_1} + k_2\sqrt{t-t_1} \qquad t > t_1 \tag{34D}$$

where T is the film thickness, t_1 is the time at which the second potential pulse is made and T_1, k_1, and k_2 are constants. While k_1 and k_2 appear to be approximately the same for the results show in Figure D33, this is probably only a coincidence. More experimental results are needed to determine the various dependence of these growth constants. However, these results support the conclusion that primary film growth may be a side reaction of the dissolution process.

Crystalization of the anodic products is observed for potentials above 200 mV. Figure D34 shows the secondary crystal thickness growth for a number of different potential step experiments. The model interpreted results show scatter. Films formed at higher potential show relatively large errors between model predicted and observed results. The crystal film growth rate is not a strong function of potential. This is similar to the conclusion reached for the galvanostatic case. However, the growth of secondary crystals under potentiostatic conditions appears to be smaller than that of the galvanostatic case (approx-

imately 21 A/sec. vs. 28 A/sec.). As with the galvanostatic data at the time of nucleation of secondary crystals, it is difficult to optically distinguish between the interpreted results of the homogeneous film model and the dual film model at early times in the potentiostatic experiments. While the film appear to be an outgrowth of an initially homogeneous primary layer, at the time when nucleation occurs the ellipsometric data gives equally good interpretations using either model 0 and model 9. This phenomenon may be attributed to the small size of the initial growing surface features, which appear as a homogeneous film because their size is much smaller than the wavelength of the incident light. However, all of our results discussed above have indicated that the initial crystals form from an initially homogeneous film. At later times in these potentiostatic experiment the calculated surface coverage of the secondary crystals decreases. We therefore have interpreted the early results as being a homogeneous film which later becomes a duplex film represented by model 9.

While the growth rate of the secondary crystals does not appear to be a strong function of potential, the number density of crystals derived from ellipsometric results and SEM observations increases markedly with potential. We believe that it is this increase in the numbers of growing centers, rather than the increase in the rate of growth of the crystals, that is mainly responsible for increases in current at higher potentials.

Figures D35 and D36 show the calculated and observed spectra for a film formed at 200 mV for 140 seconds (charge=13.1 mC/cm^2). This is the lowest potential where nucleation of secondary crystals is observed.

The model spectra are very close to the observed spectra. In general, films formed at at lower current densities or lower potentials show better model fits. This is believed to be due to the smaller degree of light scattering and shadowing of surface features in films with fewer protrusions. The primary layer film thickness derived from model 0 and model 9 is shown in Figure D37 as a function of time for a potentiostatic experiment performed at 200 mV. The primary layer thickness is seen to decrease after the thickness has reach 150 A. This is the point where the dual film model is used (model 9) to interpret the data. Figure D38 shows the secondary crystal thickness versus time for the same experiment. The initial secondary crystals thickness is only slightly larger than the maximum primary layer thickness. The surface coverage versus time is seen in Figure D39. The fractional surface coverage by crystals decrease greatly right after the formation of the secondary crystals. Finally, the calculated void fraction of the secondary crystals is shown in Figure D40. These results indicate the following:

1. The surface coverage of the crystals decrease rapidly during the early growth stage. Later, the surface coverage increases slowly with time.

2. The calculated porousity decrease rapidly after the early growth stage.

3. The apparent induction time for formation of surface crystals is due to the formation of an underlayer which acts as a precurser to the formation of the surface crystals.

Using the results of potentiostatic experiments, the calculated number

density (eq. 32D) of surface crystals is seen to decrease greatly during early crystal growth for potentiostatic experiments. Finally, the calculated number density of surface crystals compares reasonably well with those observed from SEM photographs. In Table D2 calculated results from SEM and Ellipsometric observations are compared for a number of experiments.

CONCLUSIONS

The primary current distribution over the electrode surface has been shown to be uniform over the surface area where the ellipsometer probes. Therefore, it is reasonable to assume that the growth of the film layers is also uniform over the same area.

Spectroscopic ellipsometry can be used to determine both the amount and the morphology of surface films. Films which contain equal amounts of surface material but have that material physically arranged differently yield ellipsometric spectra which are significantly different.

A homogeneous, isotropic film model accurately predicts the optical properties of films which form initially on oxidation of silver (111) surfaces in 1M KOH for a variety of different types of electrochemical experiments. Submonolayer films form for potentials below 160 mV. These films do not show any clearly defined adsorption sites, and may obey simple two dimensional phase thermodynamics. A homogeneous multilayer film forms at potentials between 160 to 190 mV. The film obey a linear growth law under galvanostatic conditions (constant flux), and a parabolic growth law under potentiostatic conditions (constant surface concentration). As the surface concentration approaches 23 times the

saturation value of silver under the conditions studies, large surface crystals (secondary crystals) are observed to form.

Secondary crystal appears to form as an outgrowth of the initially formed primary layer. The initial growth rate of secondary crystals is constant for both potentiostatic and galvanostatic experiments. The growth rate is slightly larger under the galvanostatic condition. The optically observed charge contained in the surface film increase greatly in galvanostatic experiments after the nucleation of secondary crystals.

The secondary crystals play a dual role in the oxidation process of silver. Initially, oxide crystals act as sinks to the ionic products that are formed at the surface. Under equilibrium conditions, the solution at the crystal/electrolyte phase boundary is saturated. Diffusion to these growth centers can be much greater than diffusion into a semi-infinite medium due to the very short distances involved. The rate of diffusion to the growing centers does not appear to be the controlling process. Either a chemical reaction at the oxide surface (forming the oxide product) or the rate of lattice building appear to control the overall rate of the oxidation. Later, as the oxide crystals grow and cover a large portion of the surface, they act as a passive film, offering a finite electrical and diffusion resistances to oxidation.

REFERENCES FOR CHAPTER 4

1. Farmer, Joseph C., Ph. D. thesis, Dept. of Chemical Engineering, University of California, Berkeley, March 1983. LBL-15607.

2. Farmer, Joseph C. and Rolf H. Muller, J. Electrochem. Soc. 132 (1985) 39.

3. Drude, P., Ann. Phys. Chem., N.F. 36 (1889) 865.

4. Somorjai, G. A., Chemistry in Two Dimensions Cornell University Press, Ithica, N.Y., 1981. p 79-81.

5. Bootsma, G. A. and F. Meyer, Surface Science. 14 (1969) 52.

6. Smith, Craig G., M. S. thesis, Dept. of Chemical Engineering, University of California, Berkeley, 1975.

7. Smith, Craig G., Ph. D. thesis, Dept. of Chemical Engineering, University of California, Berkeley, August 1978. LBL-8082.

8. Muller, Rolf H. and Craig G. Smith, Surface Science. 96 (1980) 375.

9. Schwager, F., Y. Geronov and R. H. Muller. J. Electrochem. Soc. 132 (1985) 285.

10. Bruggeman, D. A. G., Ann. Phys. (Leipzig). 24 (1935) 636.

11. Maxwell Garnett, J. C., Philos. Trans. R. Soc. London. 203 (1904) 385.

12. Aspens, D. E., E Kinsbron and D. D. Bacon, Phys. Rev. B. 21 (1980) 3290.

13. Aspens, D. E., J. B. Theeten and E Hottier, Phys. Rev. B. 20 (1979) 3292.

14. Stroud, D., Phys. Rev. B. 12 (1975) 3368.

15. Mayer, Steven T., M.S. thesis, Dept. of Chemical Engineering, University of California, Berkeley. Appendix. To be published. LBL-20677.

16. Cottrell, F. G., Z. Physik. Chem. 43 (1902) 385.

17. Bard, Allen J. and Larry R. Faulkner. Electrochemical Methods; Fundamentals and Applications. John Wiley and Sons, Inc., 1980.

18. Giles, R. D., J. A. Harrison and H. R. Thirsk, J. Electroanal. Chem. 22 (1969) 375.

19. Bennett, H. E. , D. K. Bruge, R. C. Peck, and J. M. Bennett, J. Opt. Soc. 59 (1969) 675.

20. Sand, H. J., Phil Mag. 6 (1901) 45.

21. Pound, Bruce G., Digby D. MacDonald and John W. Tomlinson, Electrochim. Acta. 24 (1979) 929.

22. Miller, B., J. Electrochem. Soc. 117 (1970) 491.

23. Azzam, R. M. A., and N. M. Bashard. Ellipsometry and Polarized Light. North-Holland Publishing Company, 1977. p. 340.

TABLE D1

Optical Models Proposed To Reproduce
The Spectroscopic Ellipsometry Measurements

Model Number (# of parameter)	Primary Layer	Secondary Layer
0(3)	compact film with variable n and k	none
1(2)	porous oxide film (solution and oxide)	none
2(2)	microroughness (solution and substrate)	none
3(4)	microroughness (solution and substrate)	porous oxide
4(4)	microroughness (oxide and substrate)	porous oxide
5(2)	none	island oxide
6(3)	compact oxide film	island oxide
7(4)	porous oxide film	island oxide attached to the surface
8(5)	porous oxide film	island oxide with a non-absorbing boundary layer above.
9(4)	compact oxide film	porous island oxide
A(3)	none	statistical variation of the island oxide thickness
B(4)	compact oxide film	statistical variation of the island oxide thickness
C(5)	compact oxide film	statistical variation of the island oxide thickness with a non-absorbing boundary layer above
Q(5)	compact oxide film	statistical variation of the porous island oxide thickness

TABLE D2

Comparison of Calculated And Observed Number Densities Made By Spectroscopic Ellipsometry and Scanning Electron Microscopy

Experimental Conditions	Number Density (Ellipsometry)	Number Density (SEM)
Potential Step 220 mV 131 seconds	5.4×10^8	3.4×10^8
Potential Step 200 mV 175 seconds	4.5×10^8	2.9×10^8
Potential Step 200 mV 285 seconds	4.3×10^8	2.1×10^8
Constant Current 75 $\mu A/cm^2$ 220 seconds	3.1×10^8	1.9×10^8
Constant Current 100 $\mu A/cm^2$ 235 seconds	3.2×10^8	—
Constant Current 200 $\mu A/cm^2$ 106 seconds	6.8×10^8	4.0×10^8

FIGURE CAPTIONS FOR CHAPTER 4

D1. Results of a finite difference calculation of the primary current distribution for the electrochemical cell used in this study.

D2. Effective media model calculations of the refractive index of a silver oxide/water composite versus void fraction. 1) Lorentz-Lorentz model. 2) Maxwell-Garnett model (oxide as host), Maxwell-Garnett model (water as host) and Bruggeman effective media approximation.

D3. Effective media model calculations of the extinction coefficient of a silver oxide/water composite versus void fraction. 1) Lorentz-Lorentz model. 2) Maxwell-Garnett model (water as host). 3) Bruggeman effective media approximation. 4) Maxwell-Garnett model (oxide as host).

D4. Artist representations of the various models proposed to reproduce the observed spectra.

D5. Artist representations of the various models proposed to reproduce the observed spectra. (Continued).

D6. Delta calculated spectra for the homogeneous film model (Model 0). 1) 600 Å film. 2) 450 Å. 3) 300 Å. 4) 150 Å. 5) substrate.

D7. Psi calculated spectra for the homogeneous film model (Model 0). 1) 600 Å film. 2) 450 Å. 3) 300 Å. 4) 150 Å. 5) substrate.

D8. Delta calculated spectra for a 600 Å film of various void fractions. (Model 1). Bruggeman effective media approximation was used to determine the optical properties of the film at different void fractions. 1) 100% oxide. 2) 75% oxide, 25% water. 3) 50% oxide, 50% water. 4) 25% oxide, 75% water. 5) substrate.

D9. Psi calculated spectra for a 600 Å film of various void fractions. (Model 1). Bruggeman effective media approximation was used to determine the optical properties of the film at different void fractions. 1) 100% oxide. 2) 75% oxide, 25% water. 3) 50% oxide, 50% water. 4) 25% oxide, 75% water. 5) substrate.

D10. Delta calculated spectra for a 600 Å island film (Model 5). 1) 100% surface coverage. 2) 75% surface coverage. 3) 50% surface coverage. 4) 25% surface coverage. 5) substrate.

D11. Psi calculated spectra for a 600 Å island film (Model 5). 1) 100% surface coverage. 2) 75% surface coverage. 3) 50% surface coverage. 4) 25% surface coverage. 5) substrate.

D12. Comparison of various delta model calculations of films containing the same amount of surface oxide. 0) Homogeneous film (model 0), 150 Å. 1) Porous film (model 1), 600 A, 25% oxide. 3) Island film model (model 5), 600 Å, 25% coverage.

D13. Comparison of various psi model calculations of films containing the same amount of surface oxide. 0) Homogeneous film (model 0), 150 Å. 1) Porous film (model 1), 600 Å, 25% oxide. 3) Island film model (model 5), 600 Å, 25% coverage.

D14. Psi calculated spectra for a statistically distributed island film model (Model A). Average island oxide film thickness = 600 Å, island oxide coverage = 50%. 1) Standard deviation = 200 Å. 2) Standard deviation = 100 Å. 3) Standard deviation = 0 Å.

D15. Model error calculations versus file number for a galvanostatic experiment, 0.2 mA/cm^2.

D16. Charge versus root time for a potential step experiment.

D17. Natural log of the surface concentration versus potential determined by a series of potential step experiments.

D18. Calculated current response for the dissolution/precipitation model presented in the text. Effects of changes in the crystal incorporation current density. Surface concentration = 1.25×10^{-3} M, surface crystal number density = 3.0×10^{8}. 1) incorporation current density = 0.5 mA/cm^2. 2) incorporation current density = 0.375 mA/cm^2. 3) incorporation current density = 0.25 mA/cm^2.

D19. Same as D18. Effects of changes in crystal number density. Surface concentration = 2.50×10^{-3} M, crystal incorporation current density = 0.375 mA/cm^2. 1) surface crystal number density = 3.0×10^{8}. 2) surface crystal number density = 2.0×10^{8}. 3) surface crystal number density = 1.0×10^{8}.

D20. Same as D18. Effects of changes in surface concentration. Crystal incorporation density = 0.375 mA/cm^2, surface crystal number density = 3.0×10^{8}. 1) Surface concentration = 3.75×10^{-3} M. 2) Surface concentration = 2.50×10^{-3} M. 3) Surface concentration = 1.25×10^{-3}.

D21. Optimized equivalent film thickness (model 0) versus potential for a potential sweep experiment (0.5 mV/sec).

D22. Optimized refractive index of an equivalent film (model 0) versus potential for a potential sweep experiment (0.5 mV/sec).

D23. Optimized surface coverage (model 5) versus potential for a potential sweep experiment (0.5 mV/sec). Optical properties of the monolayer were given by the optical properties of the multilayer film that formed at a higher potentials.

D24. Optimized values of the secondary crystal thickness versus potential for a potential sweep experiment (0.5 mV/sec).

D25. Optimized values of primary layer thickness versus time for galvanostatic experiments. A) 50 $\mu A/cm^2$. B) 75 $\mu A/cm^2$. C) 100 $\mu A/cm^2$. D) 125 $\mu A/cm^2$. E) 150 $\mu A/cm^2$. F) 175 mA/cm^2. G) 200 $\mu A/cm^2$.

D26. Optimized values of secondary crystal thickness versus time for galvanostatic experiments. A) 50 $\mu A/cm^2$. B) 75 $\mu A/cm^2$. C) 100 $\mu A/cm^2$. D) 200 $\mu A/cm^2$.

D27. Measured and optimized spectra (model 9) of a Ag(111) surface galvanostatically anodized at 75 $\mu A/cm^2$ for 208 seconds (electrochemical charge 15.6 mC/cm^2). 1) Substrate spectra. 2) Measured and optimized spectra.

D28. Optimized values of the primary layer thickness versus time for a galvanostatic experiment (75 $\mu A/cm^2$).

D29. Ratio of optically observed surface charge to electrochemical charge passed (integral value). This quantity represent the

fraction of the total amount of material oxidized which is present as a surface oxide.

D30. Calculated number density of surface crystals (from optimized ellipsometric parameters) versus time for a galvanostatic experiment (100 $\mu A/cm^2$).

D31. Optimized primary layer thickness (model 0) versus root time for various potential steps. 1) 160 mV. 2) 170 mV. 3) 190 mV.

D32. Optimized primary layer thickness (model 0) versus time for two subsequent potential steps (−50 to 190 mV and 190 to 210 mV).

D33. Optimized primary layer thickness (model 0) fit to equations 33D and 34D for two subsequent potential steps (−50 to 190 mV and 190 to 210 mV). The time axis refers to the time elapsed since the last potential step was made.

D34. Optimized secondary crystal thickness versus time for various potential step experiments. A) 200 mV. B) 210 mV. C) 220 mV.

D35. Calculated and observed delta spectra for a potential step to 200 mV (141 seconds, electrochemical charge passed 12.7 mC/cm^2).

D36. Same as Figure D35 except Psi calculated and measured spectra are given.

D37. Calculated primary layer thickness versus time for a potential step experiment for 200 mV.

D38. Calculated secondary crystal thickness versus time for a potential step experiment for 200 mV.

D39. Calculated surface coverage of secondary crystal versus time for a potential step experiment for 200 mV.

D40. Calculated fraction oxide is the secondary crystals versus time for a potential step experiment for 200 mV.

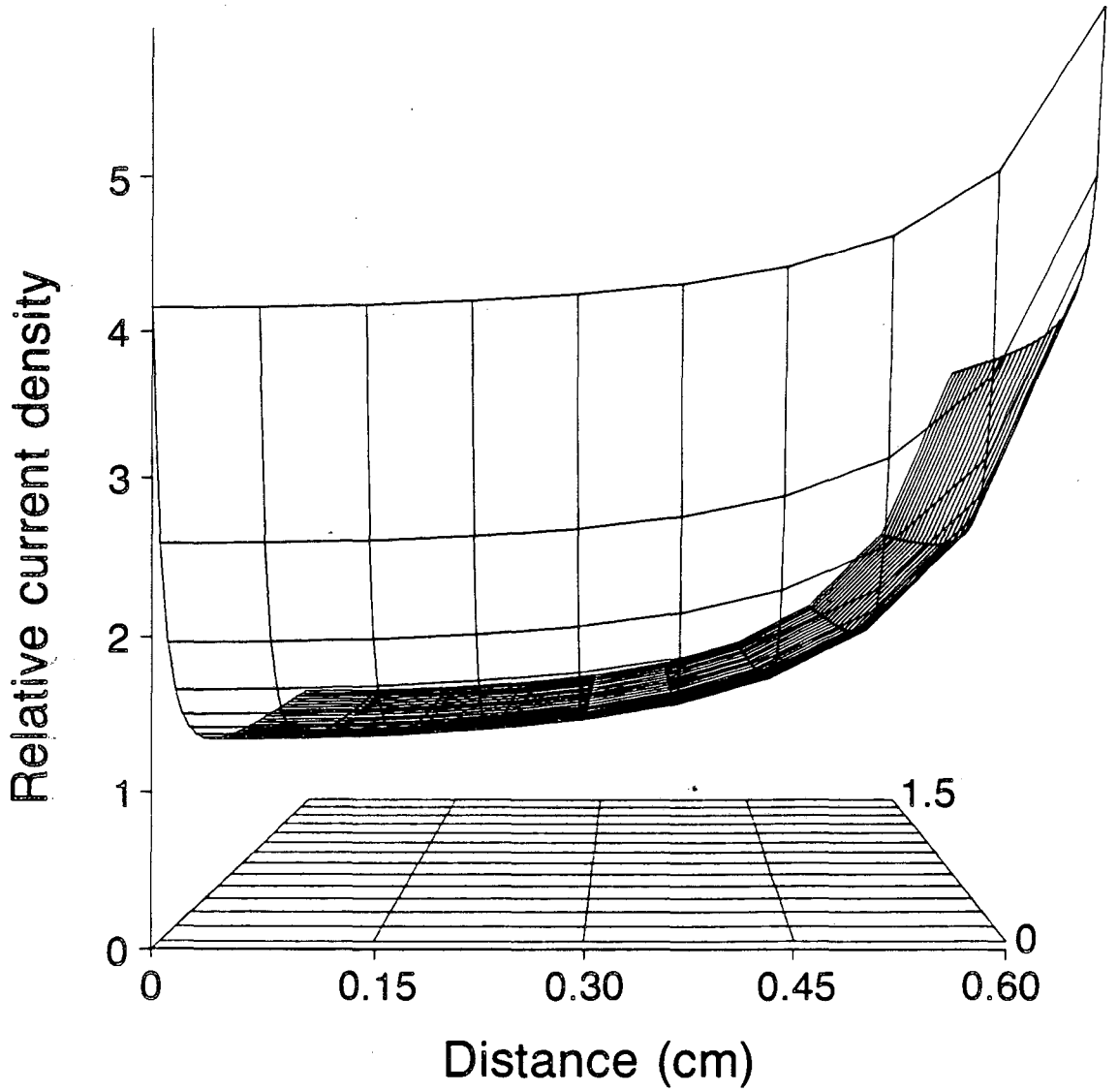

XBL 8511-11556

Figure D1

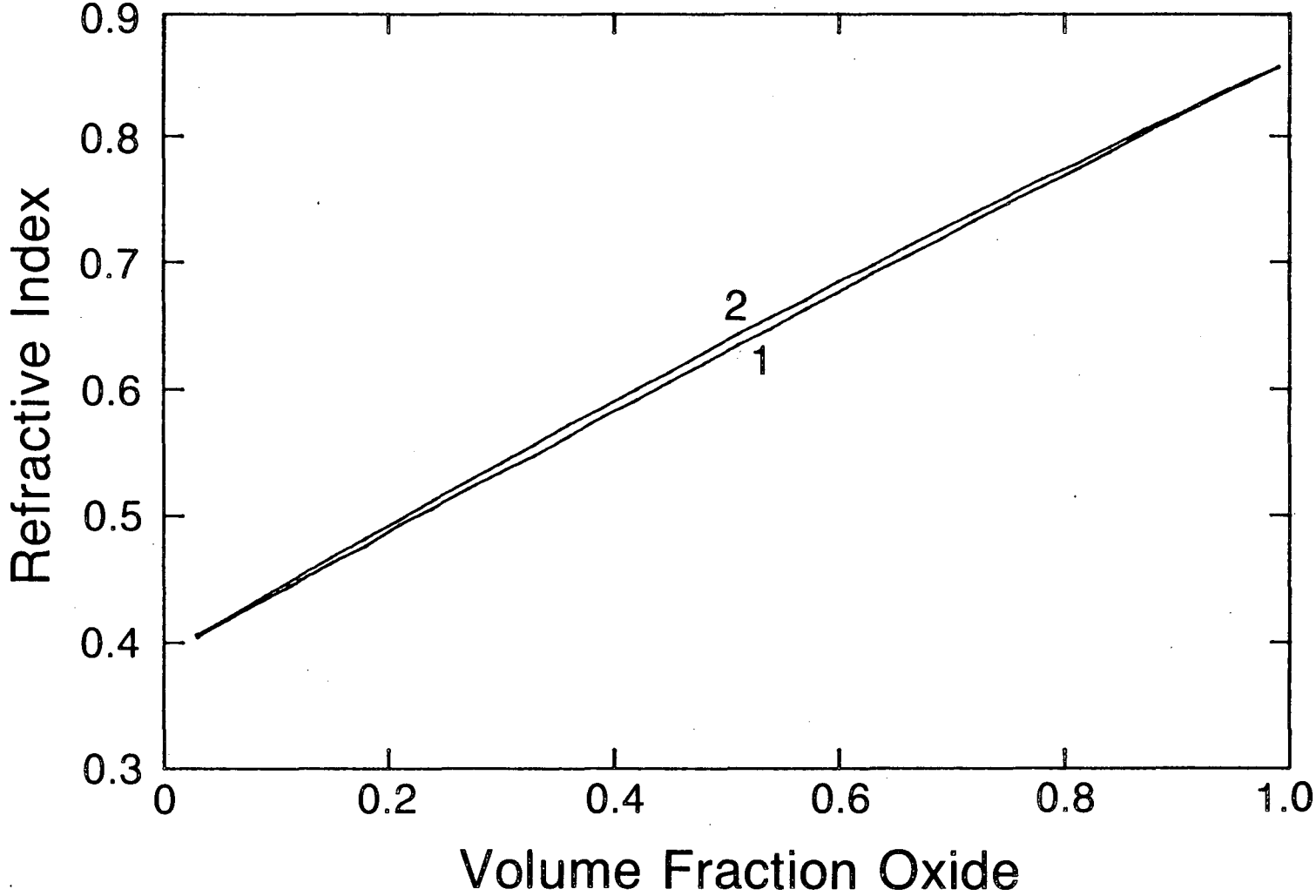

XBL 8511-11501

Figure D2

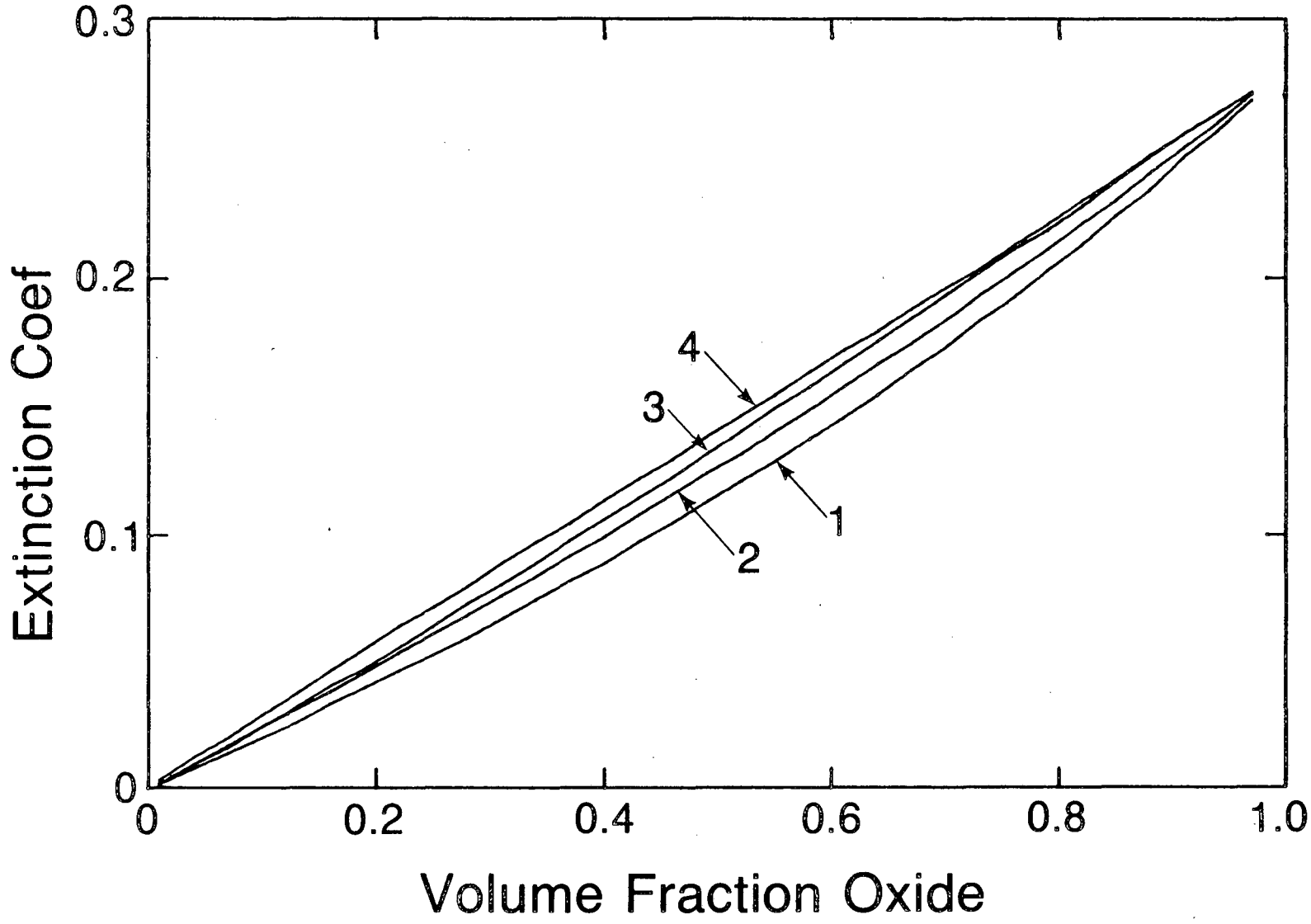

XBL 8511-11504

Figure D3

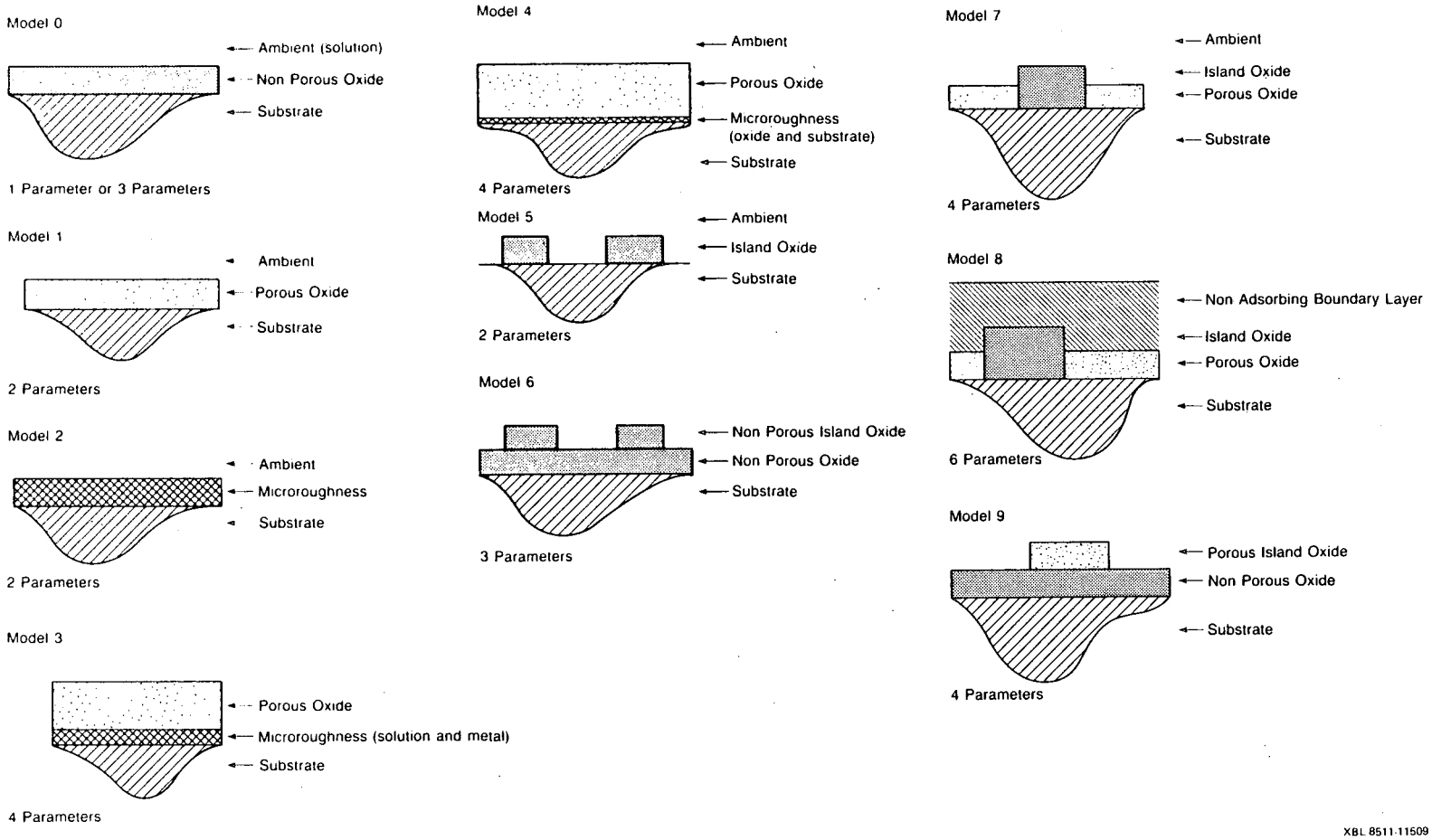
Model 0
Ambient (solution)
Non Porous Oxide
Substrate
1 Parameter or 3 Parameters
Model 1
Ambient
Porous Oxide
Substrate
2 Parameters
Model 2
Ambient
Microroughness
Substrate
2 Parameters
Model 3
Porous Oxide
Microroughness (solution and metal)
Substrate
4 Parameters
Model 4
Ambient
Porous Oxide
Microroughness
(oxide and substrate)
Substrate
4 Parameters
Model 5
Ambient
Island Oxide
Substrate
2 Parameters
Model 6
Non Porous Island Oxide
Non Porous Oxide
Substrate
3 Parameters
Model 7
Ambient
Island Oxide
Porous Oxide
Substrate
4 Parameters
Model 8
Non Adsorbing Boundary Layer
Island Oxide
Porous Oxide
Substrate
6 Parameters
Model 9
Porous Island Oxide
Non Porous Oxide
Substrate
4 Parameters
XBL 8511-11509

Figure D4

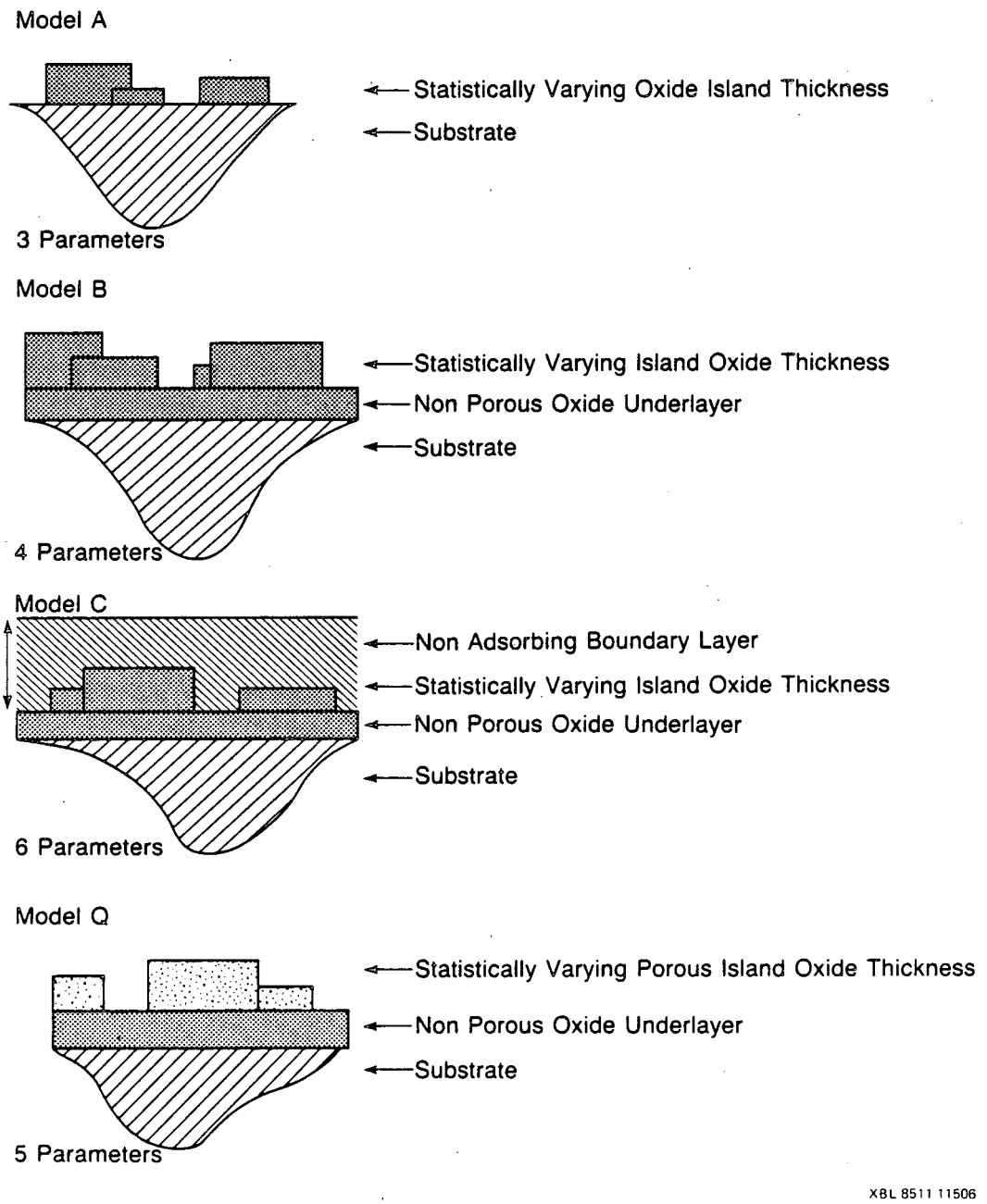
Model A
Statistically Varying Oxide Island Thickness
Substrate
3 Parameters
Model B
Statistically Varying Island Oxide Thickness
Non Porous Oxide Underlayer
Substrate
4 Parameters
Model C
Non Adsorbing Boundary Layer
Statistically Varying Island Oxide Thickness
Non Porous Oxide Underlayer
Substrate
6 Parameters
Model Q
Statistically Varying Porous Island Oxide Thickness
Non Porous Oxide Underlayer
Substrate
5 Parameters
XBL 8511 11506

Figure D5

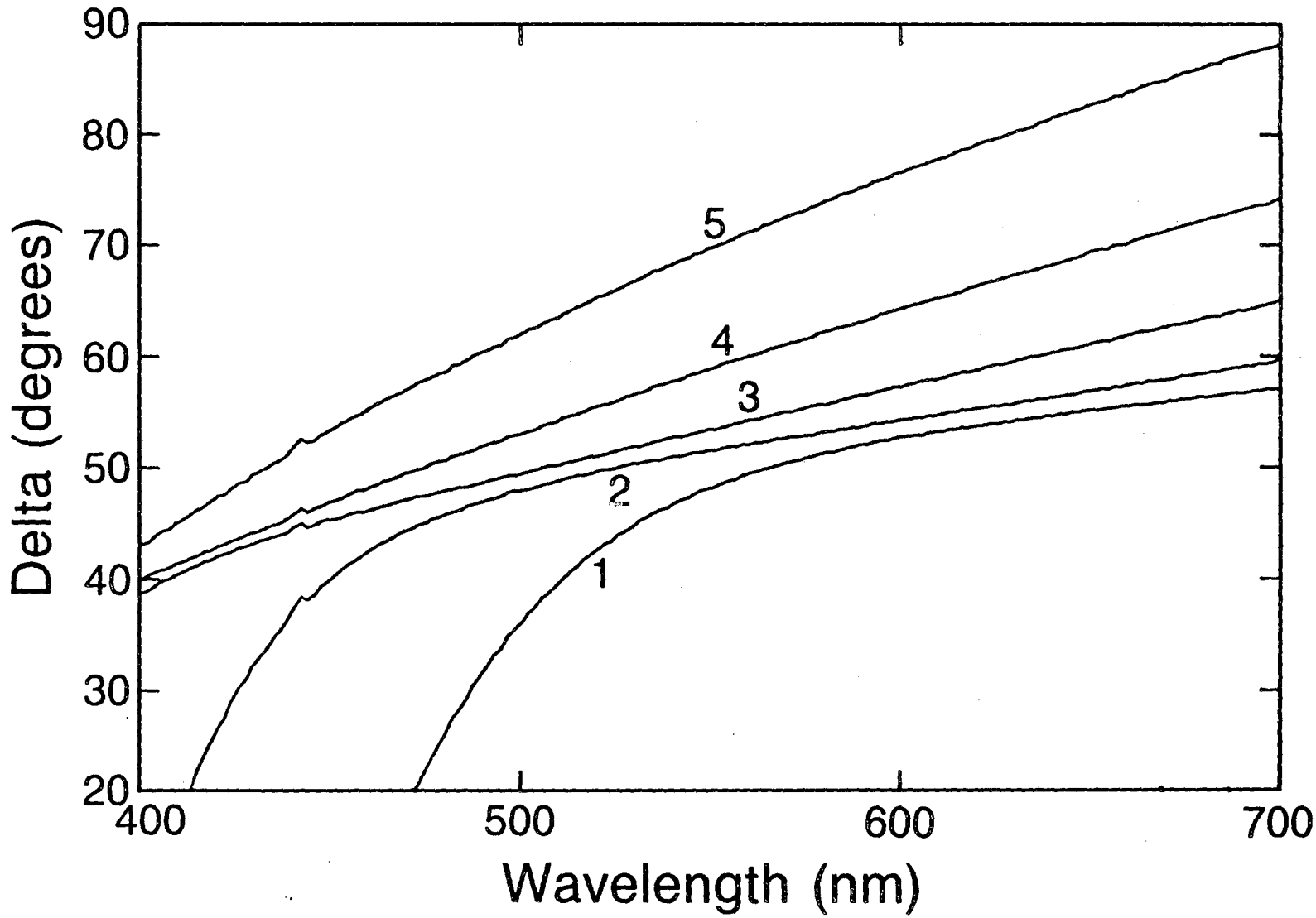

FIGURE D6

XBL 8511-11490

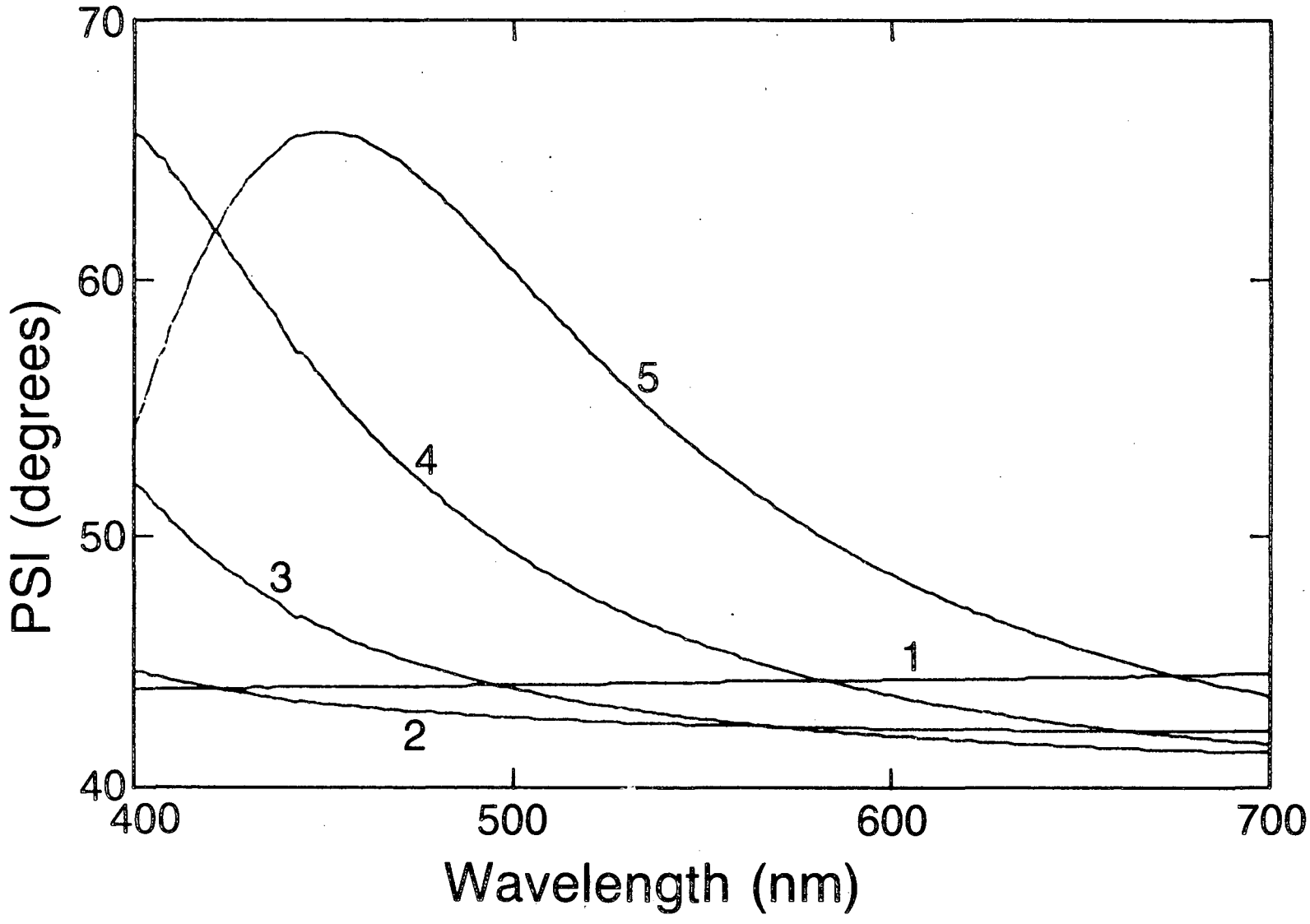

XBL 8511-11491

FIGURE D7

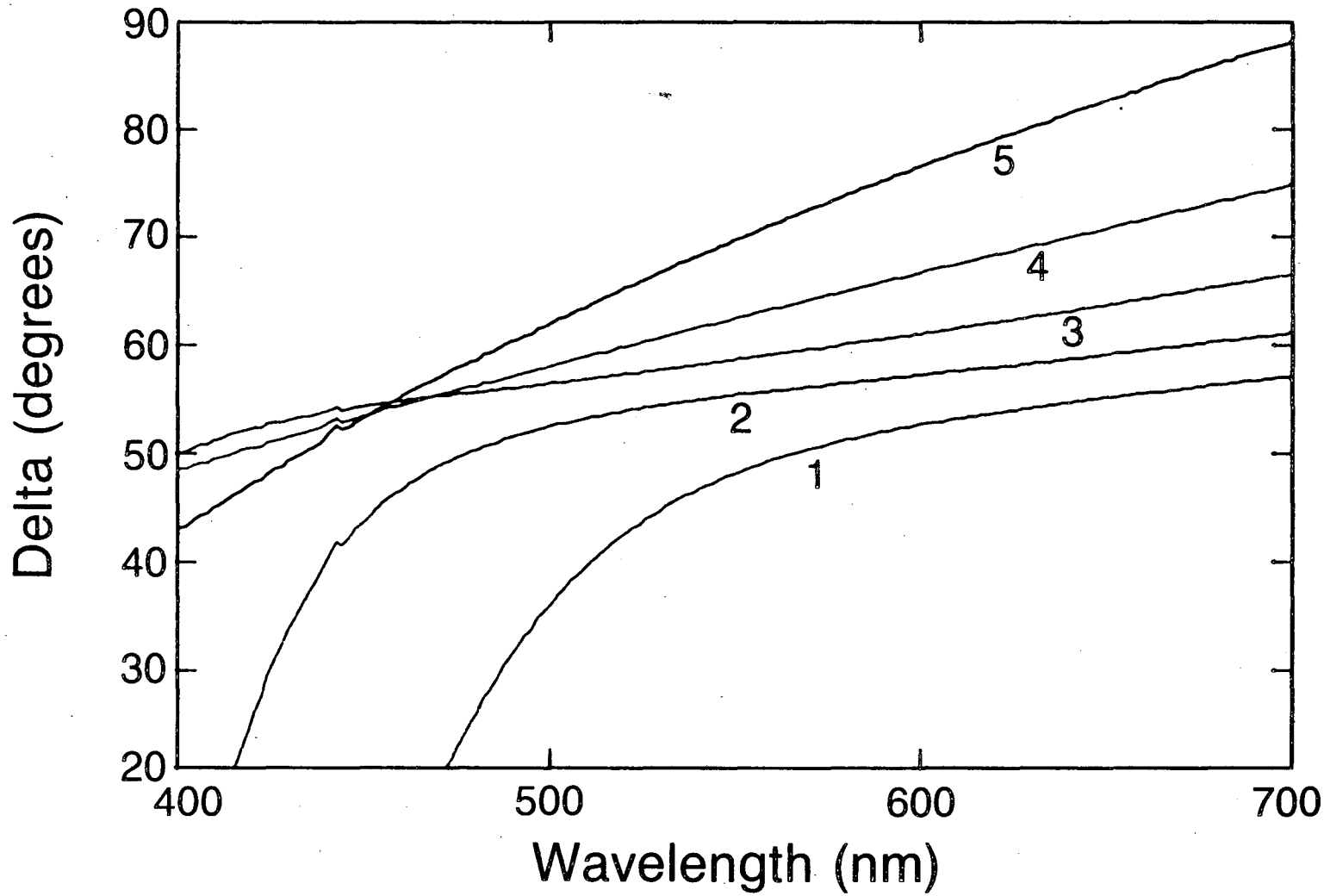

XBL 8511-11492

FIGURE D8

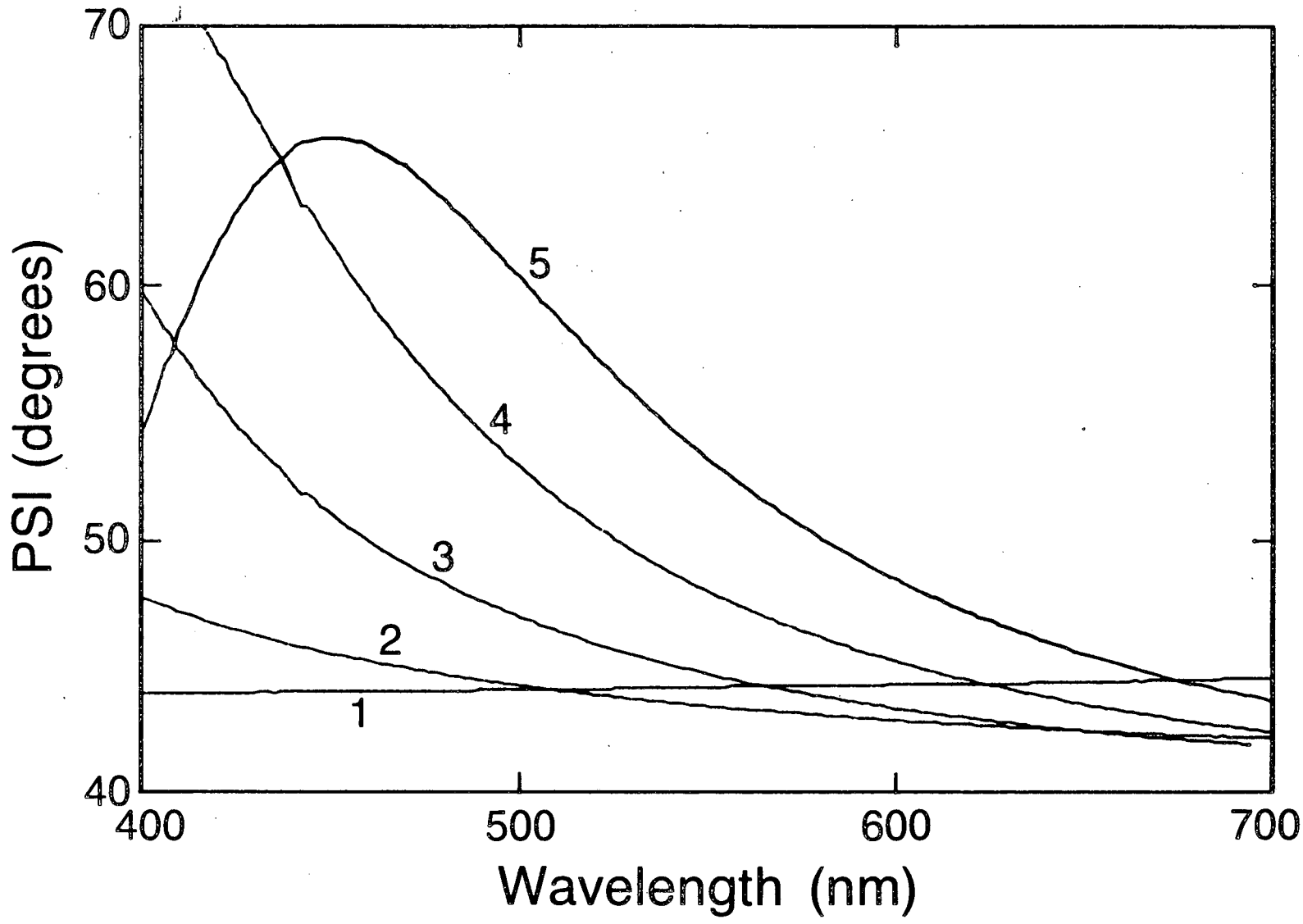

XBL 8511-11493

FIGURE D9

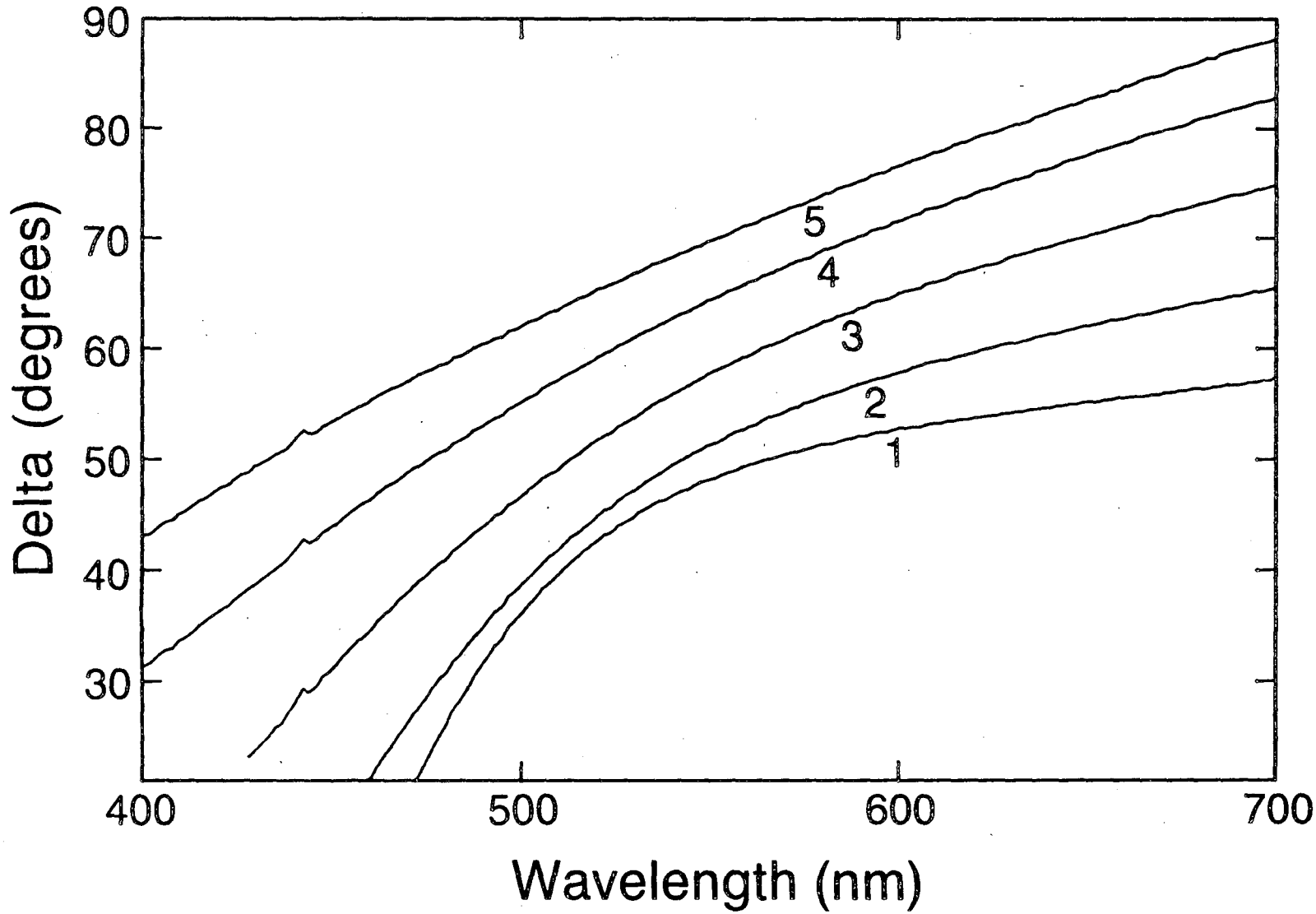

XBL 8511-11502

FIGURE D10.

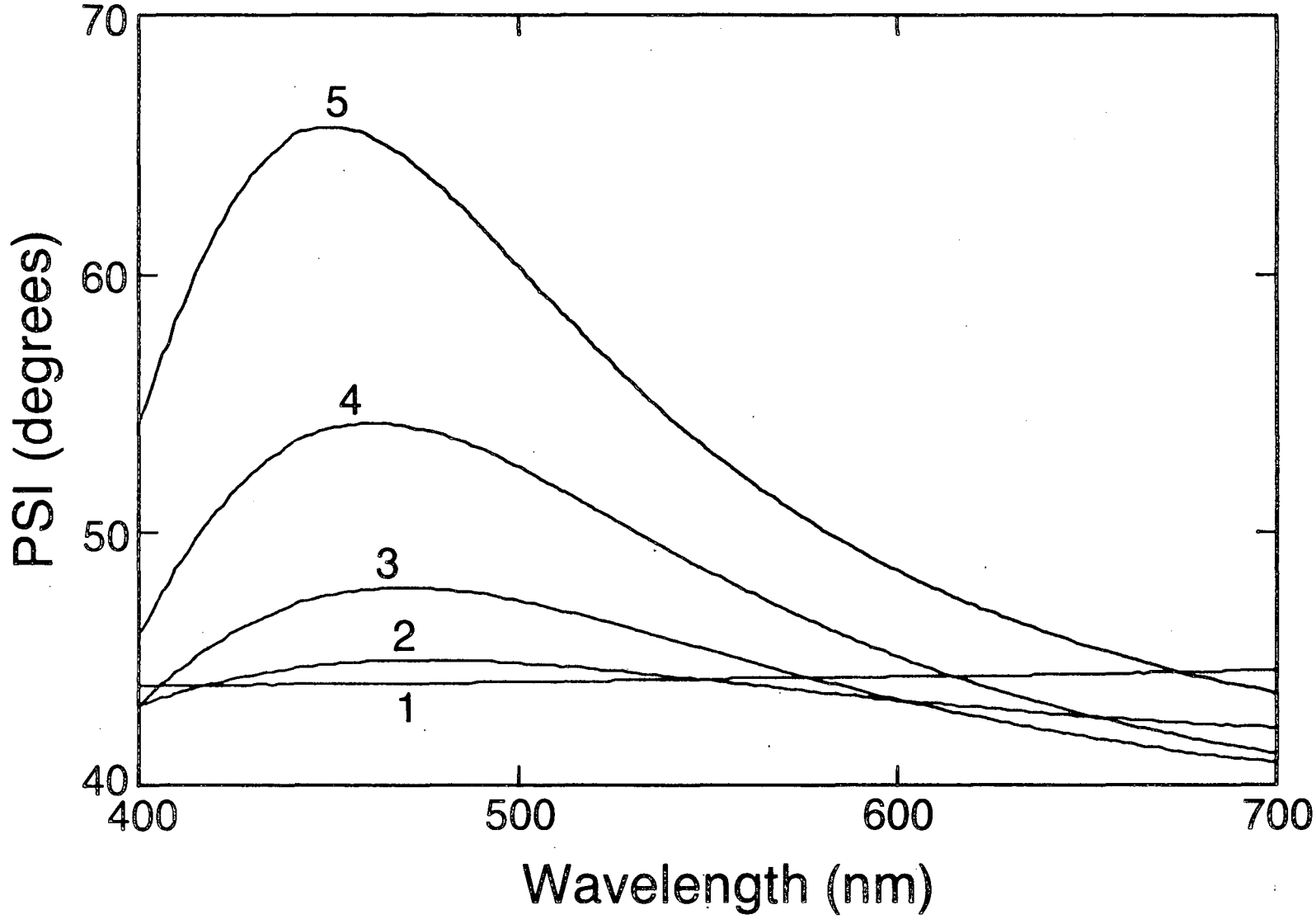

XBL 8511-11498

FIGURE D11

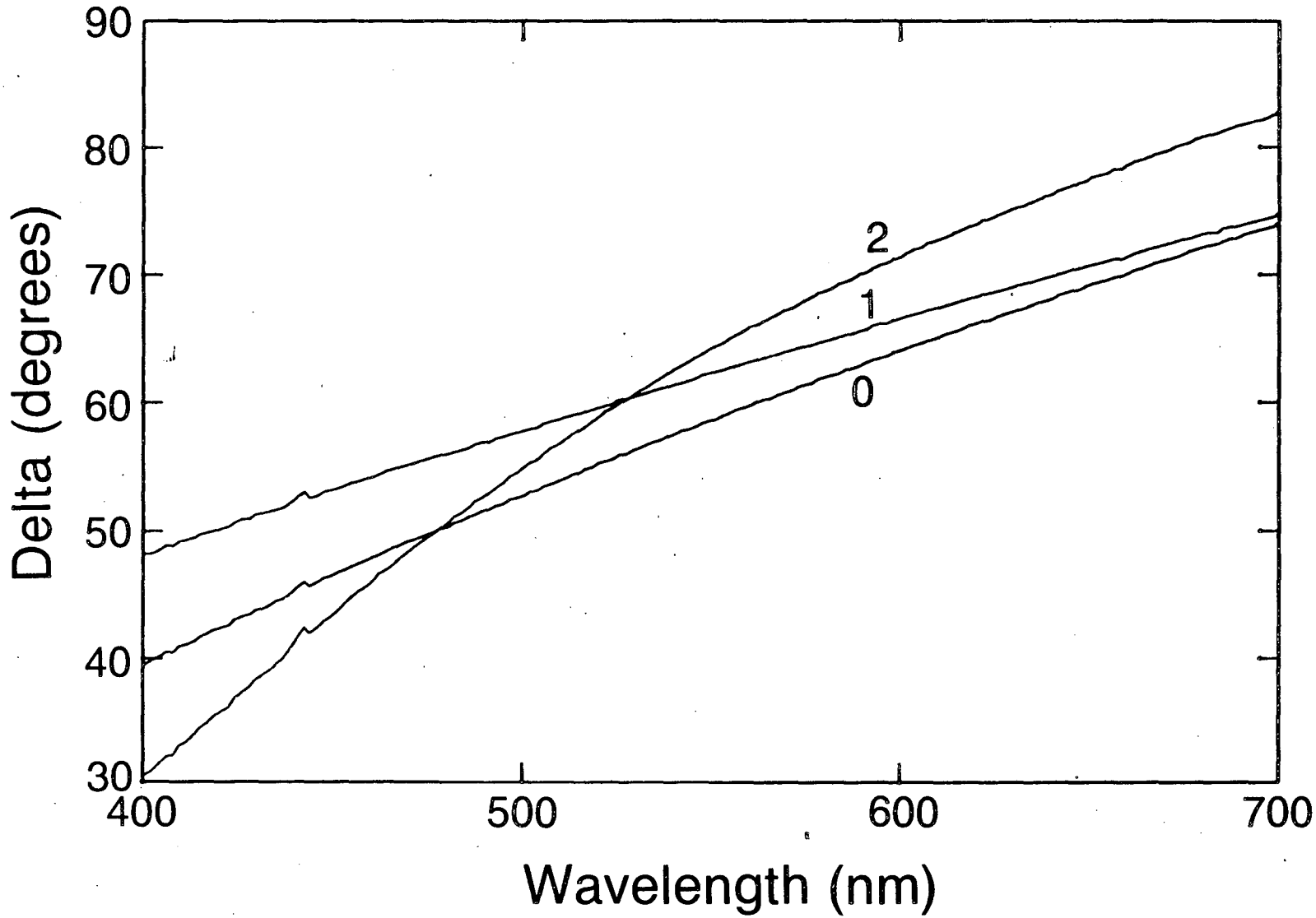

XBL 8511-11500

FIGURE D12

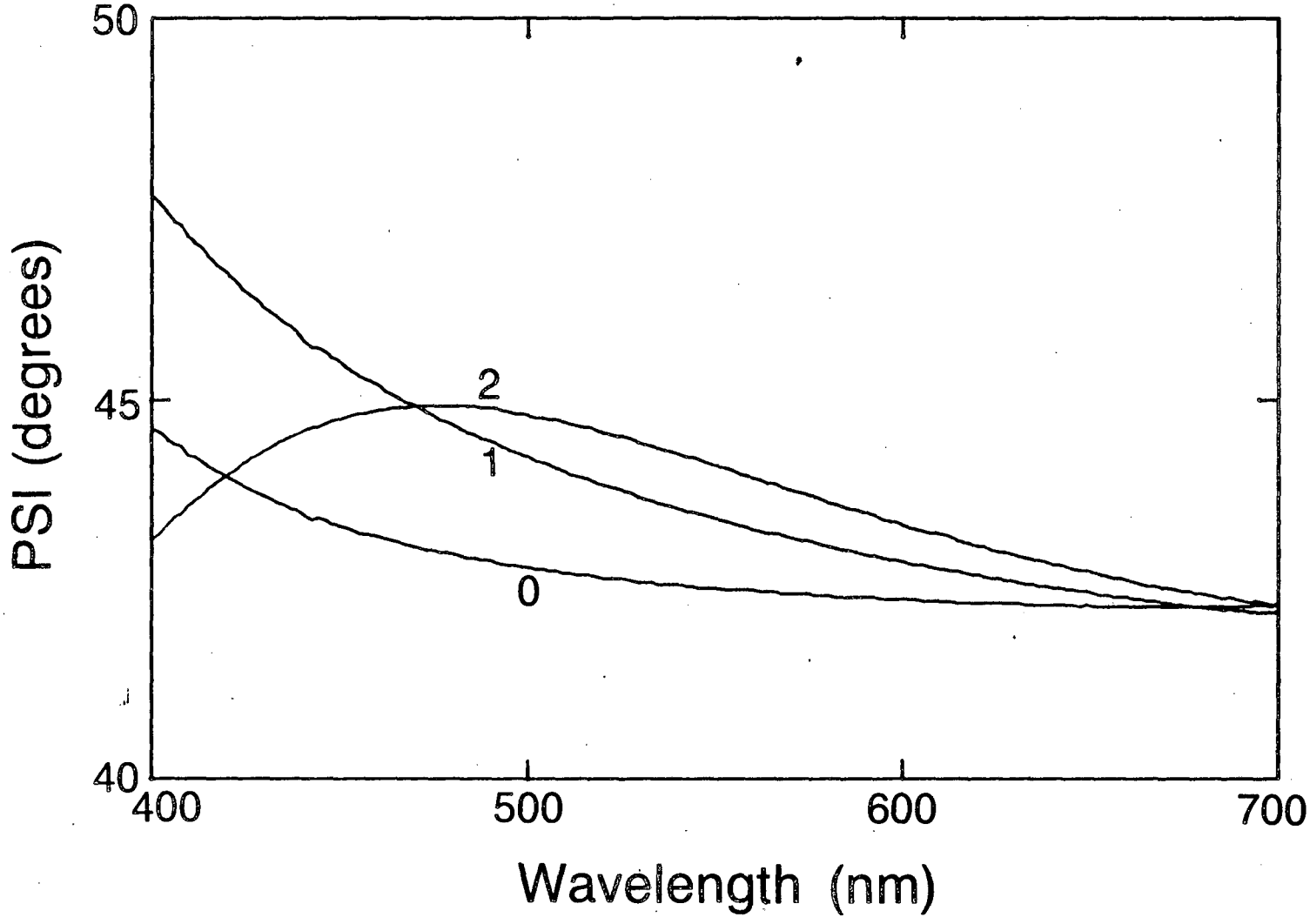

FIGURE D13

XBL 8511-11505

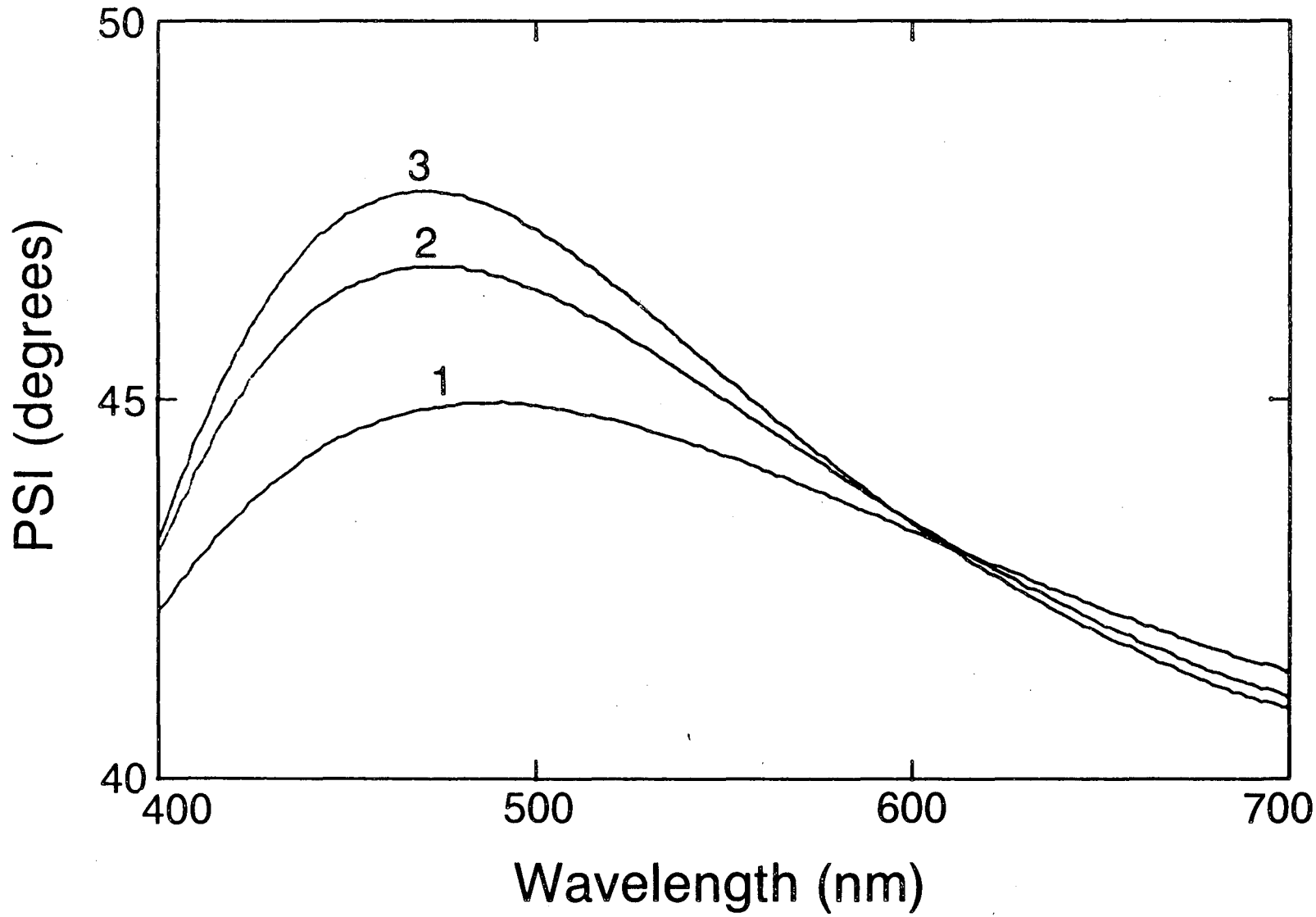

FIGURE D14

XBL 8511-11503

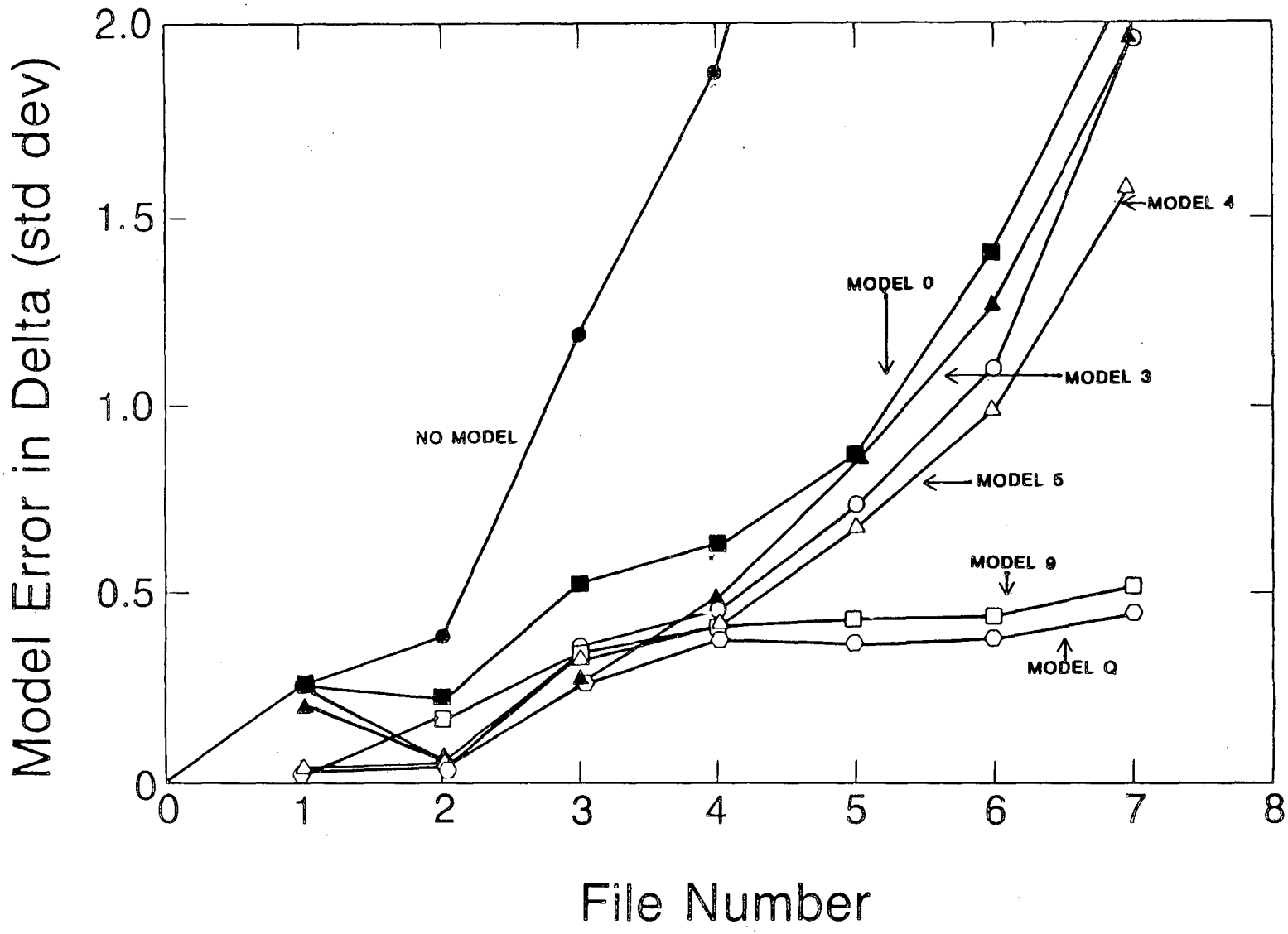

XBL 8511-12744

FIGURE D15

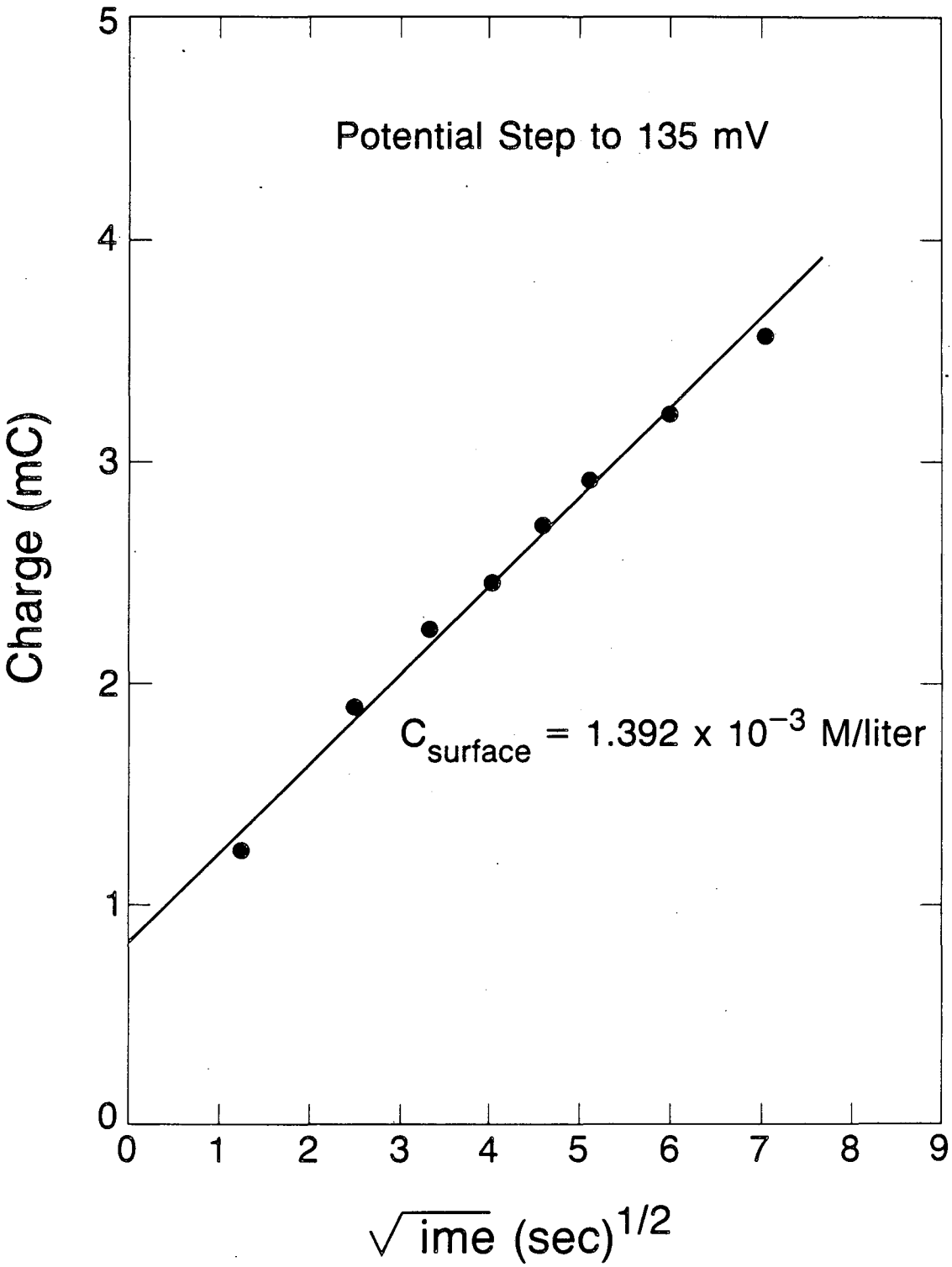

FIGURE D16

XBL 8512-5006

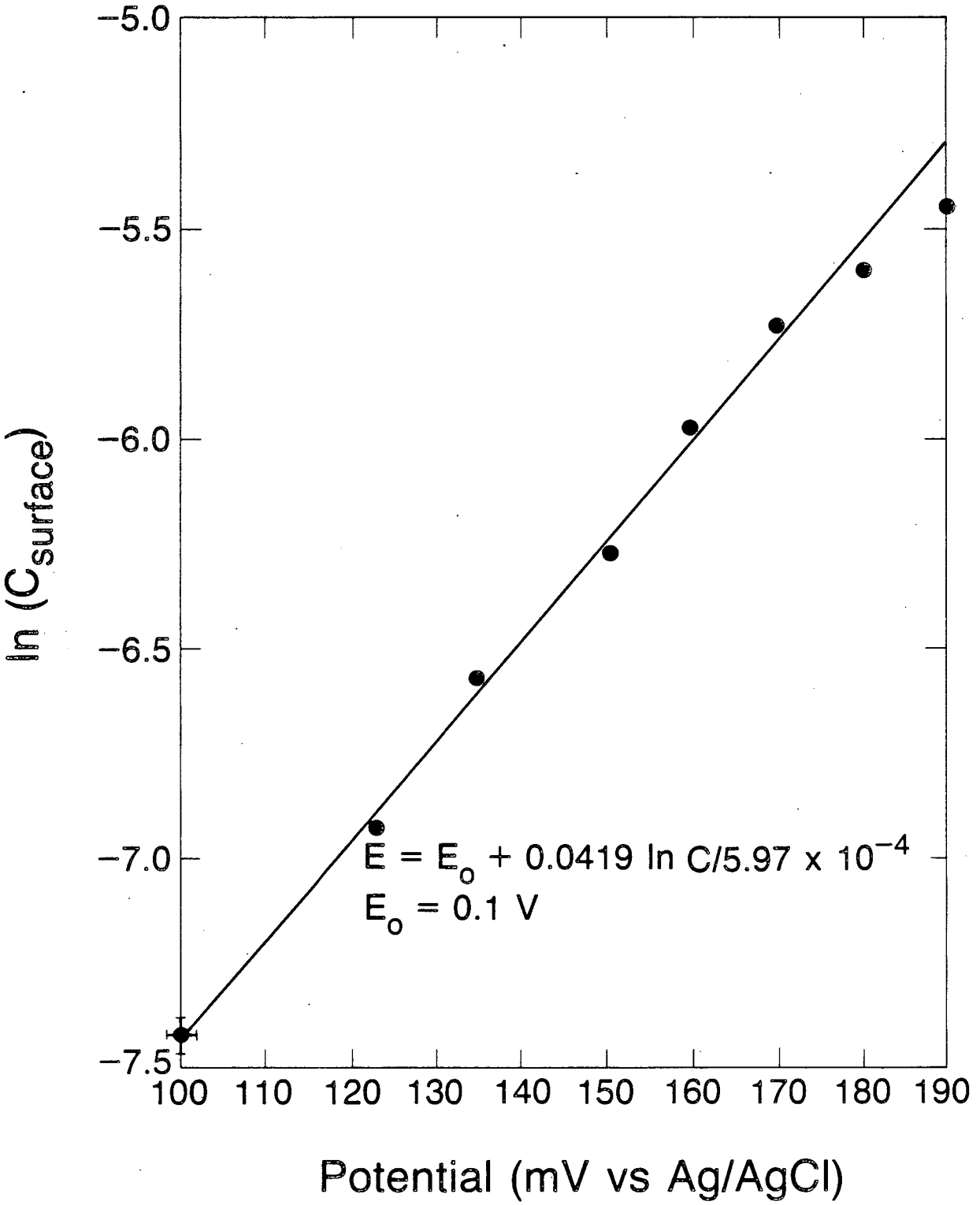

FIGURE D17

XBL 8511-12739

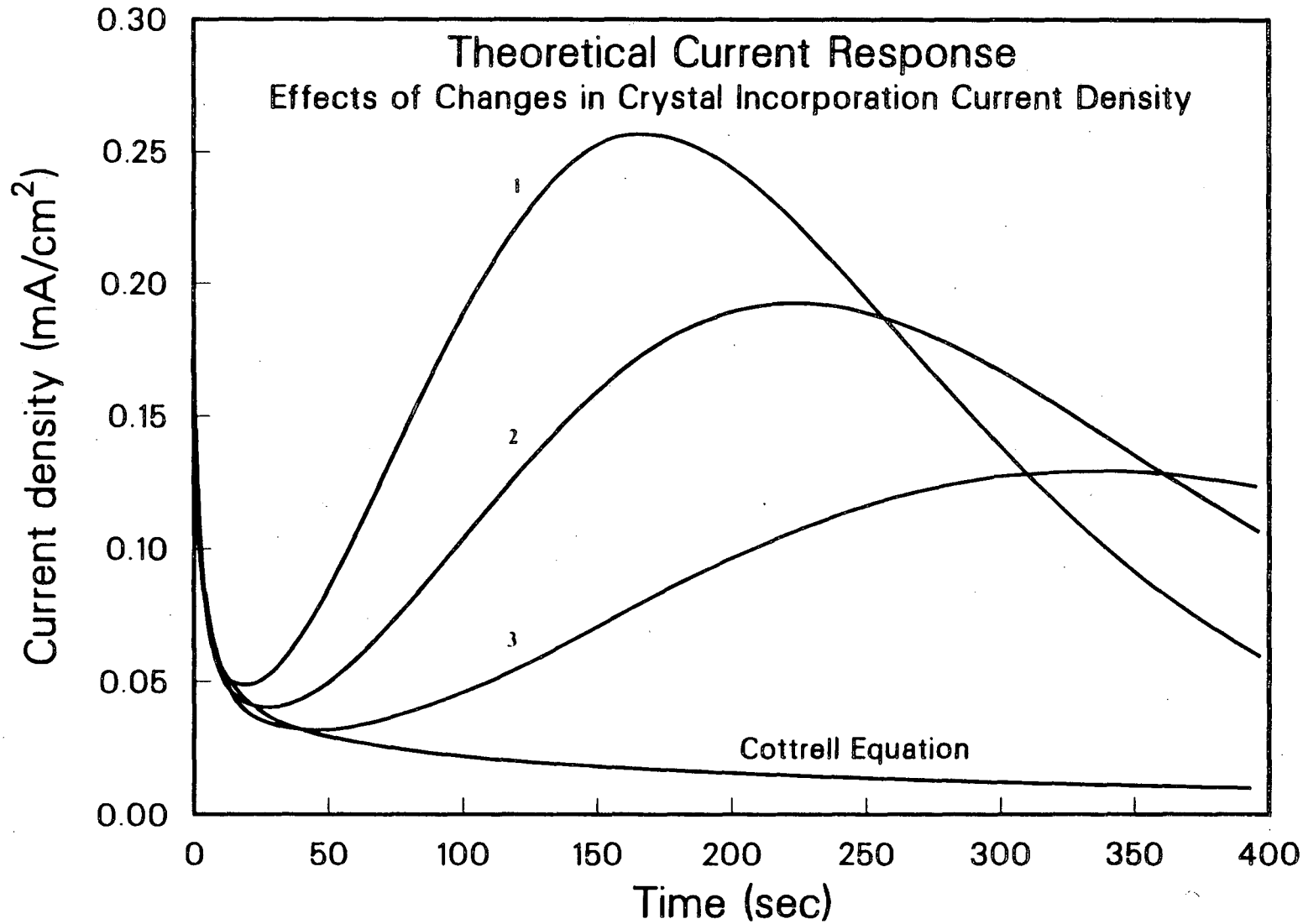

FIGURE D18

XCG 8511-500

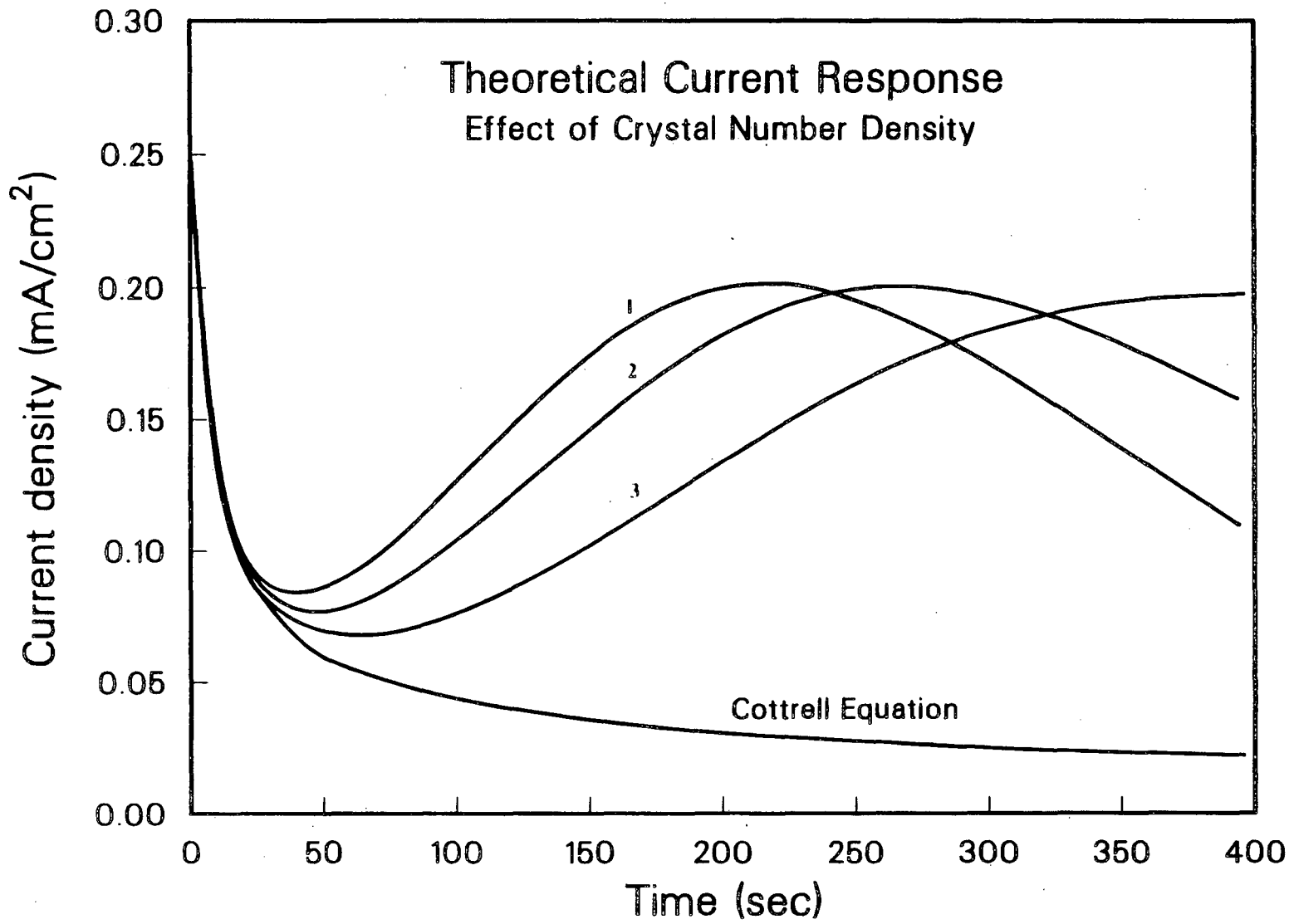

FIGURE D19

XCG 8511-501

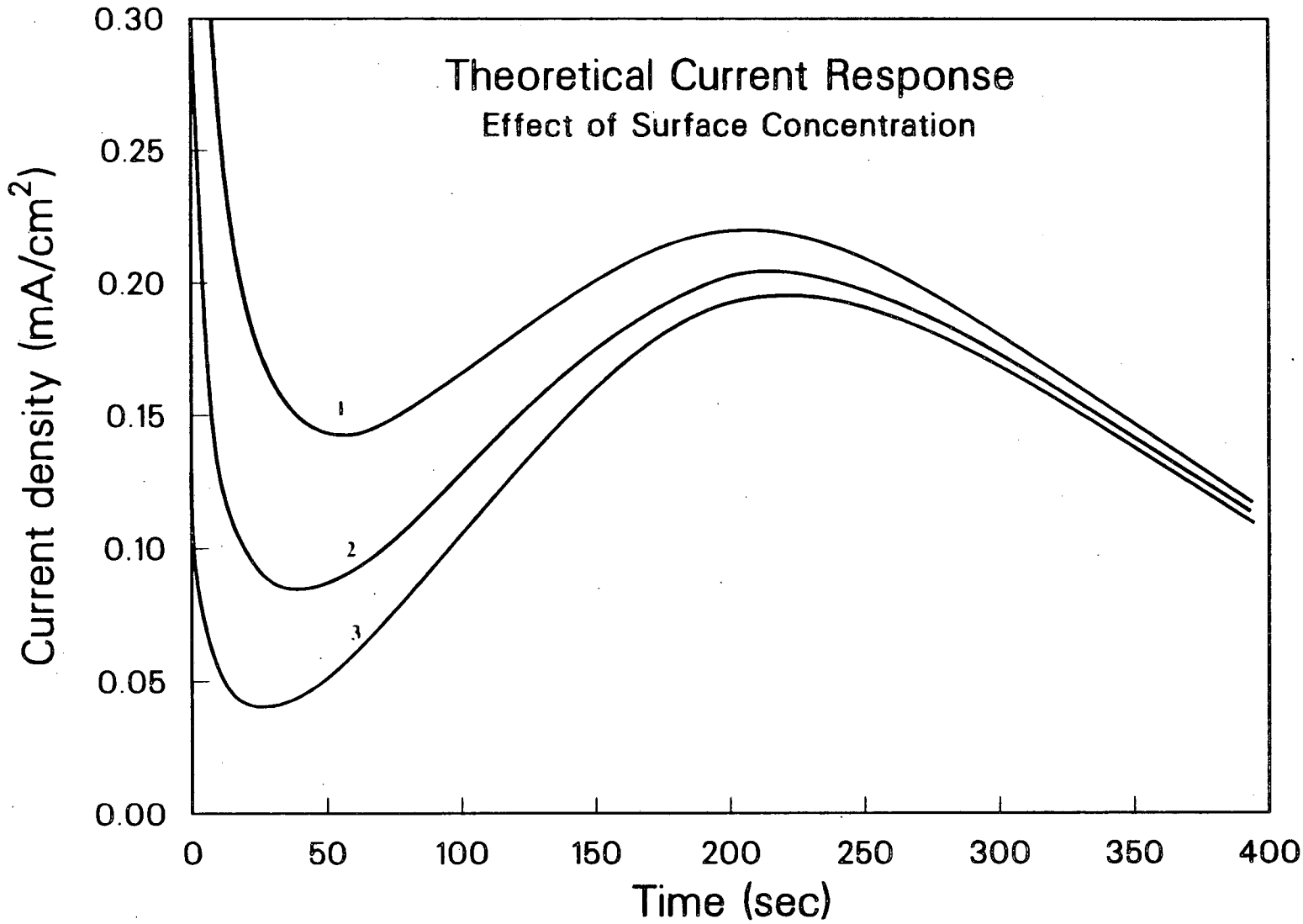

FIGURE D20

XCG 8511-499

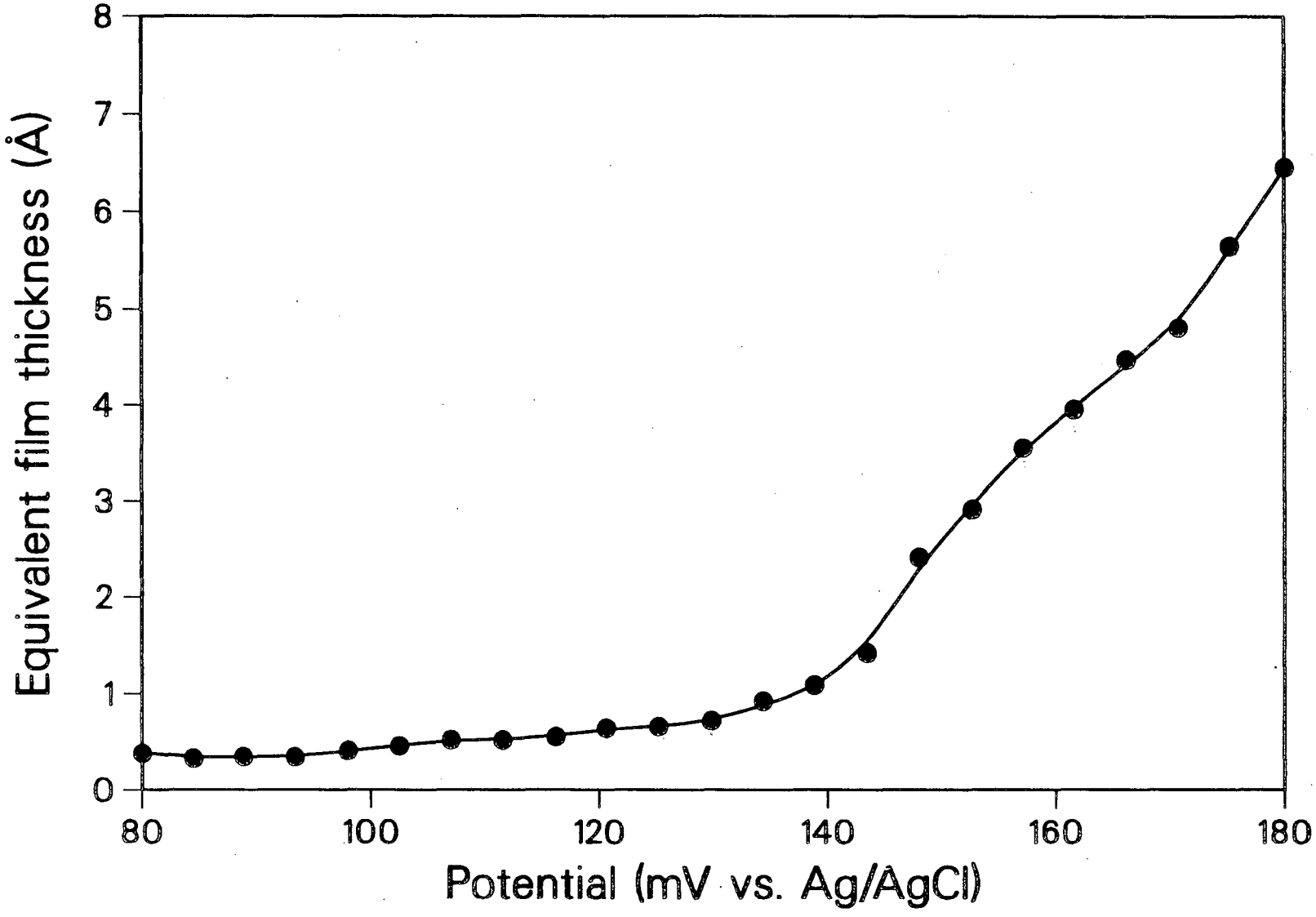

FIGURE D21

XCG 8511-497

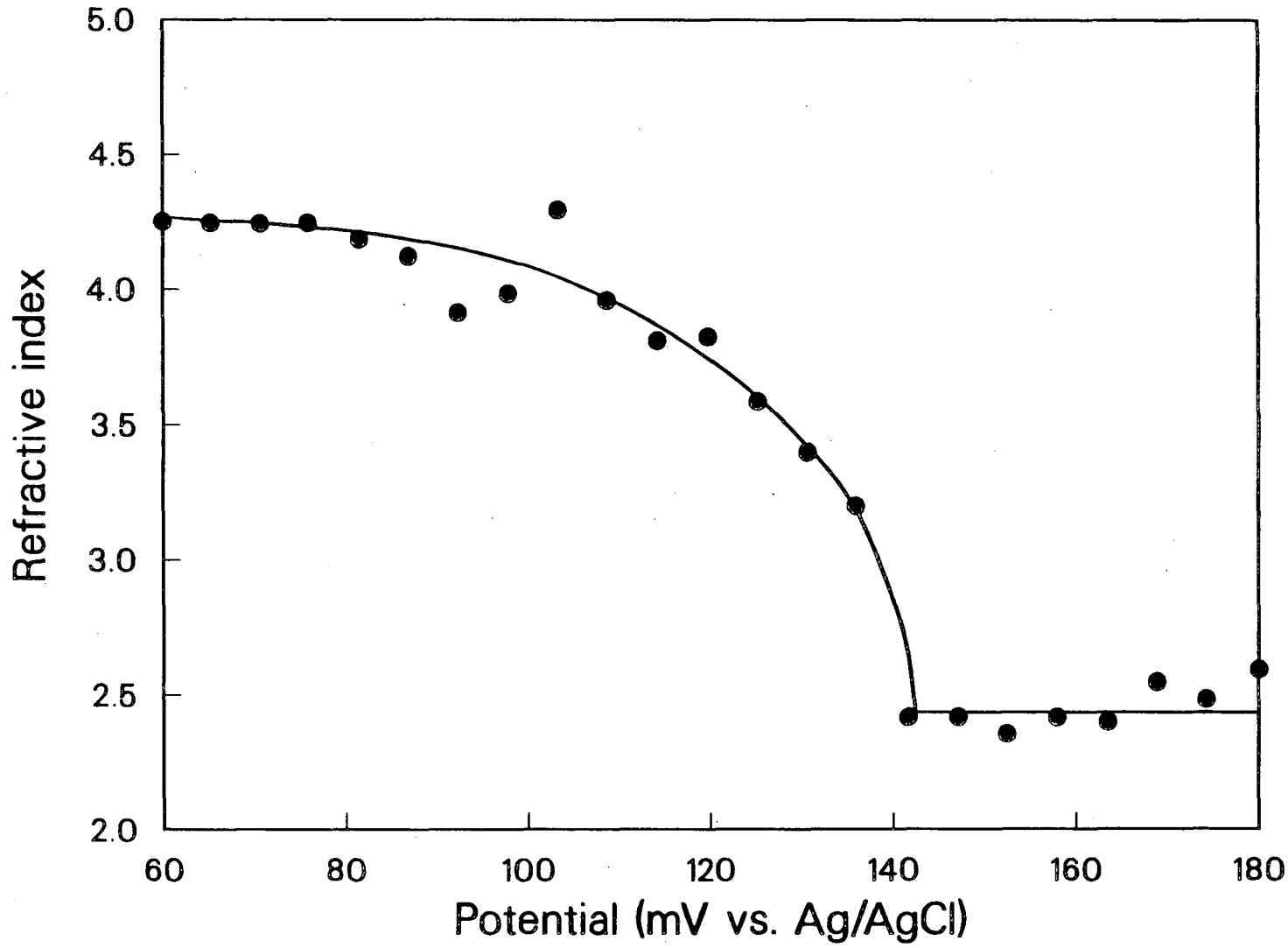

FIGURE D22

XCG 8511-498

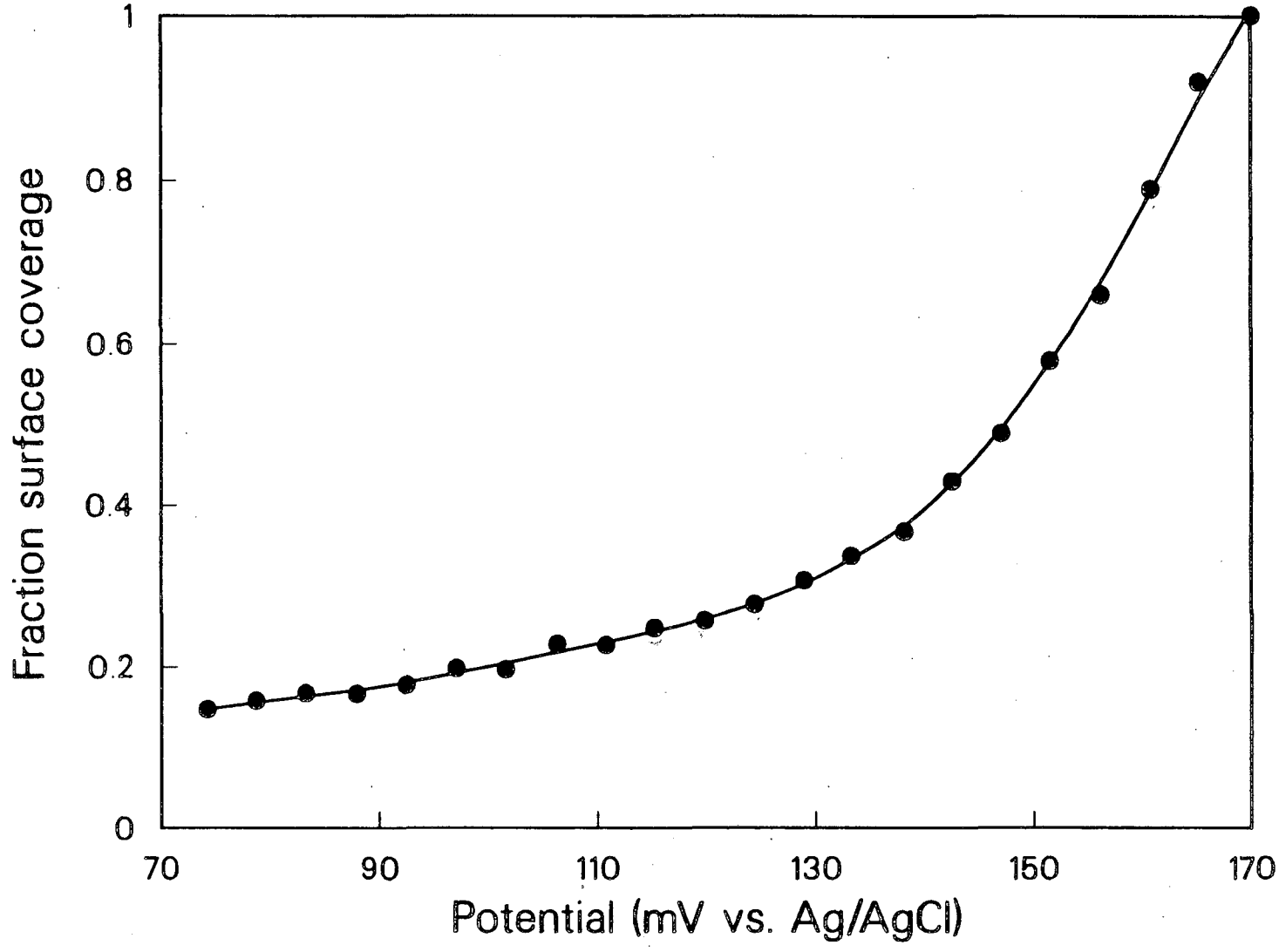

FIGURE D23

XCG 8511-496

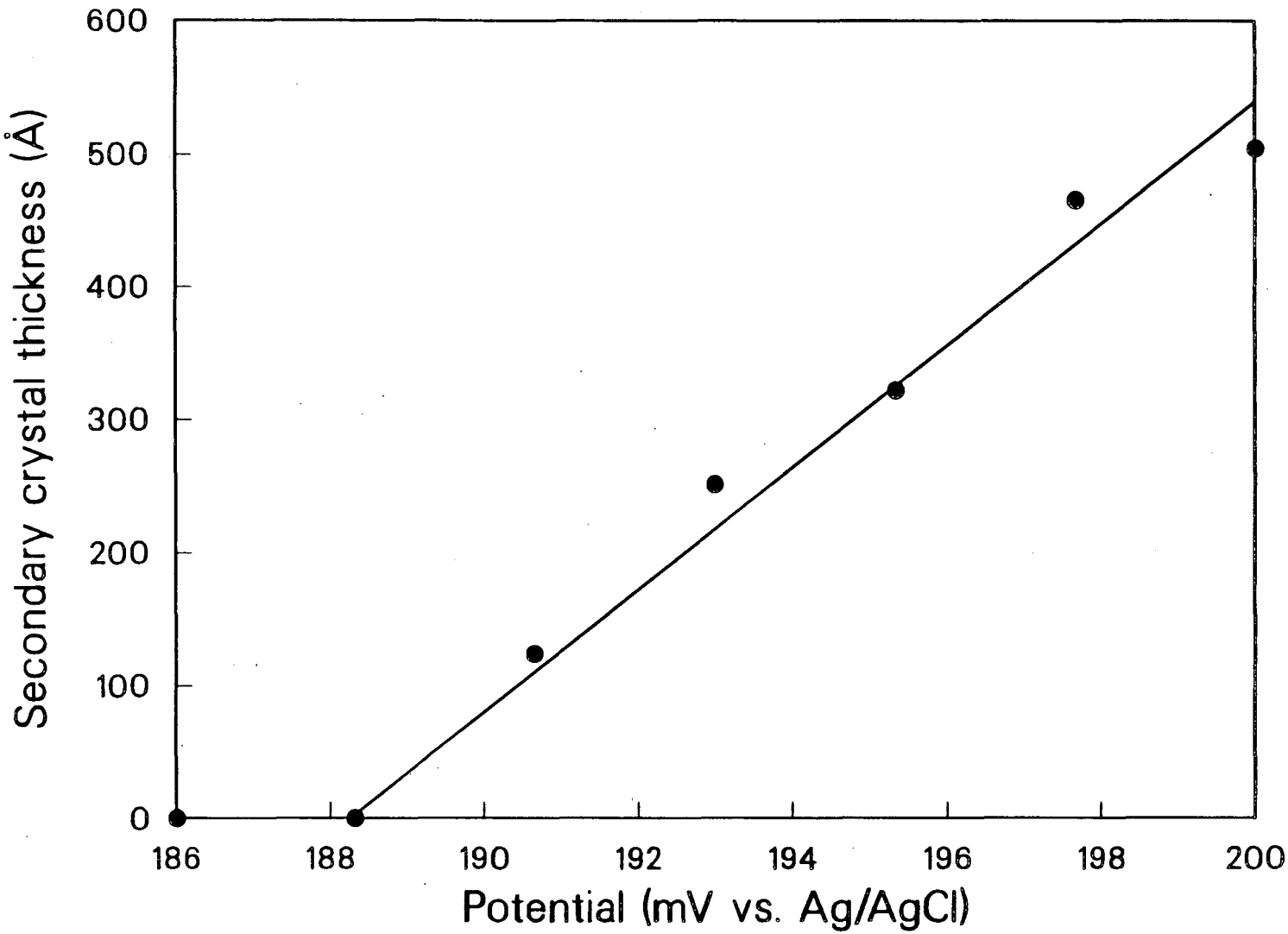

FIGURE D24

XCG 8511-495

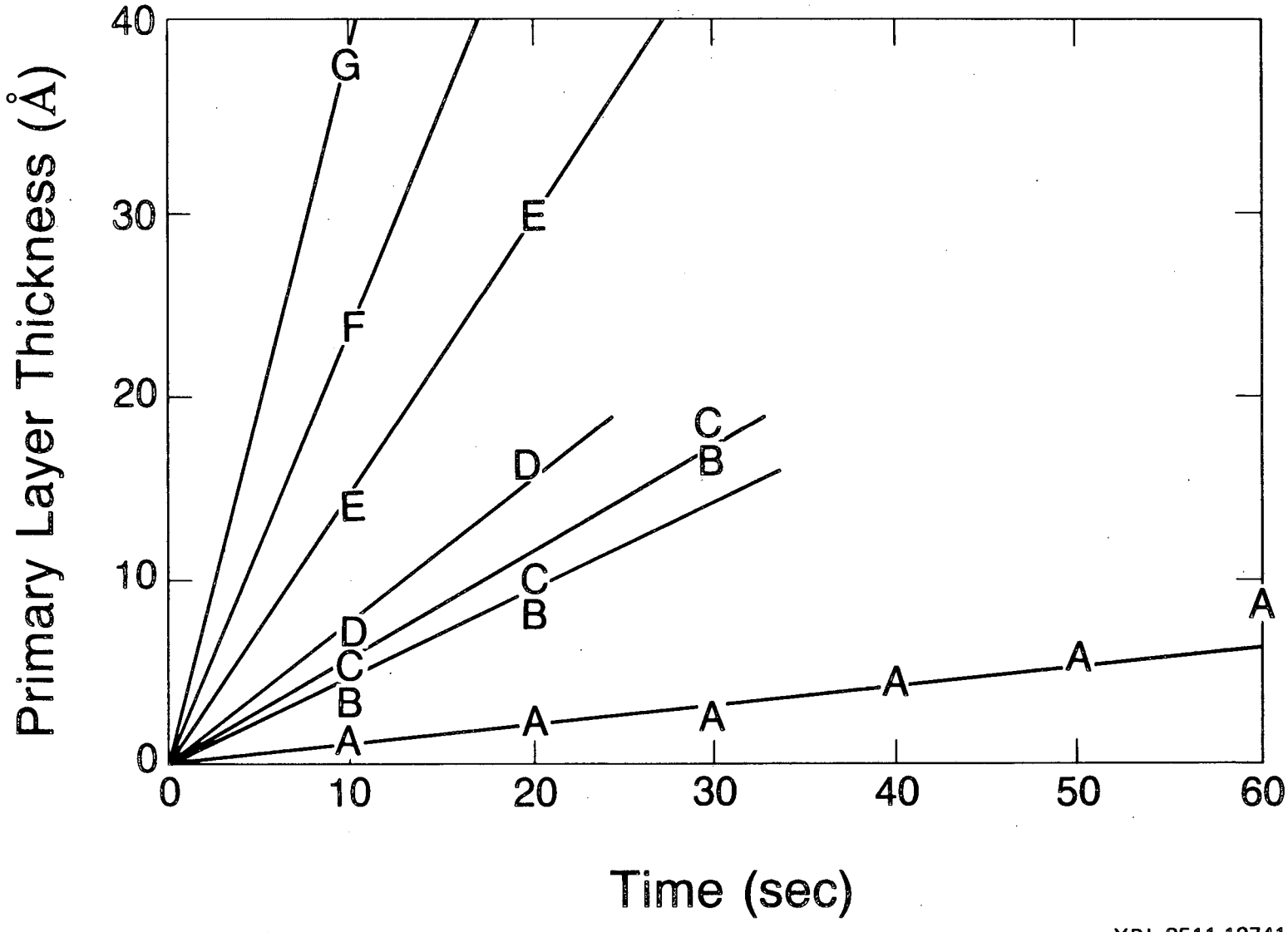

XBL 8511-12741

FIGURE D25

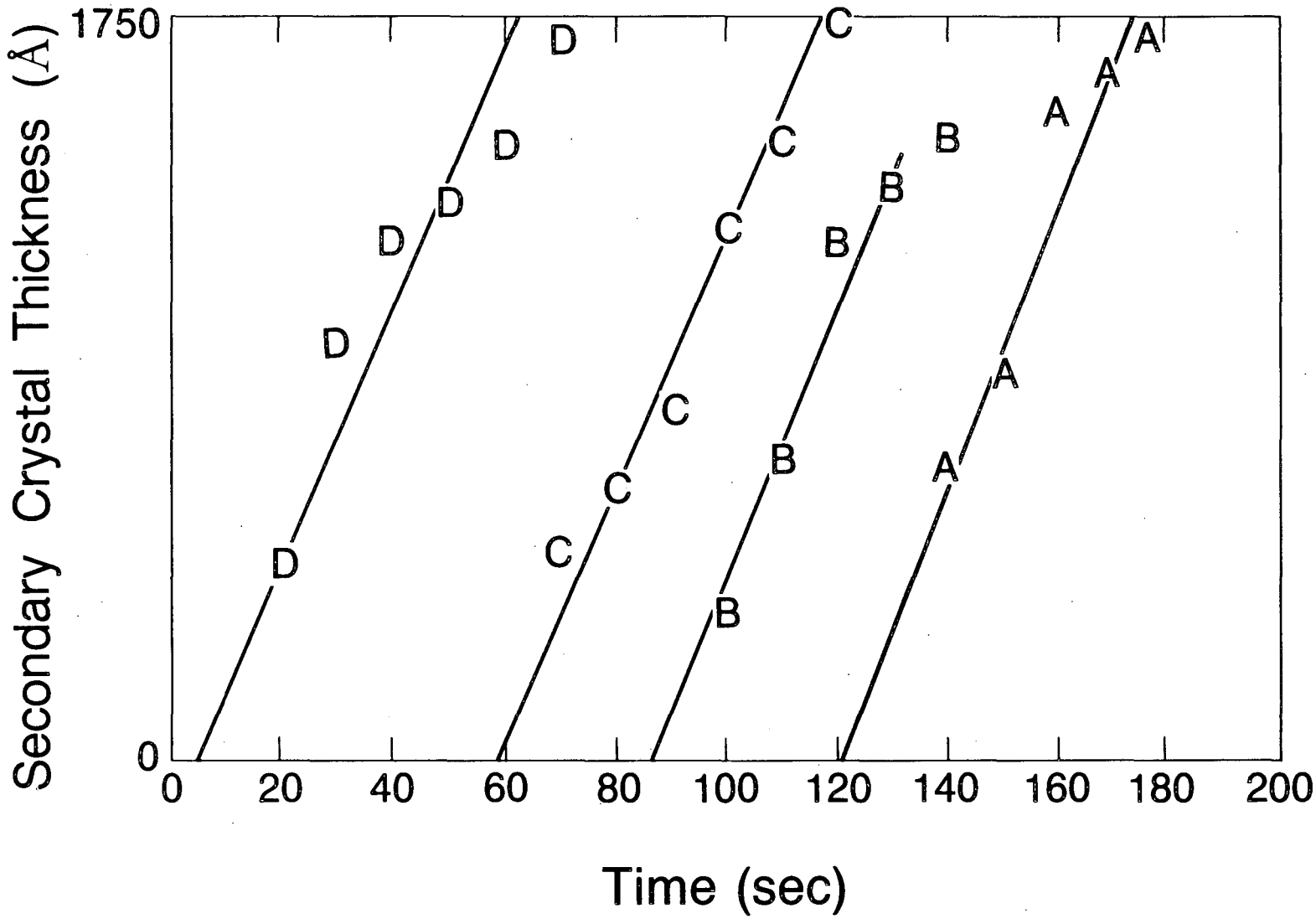

XBL 8511-12742

FIGURE D26

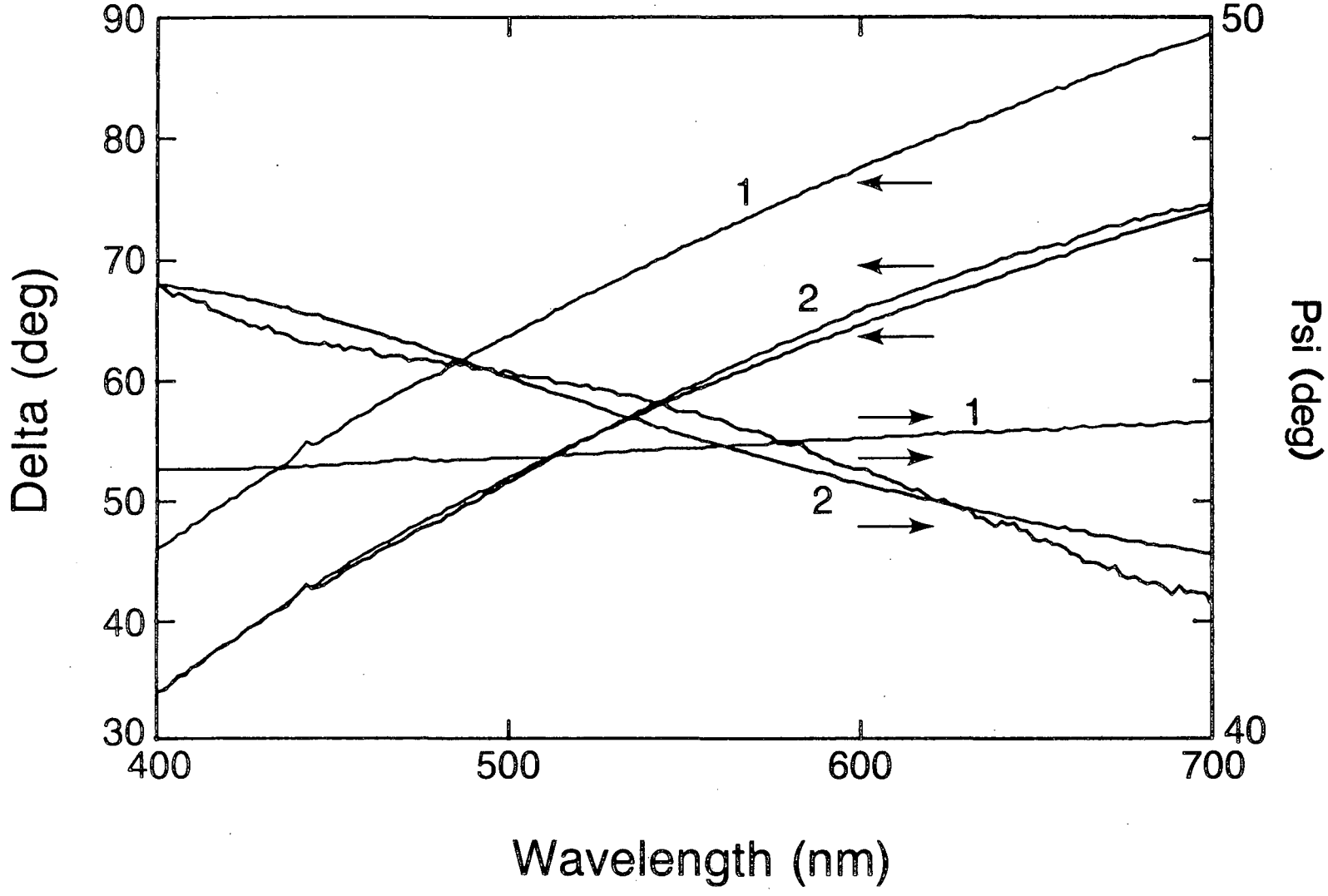

FIGURE D27

XBL 8511-12728

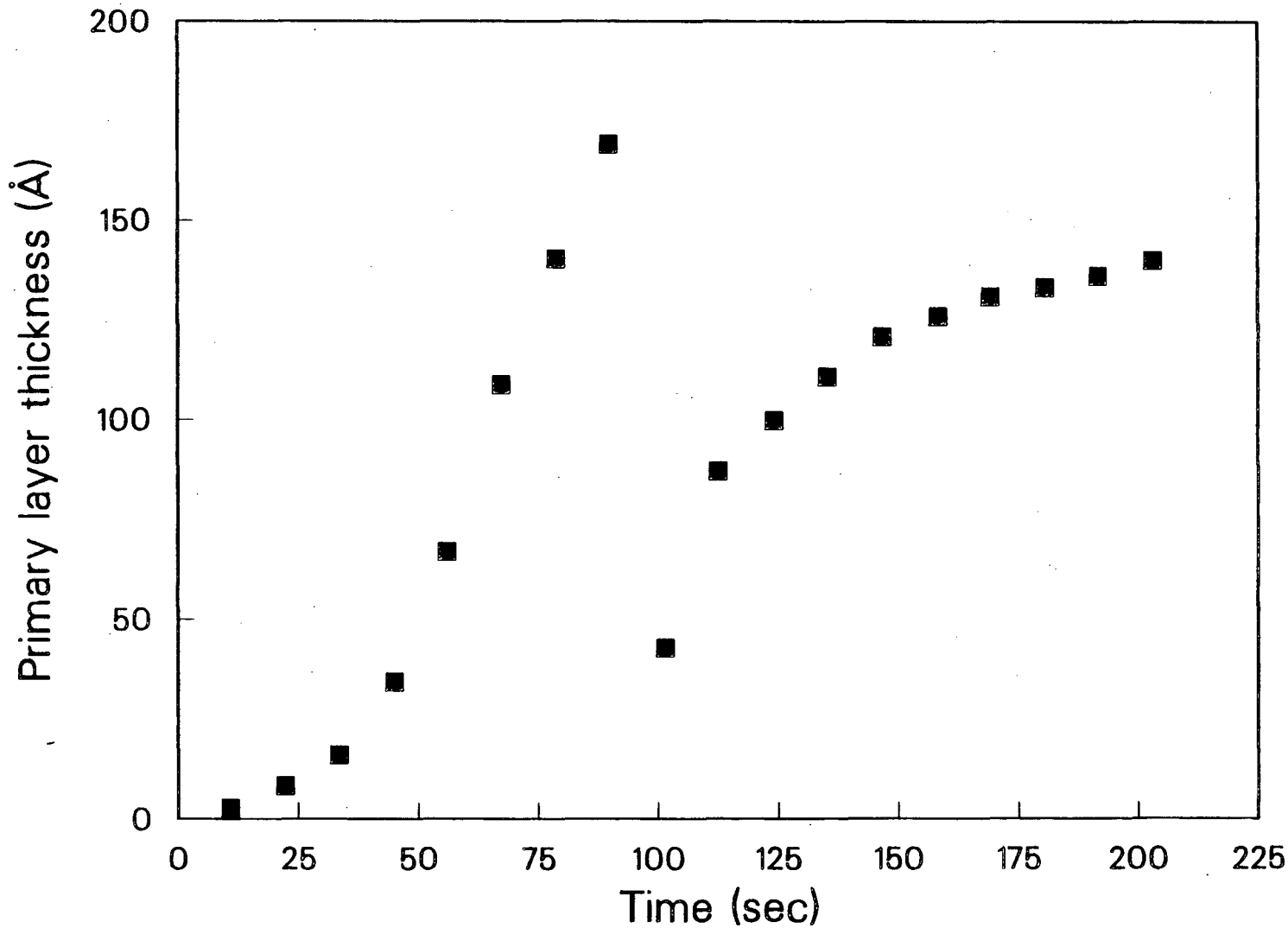

FIGURE D28

XCG 8512-543

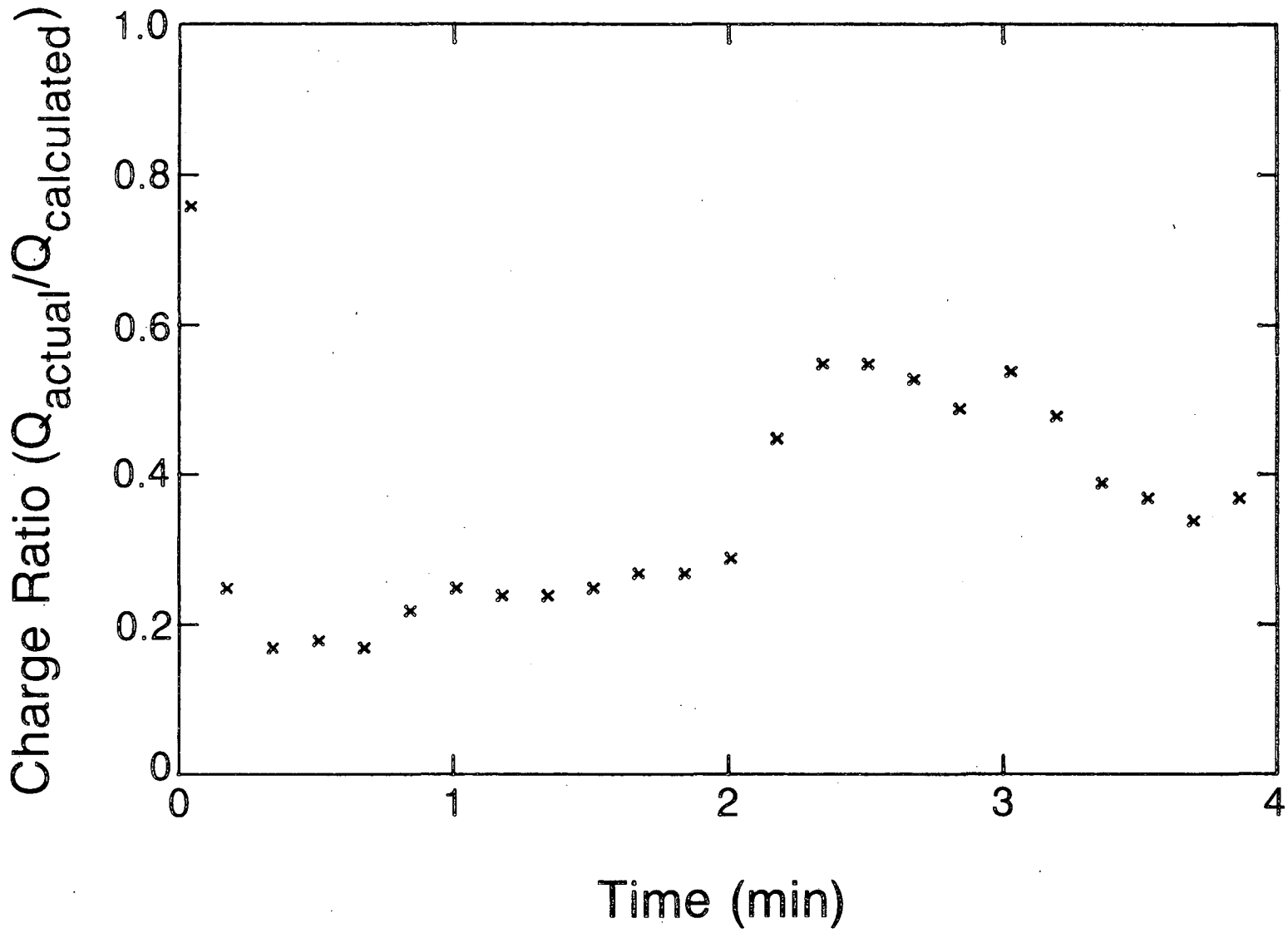

FIGURE D29

XBL 8511-12735

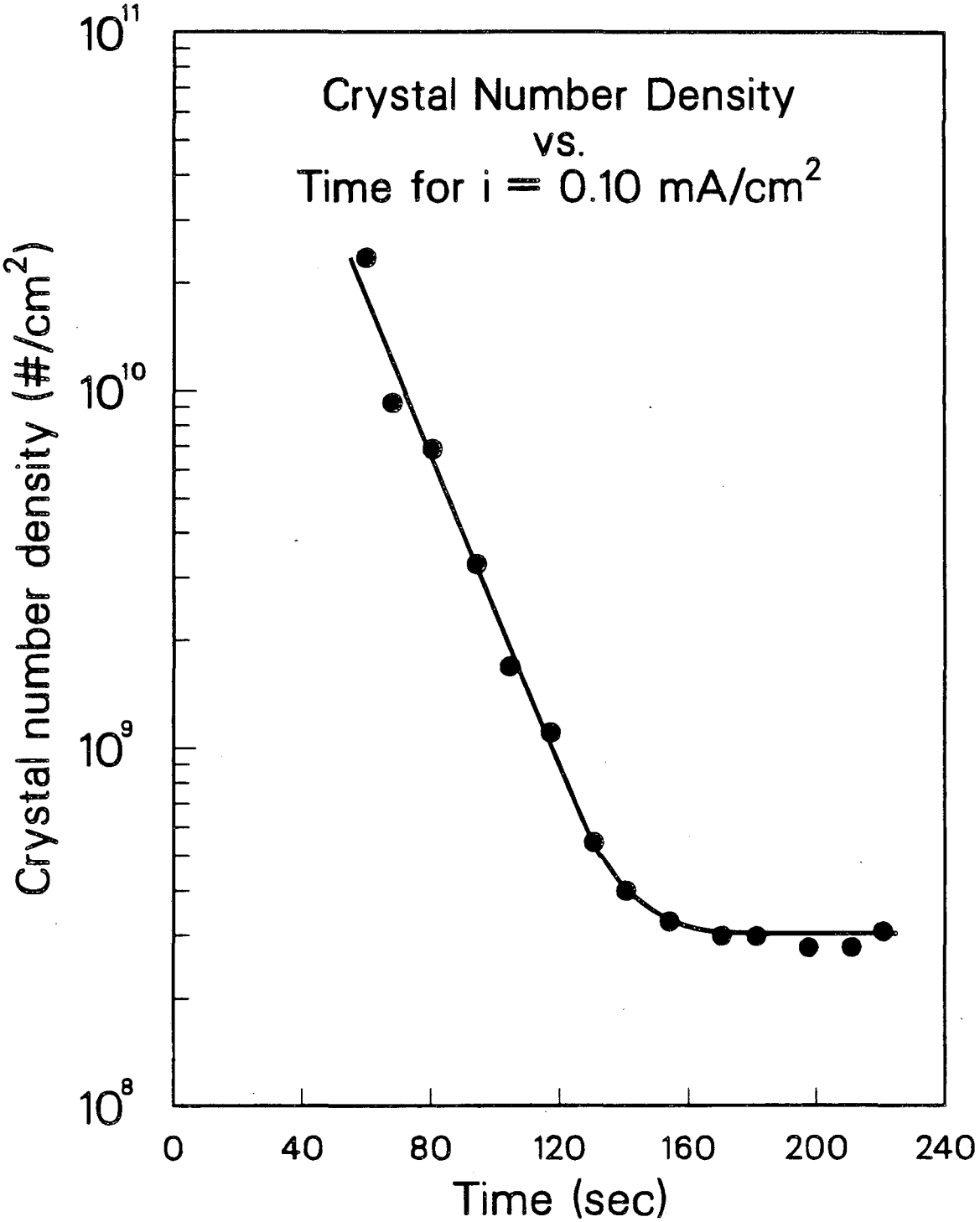

FIGURE D30

XCG 8512-544

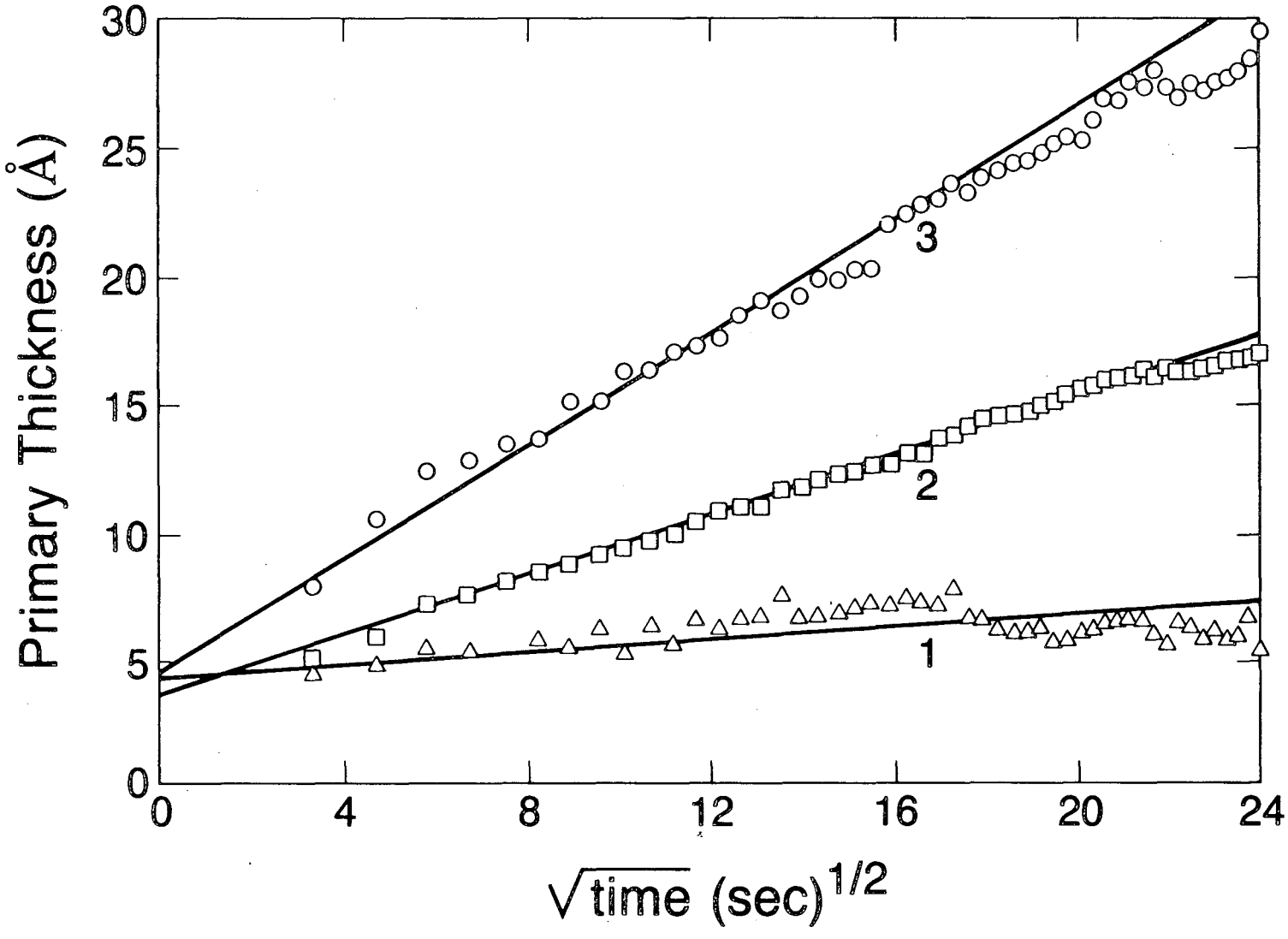

XBL 8511-12752

FIGURE D31

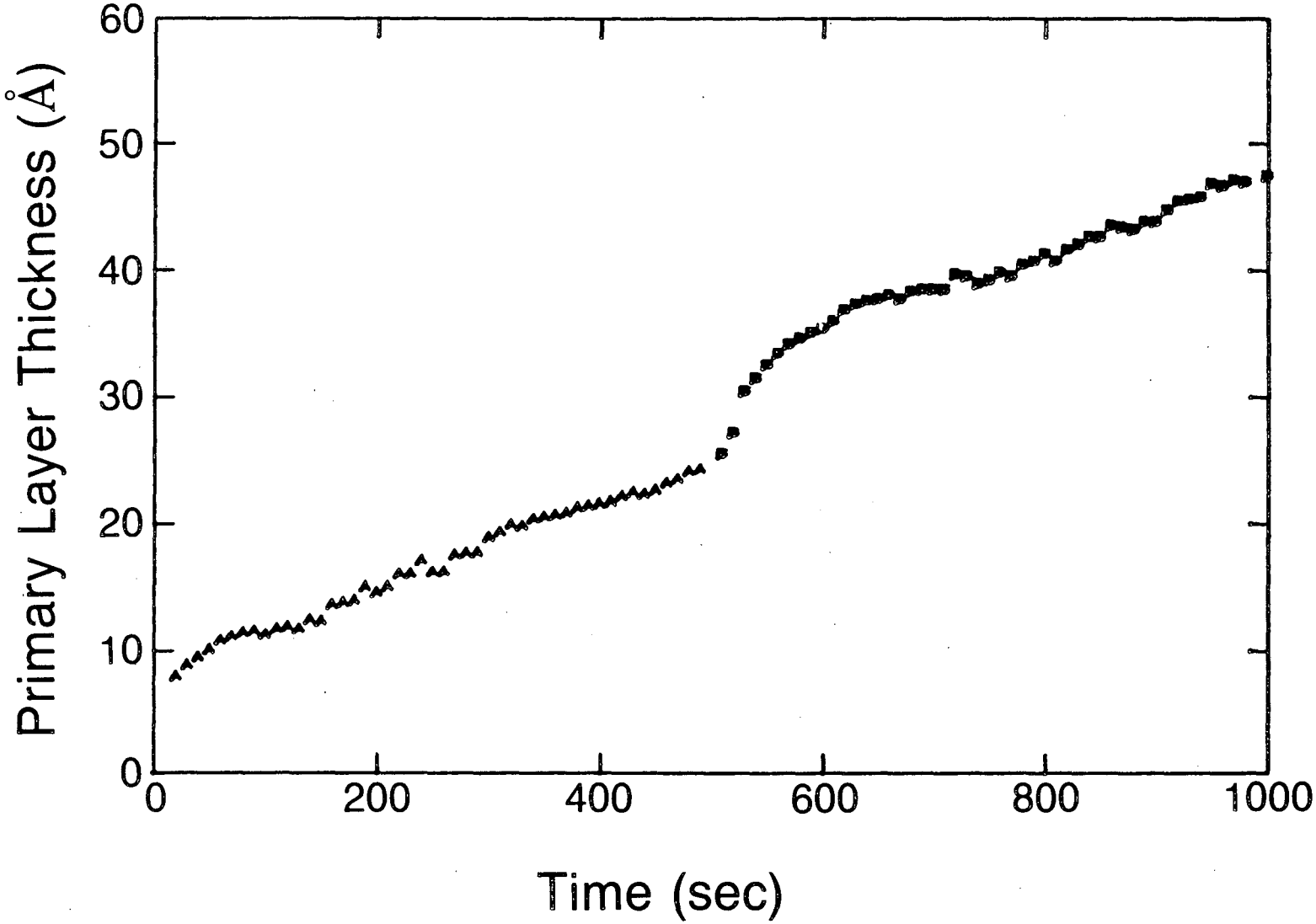

XBL 8511-12730

FIGURE D32

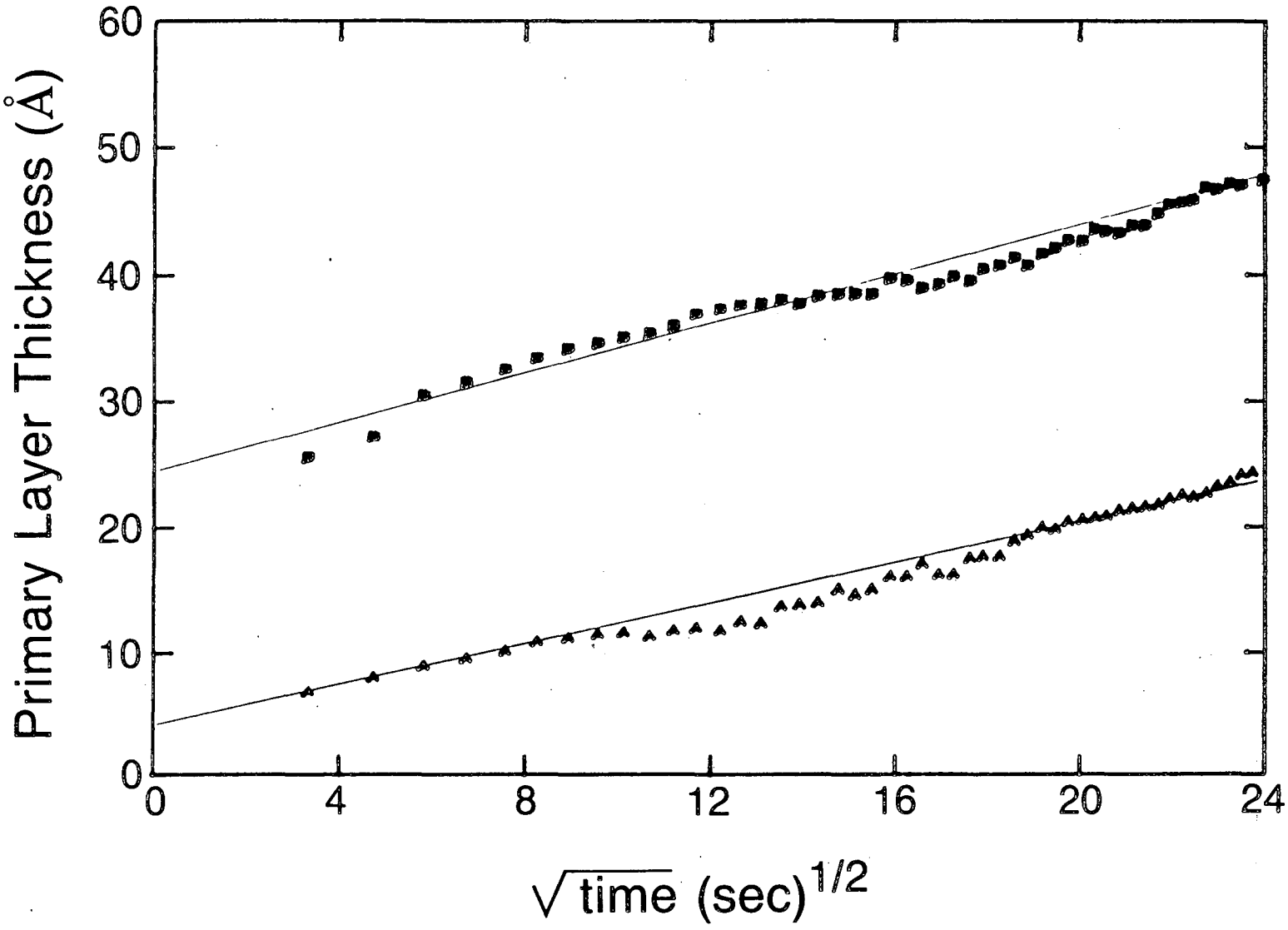

XBL 8511-12731

FIGURE D33

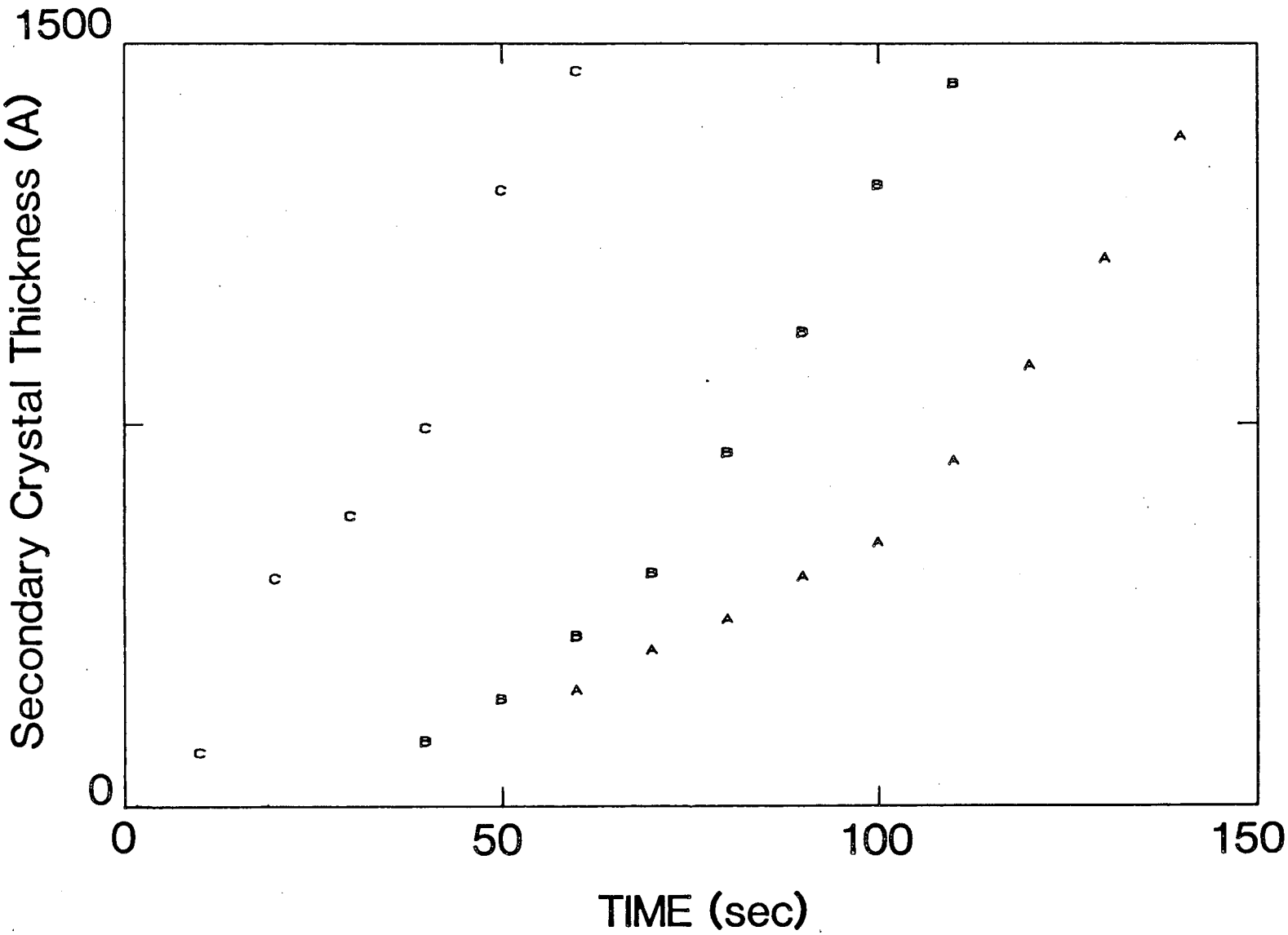

XBL 8512-5008

FIGURE D34

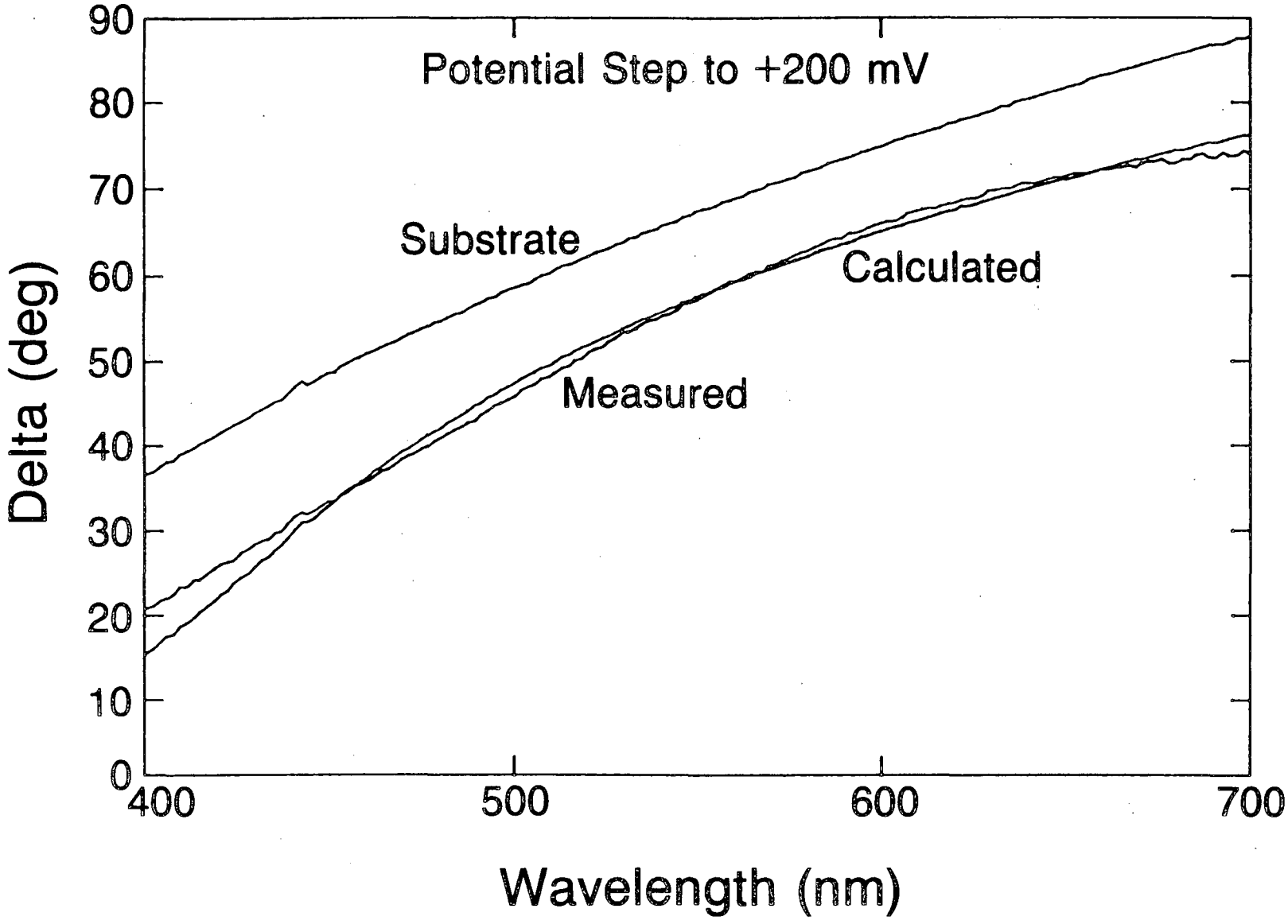

FIGURE D35

XBL 8511-12740

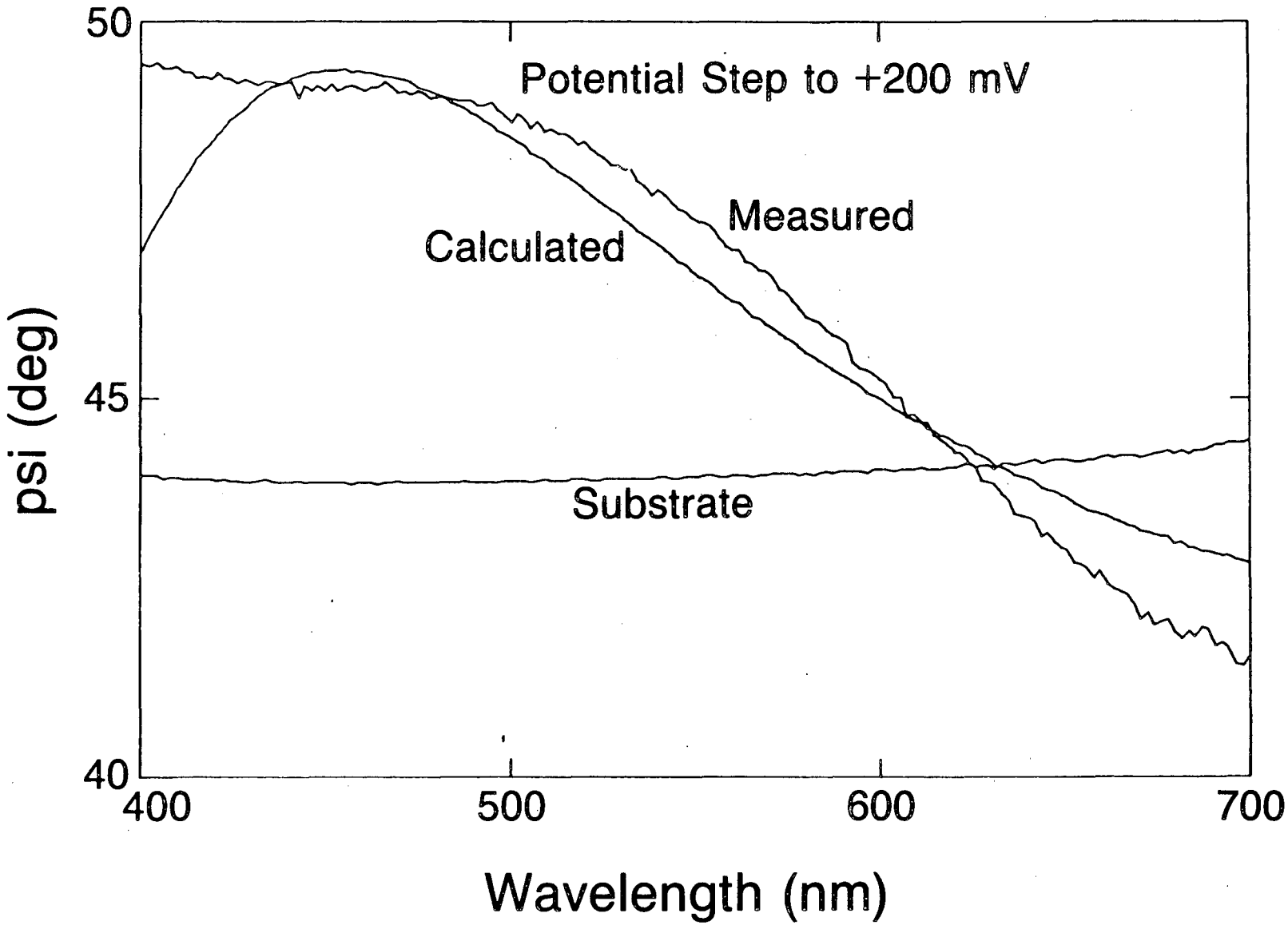

XBL 8511-12738

FIGURE D36

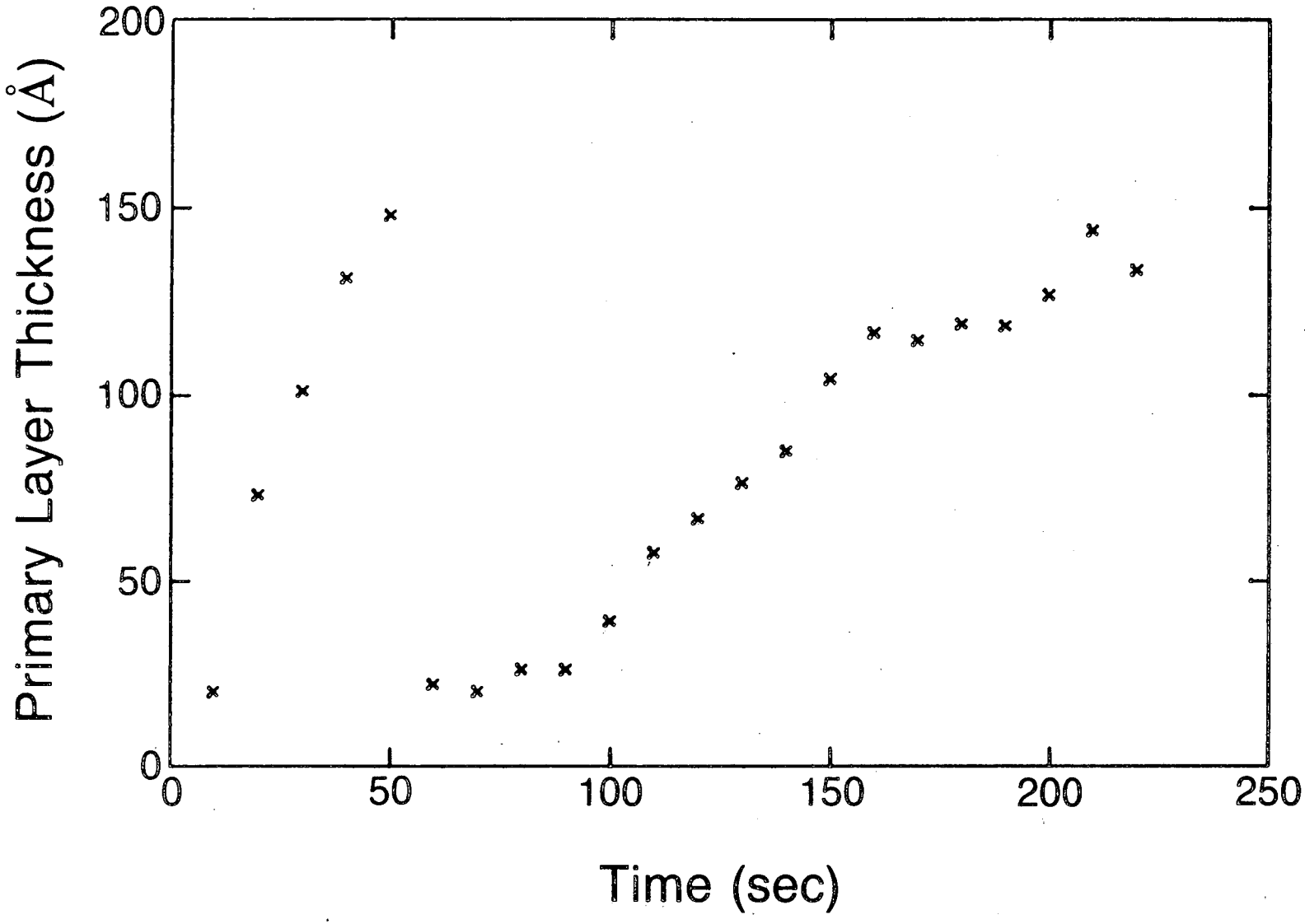

XBL 8511-12734

FIGURE D37

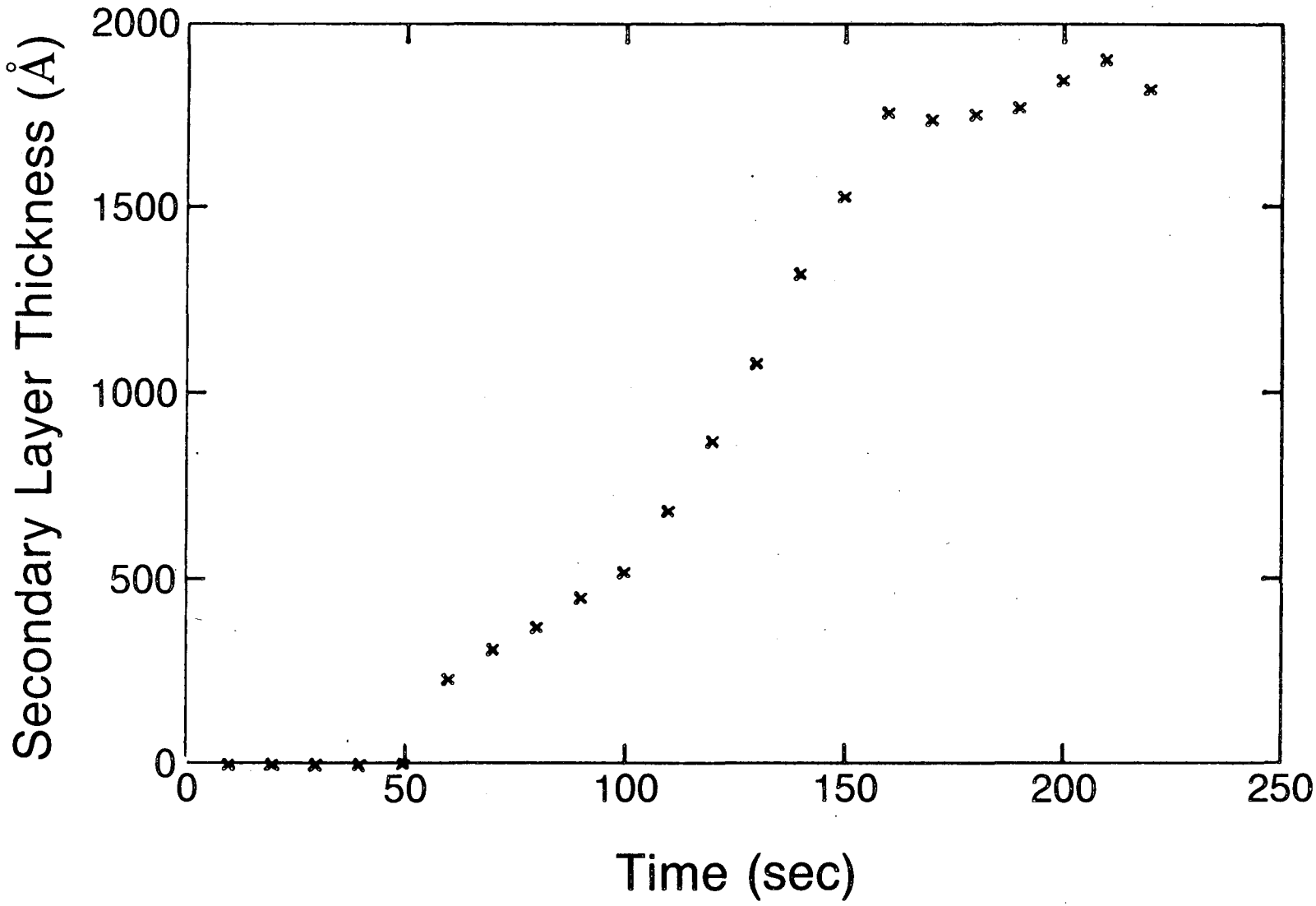

XBL 8511-12732

FIGURE D38

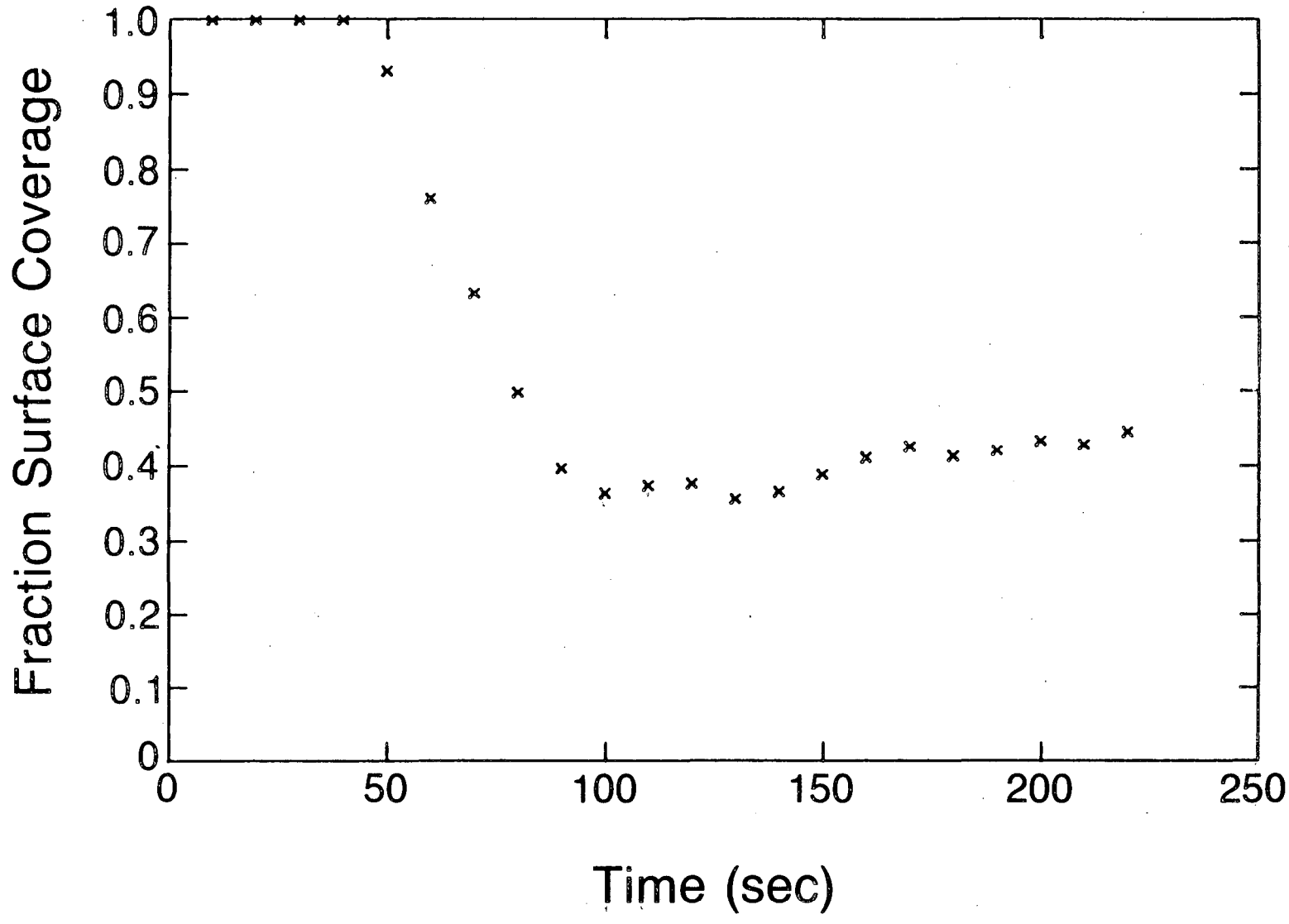

FIGURE D39

XBL 8511-12729

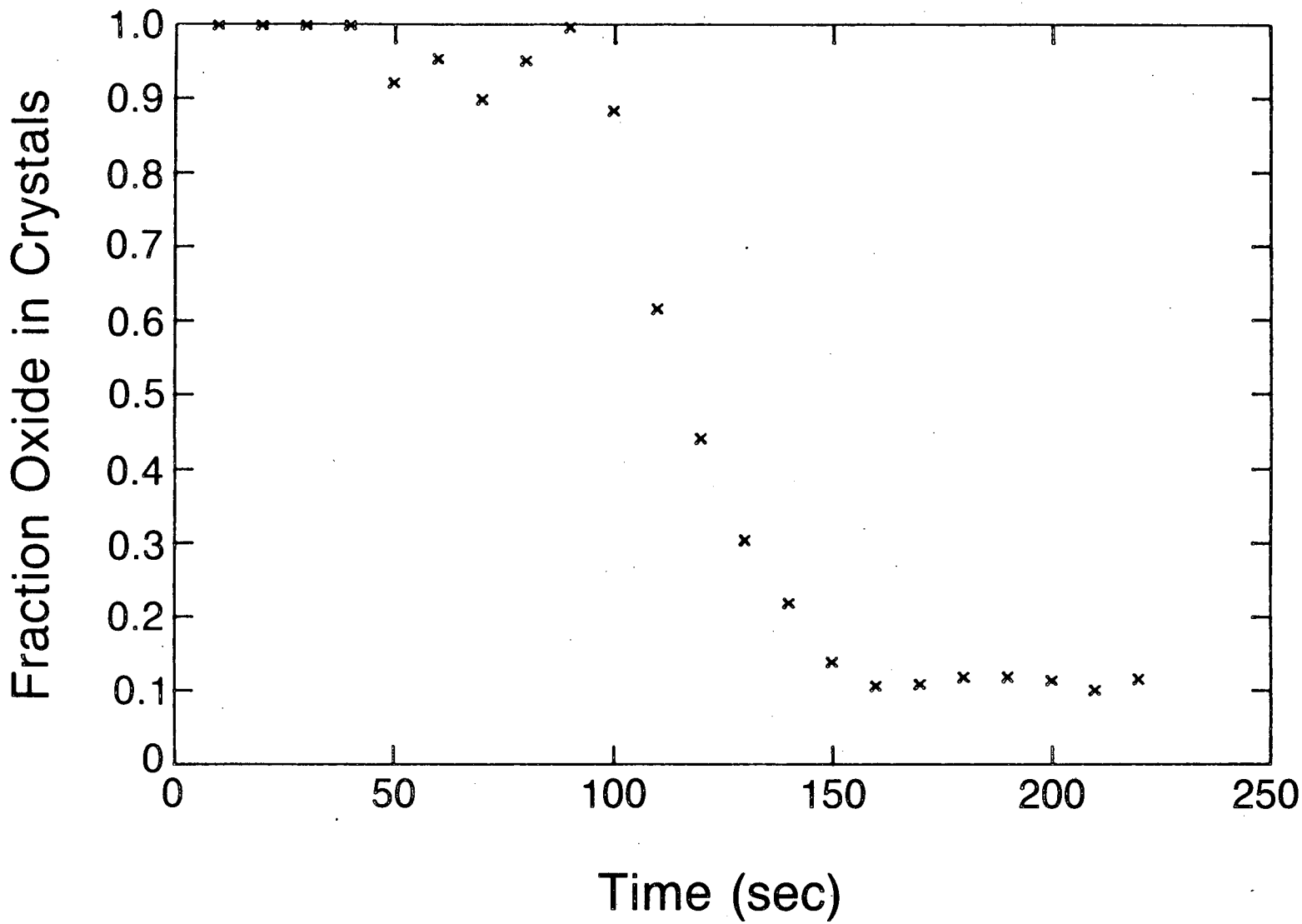

FIGURE D40

XBL 8511-12733

ACKNOWLEDGEMENTS

"No man is an island". Without the help and encouragement of my friends and fellow workers, the research for the thesis would have been nearly impossible. A thesis is a combined effort of many people, and mine is no exception.

I would like to thank Dr. Rolf H. Muller for his unending support, inspiration and scientific freedom. No one could ask for more. I would also like to express my gratitude to various professional staff members, guests, and students at Lawrence Berkeley Laboratory for their help and useful discussions: Dr. Phil Ross, Dr. Gholamabbas Nazri, Dr. Alfred T. D'Agostino, Dr. Norbert Staud, Dr. Jacques G. Thevenin, Davor Sutija, Michael Armstrong, Laura Mc Vay, and many others. Finally, I would like to express my appreciation for the friendly support offered by the technical staff at LBL. In particular, I would like to acknowledge Lee Johnson and Gay Brazil for their helpful assistance. Finally, I would like to thank Margrett Stevens, who worked as a technical assistant in the summer of 1985.

This work was supported by the Assistant Secretary of Conservation and Renewable Energy, Office of Energy Systems Research, Energy Storage Division of the U.S. Department of Energy under Contract No. DE-AC03-76SF00098.

This report was done with support from the Department of Energy. Any conclusions or opinions expressed in this report represent solely those of the author(s) and not necessarily those of The Regents of the University of California, the Lawrence Berkeley Laboratory or the Department of Energy.

Reference to a company or product name does not imply approval or recommendation of the product by the University of California or the U.S. Department of Energy to the exclusion of others that may be suitable.

LAWRENCE BERKELEY LABORATORY
TECHNICAL INFORMATION DEPARTMENT
UNIVERSITY OF CALIFORNIA
BERKELEY, CALIFORNIA 94720